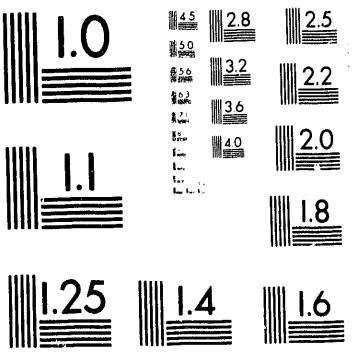
1.0
1.1
1.25
1.4
1.6
1.8
2.0
2.2
2.5
2.8
3.2
3.6
4.0
4.5
5.0
5.6

1 of 2

NUREG/CR-5907
SAND92-1563

Core-Concrete Interactions with Overlying Water Pools

The WETCOR-1 Test

Manuscript Completed: November 1993
Date Published: November 1993

Prepared by
R. E. Blose,* D. A. Powers, E. R. Copus, J. E. Brockmann,
R. B. Simpson, D. A. Lucero

Sandia National Laboratories
Albuquerque, NM 87185

Prepared for
Division of Systems Research
Office of Nuclear Regulatory Research
U.S. Nuclear Regulatory Commission
Washington, DC 20555-0001
NRC FIN A1218

*Ktech Corporation, Albuquerque, NM 87110

Abstract

The WETCOR-1 test of simultaneous interactions of a high-temperature melt with water and a limestone/common-sand concrete is described. The test used a 34.1-kg melt of 76.8 w/o Al_2O_3, 16.9 w/o CaO, and 4.0 w/o SiO_2 heated by induction using tungsten susceptors. Once quasi-steady attack on concrete by the melt was established, an attempt was made to quench the melt at 1850 K with 295 K water flowing at 57 liters per minute. Net power into the melt at the time of water addition was 0.61 $\pm$ 0.19 W/cm^3. The test configuration used in the WETCOR-1 test was designed to delay melt freezing to the walls of the test fixture. This was done to test hypotheses concerning the inherent stability of crust formation when high-temperature melts are exposed to water. No instability in crust formation was observed. The flux of heat through the crust to the water pool maintained over the melt in the test was found to be 0.52 $\pm$ 0.13 MW/m^2. Solidified crusts were found to attenuate aerosol emissions during the melt concrete interactions by factors of 1.3 to 3.5. The combination of a solidified crust and a 30-cm deep subcooled water pool was found to attenuate aerosol emissions by factors of 3 to 15.

Contents

Contents (concluded)

Figures

Figures (continued)

Figures (continued)

Figures (continued)

Figures (continued)

Figures (concluded)

Tables

Executive Summary

An important issue that has arisen in the discussion of advanced light water nuclear reactors and management of severe reactor accidents in nuclear power plants is the question of the coolability of molten core debris by water. To achieve coolability it is thought that core-debris melts deeper than about 10 cm must be fragmented for there to be sufficient heat transfer to water to quench the melt. Such fragmentation of high-temperature melts by water has not been observed in tests done to date. There has, however, been a persistent criticism of the small-scale tests that have not exhibited fragmentation. The criticism has been that a crust of solidified melt material is stabilized and prevented from fragmentation by adhering to the walls of the test fixture. Such adherence of melt to walls would not, it has been contended, inhibit fragmentation of large-scale melts exposed to water in reactor accidents.

The WETCOR-1 test was conducted to determine if preventing crust adherence to the test-fixture walls would lead to fragmentation and quenching of a melt exposed to water. Of particular interest in the WETCOR-1 test were hypotheses advanced by a peer review panel that (a) progression of the freezing from the center of the melt to its perimeter would lead to fragmentation and (b) instabilities in the initial formation of a crust unable to adhere to the test-fixture walls would lead to fragmentation.

The melt in the WETCOR-1 test was heated by induction using tungsten susceptor rings at the perimeter of the test-fixture crucible. This heating arrangement ensured that the hottest parts of the test apparatus were the test-fixture walls. Intense heating of the walls adjacent to the susceptor rings prior to water addition provided a heat source when water was added to delay cooling of the walls relative to cooling of the melt. Further, the rings were configured so that heat could be conducted from the melt to the topmost susceptor to further inhibit cooling at the perimeter of the melt.

The melt used in the WETCOR-1 test was composed of 76.8 w/o Al_2O_3, 16.9 w/o CaO, 4 w/o SiO_2, and the balance was low-concentration impurities. Simulation of the oxide phase of core debris was selected based on scaling analyses of crust growth and crust fracturing. Concrete used in the WETCOR-1 test was a limestone/common-sand concrete used extensively in previous tests of melt interactions with concrete.

Visual data obtained when a crust formed on the melt due to air cooling demonstrated that the test configuration functioned as intended. The crust formed by air cooling did not adhere to the susceptor rings. Once observations of the crust produced by air cooling were complete, power was increased to ensure no crust was present when water was added to cool the melt.

Quenching the melt was attempted with water at 295 K flowing at 57 liters per minute. At the time quenching began, the bulk melt temperature was 1850 K. The susceptor rings that constituted the boundary of the melt were heated to 2073 $\pm$ 50 K. Net power input to the melt at the start of quenching was 0.61 $\pm$ 0.19 W/cm^3.

Neither fragmentation of the melt nor indication of crust instability was observed in the test. As has been observed in most past tests of melt/concrete/coolant interactions, a crust of solidified material formed and separated the water pool from the melt. The melt continued to attack the concrete.

The long-term heat flux from the melt, through the crust and into the water, was found to be 0.52 $\pm$ 0.13 MW/m^2 when molten material was present. Determinations of this heat flux made by two methods after power input to the melt was terminated and the molten material froze were 0.25 $\pm$ 0.08 and 0.20 $\pm$ 0.08 MW/m^2.

The WETCOR-1 test also provided data on the attenuation of aerosol emissions during melt/concrete interactions by a solidified crust on the melt and by the combination of a solidified crust and a subcooled water pool. The crust was found to attenuate aerosol emissions by factors of 1.3 to 3.5. The combination of a crust and a 30-cm-deep, subcooled water pool attenuated aerosol emissions by factors of 3 to 15.

1.0 Introduction

One of the most important phenomenological issues in the progression of severe accidents after the reactor vessel has failed is whether or not the plant can be brought to a stable condition, thus avoiding the threat to containment integrity posed by basemat penetration or containment pressurization. The most commonly available mechanism for removing heat from discharged melt in light water reactor containments is the addition of water. The Department of Energy, industry, and the Nuclear Regulatory Commission (NRC) are working to develop and evaluate design criteria to address core debris coolability by water pools [Fauske, 1990]. The WETCOR experiment program has been performed at Sandia National Laboratories (SNL) as part of the NRC effort to address this issue, which is identified under the revised Severe Accident Research Plan [Office of Nuclear Regulatory Research, 1992]. These tests are intended to complement and augment the ACE/MACE program sponsored by Electric Power Research Institute (EPRI) and others.

A number of tests of the effects coolant admissions have on melt interactions with concrete have been conducted [Tarbell et al. 1987; Blose et al. 1987; Spencer et al. 1991]. All of these tests show that a crust of frozen debris forms when a water pool accumulates over the melt. Melt below this crust continues to attack the concrete. Heat extracted by water from the melt through the crust has not been greatly different than heat losses by radiation and convection. As a result, a water pool overlying the melts used in tests has hardly perturbed the rate of attack on the concrete. This general behavior has been observed when the molten material contacted by the water has been stainless steel (test SWISS-II), molten concrete (tests SWISS-I, FRAG-3 and FRAG-4) [Blose, 1987; Tarbell et al., 1987] or molten uranium dioxide (MACE scoping test) [Spencer, 1991]. That is, the crust formation result has proven to be remarkably insensitive to melt or concrete properties.

It is tempting, then, to conclude from this substantial body of test data that there is no assurance simple admission of water to core debris will quench or even significantly cool the core debris. Indeed, calculations by Copus [E.R. Copus and D.A. Powers, *A Study of the Limits of Core Debris Coolability During Interactions with Concrete*, unpublished report, Sandia National Laboratories, Albuquerque, NM, July 1990] using boiling heat flux correlations for a flat plate in conjunction with the CORCON model of core debris interactions with concrete have shown that core debris would have to be spread to a collapsed depth of less than 10 cm for an overlying water pool to arrest the attack on concrete. Prolonged, high heat fluxes to water necessary to quench deep melts have been neither observed in tests conducted to date nor calculated with existing models. Evidence from tests done to date and from existing models suggests that the interfacial crusts that form when water contacts high-temperature melts must be destabilized to achieve the high heat-extraction rates necessary to quench and permanently cool core debris. That is, the crusts must fragment or at least fracture extensively to produce sufficient surface area to sustain the necessary rates of heat transfer to the water.

There is, however, an issue that bars drawing bold conclusions from the available test data. All the tests done to date have used rather small melts relative to the size of molten core debris pools envisaged in hypothesized severe reactor accidents. Geometric characteristics of melt surfaces exposed to water in tests to date are presented in Table 1.1. The tests have been constructed to represent a typical node within the large area covered by the core debris once the core debris has been expelled into a reactor containment building. Though some effort has been expended in past test programs to ensure the essential boundaries of the test fixture are both adiabatic and do not influence the interactions being examined in the test, it is not possible to show that these boundaries have not influenced the formation and stability of crusts when water was admitted.

No quantitative, phenomenologically based hypotheses on how boundaries of the test fixture affect the crusts have yet been advanced. Three qualitative arguments have been advanced, at least informally, in the course of review of the test results and speculations about core debris coolability. One contention is that crusts grow in the tests from the perimeter of the melt toward the center. This growth from the points of highest heat loss (losses go to both the test fixture walls and to the developing water pool) might affect crust

Table 1.1 Geometric characteristics of melt exposed to water

Test	Characteristic Length (m)	Area (m^2)	Perimeter (m)
FRAG-3,4	0.22	0.04	0.69
SWISS-I,II	0.22	0.04	0.69
MACE scoping test	0.3	0.09	1.2
MACE 1B test	0.5	0.25	2.0
WETCOR-1	0.33	0.078	1.03
WETMET-1	0.41	0.13	1.29
Typical Reactor Case*	~2.5	~43	~33

* Zion Probabilistic Safety Study, Commonwealth Edison Co., Chicago, IL, 1981.

stability in a way that would not occur at the larger scales of reactor core debris where crust growth over much of the area would be insensitive to the perimeter of the melt.

It has been widely acknowledged that once an interfacial crust becomes several centimeters thick, the crust is quite strong and not easily fractured. Fairly elementary calculations [Blose et al. 1987] show that a thick crust pinned at its perimeter could resist most forces likely to arise during core-debris interactions with concrete if vent pathways exist for gases produced by the attack on concrete. Such vent pathways--either gaps in the crust or blowholes--have been observed in all crusts produced in tests to date. A floating crust would be even more resistant to fracture by external loads.

A second contention is that just as a crust of solidified material begins to form below a water pool there is an inherent instability. This instability, it has been argued, may be driven by the buoyant forces of gases generated by melt interactions with concrete, by the presence of the boiling liquid, or by some unknown aspect of simultaneous interactions of melts with concrete and coolant. Whatever the cause of the instability, it is argued that this instability is suppressed in the tests because the crust can bond or adhere to the test fixture boundaries in a way that would not be possible in a reactor accident. Were this bonding not possible, it is suspected that the inherent instability would lead to breakup of the crust as it formed. As a result, water could progressively quench the melt and fragment the solidified material into permanently coolable debris.

A third contention is that because the crust binds to the walls, it is not subjected to flexing that a crust floating on the melt would experience as gases from the attack on concrete sparged through the melt. This flexing, it is hypothesized, would rupture the crust, allow water penetration, and lead to quenching of the melt. Such behavior has not been observed in any tests to date.

The WETCOR-1 test was designed to address the first two of the contentions concerning the effects of test-fixture boundaries on the initial formation of a crust when water first contacted high-temperature melts. Both of these contentions were addressed simply by ensuring that the perimeter of the melt was hotter than the center of the melt. This was done in the WETCOR-1 test by heating the melt with an induction susceptor collar around the perimeter of the melt surface. The induction heating of the collar ensured that the hottest part of the melt was the perimeter. Furthermore, the test fixture walls behind the collar were nearly as hot as the hottest part of the melt. The heat capacity of the walls slowed cooling of the perimeter of the melt once water was added on top of the melt.

With this design of the test fixture for WETCOR-1, any initial difference in the rate of crust growth would be such that crust growth would be greatest in the center and least at the perimeter. Also, during the transient period of initial crust growth when any inherent instability in the crust is hypothesized to exist, the crust would not be able to bind to the susceptor which would still be at a temperature above the melting point of the core debris. The opportunities for instability in the crust formation were further enhanced by the selection of melt materials. Details of this selection are described in section 2.0. In essence, the melt material was selected to have a characteristic rate of crust growth that was slow relative to that expected for core debris. The crust thickness was expected, then, to be small over the time period it took for instabilities to develop and produce fragmentation. Furthermore, a material was selected that was at least as susceptible to fracture as core debris.

The WETCOR-1 test did not address the third contention concerning the long-term flexing of a crust.

Limitations on the power available for the experiment meant that eventually water could extract enough heat from the susceptor collar and the walls that temperatures would fall below the melting point of the core debris and the crust could bind to the collar. Some limited data on the long-term heat flux to the water from the core debris were obtained in the test. These data are, however, not easily interpreted because there was also a flux of heat from the susceptor collar and test fixture walls to the water. These heat fluxes and the heat flux from the debris through the crust can be separated only by calculation. Finally, the WETCOR-1 test yielded important data on the attenuation of aerosol production during melt interactions with concrete caused by crust formation and the combination of a crust and a subcooled water pool.

The WETCOR-1 test configuration and test procedures were similar to those used in the SURC tests [Copus et al., 1989; 1992]. A charge was melted within a magnesium oxide annulus with a limestone/common-sand concrete base. Once steady-state melt attack on the concrete was reached, a flowing water pool was established over the melt. The test configuration was intended to create an approximately one-dimensional melt-interaction geometry. The novel feature of the WETCOR-1 test configuration is, of course, the method by which melt was formed and sustained.

In section 2.0, the materials used in the WETCOR-1 test are described in detail. In section 3.0, the details of the experimental apparatus are described. Instrumentation employed in the test is described in section 4.0. Results of the test are described in sections 5.0 and 6.0.

2.0 Materials

Major materials employed in the WETCOR-1 test were the magnesium-oxide test fixture annulus, the concrete base, and the melt. The arrangements of the structural materials in the test apparatus are shown in Figure 2.1. The structural and melt materials are described in the following subsections. An important part of the following discussions is the rationale used to select the melt material for the WETCOR-1 test.

2.1 Magnesium Oxide (MgO) Castable Refractory

The annulus of the crucible was cast using an MgO castable material manufactured by National Refractories called K/R Cast 98-AF. This material consists of ≈98 percent MgO. The chemical composition of K/R Cast 98-AF, taken from manufacturer's specifications, is shown in Table 2.1. The maximum service temperature of the dried and fired material is 2600 K. The density is 2.95 to 2.90 g/cm^3. This material has excellent volume stability at high temperatures and has been shown to resist melt penetration in many past tests. The porosity of the material (about 19%) makes it resistent to fracture by thermal stresses induced during melt formation.

The thermal properties of K/R Cast 98-AF have been extensively investigated. In addition to industry data, experiments were conducted at SNL to study the thermal response of the MgO castable to intense heating conditions similar to those expected during an experiment. These tests yielded values of specific heat and temperature-dependent thermal conductivity [Copus et al., 1989].

2.2 Concrete

The base of the interaction crucible was constructed of limestone/common-sand concrete. This concrete was used because it is typical of the concrete used in the construction of many nuclear power plants. Materials making up this type of calcareous concrete are found throughout the United States. This concrete melts over a range of 1423-1643 K and typically liberates about 21 w/o CO_2 gas and 5 w/o H_2O vapor when heated to melting. Tables 2.2. and 2.3 summarize the engineering and chemical composition of the concrete.

The thermal behavior of this concrete has been characterized by thermal gravimetric analysis (TGA), derivative thermal gravimetric analysis, and differential thermal analysis. Typical thermograms produced by TGA for limestone/common-sand concrete are presented in Powers and Arellano [1982].

2.3 Melt Material Selection

There is no evidence from all of the tests on the effects of water on melt interactions with concrete [Tarbell et al., 1987; Blose et al., 1987; Spencer et al., 1991] that the effects depend on the nature of the melt. The available data base includes tests with melts of stainless steel, molten siliceous concrete, molten calcareous concrete and molten mixtures rich in UO_2 and ZrO_2. This evidence and a desire to avoid both the costs and delays that would accompany the use of UO_2/ZrO_2 melts led to a decision to use a simulant melt in the WETCOR-1 test. The focus of interest of the WETCOR-1 test was to ascertain if hypothesized phenomena concerning crust behavior do arise rather than to simulate a reactor accident.

Table 2.1 Chemical composition of K/R Cast 98-AF* MgO castable refractory

OXIDE	WEIGHT %
MgO	98.5
CaO	0.8
SiO_2	0.3
Fe_2O_3	0.3
Al_2O_3	0.1

* K/R Cast 98-AF is a product of National Refractories, 300 Lakeside Drive, Oakland, CA 94643

Data obtained from Basic Ramming and Casting Mixes Bulletin published by National Refractories.

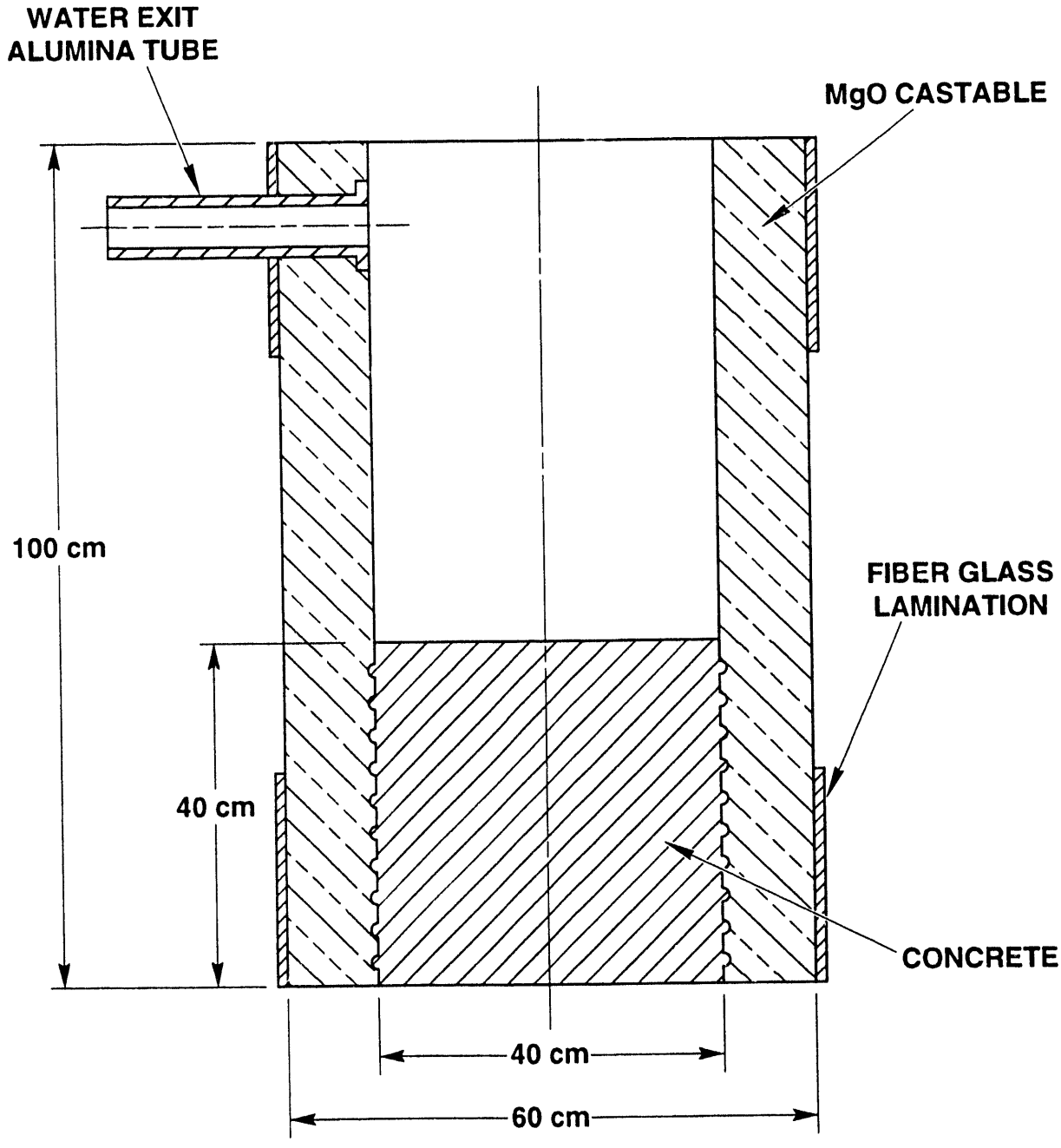

Figure 2.1 Interaction crucible, WETCOR-1 experiment

Table 2.2 Typical engineering composition of limestone/common-sand concrete

Constituents	Mass	Weight %
Coarse Aggregate	85.0 kg	30.1
Fine Aggregate	42.3 kg	15.0
Sand	93.2 kg	33.0
Cement	42.7	15.1
Water	19.1	6.8
* AEA	22.2 ml	
+ WRA	29.6 ml	
* Air Entraining Agent + Water Reducing Agent		

Table 2.3 Typical chemical composition of limestone/common-sand concrete constituents

Oxide	Type 1 and 2 Cement (%)	Common Sand (%)	Limestone Aggregate (%)
Fe_2O_3	4.11	2.5	0.33
Cr_2O_3	0.011	0.042	ND
MnO	0.08	0.02	ND
TiO_2	0.20	0.18	0.05
K_2O	0.54	2.70	0.03
Na_2O	0.27	1.74	0.15
CaO	63.5	1.52	45.56
MgO	1.53	0.34	0.80
SiO_2	20.1	82.8	12.98
Al_2O_3	4.2	7.24	1.25
CO_2	ND	ND	40.0
ND = Not Determined			

Materials

Several criteria were established for the selection of the simulant melt material:

- the simulant had to be an oxide that would melt at high temperatures,
- physical properties expected to affect crust formation had to be similar to the properties of the oxide phase of core debris,
- within other constraints the properties of the simulant needed to enhance the possibility of observing the hypothesized phenomena concerning crust formation,
- the properties of the simulant could not be changed too drastically as concrete ablated and incorporated into the melt, and
- the simulant had to be readily available at acceptable purities and at low cost.

The focus of attention in the WETCOR-1 test was on the phenomena that might affect water quenching of the oxide phase of core debris. Most students of the topic of water quenching of melts have conceded that quenching and fragmentation of steel melts (the metallic phase of core debris) are more difficult than quenching and fragmentation of molten oxides.

Attempts to find close analogues of the oxide phase of core debris are challenged by the imprecision of the state-of-the-art definition of the oxide phase of core debris. Usually the oxide phase of core debris is adequately approximated as a mixture of uranium oxide and zirconium oxide. At reasonably high oxygen potentials such a mixture would freeze at a temperature between the minimum in the liquidus of the UO_2-ZrO_2 binary system (2823 K) and the melting point of pure, stoichiometric uranium dioxide (3120 K) [Romberger et al., 1966]. At temperatures near the freezing point, the frozen material would be a homogeneous solid solution having the cubic fluorite structure. But, as temperatures fell below the temperature of the cubic-to-tetragonal phase change in ZrO_2 (2640 K), a second, zirconium dioxide rich phase would develop in the solid. (At the high cooling rates water can produce, the tetragonal-to-monoclinic phase change in ZrO_2 is not expected to be observed).

The freezing pattern of zirconium oxide-uranium oxide mixtures at low oxygen partial pressures will be somewhat different because of non-stoichiometry of the uranium oxide. The onset of freezing can begin at the monotectic in the pseudobinary Zr-U-O system (2673 K) [Skokan, 1984]. The solidification product would be a uranium-rich, hypostoichiometric solid solution of uranium and zirconium oxides, $(U,Zr)O_{2-x}$. Precipitation of this solid solution would continue until the eutectic temperature, 2173 K, is reached. At this point a second, solid, phase would also precipitate. Also at temperatures below about 2600 K, zirconium dioxide in the precipitated solid solution might separate as a phase with a tetragonal structure.

The solidification behavior observed in the Zr-U-O system at low oxygen partial pressures was deemed more pertinent to the objectives of the WETCOR test program than solidification behavior of stoichiometric UO_2/ZrO_2 melts. If crust stability is very dependent on material properties or solidification patterns, then a variety of behaviors could be produced by uranium-oxide-zirconium oxide mixtures at different oxygen partial pressures. To date, there is not evidence of this sensitivity.

Hypotheses concerning phenomena that might afflict crusting observed in small-scale tests have not been advanced in the type of quantitative detail that lends itself to easy identification of pertinent material properties. The test fixture configuration adopted for the WETCOR-1 test addresses hypotheses concerning the radial progression of the freezing front. Material properties are not essential concerns in addressing this hypothesis. The hypothesis concerning the instability of the crust during its initial formation presents an issue where properties of the solidified material are pertinent. Based on the qualitative articulation of the hypothesis, two selection criteria were defined:

- the rate at which a solidified crust of melt material grows ought to be slow enough that any inherent instability can manifest its effects, and

- the strength of the crust ought not be so great that it suppresses the effect of the instability.

Consider a pool of molten material at its melting point, T_m. The surface of this melt is suddenly reduced to some low temperature T_w taken here to be 373 K. The rate at which a crust will grow into

the melt is, initially, determined by conduction. (Convection in the melt will affect the extent of crust growth later in time.) The crust thickness is then given by:

$$l(t) = 2\lambda\,(k_s t)^{1/2} \qquad (1)$$

where
$l(t)$ = crust thickness at time t,
λ = crust growth rate constant, and
k_s = thermal conductivity of the crust.

The growth rate constant, λ, is found from

$$\lambda \exp(\lambda^2)\, erf(\lambda) = \frac{C_s\,(T_m - T_w)}{L\,\sqrt{(\pi)}} \qquad (2)$$

where
C_s = heat capacity of the solid material
L = latent heat of fusion of the solid material, and

$$erf(x) = error\ function\ of\ x = \frac{2}{\sqrt{\pi}}\int_o^x \exp(y^2)\,dy \qquad (3)$$

For this work, the average heat capacity is used.

$$C_s = \int_{T_w}^{T_m} C_p(T)\,dT/(T_m - T_w) \qquad (4)$$

From this analysis it appears that the quantity $\lambda\sqrt{(k_s)}$ for the simulant ought not be larger than that for core debris. Thermophysical properties and values of $\lambda\sqrt{(k_s)}$ for several candidate melt materials are shown in Table 2.4. Note that the material properties in this table are for polycrystalline samples at temperatures near 373 K. Crusts observed in past water quenching tests have, indeed, been polycrystalline. They have also been quite porous. Porosity may well affect thermal conductivity of the crust which would in turn affect the growth of the crust. Crusts extracted from tests done in the past seem, however, to have a thin surface layer that is relatively pore free. This thin, compact surface layer may be the portion of the crust subject to the hypothetical instability. The values of $\lambda\sqrt{(k_s)}$ shown in Table 2.4 are all quite similar for the oxide materials. The value for stainless steel is much larger. Crust growth rates on metals, as expected, do not simulate crust growth rates of oxides well.

Instabilities are hypothesized to cause the rupture of the crust during early formation. The precise mode of fracture has not been stated. Most ceramics fracture in a brittle mode. UO_2 and $MgAl_2O_4$ can undergo some plastic deformation at elevated temperatures because of the existence of five independent slip systems. This plastic deformation, which would make the materials less susceptible to rupture, is neglected here. It is assumed, then, that rupture is driven by the tensile strain, ϵ, created in the crust when it is cooled from the melting point to the water temperature:

$$\epsilon = \alpha(T_m - T_w) \qquad (5)$$

where α is the coefficient of thermal expansion. The stress in the crust is given by:

$$\sigma = E\alpha\,(T_m - T_w) \qquad (6)$$

where E is the Young's modulus. The stress is easily compared to the tensile strength of the material, σ_f, via the dimensionless parameter:

$$\frac{E\alpha\,(T_m - T_w)}{\sigma_f} \qquad (7)$$

Materials with larger values of this parameter are presumably more susceptible to rupture by the instabilities hypothesized to occur during early formation of the crust.

The above dimensionless parameter does, of course constitute a hypothesis on the mechanism of crust rupture. More detailed analysis of the potential rupture mechanisms does not seem warranted with so little information on crust failure as is now available.

Mechanical properties of various candidate melt materials and values of the dimensionless parameter are listed in Table 2.4. Again, the property values are for polycrystalline materials at temperatures near the boiling point of water. The values do not account for effects of porosity. Certainly, porosity would be expected to affect the Young's modulus of the material:

Table 2.4. Properties of candidate materials

Material	k_s	C_s	L	T_m	$\lambda\sqrt{k_s}$	E	α	σ_f	$E\alpha(T_m-373)/\sigma_f$
	W/cm-K	J/g-K	J/g	K	$cm/s^{1/2}$	G Pa	K^{-1}	GPa	-
Alumina	0.03	1.25	915	2327	0.153	414	$9x10^{-6}$	0.26	28
Calcium aluminate	0.037	1.12	1080	2050	0.147	260	$9x10^{-6}$	0.124	32
Chromia	(0.012)	0.91	853	2603	0.093	207	$7.5x10^{-6}$	0.093	37
Magnesium aluminate	0.02	1.36	1353	2408	0.114	262	$7x10^{-6}$	0.12	31
Niobium oxide	0.012	0.70	737	2175	0.083	150	$5x10^{-6}$	0.1	14
Silicon dioxide	0.01	1.15	159	1996	0.130	72.4	$0.5x10^{-6}$	0.10	0.6
Titanium oxide	0.021	0.94	838	2130	0.115	283	$8.8x10^{-6}$	0.103	42
Uranium oxide	0.02	0.41	280	3120	0.141	124	$10x10^{-6}$	0.117	29
Zirconium oxide	0.018	0.62	706	2950	0.112	138	$7.5x10^{-6}$	0.14	19
Stainless steel	0.16	0.5	191	1650	0.378	193	$17.2x10^{-6}$	0.34	12

* Thermochemical properties are from Barin et al. [1989], and Stull and Prophet [1971]. Mechanical and transport properties are from Parker [1967], and the Metals and Ceramics Information Center [1981].

$$E(p) = E(o)\ (1 - 1.9p + 0.9p^2) \qquad (8)$$

where p is the porosity and $E(o)$ is the Young's modulus at zero porosity [Mackenzie, 1950]. No account of this porosity effect on the Young's modulus is attempted here. It is evident from Mackenzie's correlation that the inherent porosity of crust formed on melts exposed to water does reduce the stress created by thermal strains.

Inspection of parametric values in Table 2.4 shows many trends among the various candidate melt materials. Most striking are differences between values for ionic oxide and parameter values for the network-forming oxide SiO_2. Quite clearly, pure SiO_2 would not be a suitable simulant for core debris early in the course of interactions with concrete. Note that the network-forming nature of SiO_2 is eliminated when strong bases such as CaO are present in CaO/SiO_2 molar ratios greater than 2. When the siliceous material is rich in a strong base, it behaves like an ionic oxide.

Based on consideration of parameter values shown in Table 2.4, as well as consideration of material availability and regulations on disposal of toxic wastes, calcium aluminate was chosen as the simulant for the WETCOR-1 test. A binary phase diagram for the $AlO_{1.5}$ - CaO system is shown in Figure 2.2. The charge mass used in the WETCOR-1 was 34.1 kg. The actual composition of the charge material is shown in Table 2.5. As is common for bulk oxide materials, there is some SiO_2 contamination of the charge material. A ternary phase diagram for the $AlO_{1.5}$ - CaO - SiO_2 system is shown in Figure 2.3 [Morey, 1964]. (Note that there are inconsistencies between the phase diagram for the CaO - $AlO_{1.5}$ system and the phase diagram for the $AlO_{1.5}$ - CaO - SiO_2 regarding the stability of $Ca_5Al_6O_{14}$. No attempt was made to resolve these inconsistencies since they do not affect conduct or analysis of the WETCOR-1 test.) As is discussed below, the presence of SiO_2 in the initial charge is not significant because the erosion of concrete prior to addition of water in the WETCOR-1 test will also introduce SiO_2 into the melt. The amount of SiO_2 is small enough that the network-forming properties of pure SiO_2 will not affect crust formation.

It is instructive to consider the pattern of equilibrium solidification for the melt charge and the melt contaminated with the condensed products of concrete decomposition. Quenching rates that can be produced by water are high enough that conditions necessary for equilibrium solidification are not likely to prevail in the WETCOR-1 test. But analyses of the equilibrium process does give some indication of how the crust composition might differ from the other limit of suddenly freezing the melt.

Consider the idealized initial melt of CaO and $AlO_{1.5}$. This composition is indicated in Figure 2.3 by a triangular symbol on the CaO-$AlO_{1.5}$ axis of the phase diagram. Cooling of this melt would, initially, yield $CaAl_{12}O_{19}$. This product would precipitate until the liquid temperature reached the peritectic between $CaAl_{12}O_{19}$ and $CaAl_4O_7$ at 2048 K. With further cooling, both $CaAl_{12}O_{19}$ and $CaAl_4O_7$ would precipitate to form any crust.

Table 2.5 Chemical composition of the charge material

Oxide	Weight Percent
Al_2O_3	76.8
CaO	16.9
SiO_2	4.0
Fe_2O_3	0.9
MgO	0.5
Other	0.9

The evolution of the melt composition as concrete is incorporated into the melt is shown by a dashed line and triangular symbols in Figure 2.3. For the purposes of preparing this figure, the calcareous concrete used in the WETCOR-1 test was approximated to be a mixture of $AlO_{1.5}$, CaO, and SiO_2. Open triangles along the dashed line indicate the melt composition when there has been an *average* erosion of the concrete base in the WETCOR-1 test of 3 and 5 cm.

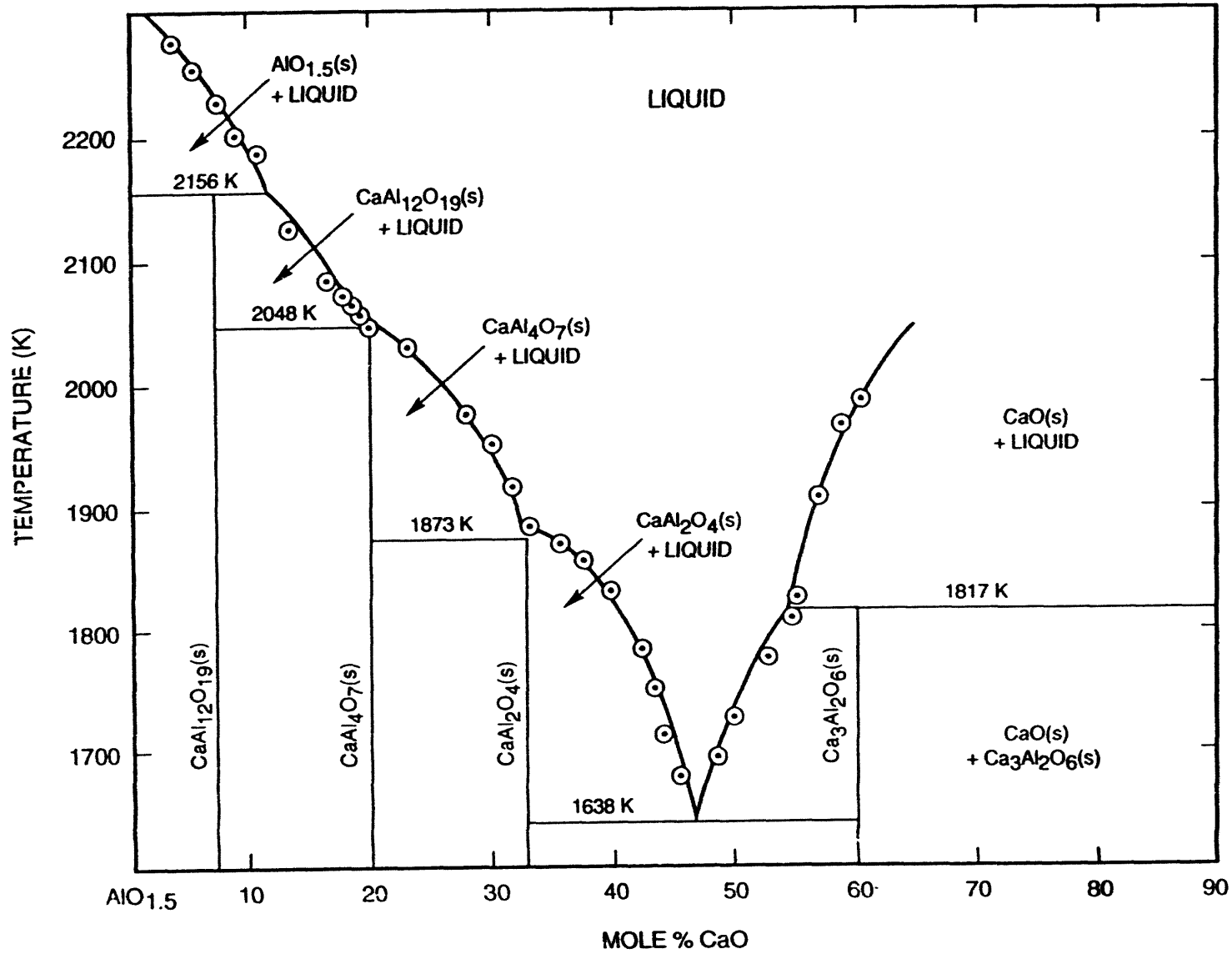

Figure 2.2 **Phase relations in the $AlO_{1.5}$ - CaO system. Invariant points are from Hallstedt, 1990. Liquidus data are from Nurse et al. 1965.**

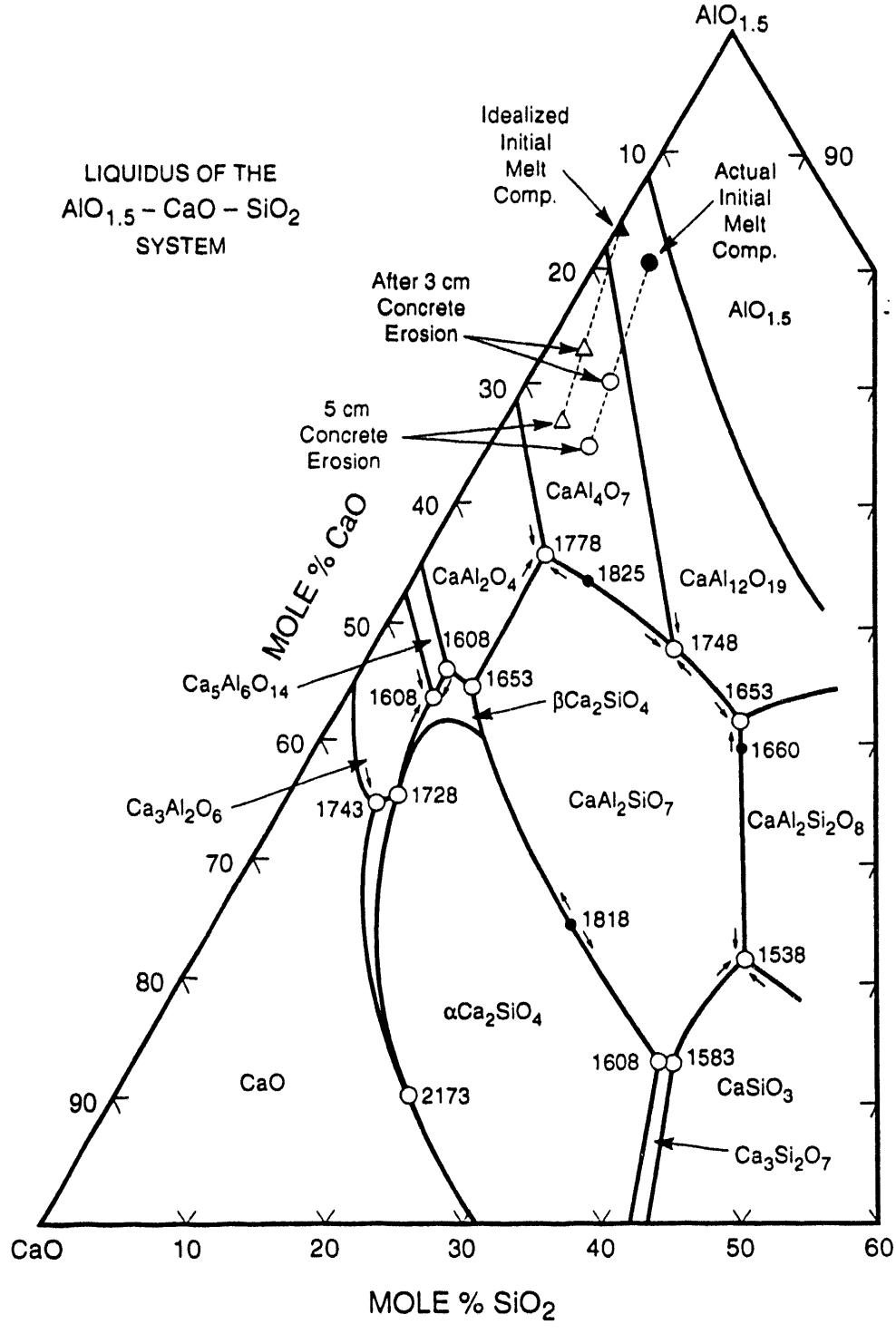

Figure 2.3 **Phase diagram for $AlO_{1.5}$ - CaO - SiO_2 system [Morey, 1964]. Invariant points are indicated by open circles. The initial melt composition in the WETCOR-1 is indicated by the filled symbols. Variations in the melt composition as concrete erosion progresses are indicated by the dashed line. Melt compositions after an average concrete erosion of 3 cm and 5 cm are indicated by open symbols.**

Once more than about 1 cm of concrete has been eroded and incorporated into the melt, the solidification pattern of the melt changes from that for the initial, idealized $AlO_{1.5}$ - CaO melt. Upon cooling to the liquidus, $CaAl_4O_7$ precipitates. The onset of this solidification occurs at a temperature 100 to 150 K below the melting point of pure $CaAl_4O_7$. This lower solidification temperature will, of course, alter the crust growth and fracture properties discussed above for selection of the melt charge. The change is not enough, however, to make the melt an unsuitable simulant for the phenomenological investigations pursued in the WETCOR-1 test.

If about 3 cm of concrete erosion has taken place, precipitation of the $CaAl_4O_7$ will persist until the composition of the increasingly silica-rich liquid reaches the phase boundary with $Ca_2Al_2SiO_7$ (gehlenite). Once this phase boundary is reached, both $CaAl_4O_7$ and gehlenite will precipitate from the cooling liquid. The remaining liquid will evolve in composition along the phase boundary until the invariant point at 1778 K is encountered. Temperatures will arrest at 1778 K, and $CaAl_4O_7$, gehlenite and $CaAl_2O_4$ will crystallize from the remaining liquid.

If 5 cm of concrete erosion have taken place, the melt will precipitate $CaAl_4O_7$ until temperatures reach 1778 K and all three solids ($CaAl_4O_7$, $CaAl_2O_4$, and gehlenite) simultaneously precipitate.

In both the case of 3 cm and 5 cm of concrete erosion, a fine-grained, multiphase solid rather similar to the multiphase solid formed when uranium oxide-zirconium oxide melts are cooled will be produced. At least to within our current understanding of the crust formation process, the simulation of core debris adopted for the WETCOR-1 test appears adequate for the phenomenological objectives of the test.

The silica impurities in the bulk materials used for the charge in the WETCOR-1 test will affect the evolution of the melt composition during cooling. These effects are also shown in Figure 2.3. The silica impurities make no qualitative change in the equilibrium solidification pattern of the melt once about 3 cm of concrete have been eroded. For this reason, water addition in the WETCOR-1 test was delayed until about 3 cm of concrete had been eroded.

3.0 Experimental Apparatus

The major components of the WETCOR-1 experimental apparatus are shown in Figure 3.1. These components are the sealed containment chamber, interaction crucible, induction sleeve susceptors, and induction coil. These items are described in the following sections. The remainder of the WETCOR-1 apparatus, including the water-tank, aerosol and gas-flow circuit, gravel filter and turbine blower are described in Section 4.0.

3.1 Containment Chamber

A large mild steel chamber was used in the WETCOR-1 experiment to ensure that nearly all the reaction products from the melt/concrete interaction would pass through the instrumented exit-flow piping. The internal dimensions of the chamber is 2.74 m in diameter and 2.26 m high. Based on these dimensions, the volume of the chamber is calculated to be 13.3 m^3. The chamber had two hinged access doors conforming to the shape of the vessel. The doors were located approximately 90 degrees apart. The large door is 2.04 m wide and 2.03 m high. The small door is 0.84 m wide and 1.90 m high. The large door was secured using 21, 3/8-16UNC hex-head bolts, and the small door was secured by 18 bolts of the same type.

Ambient air was drawn into the bottom of the chamber through an instrumented flow duct bolted to a 15-cm, ASME long weld neck flange attached to the chamber. The aluminum duct contained a prefilter and HEPA filter to remove particulates.

Effluents produced from the melt/concrete interaction flow out of a 15-cm ASME flange port located near the top of the chamber opposite the intake. This flange connected the chamber with a flow circuit instrumented to sample gases and aerosols. A gas port was installed in the top of the chamber to sample gases resident in the chamber during the experiment.

Water was delivered from the outside of the chamber to the crucible using a 2-cm-diameter 304 stainless steel tubing in combination with 304 stainless steel Swagelok fittings. Water exiting the crucible flowed into a 2150-liter aluminum storage tank.

Two video cameras mounted behind heated, gas-purged view ports were used to record the events inside the containment chamber. One camera was focused across the top of the crucible to observe steam, gas, aerosol and ejected debris. The other camera, located above the crucible, was focused into the cavity to observe the melt/concrete interaction, crust formation, and water behavior.

A transducer was mounted to the chamber to measure vessel pressure during the experiment. A type-K thermocouple was installed in the chamber to measure temperature. The chamber was fitted with a 30.5-cm-diameter, spring-loaded pressure-relief diaphragm calibrated to relieve pressure when the internal pressure reached 110 Kpa.

Two 6.35-cm-diameter, water-cooled copper power leads were connected to the base of the induction coil. These buss bars were passed through a water-cooled 30.5-cm, ASME long weld neck flange port. No. 32 water-cooled flexible leads were used to connect the copper power leads to the induction power supply.

The floor of the chamber was lined with a layer of 5 x 10 x 20-cm MgO bricks. This was done to protect the floor of the chamber from melt attack by molten material should the melt breach the interaction crucible during the experiment.

3.2 Interaction Crucible

The interaction crucible for WETCOR-1 was constructed like those used in the SURC series of experiments [Copus et al., 1989]. The crucible was designed to limit concrete erosion to be in the downward or axial direction. The materials used in the construction of the crucible have been discussed in Section 2.1 and 2.2. The crucible was of cylindrical geometry and is shown in Figure 2.1. The annulus of the crucible was cast in one monolithic section forming a thick-walled cylinder. The overall dimensions of the crucible were 60-cm outside diameter x 100-cm height with a 40-cm inside diameter. Cast into the bottom of the crucible was an instrumented calcareous concrete cylinder with a 40-cm diameter x 40-cm thickness.

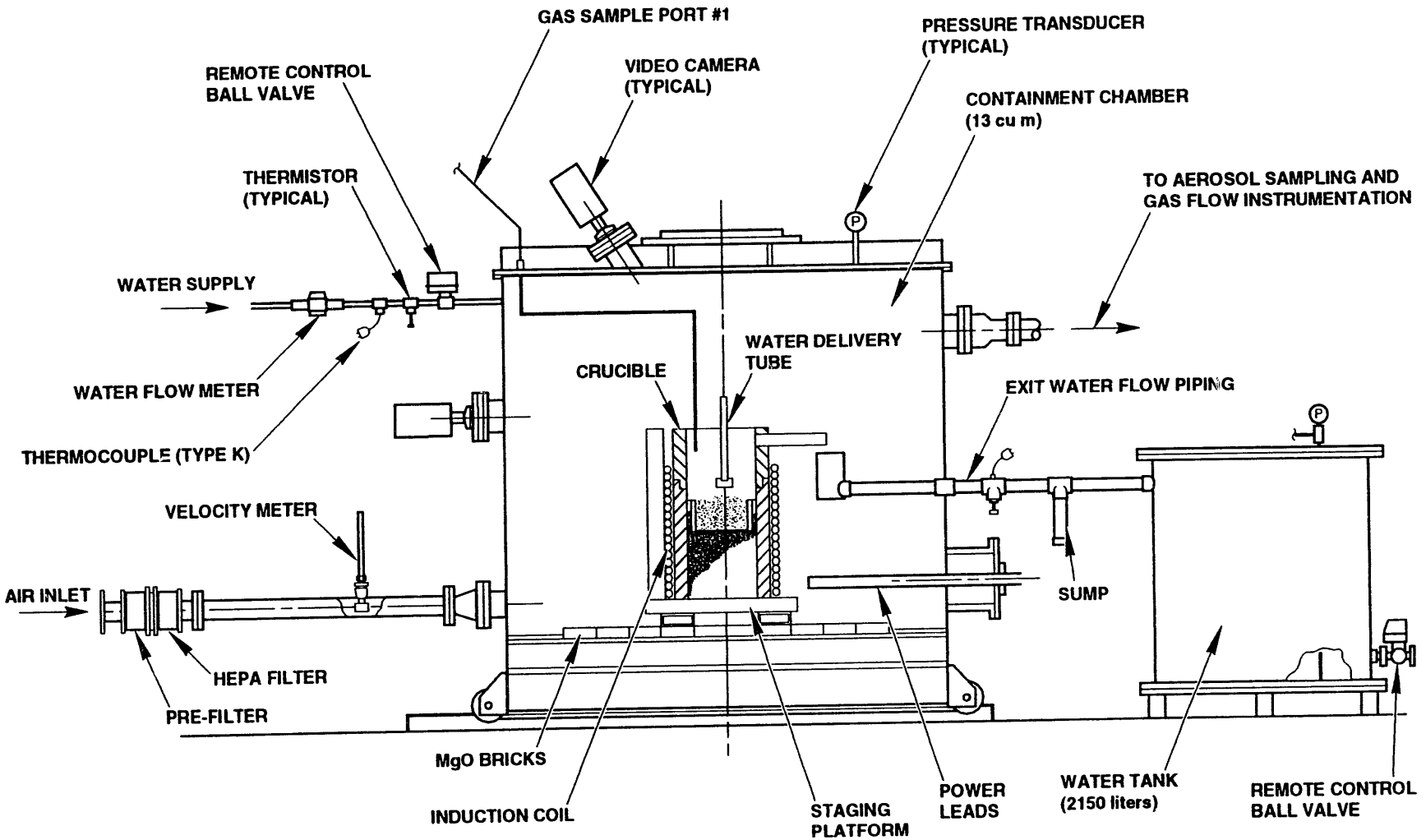

Figure 3.1 Experimental apparatus and containment chamber, WETCOR-1 experiment

The annulus of the crucible was cast using reusable steel casting forms constructed in a clam shell configuration. A detailed description of the casting forms and fabrication procedures is presented elsewhere [Copus et al., 1989].

The outside diameter of the crucible was laminated with three layers of grade-1000 fiberglass cloth and bonded using Shell 828 epoxy resin. This was done to strengthen the crucible and minimize leakage from the cavity during the addition of water.

The annulus and concrete cylinder were instrumented with 90 type-K thermocouples cast into the crucible in 14 arrays. These arrays of type-K thermocouples were used to obtain temperature data needed to estimate heat fluxes into the magnesium oxide walls. Figure 3.2 shows the relative thermocouple locations and the various arrays cast into the crucible. The figure also shows the nomenclature used to describe the locations of the thermocouples in cylindrical coordinates, specifically, r, θ, z and t.

Thermocouples used to monitor sidewall temperatures in the cast MgO outer annulus of the crucible were installed into precast MgO castable cylinders. These cylinders, shown in Figure 3.3, were attached to the casting form prior to casting the annulus. The ends of the cylinders conformed to the curvature of the annulus of the casting forms. The cylinders were bolted to the inside diameter of the outer steel crucible form by threading a wire-wound tungsten bolt into a small wire-wound tungsten nut cast into the cylinders. This method for installation of sidewall thermocouples accurately positioned the thermocouples, which is critical for making heat flux calculations. The thermocouple tips were oriented in a horizontal plane parallel to the base of the crucible and perpendicular to the propagating thermal front. The specific locations of the sidewalls thermocouples are tabulated in Table 3.1.

Fifty-one thermocouples were cast into the concrete in three arrays. These thermocouples indicated the thermal response of the concrete to melt attack; temperatures in excess of about 1650°C were taken to be indicative of melt location. The tips of the thermocouples in these arrays resided in a line parallel to the center axis of the crucible at radial distances of 0, 10 and 18 cm. The thermocouples in each array were spaced 1 cm apart from 0 cm through 8 cm, 2 cm apart from 8 cm through 20 cm, and 5 cm apart from 20 cm through 30 cm. The tips of the thermocouples designated C1 through C17 were located in depth at a radial distance of 10 cm. The tips of thermocouples C18 through C34, and C35 through C51 were located at radial distances of 0 cm and 18 cm, respectively. The locations of the thermocouples cast into the concrete cylinder are tabulated in Table 3.2.

The sheath of each thermocouple was bent at an angle of 90 degrees 10 sheath diameters from the tip. This was done to minimize the error caused by heat conduction down the metal sheath. Installation of a typical concrete thermocouple array is shown in Figure 3.4.

Two 4-hole alumina protection tubes were cast into the concrete cylinder parallel to the axial centerline, 120 degrees apart at a radial distance of 14 cm. Installed in each tube were 3 type-C thermocouples located at various depths from the surface of the concrete. Figure 3.4 shows the installation of a typical alumina protection tube cast into the concrete with the type-C thermocouples. These thermocouples were used to measure melt temperature. Their locations are tabulated in Table 3.3.

Four alumina-tube feed-throughs were cast into the concrete cylinder. These provided a path through which two type-C thermocouples were placed terminating in an argon-purged tungsten thermowell. These assemblies were located at different elevations and radial positions in the oxide charge to measure temperature. Specific locations for these thermocouples are presented in Table 3.4.

3.3 Annular Sleeve Induction Susceptors

The debris for the WETCOR-1 experiment was heated and sustained using thick-walled annular tungsten sleeves as shown in Figure 3.5. Three annular tungsten sleeves were placed on a 1.3-cm-

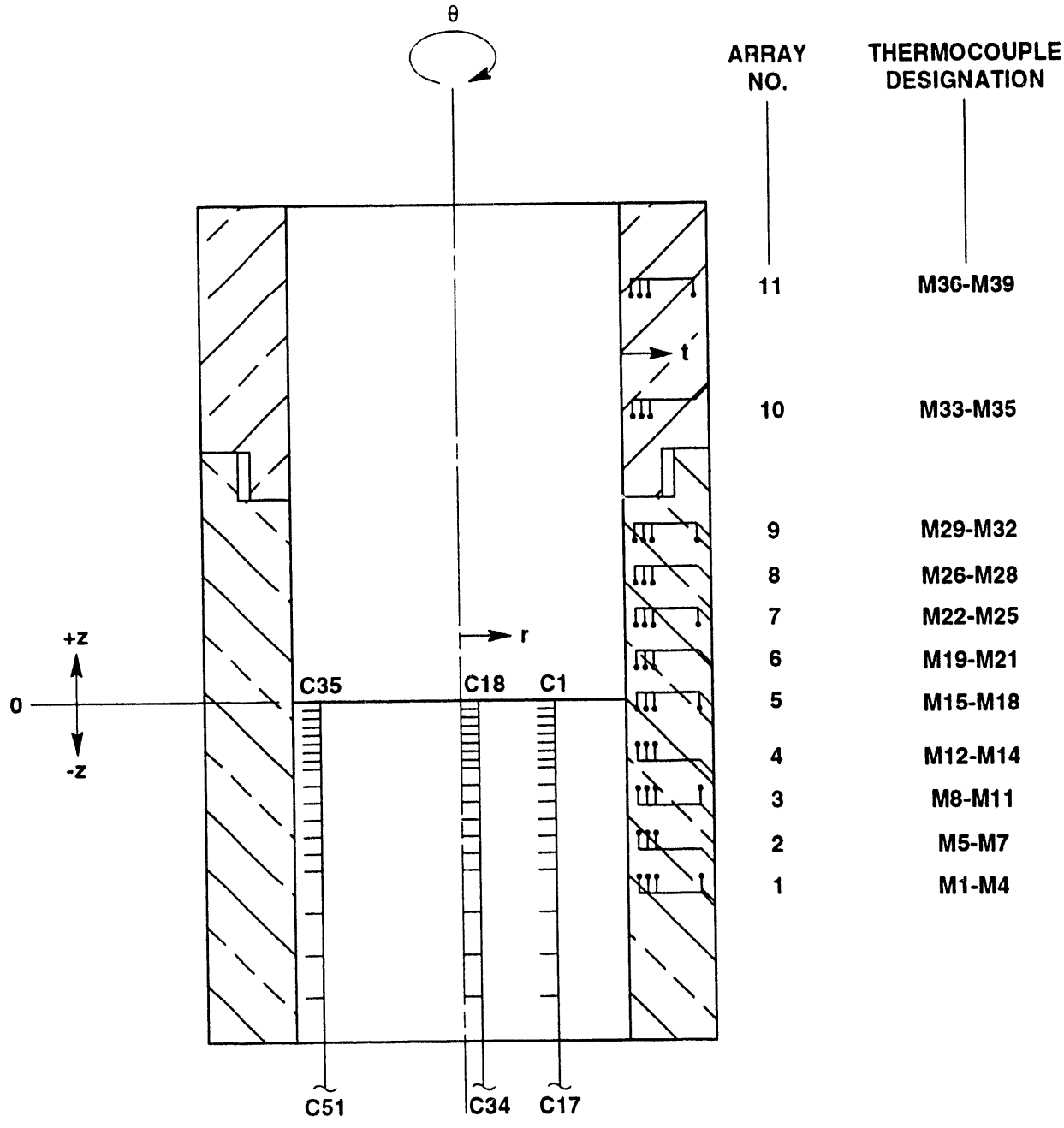

Figure 3.2 Relative thermocouple locations, WETCOR-1 crucible

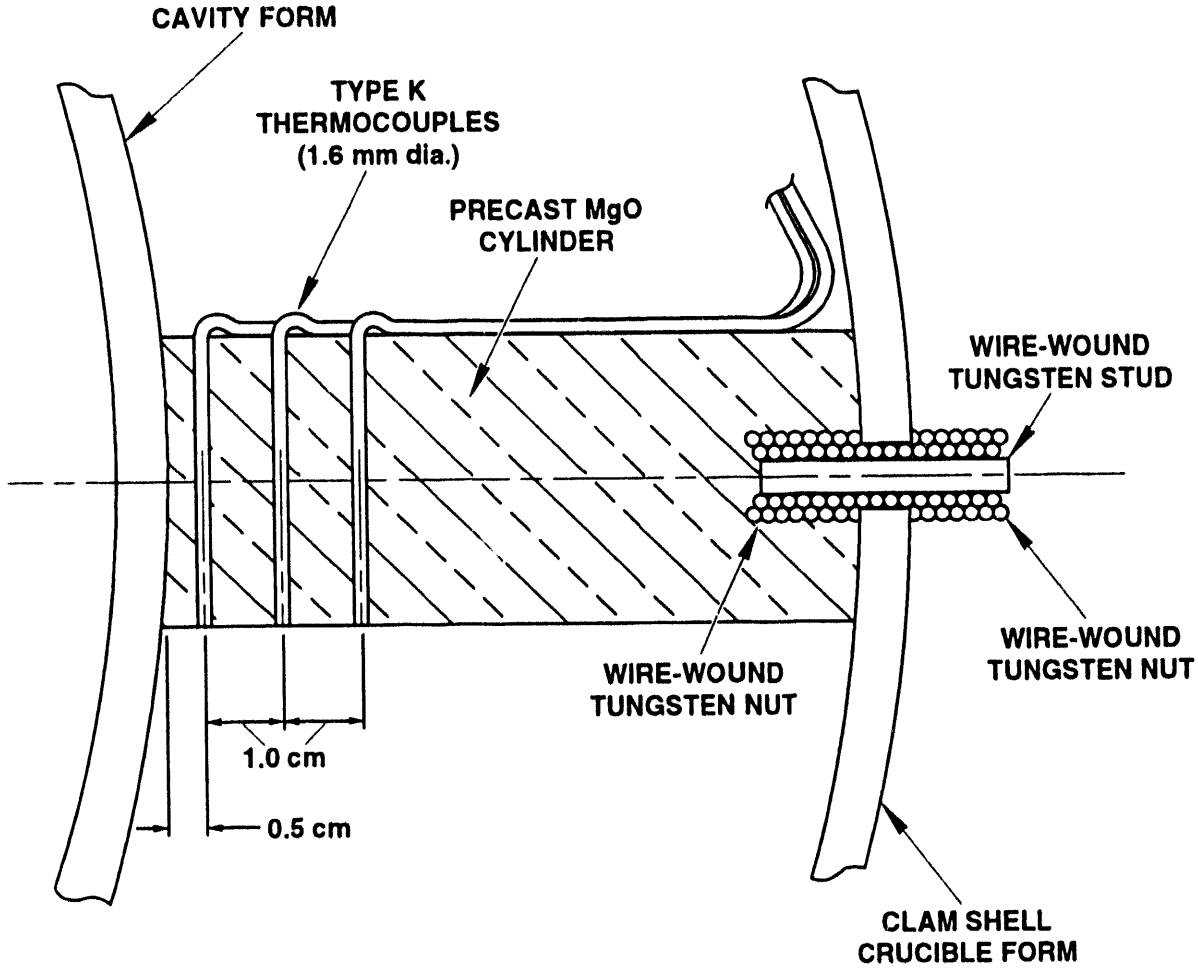

Figure 3.3 Thermocouple array installation, MgO annulus

Table 3.1 Location of thermocouples cast within the MgO castable sidewall, WETCOR-1 (See Figure 3.2)

Array No.	Thermocouple No.	t (cm)	θ (degrees)	z (cm)
1	M1	0.5	0	-20
	M2	1.5	0	-20
	M3	2.5	0	-20
	M4	9.0	0	-20
2	M5	0.5	0	-15
	M6	1.5	0	-15
	M7	2.5	0	-15
3	M8	0.5	0	-10
	M9	1.5	0	-10
	M10	2.5	0	-10
	M11	9.0	0	-10
4	M12	0.5	90	-5
	M13	1.5	90	-5
	M14	2.5	90	-5
5	M15	0.5	90	0
	M16	1.5	90	0
	M17	2.5	90	0
	M18	9.0	90	0
6	M19	0.5	165	+5
	M20	1.5	165	+5
	M21	2.5	165	+5
7	M22	0.5	165	+10
	M23	1.5	165	+10
	M24	2.5	165	+10
	M25	9.0	165	+10
8	M26	0.5	270	+15
	M27	1.5	270	+15
	M28	2.5	270	+15
9	M29	0.5	270	+20
	M30	1.5	270	+20
	M31	2.5	270	+20
	M32	9.0	270	+20

Table 3.1 Location of thermocouples cast within the MgO castable sidewall, WETCOR-1 (See Figure 3.2) (Concluded)

Array No.	Thermocouple No.	t (cm)	θ (degrees)	z (cm)
10	M33	0.5	0	+35
	M34	1.5	0	+35
	M35	2.5	0	+35
11	M36	0.5	0	+50
	M37	1.5	0	+50
	M38	2.5	0	+50
	M39	9.0	0	+50

Table 3.2 Location of thermocouples cast within the concrete cylinder, WETCOR-1 (see Figure 3.2)

Thermocouple No.	r (cm)	θ (degrees)	-z (cm)
C1	10	0	0.0
C2	10	0	1.0
C3	10	0	2.0
C4	10	0	3.0
C5	10	0	4.0
C6	10	0	5.0
C7	10	0	6.0
C8	10	0	7.0
C9	10	0	8.0
C10	10	0	10.0
C11	10	0	12.0
C12	10	0	14.0
C13	10	0	16.0
C14	10	0	18.0
C15	10	0	20.0
C16	10	0	25.0
C17	10	0	30.0
C18	0	0	0.0
C19	0	0	1.0
C20	0	0	2.0
C21	0	0	3.0
C22	0	0	4.0
C23	0	0	5.0
C24	0	0	6.0
C25	0	0	7.0
C26	0	0	8.0

Table 3.2 Location of thermocouples cast within the concrete cylinder, WETCOR-1 (see Figure 3.2), (Concluded)

Thermocouple No.	r (cm)	θ (degrees)	-z (cm)
C27	0	0	10.0
C28	0	0	12.0
C29	0	0	14.0
C30	0	0	16.0
C31	0	0	18.0
C32	0	0	20.0
C33	0	0	25.0
C34	0	0	30.0
C35	18	180	0.0
C36	18	180	1.0
C37	18	180	2.0
C38	18	180	3.0
C39	18	180	4.0
C40	18	180	5.0
C41	18	180	6.0
C42	18	180	7.0
C43	18	180	8.0
C44	18	180	10.0
C45	18	180	12.0
C46	18	180	14.0
C47	18	180	16.0
C48	18	180	18.0
C49	18	180	20.0
C50	18	180	25.0
C51	18	180	30.0

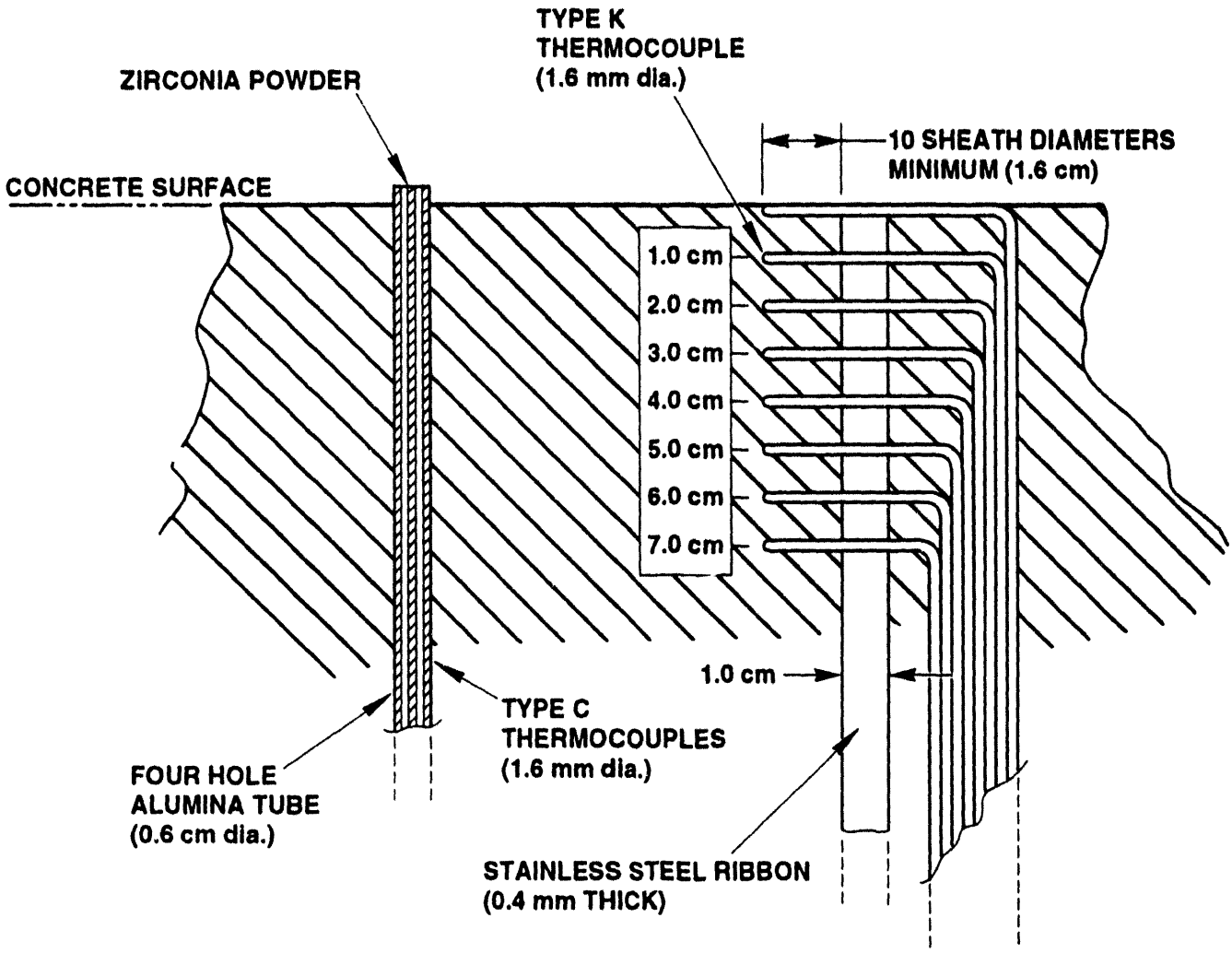

Figure 3.4 Typical thermocouple array cast into the concrete

Table 3.3 Location of thermocouples installed in the alumina protection tubes and cast into the concrete cylinder, WETCOR-1 (See Figure 3.2)

Tube No.	Thermocouple No.	r (cm)	θ (degrees)	-z (cm)
T1	T1C17	14	90	0
	T1C19	14	90	4
	T1C21	14	90	8
T2	T2C18	14	330	2
	T2C20	14	330	6
	T2C22	14	330	10

Table 3.4. Location of Type C thermocouples installed in tungsten thermowells and positioned in the oxide charge

Tungsten Protection Tube	r (cm)	θ (degrees)	+z (cm)
1	2	270	8
	2	270	12
2	6	30	4
	6	30	8
3	10	150	2
	10	150	6
4	14	210	6
	14	210	10

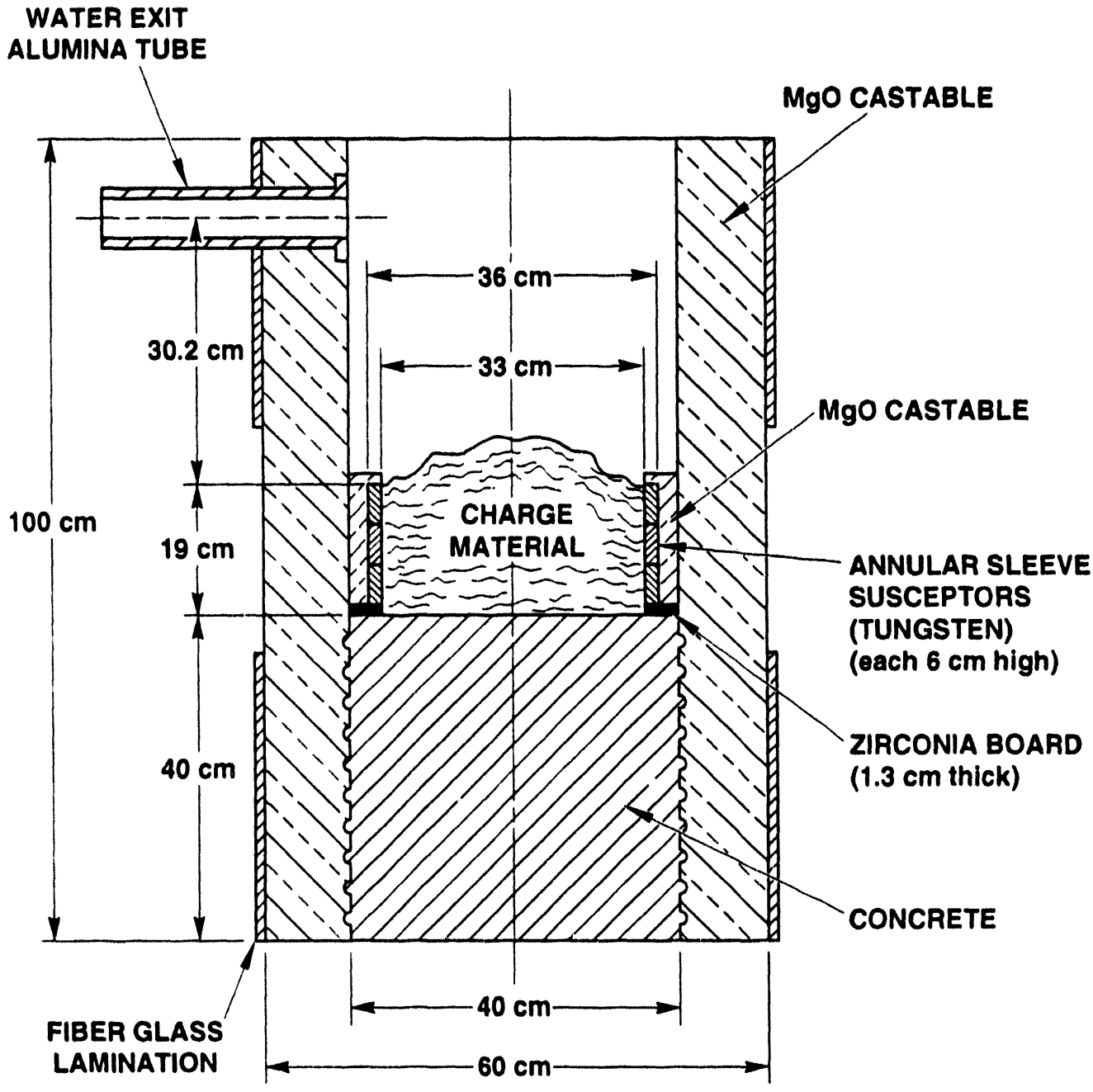

Figure 3.5 Interaction crucible with annular sleeve susceptors and charge material installed

thick zirconia board and were installed on the concrete basemat. The sleeves were stacked on top of each other. The sleeves were 35.6-cm-O.D. x 33.0-cm-I.D.x 5 cm high. The charge material was also placed inside the stacked sleeve assembly as shown in Figure 3.5. MgO castable was mixed and placed between the outside diameter of the sleeve assembly and crucible cavity. A layer of castable magnesium oxide was also placed over the top of the tungsten sleeves. This heating configuration was designed to eliminate the cold sidewalls that have been thought to stabilize crust formation when water is admitted to a high temperature melt interacting with concrete in a small diameter test fixture. Type-K thermocouples were installed between the sleeves to monitor susceptor temperatures. Type-C thermocouples were installed in the MgO castable near the tungsten sleeves inside alumina protection tubes. These thermocouples were used to monitor susceptor temperatures and to infer radial heat flux adjacent to the sleeves.

3.4 Induction Coil

The induction coil used in the WETCOR-1 experiment was designed and built by Inductotherm Corporation. The coil was fabricated with 3.8-cm-O.D. copper tubing having twenty turns with a pitch of 4.2 cm. The coil was supported by six equally-spaced Transite columns 7.5 cm x 5.5 cm x 100 cm long attached to the outside of the coil. After the coil was placed around the crucible and centered inside the containment chamber, Fiberfrax insulation was packed in the gaps in the coil. Fine MgO powder was then placed between the crucible and coil. This was done to provide a barrier to contain any melt that might escape the crucible and to protect the coil from contact with molten debris should the crucible be breached.

4.0 Instrumentation and Calibration

The instrumentation employed in the WETCOR-1 test is displayed schematically in Figure 4.1. The instrumentation and the calibration of the instrumentation are described in the following subsections.

4.1 Thermocouple Instrumentation

A description of the location and orientation of thermocouples cast into the interaction crucible was presented in Section 3.2 of this report. In addition, four type K thermocouples were suspended above the charge to record the temperature of the water pool that formed over the melt. Other thermocouples were used in conjunction with other measurements as described in subsections below.

4.2 Gas Analysis Instrumentation

Gas composition analysis for the WETCOR-1 experiment was performed using two techniques: grab samples and an Infrared Industries Series 700 CO/CO_2 Detector. A schematic layout of the WETCOR-1 gas composition sampling apparatus is included in Figure 4.2. The CO/CO_2 detector yielded real-time data which were viewed during the test and stored on computer disks. The grab samples were stored and analyzed after the test using both gas chromatography and mass spectrometry.

Gases could be drawn from one of three selected sample ports located on the experiment apparatus. The sample ports were located on the containment chamber, in the flow circuit just above the aerosol sample nozzle for the filters and impactors, and downstream from the exit of the gravel filter. Sample transport lines to the gas analysis instrumentation were 6.4 mm O.D. stainless steel tubing and fittings, with Nupro plug valves. Each line, approximately 9.5 m in length, was fit with an electrically actuated solenoid valve to control the location from which the gas sample was taken. The containment chamber and gas sample lines were both equipped with a stainless steel particulate filter. These filters were located 1.5 m and 4.5 m respectively, from the sample port.

Type-K thermocouples were used to monitor sample gas temperatures in two different locations. One location was in the main flow circuit at the sample port just above the aerosol sample nozzle. The other location was near the grab sample and gas analysis instrumentation.

A gas diaphragm-type vacuum pump pulled the gas sample from one of the three sample ports into a single line where the gas could be sampled by a grab sampler and the CO/CO_2 monitor. A Dwyer 0-10 standard cubic-foot-per-minute air rotameter and a dial indicator vacuum/pressure gauge were used to monitor gas flow and pressure. These were viewed remotely with a video camera.

The gas analysis instrumentation was calibrated prior to the experiment. The calibration procedures are presented in previous test descriptions [Copus et al., 1989].

4.2.1 Gas Grab Samples

The grab sample system consisted of seven 150-cm^3 stainless steel sample bottles each equipped with isolation valves and an electrically operated solenoid valve. Each bottle was connected to a manifold from the 6.4-mm-O.D. stainless steel sample line with a dead volume of 10 cm^3. The sample bottles were evacuated to a pressure of 100 torr just prior to the test. The solenoid valves were actuated remotely from the control room.

Grab samples were analyzed by Battelle Pacific Northwest Laboratories. The analysis was performed on a quantitative gas mass spectrometer in accordance with PNL-MA 597 procedure 7-14.18. The precision and accuracy of the analyses are between 1% and 2%.

4.2.2 Infrared CO/CO_2 Monitor

The CO/CO_2 monitor was located in a shielded computer room where it provided real-time analysis of the volume percent of CO and CO_2 gas species in the system. It was connected to the main gas sample line using a 6.4 mm stainless steel tube and Swagelok fittings. The monitor used infrared absorption and was Infrared Industries Model 702 and 703 detectors. The carbon monoxide was analyzed on a range of 0-50% and carbon dioxide on a range of 0-20%. The detectors provided a 0-

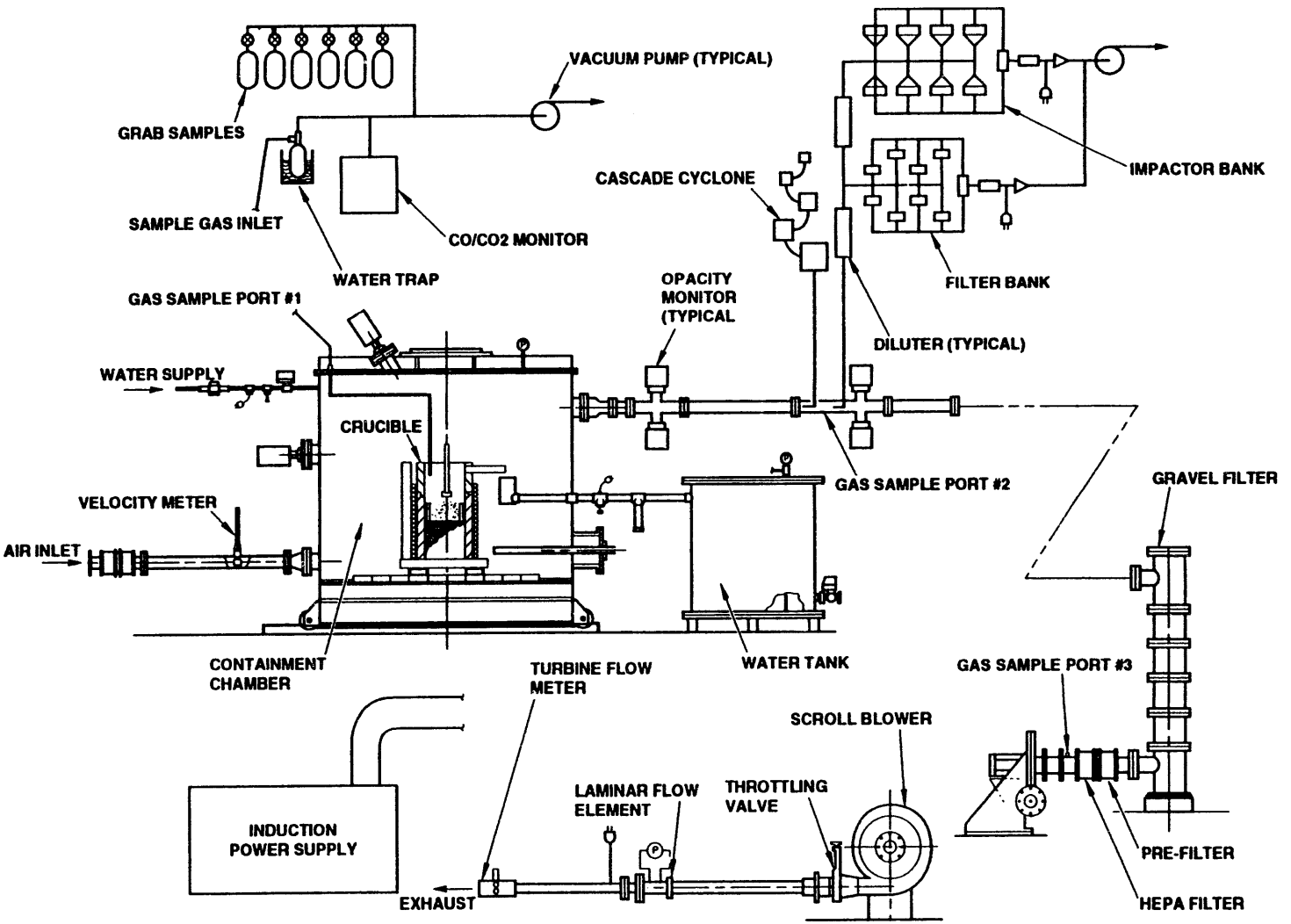

Figure 4.1 Overall instrumentation schematic

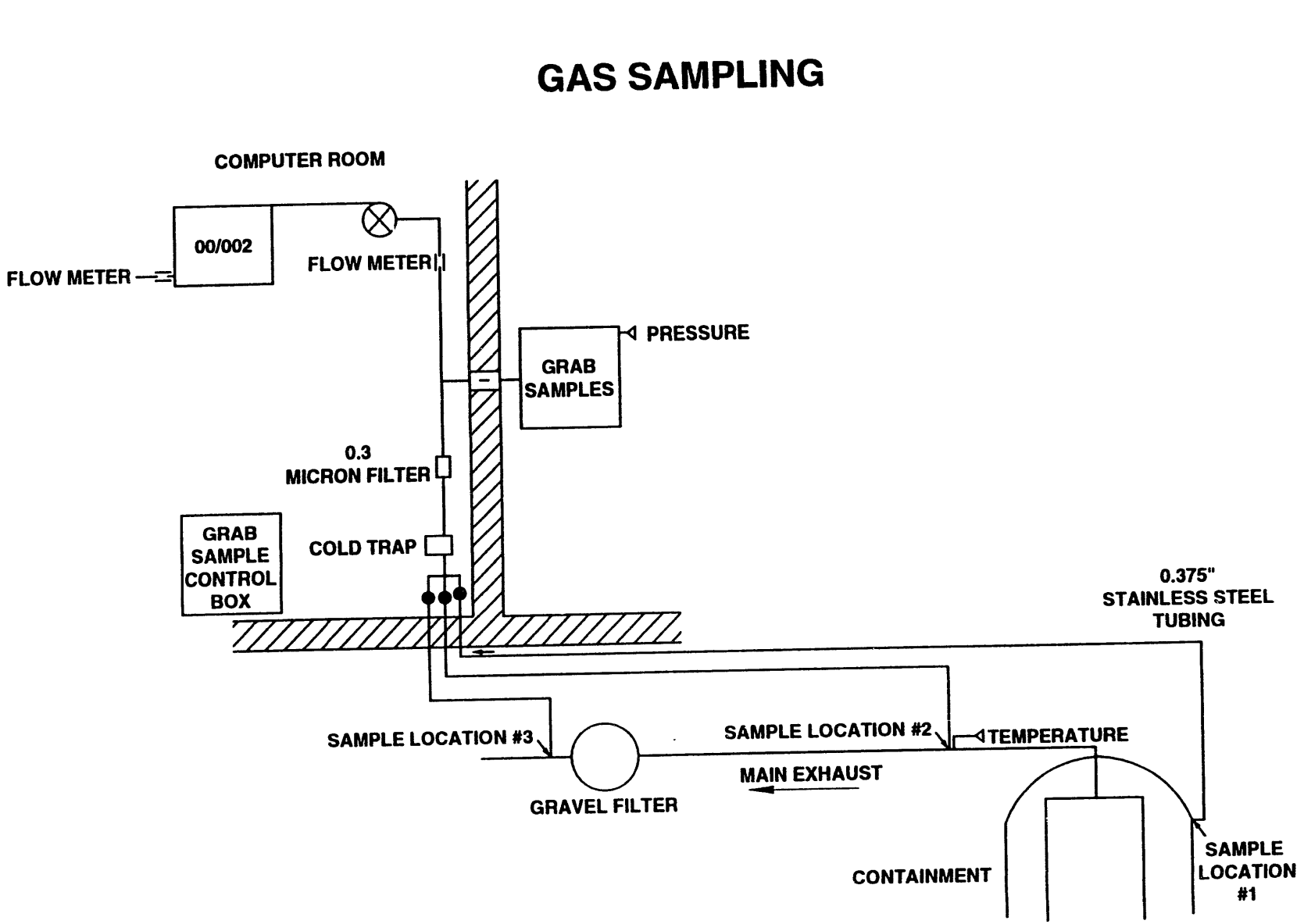

Figure 4.2 Schematic of gas sampling system

5-volt, full-scale output to the data acquisition system. Response time is 5 seconds for 90% of full-scale with a sensitivity of ± 2%.

4.2.3 Procedures

Gas flow through the sample line was established several minutes before the start of the test using the diaphragm pump. The flow was manually regulated to provide 2 actual liters per minute (alpm) from the main sample line as indicated by the Dwyer rotameter and Sierra mass flow meter. The sampling line flow was continuously monitored by a video camera focused on the rotameter. When a grab sample was taken, a transient was produced in the flow system that caused a sharp rise in the signal from the rotameter. Restoration of the original flow, indicated by the rotameter, showed that a grab sample of gas had been obtained. Sample times were recorded manually by the operator.

The CO/CO_2 monitor was warmed up for at least 30 minutes prior to the experiment. The readings on the front panel were checked to make sure they corresponded to the values displayed on the data acquisition system.

4.3 Gas Flow Instrumentation

The flow system in the WETCOR-1 experiment consisted of a series of piping and tubing with a gravel filter and turbine blower instrumented with a variety of devices for measuring gas flow rates (see Figure 4.1).

Ambient air was drawn into the containment chamber through a 1.5-m long, 10.2-cm diameter aluminum tube. This duct was bolted to the 15.2-cm ASME flange port welded to the 13.2 m^3 containment vessel with a steel reducer. Bolted to the upstream end of the air intake was a Donaldson prefilter and HEPA filter. The prefilter is rated at 1980 standard liters per minute (slpm) with a pressure drop of 1.0 cm of water and the HEPA filter is rated at 1130 slpm with a pressure drop of 2.3 cm of water. The HEPA filter is certified to be at least 99.97% efficient filtering particles greater than 0.3 microns in diameter.

Installed 1 m downstream from the inlet of the aluminum tube was an insertable turbine air velocity meter manufactured by EG&G Flow Technology Inc. This device measured the inlet flow to the test fixture. The velocity limits of the meter were 0.2 - 15 m/seconds. The full-scale linearity was ± 1.5% and repeatability ± 0.25%.

Exhaust gases flowed from the containment chamber through a 15.2-cm ASME flange into the exit-flow circuit. Bolted to the ASME flange on the containment chamber was an adapter reducing the 15.2-cm ASME flange to 10.2 cm stainless steel tubing. Several lengths of tubing with conflat flanges connected the containment chamber with the gravel filter. The tubing was configured with adapters and fittings for mounting aerosol photometers, gas sample ports, and aerosol sampling nozzles.

The flow line from the containment chamber was connected to a gravel filter to remove particulates from the exhaust gas stream before entering flow-measuring devices installed downstream of the filter. The gravel filter (Figure 4.3) was constructed of 304 stainless steel and contained five sections. The filter was 2.1 m high, had a 45.7 cm O.D. with a 0.6-cm wall. The upper and lower sections of the filter were 45.7 cm in height with a 10.2-cm stainless lap-joint flange welded at one end. A 10.2-cm-O.D., 15.2-cm long stainless steel tube with one end fitted with a rotatable conflat flange was welded to the upper and lower sections of the gravel filter directly opposite the lap-joint flange. The center sections of the filter were 30.5 cm high with a 45.7 cm O.D. The top section of the filter contained approximately 45 kg of river stone measuring between 5 and 10 cm nominal diameter. The second section contained approximately 22.7 kg of 1.9-cm alumina spheres. The third section contained approximately 45.4 kg of 1.3-cm-diameter solid alumina spheres. The fourth section contained approximately 45.4 kg of 0.6-cm-diameter solid spheres. The fifth section contained approximately 45.4 kg of 0.5-mm-diameter fused silica particles.

A Spencer single-stage turbine blower was installed downstream of the gravel filter to draw ambient air into the containment chamber and flow system.

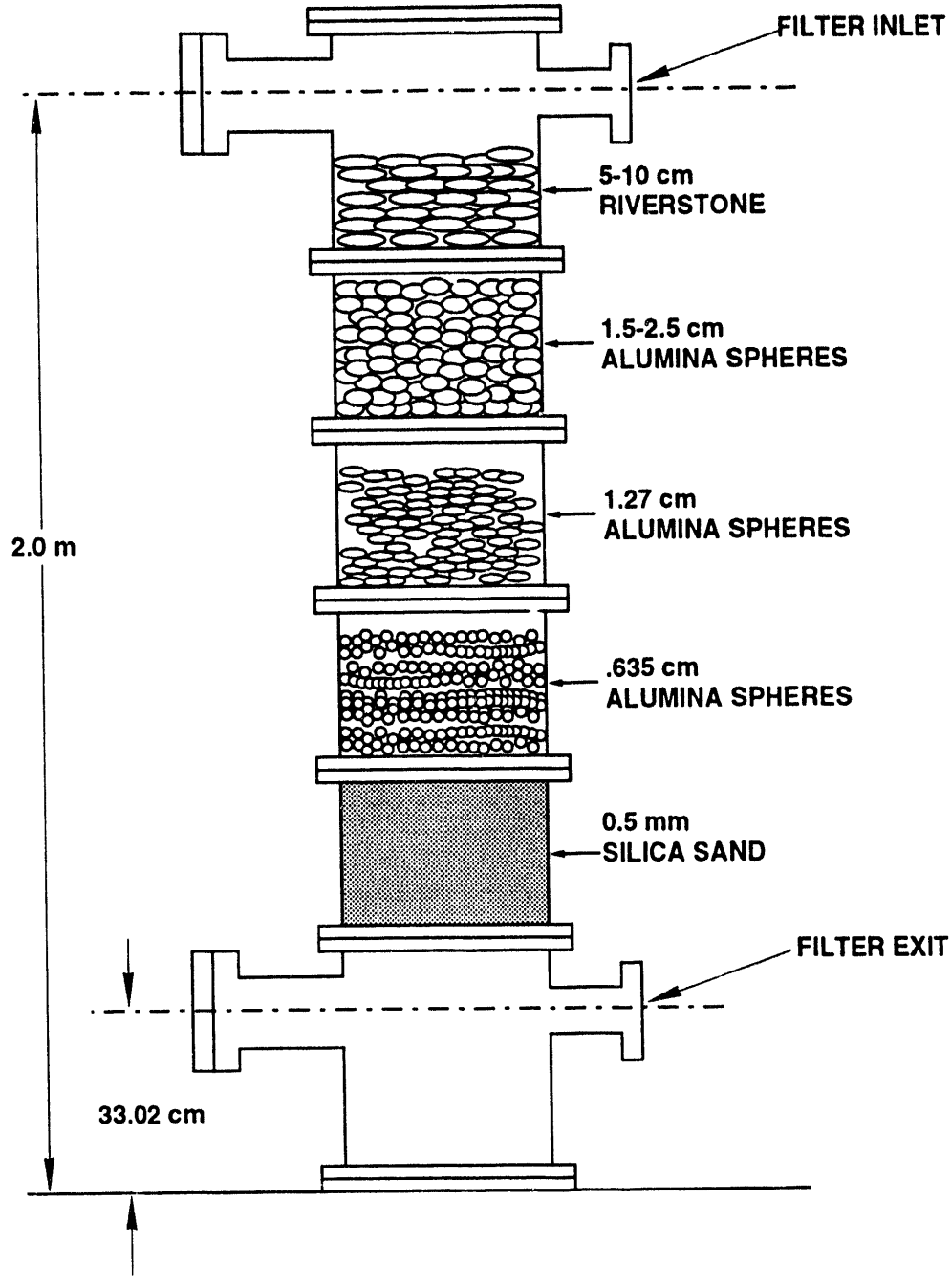

Figure 4.3. Schematic of modular gravel filter

The blower was capable of delivering 14155 slpm of 25 C air with a pressure drop of 69 cm of water when the discharge pressure was 100 KPa. A 10.2-cm butterfly valve was installed at the blower exhaust to regulate the flow-rate of air through the system.

A Donaldson cylindrical prefilter in series with a HEPA filter was installed between the gravel filter and blower. These filters were designed to remove particulate matter as small as 0.3 microns that might pass through the gravel filter and foul the blower laminar-flow element or turbine meter located downstream. These were the same types of filters used on the air intake described above.

Bolted to the butterfly valve was a 1.2-m length of aluminum tubing with an I.D. of 7.5 cm. Bolted to the end of this pipe section was a Mariam laminar-flow element. This device was capable of measuring flow rates to 2550 slpm with a pressure drop of 23 cm of water. A Setra 0-to-38.1-cm water differential-pressure transducer and Dwyer 0-to-76.2-cm water Magnehelic gauge were connected in parallel to measure flow pressure.

Bolted to the exit of the flow element was a 7.62-to-5.08-cm ASME reducer. Bolted to the reducer was a 1.5-m length of 5.08-cm black pipe terminated with a turbine flow meter to provide a redundant measure of gas flow from the test fixture. The turbine flow meter is capable of measuring flow rates to 6372 liters per minute (lpm). A type-K thermocouple was installed in the flow pipe just upstream of the orifice to measure the temperature of the exhaust gases.

After the experiment setup was completed for the WETCOR-1 experiment, an *in situ* calibration was performed with the turbine blower drawing air through the flow system. This was done to validate the laboratory calibrations, to evaluate the performance of the flow system, and to determine the system flow pressure as a function of flow rate.

4.4 Aerosol Instrumentation

It has been well established that high-temperature melt interactions with concrete produce aerosols. Aerosol production during the interaction of molten core debris with concrete could be an important source of radioactive materials to the reactor containment during a severe accident. There is, then, great interest in how water pools overlying melts interacting with concrete might attenuate the aerosol production [Powers and Sprung, 1992]. Though the primary purpose of the WETCOR-1 test was to study the issues of crust stability, the test was also instrumented to monitor aerosol production. This instrumentation is shown schematically in Figure 4.4. The instrumentation was essentially the same as that used in previous tests [Copus et al., 1989]. The main components of the aerosol instrumentation were (1) sample extraction and dilution components, (2) aerosol filter samplers, (3) cascade impactors, (4) a cascade cyclone, and (3) an opacity meter. These components are described in the subsections below.

4.4.1 Sample Extraction and Dilution

Aerosols were sampled from the exhaust line from the containment chamber. The sample for the cascade cyclone was drawn through a 1.27 cm stainless steel gooseneck probe. Samples drawn through this probe passed into the cascade cyclone without dilution.

Aerosol samples for the filter samples and cascade impactors were obtained from a common inlet. This inlet was a stainless steel gooseneck probe with a 6.4 mm opening. The inlet opening was selected so that gas velocities through the inlet were nearly the same as gas velocities in the exhaust pipe and the aerosol sampling was essentially isokinetic.

Samples drawn for the filters and the cascade impactors were diluted with air to meet the requirements of the sampling devices. A single stage of dilution was done for the filter samplers. Two dilutions were done for the impactors.

A diluter consisted of a 6.4 cm O.D. aluminum outer tube 15 cm long and a 1.9 cm I.D. sintered stainless steel inner tube. Dry dilution gas was fed to the annulus between the two tubes. The mass

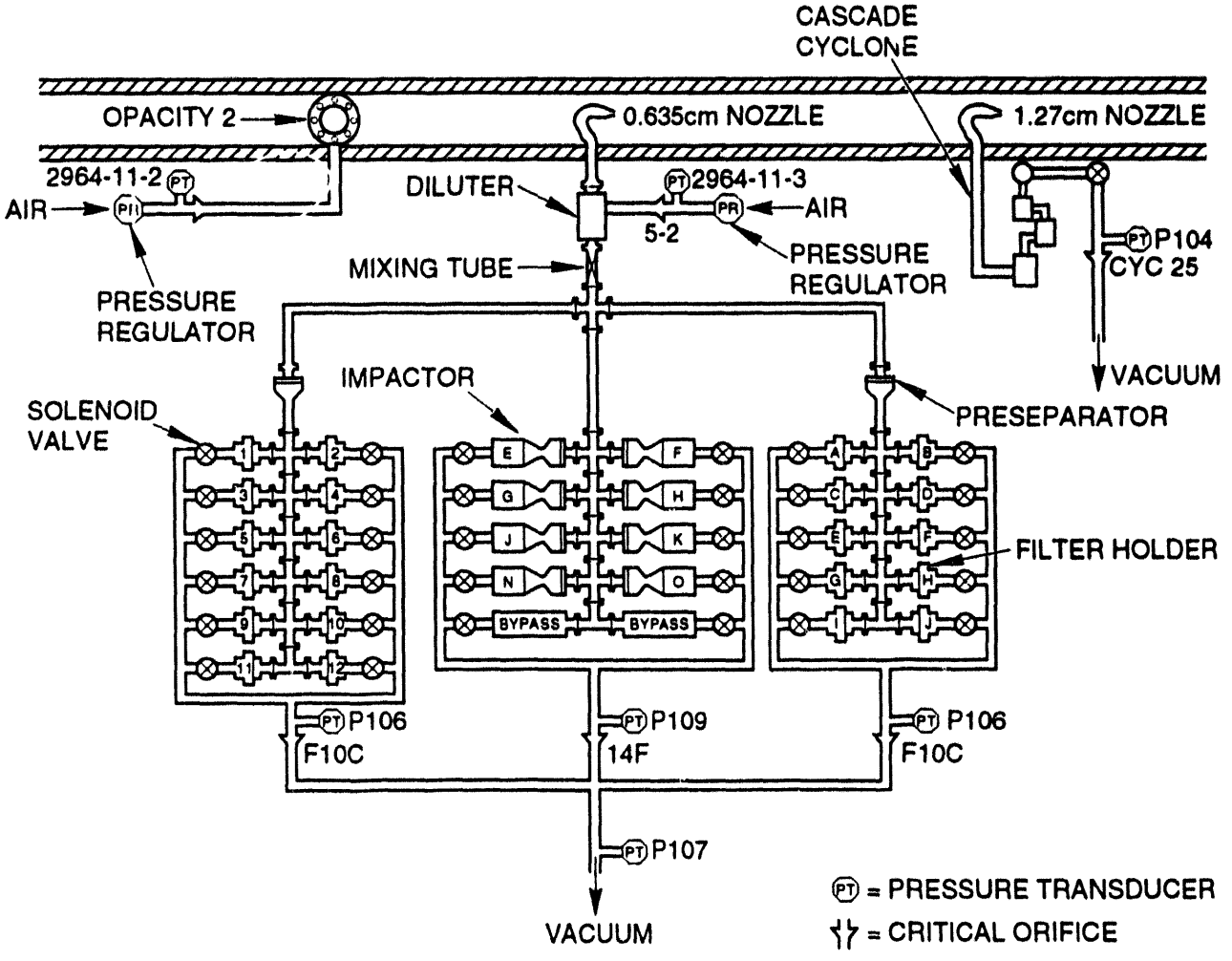

Figure 4.4. Schematic of the aerosol instrumentation

flow of this gas was controlled by a calibrated critical oriface. A strain gauge pressure transducer (Kulite) was used to monitor this flow.

Calculation done with the ASTEC computer code [Yamano and Brockmann, 1989] indicated that the aerosol sampling system would pass particles less than 5μm in size to samplers with greater than 90% efficiency. Sampling efficiency was calculated to degrade to about 50% for 10μm aerosol particles.

4.4.2 Filters

Each filter sample provided a collected mass of aerosol with an aerodynamic equivalent particle diameter less than 10 to 15 micrometers. Filter banks were plumbed to a single critical orifice giving a nominal filter sample flow rate of 10 lpm. The filter banks consisted of 22 Gelman in-line stainless-steel filter holders. These 5.9-cm-diameter, 5.7-cm-long stainless-steel filter holders (Gelman catalog number 220) were designed for pressure applications of up to 1.4 MPa. The filter holders used 47-mm-diameter silver membrane filtration media (Hytex filter, 0.45 micron Silver Membrane). These filters were chosen because they are better suited for higher temperature applications and for posttest chemical analysis. The effective filtration area was 9.67 cm^2 for each filter sample. The filters were connected to the Leybold-Heraeus quick-disconnect fittings and installed between the first and second stage of dilution on the impactor assembly. The filter-sample section was wrapped with silicone-coated heater tapes and covered with aluminum-backed fiberglass insulation to prevent water condensation. The heater tapes were controlled by the 120 VAC variable transformer. Type-K thermocouples were used to monitor filter bank temperatures.

Filters were desiccated for two days prior to weighing and installation. Post test the filters were again weighed on a calibrated balance ($\pm$0.0002 grams)

4.4.3 Cascade Impactors

The Anderson MK-III Cascade Impactors used in the test were aerosol particle sampling devices which yielded aerosol mass concentration as a function of aerodynamic particle size. An Anderson MK-III cascade impactor inertially classifies aerosol particles into nine size bins. This inertial classification was accomplished by accelerating the particles through successively smaller holes (and higher velocity jets) in a stack of orifice plates. Under the jets of each plate was a glass fiber collection substrate. Particles were collected by impaction on the substrate. Those small enough to follow the gas stream in one stage pass onto the subsequent orifice plates or stages where they could be collected. The impactor was 8.2 cm in diameter, 18 cm in length, and was constructed of stainless steel. A preseparator on each impactor removed particles larger than 10μm. Each impactor contained eight collection plates and a backup filter. On each stage a glass fiber substrate was installed. Substrates and the backup filter were desiccated and assembled in a manner similar to that used for the filters (see section 4.4.2).

4.4.4 Cascade Cyclone

The cascade cyclone was manufactured by Sierra. This device inertially classified aerosol particles and yielded a mass distribution with respect to aerodynamic equivalent particle diameter. The classification was performed by flowing the aerosol sample through a succession of six cyclones. The flow was introduced tangentially into the circular body of the cyclone where the circulating swirling flow caused larger particles to move by centrifugal force to the walls where they could be collected. Typically, several hundred milligrams of sample were collected on each stage. The cascade cyclone was operated long enough (10 minutes) to collect enough size-segregated material to obtain a size-segregated bulk analysis of the aerosol composition.

The assembled cascade cyclone was 12.7 cm in diameter and 60 cm long. The cyclone aerosol sample was drawn through a 12.85-mm-I.D. stainless steel gooseneck nozzle (Anderson) located coaxially in the center of the exhaust line. The cyclone was operated nominally at 25 alpm.

4.4.5 Opacity Meter

Two Dynatron Opacity Monitors were installed in the exhaust line. Opacity Monitor #1 was installed 12.7 cm upstream of the aerosol sampling nozzle.

Opacity Monitor #2 was installed approximately 40 cm downstream of the containment vessel. Quartz windows isolated the light source and photodetector from the aerosol flow. A sheath gas injection system was used to keep the windows from becoming covered with deposited aerosol.

The sheath gas (dry air) flow rate was maintained at approximately 6 alpm with two critical orifices for each opacity monitor operating at approximately 3 atmospheres upstream pressure. The combined flow rate for both opacity monitors was 20 alpm. The opacity measured the extinction of light across a stream of flowing particulates. Calibration of the monitor was performed by correlation of the monitor output with the filter measurement of aerosol mass concentration.

4.5 Induction Power Instrumentation

The tungsten sleeve susceptors were heated using an Inductotherm 250 kW, 1 kHz induction power supply. Power was applied to the coil from a remote control panel located in the control room. Power was delivered from the power supply to the coil using two pairs of No. 32 high-current, water-cooled flexible leads. The leads were configured in a 4-lead arrangement. During the melting process, the induction power supply automatically controlled voltage and frequency to maintain the selected power. Maximum efficiency was maintained throughout the experiment without switching capacitors or voltage taps. The power to the coil was measured using a power transducer manufactured by Research Incorporated. This device converted the current and voltage measured near the coil just outside the containment chamber into a voltage equivalent to power. A water-cooled current transformer (Rogowski coil) manufactured by Amecon was placed around one pair of the flexible leads. The transformer ratio was 5:10,000. A 3-ohm resistor was placed across the output leads of the transformer to convert the current to a voltage input for the power transducer.

In order to conduct a posttest power balance and monitor the operational parameters of the power supply, the flow rate and differential temperature of the cooling fluid in the coil and power supply were measured during the experiment. The cooling fluid was an 8 weight percent mixture of ethylene glycol in water. The flow rate of the coolant flowing through the coil and power supply (separate circuits) was measured using a 3.8-cm (1.5 NPT) turbine flow meter installed in the flow line of each circuit. The flow meter was manufactured by Signet Scientific. The flow meter was connected to a separate power supply and signal conditioner to produce a voltage output equivalent to a calibrated flow rate.

The differential temperature across the water inlet and exit of power supply was measured using two Omega ON-970 (33K-44K ohm range) thermistors arranged in a half bridge circuit. The differential temperature across the coil was measured using a differential temperature transducer manufactured by Delta-T Co.

4.6 Water Flow and Inventory Instrumentation

At a prescribed time during the experiment (529 minutes), water was injected into the crucible cavity and on top of the molten charge. A schematic of the water flow control and collection system was shown in Figure 3.1. Ambient temperature water was delivered to the crucible using 1.9-cm-O.D. stainless steel tubing. A vertical length of tubing entered the crucible cavity from above. The tube was terminated by a 1.9-cm stainless steel Swagelok cross and a Swagelok tee having the same tube dimensions. The delivery tube was located adjacent to the cavity sidewall, and the tee terminating the delivery tube resided a few centimeters above the charge. This configuration provided four horizontal outlets for discharging water into the cavity. The cross and tee were wrapped with stainless steel wool to reduce the heating of the fittings and to prevent plugging of the outlets by melt splashing up from the molten pool during the early phase of the experiment.

The flow rate of water was controlled using a Jamesbury, remotely actuated, 1.9-cm (3/4 NPT) ball valve. The electric motor actuator could provide a full 90-degree rotation of the ball in approximately 10 seconds. Installed upstream of the ball valve was a Signet turbine flow meter, installed with a high-frequency pulsar and connected to a rate of flow transmitter. This meter was capable of measuring water flow rates up to 75

lpm with an accuracy of 1.5%. This meter was laboratory calibrated prior to the test.

Cast into the annulus of the crucible was an alumina tube used to channel water from the crucible to exit flow piping. The tube was 6.3 cm O.D.x 46 cm long. A series of 5.1-cm (2 NPT) galvanized pipe and associated fittings were used to connect the tube with a 2150-liter aluminum water storage tank (Figure 3.1). The exit-flow piping contained a 5.1-cm (2 NPT) diameter 45.7-cm deep sump in series with a reservoir having the same diameter but with a depth of 30.5 cm. The sump was installed to remove debris and particulates from the exit water flow stream. The reservoir was installed to maintain a volume of exit water from which samples could be taken.

The differential temperature between the inlet and exit water was measured using Omega ON-970-44008 thermistor probes configured in a half bridge circuit. Type-K thermocouples were installed in parallel with the thermistor probes as a backup for temperature comparisons. The thermistor bridge was calibrated prior to the experiment as were the thermocouples.

The 2150-liter water collection tank was instrumented to measure the volume of water in the tank. This was accomplished using a scheme to measure the pressure head exerted by the water column forming in the tank. A 0.64-cm-O.D. stainless steel tube was installed in the cover of the tank and positioned approximately 1 mm above the bottom of the tank. A Swagelok stainless steel cross was mounted to the end of the tube protruding through the cover. One outlet of the cross was connected to a Setra differential pressure transducer having a range of 0-35 kPa. The other outlet was connected to a Dwyer differential pressure transducer having a range of 0-18 kPa. This transducer provided a backup to the Setra. An argon gas bottle was connected to the third outlet of the cross to provide the back pressure to the water column. The flow of gas was controlled using a low-pressure regulator and needle valve. The regulator was adjusted to provide a back pressure of approximately 70 kPa, and the needle valve was set to provide a gas-flow equivalent to form one bubble per second through the water column that formed in the stainless-steel tube installed in the water tank.

4.7 Video Monitoring Instrumentation

Three video cameras were used to obtain visual, real-time records of the test. One camera was focused on the apparatus providing an overview of any events happening external to the containment vessel. Two video cameras, each with a variable iris and zoom control, were mounted to the outside of the containment vessel. These cameras were focused on the interaction crucible through a 15-cm, gas-purged glass port. One camera, which was mounted to the top of the vessel, was focused directly into the crucible cavity to record core/concrete/water interaction phenomena. The other camera was mounted on the large chamber access door and focused at an elevation to view the top of the crucible. This camera captured images of the atmosphere inside the containment vessel. All the cameras were connected to VHS recorders, color monitors, and time generators. The time generators provided a time image visible on the screen for documenting events.

4.8 Data Acquisition System

The Hewlett Packard 1000 data acquisition system recorded data from 165 channels every 15 seconds for the first 176.5 minutes of the experiment and every 5 sec thereafter. Two-hundred and ten channels of data may be acquired during an experiment. Of the 210 channels, 150 are for type-K thermocouples, 20 are for either type-S or type-C thermocouples, and the remaining 40 are DC voltage channels. A patch panel routes all the analog data channels from the test location to the Hewlett-Packard Model 2250 measurement and control unit. This unit houses an analog-to-digital converter capable of multiplexing 216 data channels. The voltage range of the data acquisition unit was $\pm$ 10 volts DC with a programmable gain to increase sensitivity if the expected voltages were small (millivolts). A Hewlett-Packard Model 1000 series A-600 mini-computer was used to control all remote devices and manipulate the data received from the Measurement and Control Unit. Data were stored on a Hewlett-Packard Model 7946, 15 megabyte hard disk. A Hewlett-Packard Model 2623 terminal was used to command the microcomputer during the test and to display real-

time data in a tabular format as data acquisition progresses. A desktop terminal (Hewlett-Packard Model 9836) was used to display real-time data in both the graphical and numeric format. The terminal provided the capability of selecting five individual graphs of eight channels each during the test. This terminal could also be used to provide interrupt control over the mini-computer during the experiment. A Hewlett-Packard Model 9872 four color plotter and Series 33449A LaserJet III laser printer were used for posttest data plotting. Data were transferred to magnetic streaming tape, high-density 5.25-in or 3.5-in floppy disks.

The measurement accuracy of the 14-bit analog-to-digital converter was 1.56 microvolts in the most sensitive range, and 1.25 millivolts at the highest range (-10 to +10 volts). With the appropriate range setting, the resolution for a type-K thermocouple is $\pm$ 1°C, and for type-S or type-C thermocouples, the resolution is $\pm$ 1.1°C.

Prior to the experiment, both the analog-to-digital converter and real-time clock on the computer were calibrated.

5.0 Test Procedures and Posttest Observations

The power calibration, operational procedures, table of critical events and posttest observations in the WETCOR-1 test are presented in this section. A summary of the major operations and events of the test is shown in Table 5.1.

5.1 Power Calibration

Power calibration tests were performed to determine the coupling efficiency and overall losses of the tungsten sleeve susceptor geometry. Calibration tests were conducted with the power supply operating at 100 and 150 KW. The results are presented in Appendix A. The net coupling efficiency determined from these tests was 14 $\pm$ 0.5% of the buss power. Coupling efficiencies were found to be within 1 KW in the calibration tests at different buss bar powers.

5.2 Operational Procedures

On the day of the experiment, after final calibration and pretest checkouts were performed, the data acquisition started recording 163 data channels plus time. Data was acquired from 133 thermocouple channels and 30 voltage channels. The initial sample rate was set at 1/minute. About 15 minutes later, voltage was applied to a 3 KW Calrod heater imbedded in the charge. The Calrod, 1.6 cm diameter and 122 cm long, was formed into a coil geometry with three turns having overall dimensions of 11.8 cm O.D. and 10.2 cm high. The Calrod was used to assist in heating the center of the charge material due to the low conductivity of the material. The Calrod heater failed at 339.5 minutes when the average charge temperature was 798 K.

The induction power supply was started at 184.5 minutes applying 51 KW to the induction coil. The power history is presented in Figure 5.1. The power supply operational data are shown in Appendix B. The power history shown in Figure 5.1 is a plot of power supplied to the buss bars of the apparatus as a function of time. Also shown is the power supplied to the susceptors assuming a 14% coupling efficiency as determined in the calibration tests described in Appendix A. Estimation of the power deposited in the melt is complicated by the fact that the uppermost susceptor radiates to the air during the heatup phase of the test and is exposed directly to the water pool once water was admitted. This estimation is discussed further in section 6.1.2. The discussions below of the events of the tests are keyed to the power supplied to the buss bars. The heating approach followed a procedure determined from pretest calculations. Power was increased to 100 KW at 215.5 minutes. The power supply was turned off at 262.5 minutes, 345.5 minutes, and 434.5 minutes to soak the charge, minimizing the thermal gradient from the perimeter to the center. The onset of concrete erosion at the perimeter of the charge began at 466.5 minutes. Erosion of concrete was detected at the mid-radius thermocouple array at 475.7 minutes.

At 519.5 minutes the oxide charge became completely molten, forming a gas-sparged pool. Two minutes later, a floating crust completely covered the melt surface. The video data showed solid islands float on the surface of the melt. The islands welded together to form a single porous, floating crust by episodic eruptions of liquid melt through gaps in the plates of crust. The sampling period of the data acquisition system was reduced from 60 to 5 seconds during the period. The power was increased to 200 KW at 522.4 minutes. Six minutes later (528.3 minutes) the crust remelted and collapsed into the molten pool.

At 529.0 minutes the water quench was initiated with an inlet temperature of 295 K. At the time of water addition, the melt was vigorously agitated and the meltpool temperature averaged 1853 K. Arrays of thermocouples embedded in the concrete indicated that an average of 3 cm of concrete had been eroded. A constant flow rate of 57 lpm was maintained for the next 28 minutes sustaining a subcooled water pool. Following water addition, expulsion of molten material into the water continued for approximately 1.5 minutes. No energetic melt/coolant interactions were observed. During this melt/coolant period the power supply operated at 200 KW. At 554.9 minutes, a pressurized release of melt was observed at the side of the crucible with the overhead video camera. The power supply was shut off. At 557.0 minutes the water was turned off to observe the heating of the water pool above the melt. The average charge

Table 5.1 Summary and timing of major events during the WETCOR-1 experiment

TIME (Minutes	EVENT DESCRIPTION
0.0	September 5, 1991, 10:22 am MST, data acquisition system started sampling 163 channels (133 thermocouples and 30 voltage) at an initial scan rate of 60 sec. Charge material 34 kg 76.8 w/o Al_2O_3 + 17.9 w/o CaO + 4.0 w/o SiO_2 (melting point 2025 K)
15.0	Applied 203 V to Calrod heater
23.5	Type-K thermocouple channel 92 not reading; problem at patch panel corrected
25.0	Calrod temperature 725 K
49.5	Checked operation of remote control ball valve on water reservoir
54.5	Calrod temperature 1080 K, voltage 297 vac; reducing voltage to maintain 1075 K
59.5	Charge temperature: r = 2 cm, z = +8 cm; 708 K r = 6 cm, z = +4 cm; 424 K r = 10 cm, z = +2cm; 313 K
67.0	Calrod temperature 1155 K, voltage 201 vac; reducing voltage
77.0	Calrod temperature 1145 K, voltage 173 vac
119.5	Charge temperature: r = 2 cm, z = +8 cm; 986 K r = 6 cm, z = +4 cm; 491 K r = 10 cm, z = +2 cm; 313 K
170.0	Power supply on to check capacitor setting and pressure of coolant through the system
173.0	Power supply off
179.5	Charge temperature: r = 2 cm, z = +8 cm; 1006 K r = 6 cm, z = +4 cm; 518 K r = 10 cm, z = +2 cm; 370 K
184.5	Power supply on, 51 kW (Note induction power is power to buss)
215.5	Power increased to 100 kW
239.5	Charge temperature: r = 2 cm, z = +8 cm; 1038 K r = 6 cm, z = +4 cm; 552 K r = 10 cm, z = +2 cm; 390 K
250.0	Onset of concrete dehydration
262.5	Power supply off to soak oxide charge; added electrical low pass filters to thermocouple chennels 152, 153, 155, 158, 160, 161, 163, 165, 166, 169, 170 and 171
282.5	Power supply on, 100 kW

Table 5.1 Summary and timing of major events during the WETCOR-1 experiment

TIME (Minutes	EVENT DESCRIPTION
299.5	Charge temperature: r = 2 cm, z = +8 cm; 1026 K r = 6 cm, z = +4 cm; 588 K r = 10 cm, z = +2cm; 527 K
339.5	Calrod heater failed
345.5	Power supply off to soak charge, covered pressure transducers with plastic (rain potential); changed coolant filter to power supply (plugging)
359.5	Charge temperature: r = 2 cm, z = +8 cm; 1122 K r = 6 cm, z = +4 cm; 730 K r = 10 cm, z = +2 cm; 792 K
363.5	Power suppply on, 150 kW
389.5	Power reduced to 101 kW
412.5	Outer-array thermocouple C35 failed, depth 0 cm
419.5	Charge temperature: r = 2 cm, z = +8 cm; 949 K r = 6 cm, z = +4 cm; 849 K r = 10 cm, z = +2 cm; 1022 K
434.5	Power supply off to soak charge; gas burning observed at tungsten sleeve/charge interface
450.5	Power supply on, 150 kW
466.5	Outer-array thermocouple C36 failed, depth 1 cm; onset of ablation
468.5	Reduced power to 100 kW
475.7	Axial-array thermocouple C19 failed, depth 1 cm
479.5	Charge temperature: r = 2 cm, z = +8 cm; 1047 K r = 6 cm, z = +4 cm; 1121 K r = 10 cm, z = +2 cm; 1087 K
489.5	Alumina-tube thermocouple failed, depth 0 cm
500.5	Axial-array thermocouple C20 failed, depth 2 cm
505.5	Increased power to 149 kW
511.5	Axial-array thermocouple C21 failed, depth 3 cm
514.0	Gas grab sample #1
514.5	Axial-array thermocouple C22 failed, depth 4 cm
515.5	Outer-array thermocouple C37 failed, depth 2 cm
518.5	Scan time changed from 60 sec to 5 sec

Table 5.1 Summary and timing of major events during the WETCOR-1 experiment

TIME (Minutes	EVENT DESCRIPTION
519.4	Reduced power to 95 kW
519.5	Charge completely molten, gas-sparged pool
520.0	Gas grab sample #2
520.7	Filter-sample #1, duration 60 sec; cascade cyclone sample, duration 10 minutes
521.4	Power increased to 148 kW
522.4	Crust frozen; power increased to 200 kW; lots of aerosol generation observed
522.7	Filter-sample #2, impactor sample E, duration 60 sec
523.3	Mid-radius-array thermocouple C1 failed, depth 0 cm
524.7	Filter-sample #3, duration 60 sec
526.7	Filter-sample #4, impactor sample F, duration 60 sec
528.3	Crust collapsed; gas-sparged pool established
528.6	Charge temperature: r = 2 cm, z = +8 cm; 1845 K r = 6 cm, z = +4 cm; 1807 K r = 10 cm, z = +2 cm; 1606 K
528.8	Filer-sample #5, duration 60 sec
529.0	Water quench initiated, 57 lit/minutes
530.6	Filter-sample #6, impactor sample G, duration 60 sec
532.7	Filter-sample #7, duration 60 sec
533.8	Mid-radius-array thermocouple C2 failed, depth 1 cm
534.7	Filter-sample #8, impactor sample H, duration 60 sec
535.5	Outer-array thermocouple C38 failed, depth 3 cm
536.7	Filter-sample #9, duration 60 sec
537.0	Power supply off to operate zoom on overhead camera to expand field of view
537.4	Restart power to the melt
538.5	Mid-radius-array thermocouple C3 failed, depth 2 cm
538.7	Filter-sample #10, impactor sample J, duration 60 sec
542.0	Gas grab sample #3
543.2	Charge temperature: r = 2 cm, z = +8 cm; 1692 K r = 6 cm, z = +4 cm; 1842 K r = 10 cm, z = +2 cm; 1636 K

Table 5.1 Summary and timing of major events during the WETCOR-1 experiment

TIME (Minutes	EVENT DESCRIPTION
543.3	Mid-radius-array thermocouple C4 failed, depth 3 cm
546.8	Outer-array thermocouple C39 failed, depth 4 cm
547.3	Filter-sample #11, duration 60 sec
548.3	Mid-radius-array thermocouple C5 failed, depth 4 cm
549.4	Filter-sample #12, impactor sample K, duration 120 sec
551.0	Gas grab sample #4
552.4	Filter-sample A, duration 120 sec
554.0	Outer-array thermocouple C40 failed, depth 5 cm
554.9	Power supply off
555.0	Pressurized melt runout observed on overhead camera
555.3	Mid-radius-array thermocouple C6 failed, depth 5 cm
555.7	Filter-sample B, impactor sample N, duration 120 sec
556.1	Axial-array thermocouple C23 failed, depth 5 cm; ablation stops
556.9	Water flow off Charge temperature: r = 2 cm, z = +8 cm; 1807 K r = 6 cm, z = +4 cm; 1776 K r = 10 cm, z = +2 cm; 1760 K
557.7	Filter-sample C, duration 120 sec
560.1	Filter-sample D, duration 120 sec
562.4	Filter-sample E, duration 120 sec
563.0	Water flow on, 57 lit/minutes
565.6	Fitler-sample F, duration 120 sec
567.9	Filter-sample G, duration 120 sec
569.9	Charge temperature: r = 2 cm, z = +8 cm; 1582 K r = 6 cm, z = +4 cm; 1592 K r = 10 cm, z = +2 cm; 1534 K
570.1	Filter-sample H, duration 120 sec
572.4	Filter-sample I, duration 120 sec
574.6	Filter-sample J, duration 120 sec
578.0	Water flow rate reduced to 29 lit/minutes

Table 5.1 Summary and timing of major events during the WETCOR-1 experiment

TIME (Minutes	EVENT DESCRIPTION
592.8	Water flow terminated
594.0	Gas grab sample #5
600.9	Charge temperature: r = 2 cm, z = +8 cm; 1183 K r = 6 cm, z = +4 cm; 1193 K r = 10 cm, z = +2 cm; 1123 K
635.0	Charge temperature: r = 2 cm, z = +8 cm; 945 K r = 6 cm, z = +4 cm; 940 K r = 10 cm, z = +2 cm; 864 K
638.0	Test terminated; total erosion depth 5 cm

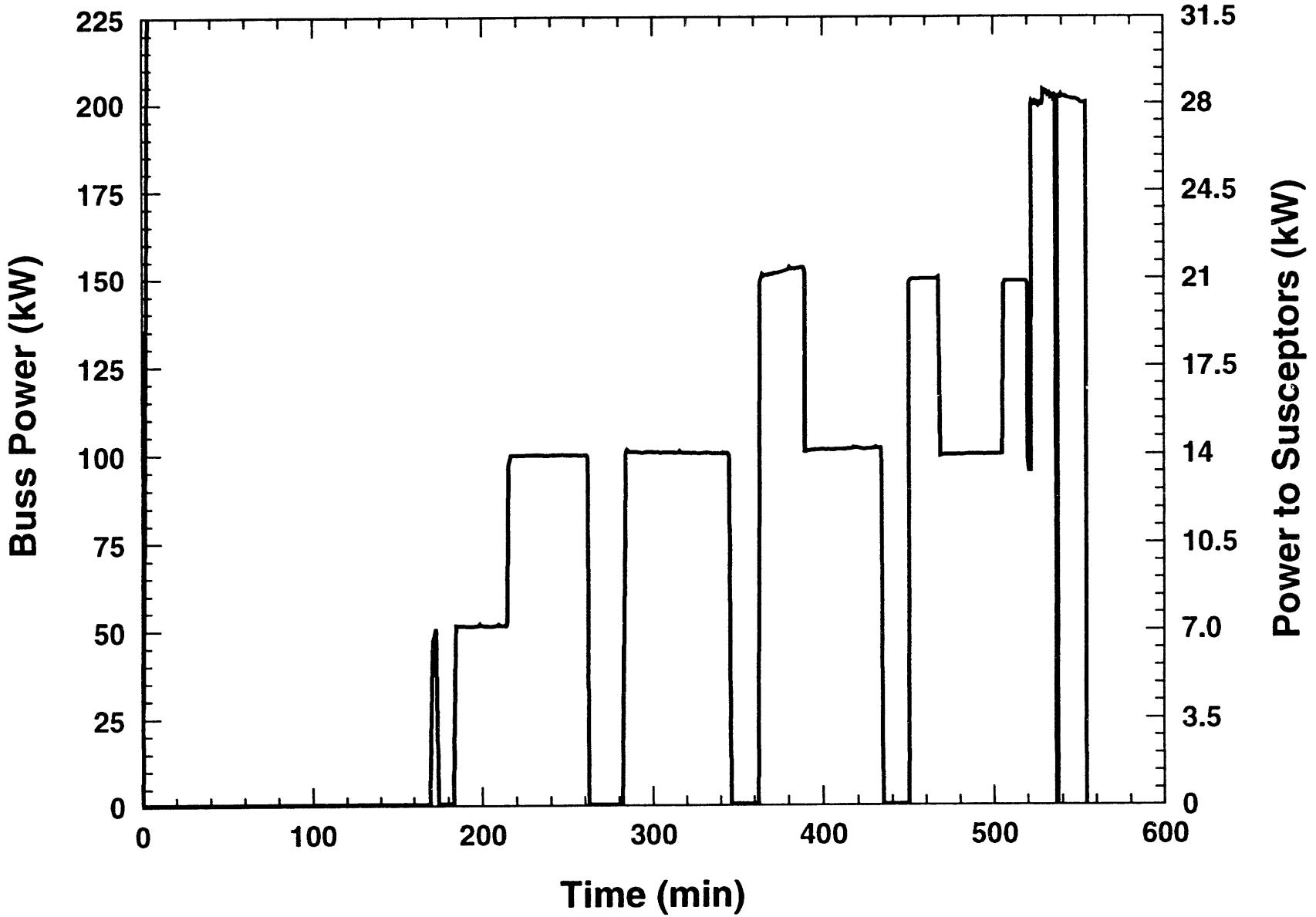

Figure 5.1 **Power history, WETCOR-1. Input power to the susceptors is 14% of the buss power and is indicated by the right hand scale on this figure.**

temperature at this time was 1781 K, but temperatures as high as 1880 K were measured. At 562.8 the water flow was initiated again at a flow rate of 57 lpm. The flow rate was reduced to 29 lpm at 578.0 minutes. The water was turned off at 592.8 minutes. The data acquisition was turned off at 638.0 minutes, terminating the experiment. The total concrete ablation indicated by thermocouples in the concrete was 5-6 cm.

5.3 Observations

A video record was made of the events just prior to and immediately after water was added to the molten-oxide pool. Initial conditions at the time the water was added were a tungsten temperature of 2100 K, a meltpool temperature of 1851 K, and MgO sidewall temperatures of 700 - 1200 K. The events of the test at the time of water addition are described briefly in sequential order using the timing marks from the computer record.

At 519 minutes the oxide charge became fully molten, and a thin veneer of crust material collapsed into the meltpool. Crust islands (about 5 plates of crust) began to form on the melt surface at 520 minutes. Episodically, there were eruptions of melt from between the islands of crust. The melt splashing over the islands eventually froze them together to form a stationary crust at 523 minutes. The tungsten sleeves were white hot at the crust boundary, and the crust materials were clearly not attached to these tungsten sleeves that formed the crucible perimeter. The plates of crust could be seen to be clearly moving independently initially. As episodic eruptions of melt continued, the islands of crust welded together, but remained unattached to the susceptor. The crust mass moved easily in response to the gases liberated from the concrete.

At 523 minutes, power to the tungsten sleeves was increased and the crust material once again collapsed into the meltpool. The meltpool was vigorously sparged by gases evolved from the concrete below the melt at this time. Some small amount of melt was ejected from the crucible due to the stirring gas action. Water was introduced to the molten pool at 529 minutes. The surface of the melt at 529 minutes was 3 to 4 cm below the top susceptor lip. No steam explosion was observed. Melt and water mixed together for the next 100 - 150 seconds again without explosion or significant water ejection from the crucible.

Glowing droplets of melt could be seen swirling through the water pool. It appeared that these droplets were formed by the same sort of eruptions of melt between floating islands of crust observed during the crust formation event in air. Certainly, the episodic nature of droplet appearance in the water pool was analogous to the random eruptions of melt that took place during the air-crusting event.

At 534 minutes, the view of the water pool clearly showed that a crust had formed and that gas was continuously being released through that crust into the subcooled water (320 K). This camera view held constant for the remainder of the test with no disruptions of the upper crust material.

Posttest observation of the solidified meltpool surface showed that the tungsten sleeves were bridged by a convoluted crust. The top of the crust was covered with detached spherical droplets of frozen oxide material a few millimeters in diameter. This particulate material weighed 1.5 kg. The crust itself was concave and appeared to be made up of connected black spheres, which ranged in diameter from a millimeter to a centimeter. The material was very solid and had significant mechanical strength. There were numerous blowholes (1-2 mm) in the surface. These blowholes were, apparently, vent pathways for gases produced by melt ablation of concrete.

The coil was removed from the crucible and the exterior was examined. Large circumferential cracks appeared in the crucible sidewall at a position adjacent to the original concrete interface. It was apparent that some melt had been ejected through these cracks. The video record was re-examined and it was determined that a minor, forced melt ejection did occur through the sidewalls at about 555 minutes. Melt debris weighing 3.5 kg was collected from the containment floor. This forced melt ejection occurred very late in the test and did not affect any of the principal test results.

The crucible was x-rayed and sectioned so that the interior structures could be examined. The x-rays showed that the bottom susceptor sleeve had collapsed downward and that there were some voids

in the resulting gap between the susceptor sleeves. A schematic of the posttest debris configuration is shown in Figure 5.2. The topmost crust material was very undulating and was several centimeters higher on one side of the crucible than on the other. Large, irregular voids appeared below the top crust for another 5 - 10 cm. The remaining meltpool material was below this voided area for a depth of 5 - 10 cm. The total erosion depth was 5 - 6 cm and the concrete was eroded all the way to the MgO sidewalls (40-cm diameter).

Photographs taken of the posttest examinations are shown in Figures 5.3 - 5.6. Figure 5.3 shows the top of the meltpool and features the blobs of shiny black material that made up the top crust. These globules are thought to be the solidified remains of melt ejected into the water pool during the early stages of water addition as seen in the videotape record of the test. There were 1.5 kg of frozen globules. Such globules are consistent with the observed ejection of melt through gaps in crust plates during the formation of a crust in air. As in the air-crusting event, solidified material appears to have sealed any major gaps in the crust. Closeup views of the shiny black material are shown in Figure 5.4. Though the material looks "glassy", upon fracturing it reveals a crystalline structure.

Figures 5.5 and 5.6 show the sectioned crucible. The cross-section of the crucible shows that erosion of the concrete was not entirely uniform across the concrete. As detected with the thermocouple arrays embedded in the concrete, erosion at the perimeter of the melt was more extensive than along the centerline. Note also that one susceptor ring collapsed to the base of the cavity. The upper rings remained in place. Frozen melt is quite porous; gases could easily pass through this crust material. Cracks, on the other hand, might be difficult to propagate through material with so many voids.
A sample of the crust material and a sample of the frozen melt pool were chemically analyzed for MgO, CaO, SiO_2, Al_2O_3, and iron oxide which was assumed to be present as ferrous iron oxide (FeO), for the purposes of reporting the results of the analysis. Results are shown in Table 5.2. In addition, x-ray fluorescence indicated that small amounts of chromium, titanium, sodium, potassium, and boron were present presumably as oxides in the samples. The results of quantitative analyses showed the samples to be essentially identical. The sample from the frozen melt pool contained somewhat more SiO_2 from the concrete as would be expected since the pool continued to ablate concrete after the crust was frozen.

Table 5.2 Chemical Analysis Results

	Wt. %				
Sample	MgO	FeO	Al_2O_3	SiO_2	CaO
Crust	5.3	1.8	50.3	19.0	23.3
Frozen Pool	4.8	1.7	49.0	22.2	21.0

Both samples contained MgO which came from the concrete and a small amount of ablation of the annular test fixture. Interestingly, there was no indication of significant amounts of tungsten oxide. Chemical conditions in the melt pool must have been sufficiently reducing that oxidation of the tungsten susceptor rings did not occur to any significant extent.

All samples were dark or black. The coloring of the samples is thought to be due to charge transfer absorption bands created by the ferrous-ferric iron equilibrium in the samples. Intensification of the coloring by charge-transfer absorptions due to interactions with manganese ions and titanium ions may also affect sample colors.

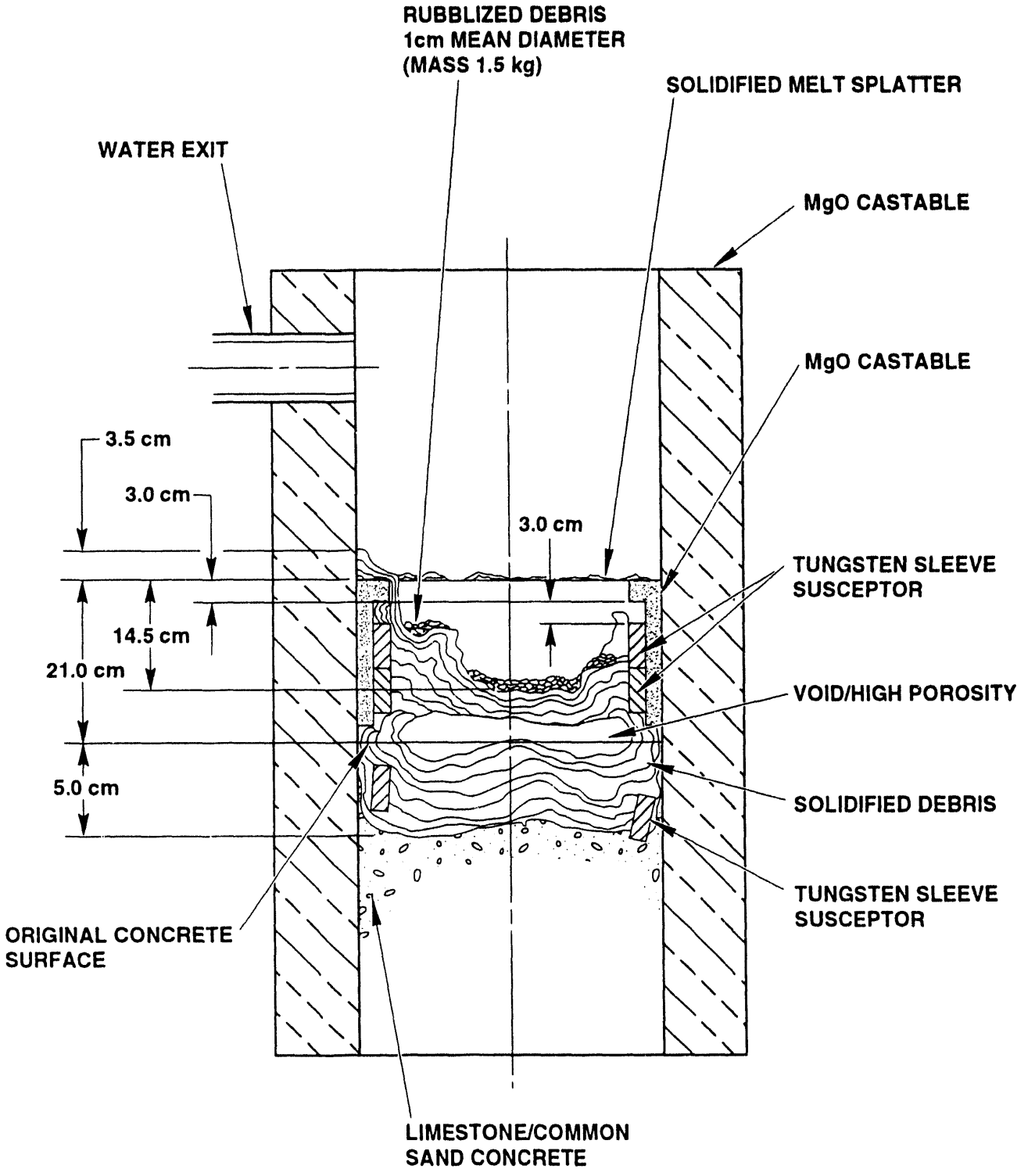

Figure 5.2. Posttest configuration, WETCOR-1

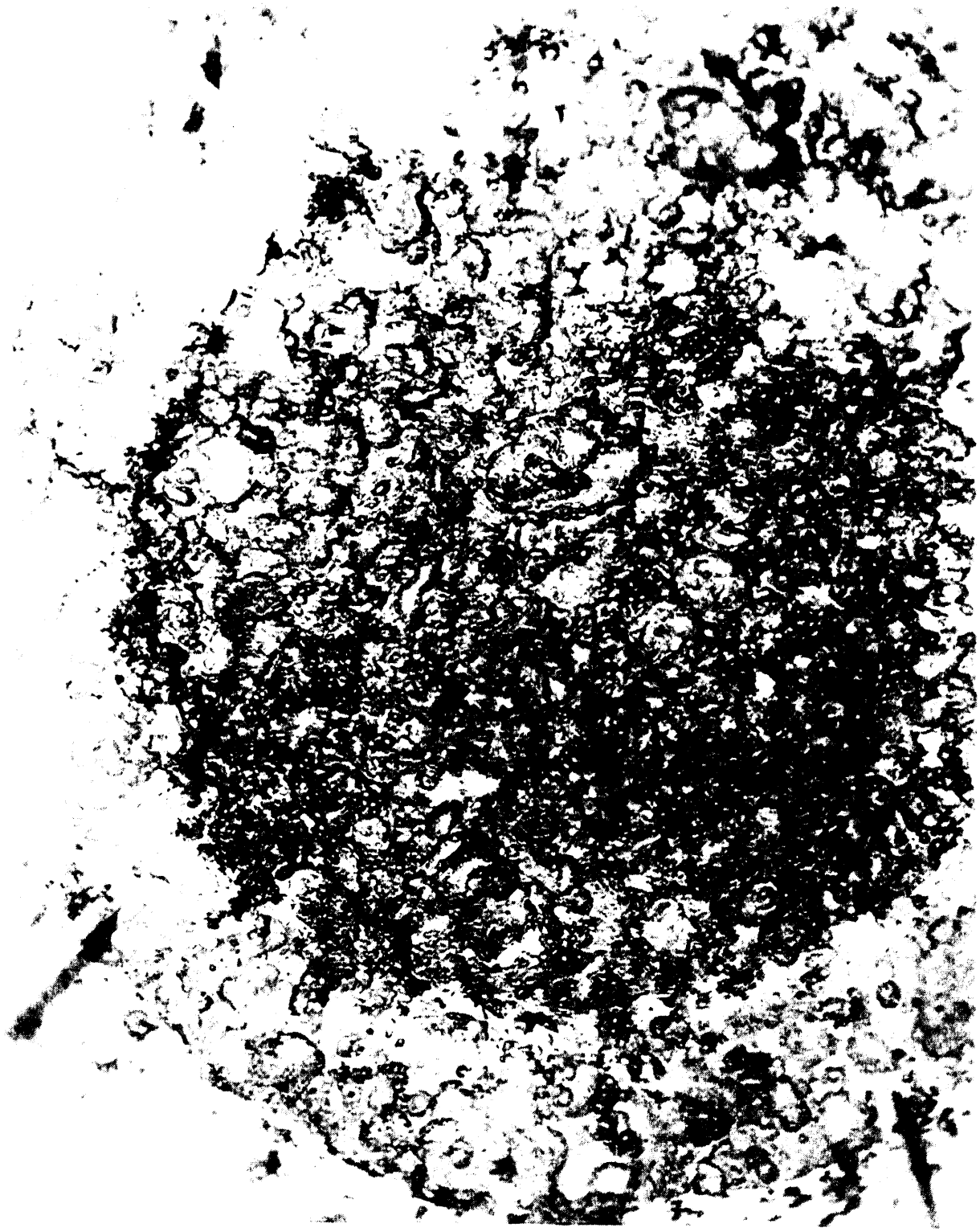

Figure 5.3 Top of WETCOR-1 meltpool

Figure 5.4 Oxide debris, WETCOR-1

Figure 5.5 Section of crucible, WETCOR-1

Figure 5.6 Top crust close-up, WETCOR-1

6.0 Data Presentation and Results

The most important objective of the WETCOR-1 test was met immediately after water introduction when it was observed that a stable crust formed despite elaborate efforts taken to ensure freezing melt did not immediately adhere to the crucible walls. The test was, however, continued to ascertain if some longer-term instability might develop which could lead to more rapid heat extraction by a water pool overlying the high-temperature melt. There was also interest in obtaining data on the aerosol emission through the water pool. During this continuation of the test, additional quantitative data pertinent to heat transfer during simultaneous melt interactions with concrete and water were collected. These quantitative data are presented and discussed in the following subsections. Important elements of these discussions are improvements that need to be made in the test configuration, operation, and instrumentation for future tests directed toward the issues of the heat transfer processes.

6.1 Temperature Data

Temperature data were obtained from the melt, the magnesium oxide walls of the crucible, and the concrete. These data will, in future tests, be essential for the determinations of heat balances and heat partitioning from the melt. Temperature data obtained in the WETCOR-1 test are discussed below.

6.1.1 Concrete Temperatures

Some example temperatures measured in the concrete are shown as functions of time in Figure 6.1. A complete set of temperature plots for the concrete are presented in Appendix C. Typically, temperature at a particular location in the concrete increased slowly between 400 and 600 K as the concrete dehydrated. Once the concrete was completely dehydrated at the particular location, the temperature increased rapidly. The failure temperature for type-K thermocouples is approximately 1645 K. Figure 6.1 shows that the concrete began to heat after 60 minutes, but did not begin to ablate until 520 minutes. The ablation process caused the thermocouples to sequentially approach and then contact the meltpool. Meltpool contact resulted in temperatures above 1650 K which were indicated as vertical off-scale lines in Figure 6.1.

Figures 6.2 - 6.4 show the concrete thermal response for the period between 400 and 600 minutes. The centerline response (Fig. 6.2) indicates that ablation began at 470 minutes and that 1-3 cm of localized erosion had occurred before water was added to the melt/concrete interaction at 529 minutes. Concrete erosion continued at the centerline location after water was added and was 5-6 cm at 555 minutes. Ablation stopped after 556 minutes when the power to the experiment was shut down. The response of the centerline thermocouple after 556 minutes shows temperatures in the concrete decreasing at approximately 3 K/minute.

Results were also obtained from thermocouples at the mid-radius (R = 10 cm) and outer-radius (R = 18 cm) locations within the concrete. The outer-radius monitor (Figure 6.3) indicated that localized ablation started at 410 minutes and that approximately 2 cm of ablation had occurred when water was added at 529 minutes. Ablation continued until power was shut down at 555 minutes. Temperatures dropped at 6 K/minute once induction power input ceased. The mid-radius thermocouple (Figure 6.4) showed that localized ablation did not start until 515 minutes. Ablation here continued to cause thermocouple failure until 555 minutes after which temperatures at the 6-cm depth started to decrease at 4 K/minute.

A combined plot of the ablation profile is shown in Figure 6.5. At the start of the principal period of interest (528-556 minutes) there were approximately 3 cm of ablation at the centerline of the concrete basemat, zero erosion at the mid-radius of the concrete basemat, and 2 cm of erosion at the far radius of the concrete basemat. At the end of the water-power period (555 minutes), the erosion front was very uniform at a depth of 5-6 cm in all locations. The ablation rate appeared fairly constant during the period from 530 to 555 minutes at a rate of 6-11 cm/hr. (Overall erosion rates from the onset of concrete ablation are, on average, 2.9 ± 0.9 cm/hr for the center and outer radius arrays and about 11 cm/hr for the mid-radius array. Ablation and isotherm data are presented in Appendix C.

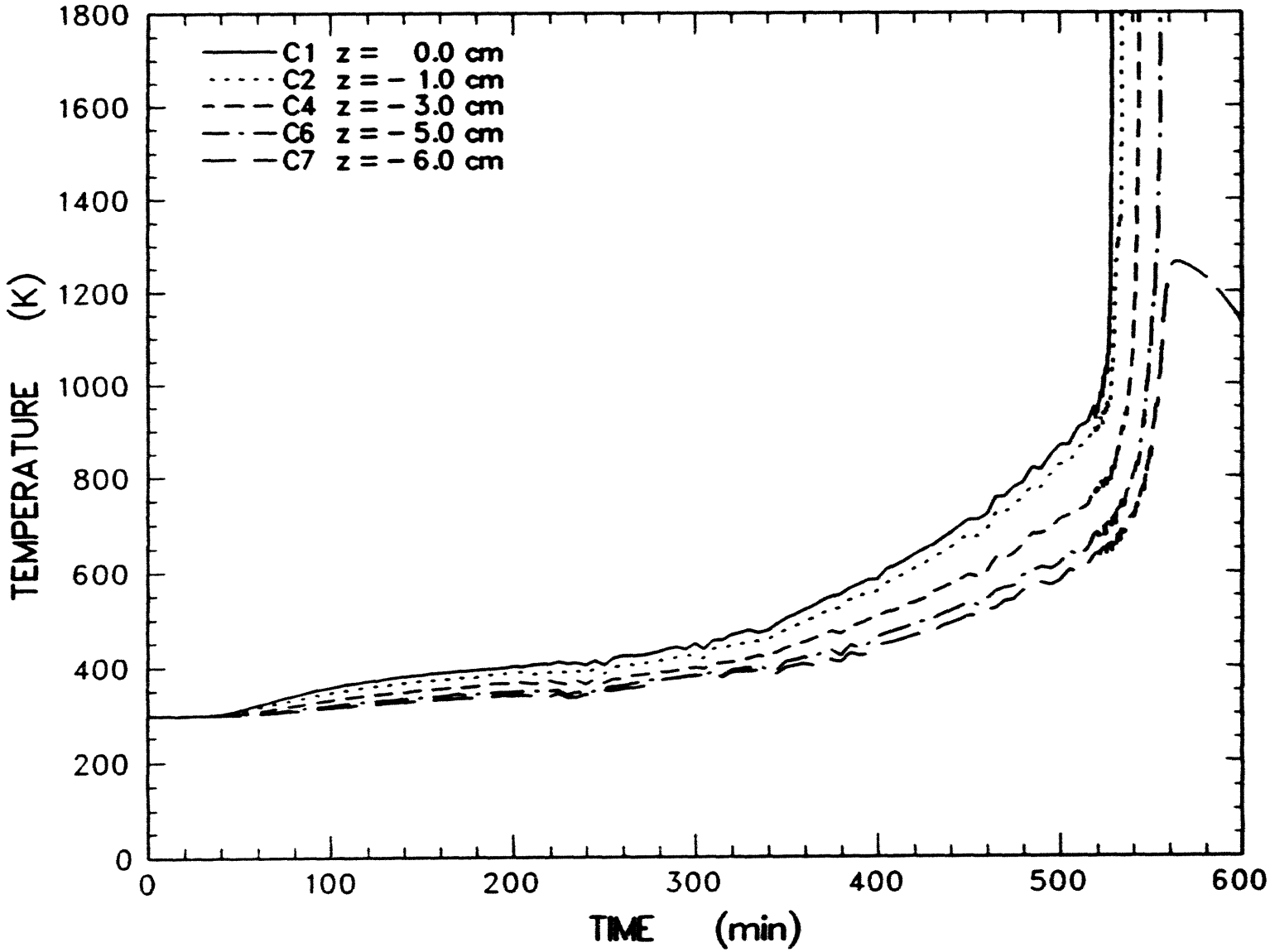

Figure 6.1 Midradius array concrete response at five depths (0-6 cm)

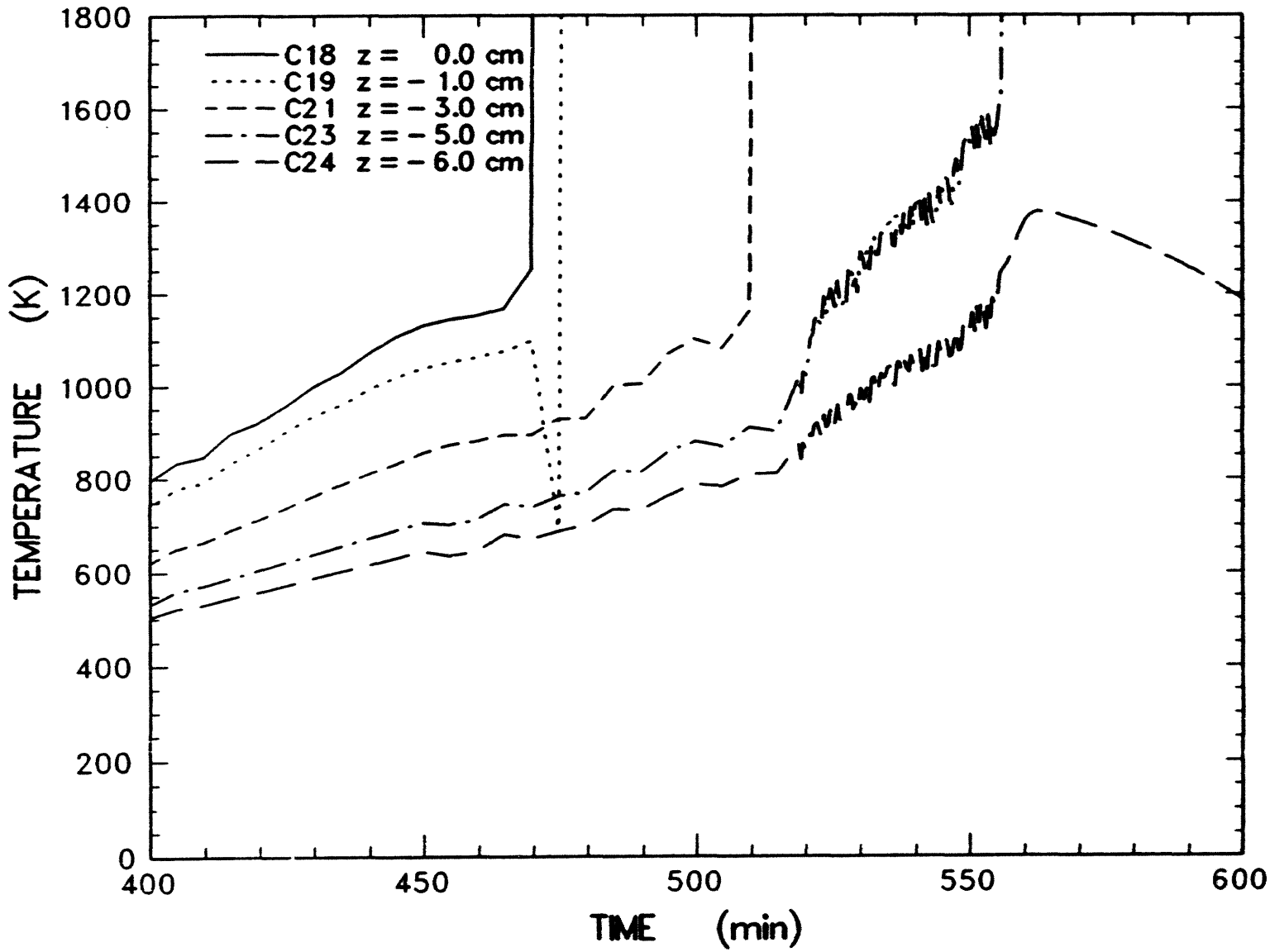

Figure 6.2 Axial centerline concrete response at five depths (0-6 cm)

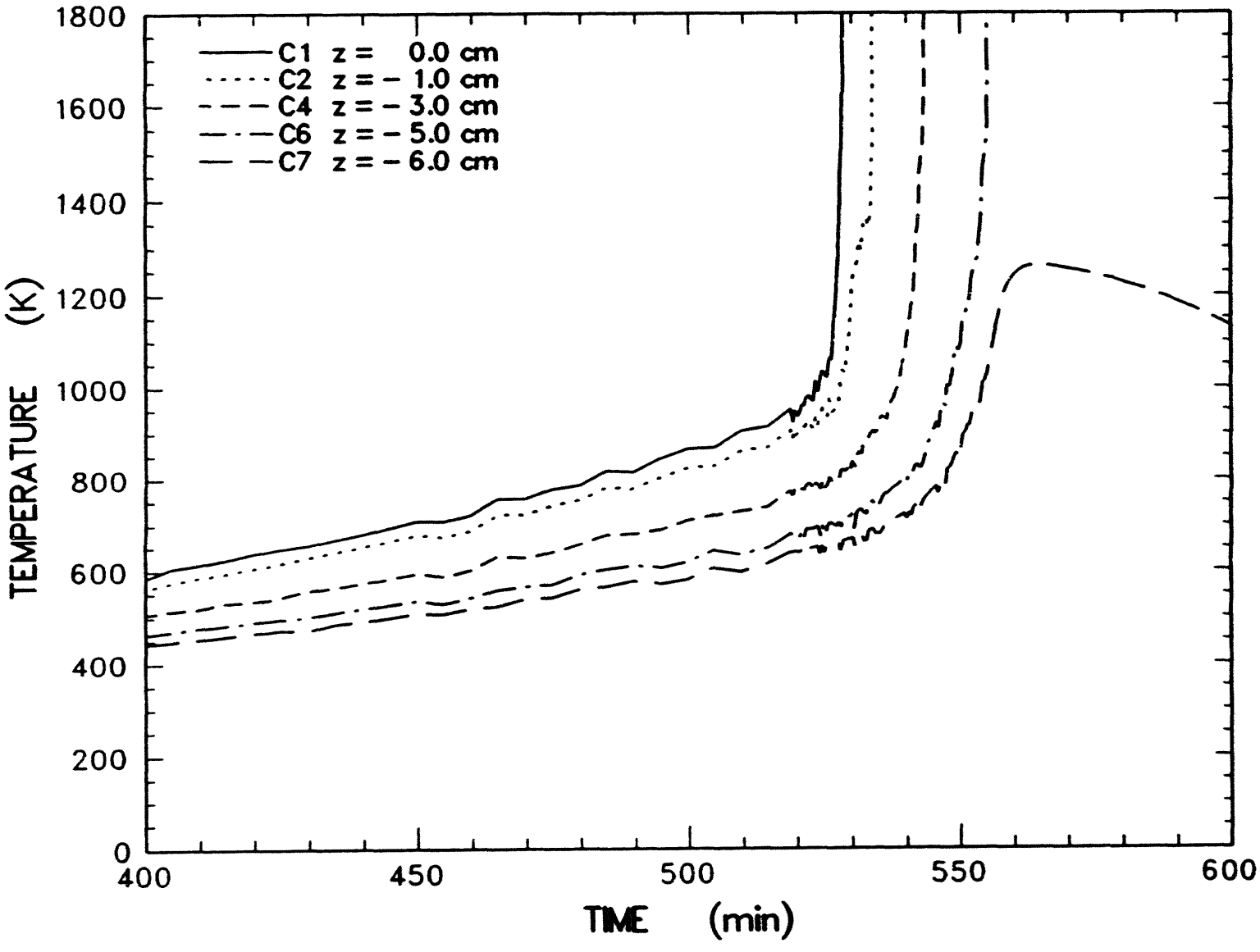

Figure 6.3 Expansion of midradius array concrete response at five depths (0-6 cm)

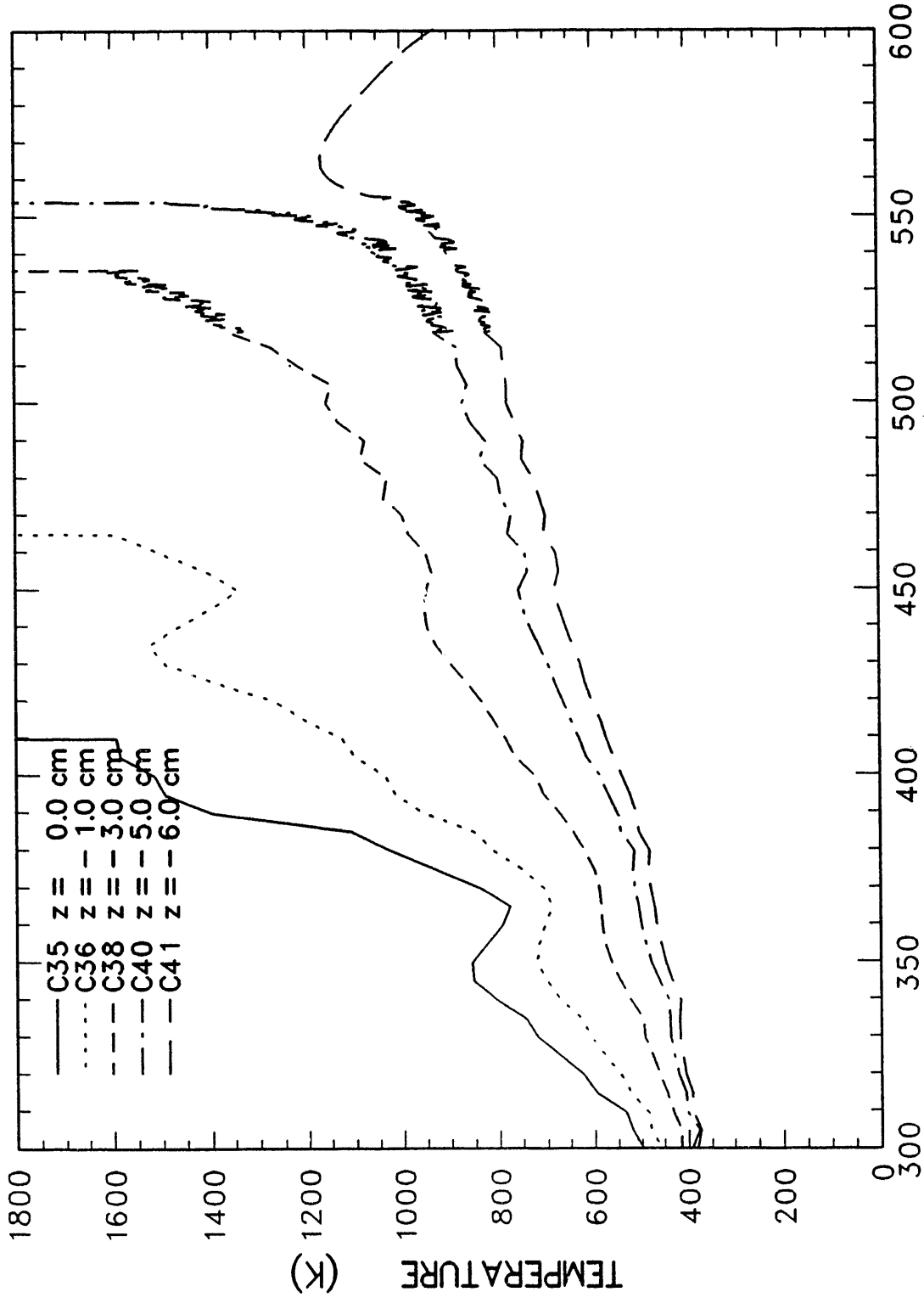

Figure 6.4 Perimeter array concrete response at five depths (0-6 cm)

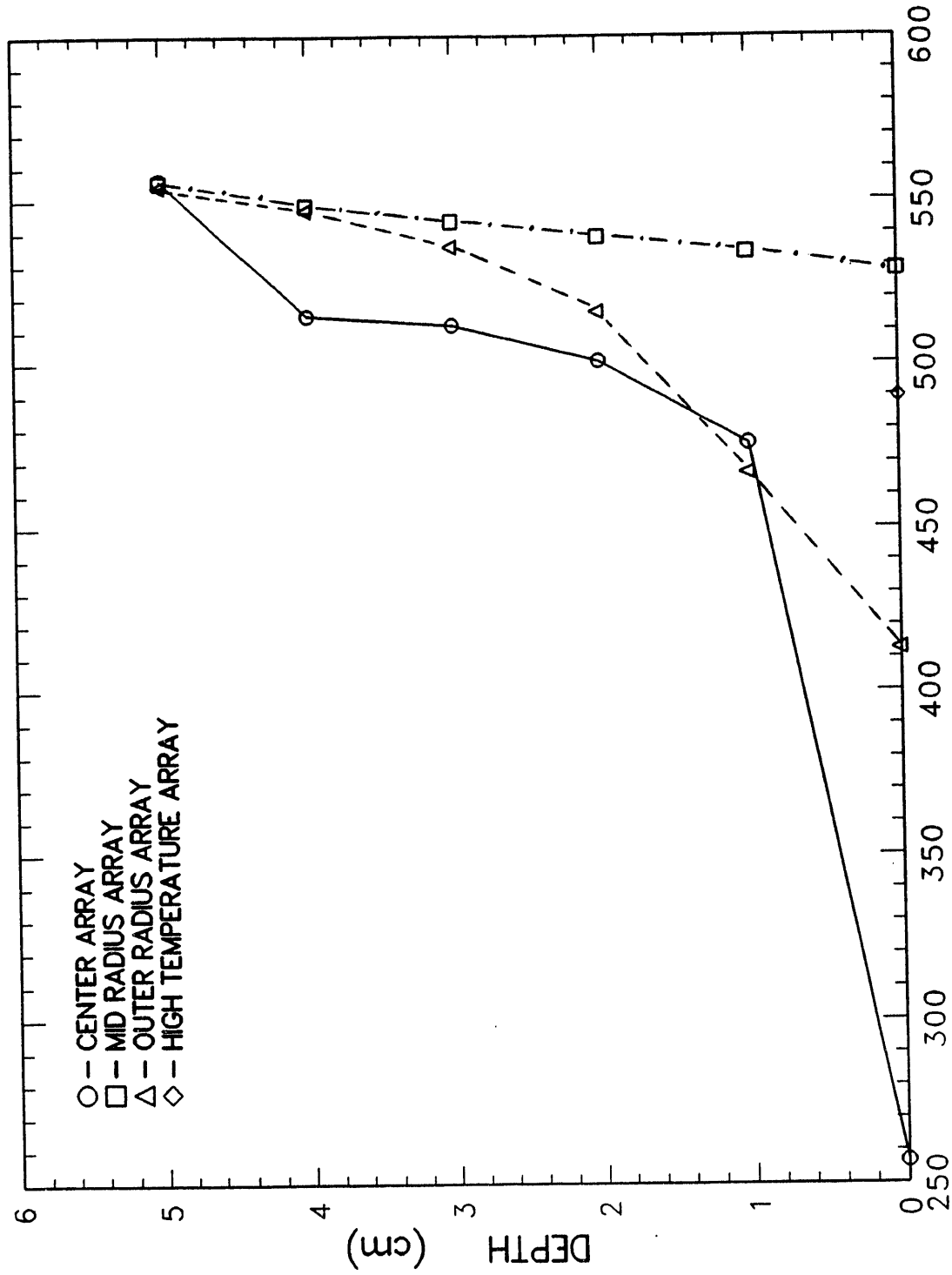

Figure 6.5 Concrete ablation profile, WETCOR-1. Points in this figure show times and locations of thermocouples indicating temperatures in excess of 1650 K. Lines are intended to aid the eye in relating thermocouples in individual arrays.

6.1.2 Meltpool Temperatures

The charge material was initially heated by a coiled heating rod for 330 minutes and also by the tungsten susceptor sleeves for an additional 350 minutes. The total time to melt the charge was approximately 520 minutes. Early in the heating process there were significant temperature gradients in both the axial and in the radial directions with the hottest regions in the immediate vicinity of the heating sources. The power to these sources was intermittently shut off to reduce the thermal gradients and to promote uniform melting. A plot of the charge temperatures between 500 and 600 minutes (Figure 6.6) shows the initial charge gradients, the meltpool temperature at the start of water addition, and the meltpool temperature history after water addition. Appendix D presents temperature data for the charge, melt/concrete interface and tungsten sleeve susceptors.

The initial gradients across the height and width of the charge were 300-400 K at 500 minutes. Visual records indicate that the charge became fully molten at 520 minutes. This was confirmed by the thermocouple responses within the pool since all six thermocouples indicated temperatures of 1823-1853 K between 520 and 529 minutes, as shown in Figure 6.6. Many of the melt temperature thermocouple signals became erratic after the pool was molten and when water was added. The best measure of the melt temperature in this interval was at the 4-cm elevation. This was in the approximate center of the molten pool, which extended from -5 cm to +15 cm in the axial direction. Melt temperatures in this location held constant at 1853 K, and may even have increased slightly during the interaction period (529-555 minutes) when water was added. After the power was shut down at 555 minutes, uniform pool cooling was indicated by the thermocouples located at the +4, -4, and +8 cm locations at a rate of 15°C/minute.

During the period from 520 to 554.9 minutes, power supplied to the buss was 200 kW. Of this, about 28 $\pm$ 2 kW were imparted to the susceptors. Prior to water addition the susceptors lost heat to the melt charge and to the magnesium oxide walls of the test fixture. Because some small portion of the upper-most susceptor was exposed, there was some heat loss due to radiation. Heat fluxes to the magnesium oxide walls could be calculated using an inverse heat flux calculational method and temperatures measured in the magnesium oxide walls. Results shown in Appendix E indicate the heat flux to be $7 \pm 1 \times 10^4$ W/m^2. Thus, 17.6 kW were lost to the sidewalls. Heat input to the molten pool immediately prior to water addition was then no more than 10.4 $\pm$ 3.2 kW. This heat input amounts to 0.30 $\pm$ 0.09 W/gram or 0.61 $\pm$ 0.19 W/cm^3 of initial melt. Such low power generation rates per unit volume are consistent with power generation rates per unit volume expected to occur in core debris very late in a reactor accident.

6.1.3 Tungsten and MgO Thermal Response

The tungsten and MgO materials were heated for 520 minutes prior to water addition and consequently retained a large amount of energy. High temperatures in both the susceptor and the MgO walls were, of course, essential features of the WETCOR-1 test. The plots of the tungsten and MgO temperatures shown in Figures 6.7 and 6.8 indicate the initial temperatures of these materials when water was added to the crucible, and the subsequent cool-down histories of these materials, which can be translated into an important source term for the overall energy balance.

The type-C thermocouples located directly on the sleeve susceptors all failed due to high-temperature overload at times after 300 minutes. However, thermocouples located immediately adjacent to the tungsten susceptors were used to estimate the tungsten temperatures shown in Figure 6.7. The estimated tungsten temperature at 529 minutes when water was added was 2073 $\pm$ 50 K. The top tungsten collar was exposed to the water pool and began to cool rapidly when water was added at an average rate of 30°C/minute. This cooling rate continued throughout the water-addition period and after the power was turned off at 554 minutes. The temperature was 373 K at 580 minutes.

The MgO wall temperatures at four elevations are shown in Figure 6.8. MgO wall temperatures 0.5cm within the MgO varied from 1573 K in regions adjacent to the melt to about 500 K at the elevation 50cm above the original concrete surface. After water was added at 529 minutes, the walls cooled quickly, starting at the top of the crucible

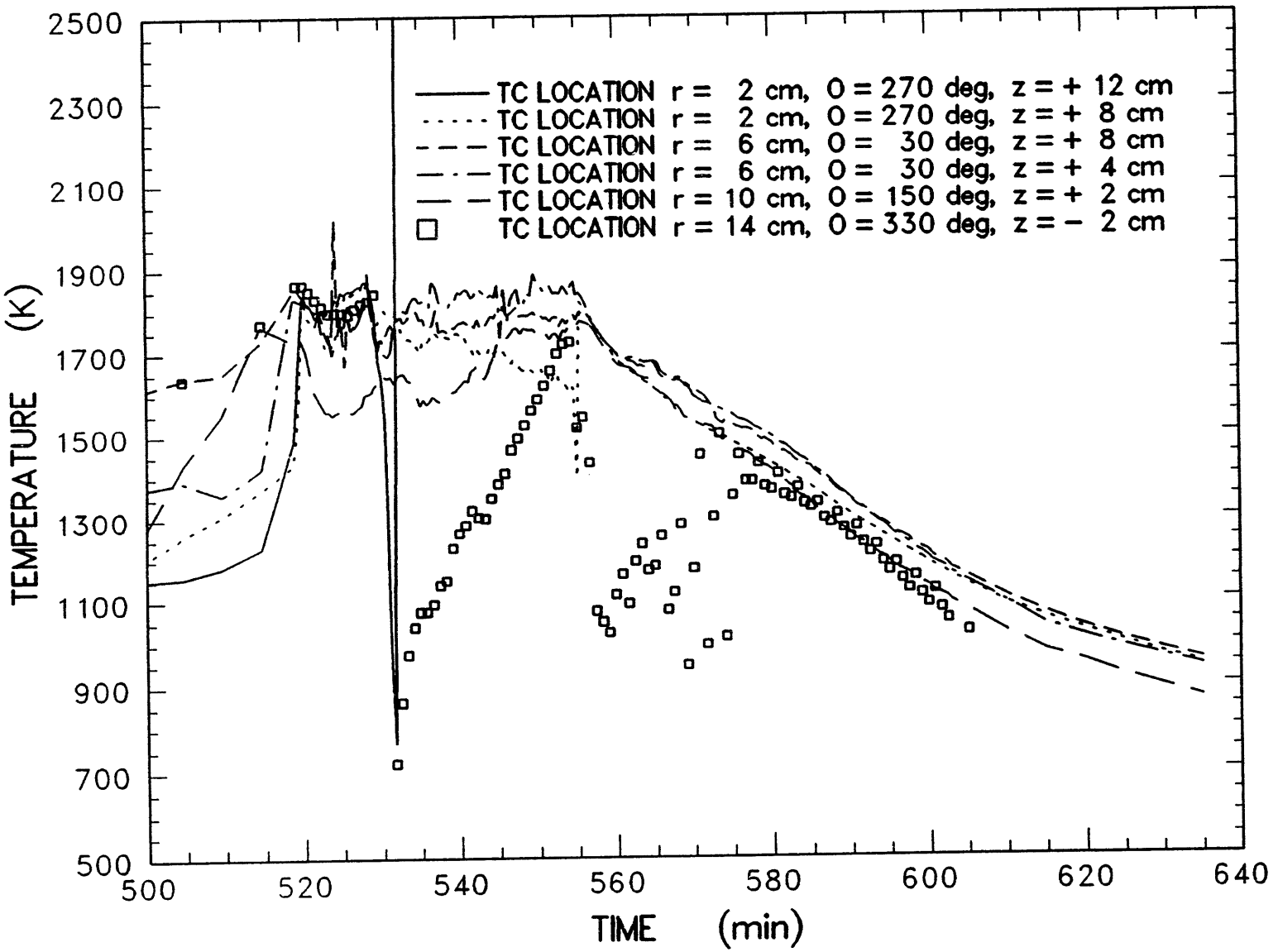

Figure 6.6 Meltpool temperatures at six axial locations (-2 to 12 cm)

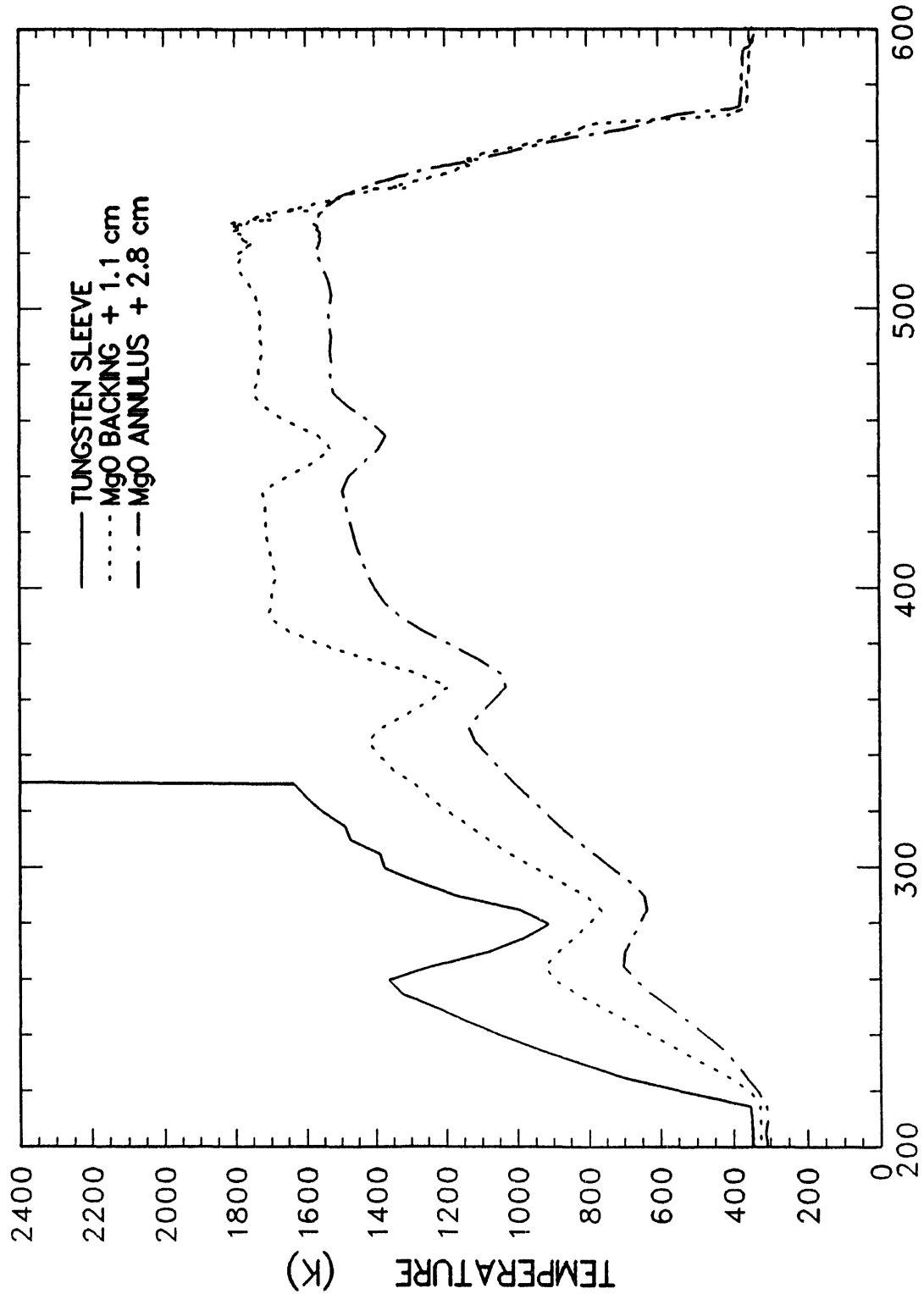

Figure 6.7 Tungsten and MgO wall temperatures at z = +10 cm

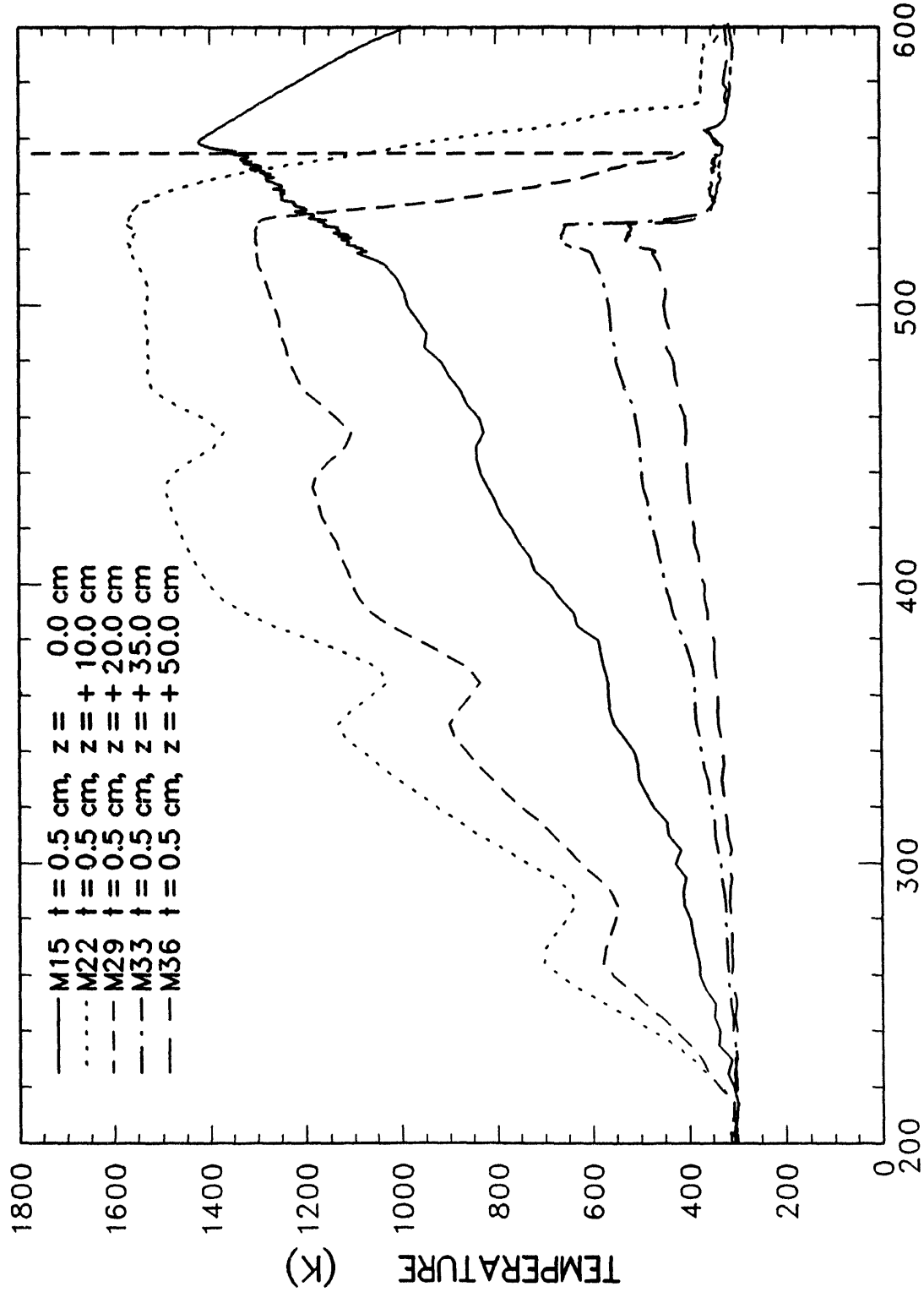

Figure 6.8 MgO annulus temperatures at five elevations

and proceeding downward in the axial direction. The +35-cm elevation in the MgO cooled rapidly after 530 minutes and cooled to 298 K at 540 minutes. The MgO wall at the +20-cm location began to cool after 535 minutes, but at a slower rate, and cooled to 373 K 560 minutes. The +10-cm elevation was adjacent to the meltpool and did not come in direct contact with the water pool. Temperatures at this location began to fall at times after 540 minutes and were 373 K at 580 minutes. The MgO at the concrete interface (0 cm) continued to heat throughout the water addition period and only began to cool after power was shut off at 554.9 minutes. Heat fluxes were calculated from temperature data obtained from thermocouples embedded in the sidewall. These results are presented in Appendix E.

The MgO/tungsten materials in the upper crucible were significant sources of energy to the water pool throughout the water-addition period of the WETCOR test due to their mass and temperature. The MgO materials below the concrete interface were unaffected by water addition.

6.2 Heat Transfer to the Water Pool

The purpose of the WETCOR-1 test was to determine if the configuration of heating in small-scale tests affected the initial crust formation when a water pool was formed over a high-temperature melt interacting with concrete. This focus of the test program was endorsed by a peer review panel of experts from various organizations in the USA and abroad. The several possible outcomes of the test that were hypothesized included:

- quenching of the melt because progressive fragmentation of the crustal material allowed enhanced heat transfer to the coolant,
- explosive steam generation (a steam explosion), or
- low levels of heat transfer to the water pool entirely similar to what has been observed in the past tests of simultaneous interactions of high temperature melts with concrete and with water.

The primary objectives of the test were met, then, shortly after water addition took place. (The benefit of an initial, temporary crust formation before water was added showed that the test fixture operated as anticipated, and certainly aided in the interpretation of events taking place in the first few minutes after water addition.) Heating of the melt was continued after the initial crust formation under water to see if fragmentation or at least fracture of the crust would occur in time. In fact, no such fragmentation or fracture was anticipated. Analyses and opinions solicited from the expert panel strongly suggested that once a stable crust formed it would be able to withstand any of the forces that could be generated by boiling or melt/concrete inter-actions. Propagation of a fracture through a stable crust would be limited by (1) voids in the crust and (2) the increasing ductility of the crustal material with the increase in the temperature of the material from the side exposed to water to the side exposed to the high temperature melt. That is, voids in the crust blunt crack tips and decrease the stress intensity. With increasing temperature across the crust the material becomes more ductile and less prone to fracture. Also, the thermal stresses that would drive a fracture become weaker. It is, then, difficult for cracks to propagate across the crust. Certainly, there was no evidence in the test that any fracturing of the crust took place.

Because the WETCOR-1 test focused on issues associated with initial formation of a crust, the test fixture was not well suited for quantitative determination of the long-term heat transfer from the melt, through the crust and into the water pool. Difficulties that arose in trying to determine the heat transfer through the crust in the WETCOR-1 test included:

(1) the susceptor collar at the top of the melt, which was so critical to meet the principal test objectives, protruded into the water pool and provided another pathway for heat transfer to the water pool,
(2) high temperatures deliberately established in the test-fixture walls to delay melt freezing to the walls meant that the test fixture walls were a source of heat to the water pool, and
(3) the susceptor system, which extended into the melt, acted as a fin to provide another heat transfer pathway to the crust and the water pool (a deliberate design feature of the test to meet the primary objectives).

It would, in principle, be possible to account for these heat transfer pathways to the water pool and then determine the heat transfer through the crust. The necessary multi-dimensional analyses have not been attempted here. The compounding of uncertainties would lead to uncertain results of such an analysis. Rather, a more integral, average heat transfer analysis is presented below.

Since the objectives of the test had been met, the experimenters took steps to obtain better heat transfer data. At 554.9 minutes they shut off induction power, and at 557 minutes they shut off water flow. Shutting off induction power eliminated at least one source of heat input to the water pool. Shutoff of water flow led to a temperature rise in the water pool which could be monitored to determine the rate of heat transfer to the water.

At 563 minutes water flow was re-established at 57 lpm. In principle, heat transfer rates to the water could be determined from the water flow rate and the temperature difference between the inlet and the outlet water. It was, however, apparent that the temperature difference was small and could not be used to obtain an accurate measure of heat transfer to the water pool. At 578 minutes water flow was reduced to 29 lpm. At 592.8 minutes water flow was again stopped. These changes in the test operation provide additional opportunities to determine the rate of heat transfer to the water pool. Note, however, that heat was no longer being provided to the melt and the melt was cooling and solidifying during this time.

The temperature rise in the water pool during the period from 557 to 563 minutes when water flow was stopped is shown in Figure 6.9. The heat transfer rate to the pool is simply calculated from

$$\int_{t_o}^{t} \dot{Q}dt = M(H_2O) \int_{T_o}^{T} C_p(T)dT \qquad (9)$$

where

$\dot{Q}(t)$ = heat transfer rate to the water (W),
t_o = 33420 seconds = 557 minutes,
$M(H_2O)$ = water pool mass (g),
$C_p(H_2O)$ = heat capacity of water (J/g-K),
T = water pool temperature (K) at time t, and
T_o = temperature at t_o

Note that vaporization of the water has been neglected in this equation because of the low temperature of the water through much of the heatup.

For the analysis of data such as that obtained in the WETCOR-1 test a satisfactory approximation to the above equation assuming a constant heat rate is

$$\dot{Q}(t-t_o) = C_p(T)(T-T_o)M(H_2O) \qquad (10)$$

where $C_p(avg)$ is the average heat capacity over the temperature interval of interest. Then, a plot of pool temperature against time has a slope of

$$slope = \dot{Q}/C_p(T)M(H_2O) \qquad (11)$$

from which a more accurate determination of $\dot{Q}$ can be made.

From the location of the crust at the end of the test and the geometry of the test fixture, the volume of water being heated after flow was stopped is estimated to be 40400 cm^3. There is, however, a significant uncertainty in this volume. The crust configuration found at the end of the test might suggest that there has been some sagging of the crust. If such sagging did occur, it is certainly not known when it occurred. If the crust sagged after the period of no water flow, then a smaller volume of water might have been heated during the period of no water flow. This smaller volume is estimated to be 32670 cm^3.

Some properties of pure water are listed in Table 6.1. Water overlying the melt, especially during the period of no flow, was certainly not pure. The SWISS test series [Blose et al., 1987] established that water overlying high temperature-melts interacting with concrete quickly becomes contaminated with dissolved and suspended materials. The amount of suspended material can be enough to make the water opaque. Even so, concentrations of suspended and dissolved materials are not expected to be large. Concentrations reported for samples of the water in the SWISS II test were only 4 to 30 mg/100 cm^3 H_2O. Such low

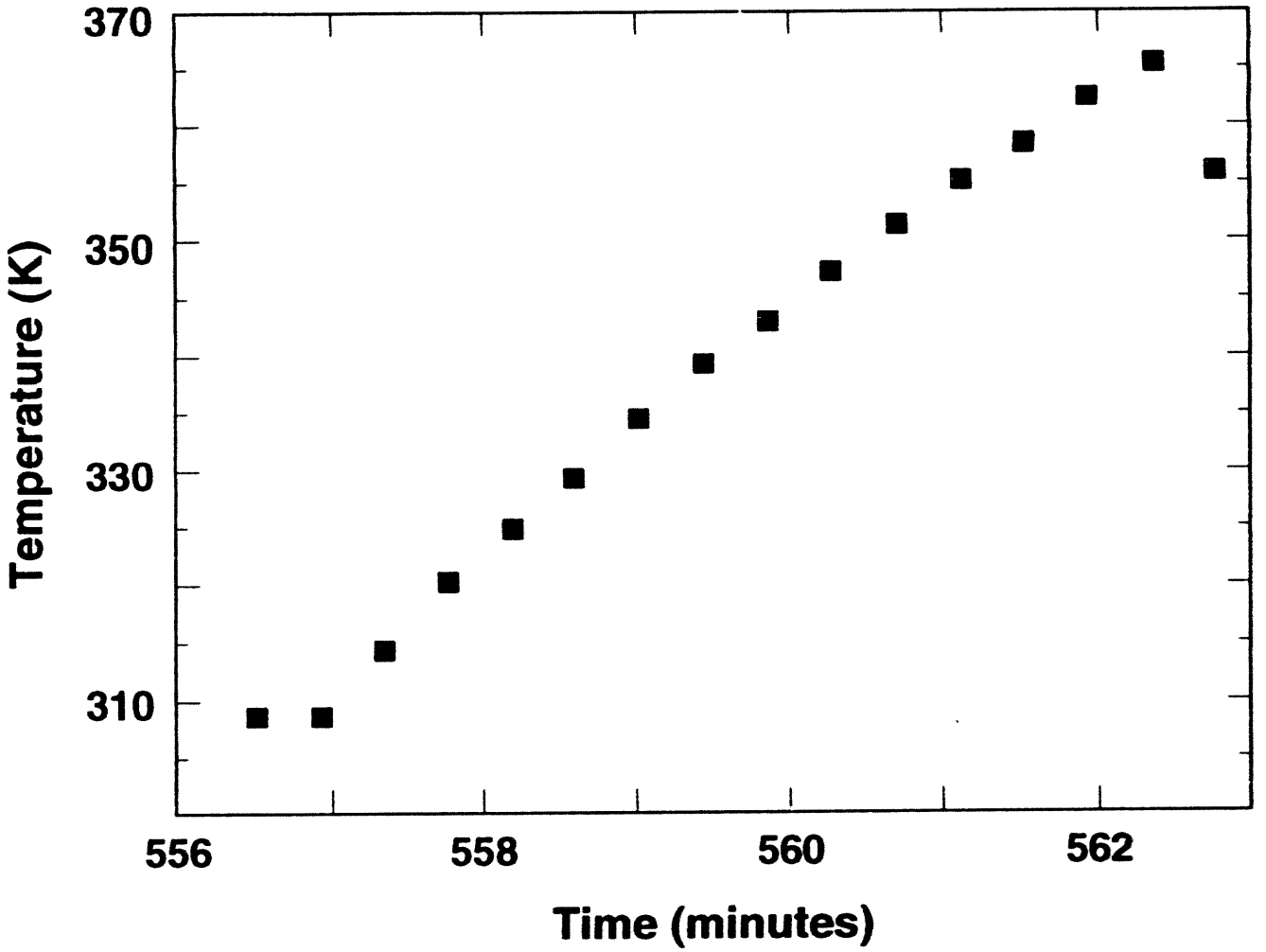

Figure 6.9 Temperature rise in the water pool following shutoff of water flow at 557 minutes. Water flow was restored at 563 minutes.

Table 6.1 Thermophysical properties of water[a]

Temperature (K)	Density (g/cm^3)	Enthalpy[b] (J/g)	Heat Capacity (J/g-K)
273	0.99987	0	4.2177
283	0.99973	42.0363	4.1922
293	0.99823	83.9034	4.1819
303	0.99567	125.7063	4.1785
313	0.99224	167.4949	4.1786
323	0.98807	209.2964	4.1807
333	0.98324	251.1289	4.1844
343	0.97781	293.0087	4.1896
353	0.97183	334.9519	4.1964
363	0.96534	376.9773	4.2051
373	0.95838	419.1053	4.2160

[a] *Handbook of Chemistry and Physics*, R.C. Weast, Ed. in chief, The Chemical Rubber Publishing Co., 45th edition, 1964.

[b] Enthalpy = $\int_{273}^{T} C_p(T)dT$

concentrations will not drastically affect the properties of water of interest here. Consequently, heat transfer analyses were done using the properties of pure water.

The density of water at 309 K, the water temperature when flow was stopped at 557 minutes, was 0.9936 g/cm^3. The mass of water that was heated when water flow was stopped was 40140 to 32460 g. The temperature rise of the water pool then indicates a heat transfer rate of 25230 ± 2670 W.

The heat is transferred to the water pool by
- heat passing from the melt through the solidified crust,
- heat transfer from the test fixture walls above the crust that are in contact with the water pool, and
- heat transfer from the susceptor collar protruding into the water pool.

The heat transfer through the solidified crust into the water pool is, of course, a critical issue for the analysis of severe reactor accidents. The heat flux through the crust is a quantity that will be the focus of other tests. An estimate of this quantity is sought in the analyses presented here.

The walls of the test fixture were deliberately heated to high temperatures in the WETCOR-1 test prior to admission of water. This was one element of an overall strategy to delay the freezing of melt materials to the test fixture walls so that the hypothesized instability of crust formation could be observed. Temperature data obtained from thermocouples embedded in the magnesium walls show that, even late in the test, heat was being transferred from the walls to the water pool. Temperature data for the water pool and for a point in the wall 0.5 cm from the interface between the wall and the water pool are shown in Figure 6.10. The thermal gradient in the magnesium oxide at the interface with the water pool was estimated from these data. This thermal gradient is shown as a function of time in Figure 6.11. Note that as the water temperature rises during the period from 557 to 563 minutes, the thermal gradient decreases and eventually becomes negative. That is, eventually the water becomes hot enough that it loses heat to the adjacent walls. Similarly, when water flow is stopped after 598 minutes, the thermal gradient becomes negative.

The thermal conductivity of the cast magnesium oxide has been measured [Copus et al., 1989] and is presented in Table 6.2. These data were obtained in air. The cast magnesium oxide is porous (porosity ≈ 0.19). Thus, air in the pores contributed to the thermal resistivity of the castable material. In the WETCOR-1 test during the period in question the pores in the castable were probably filled with water, which is far more thermally conductive than air. The thermal conductivity of the water-saturated magnesium oxide can be estimated from [Kingery, 1967]:

$$k = k_o \left[\frac{1 + 2p\,(1 - k_o/k_w)/(2k_o/k_w + 1)}{1 - p(1 - k_o/k_w)/(k_o/k_w + 1)} \right] \quad (12)$$

where
k_o = thermal conductivity of pore-free magnesium oxide,
k_w = thermal conductivity of water,
p = porosity, and
k = thermal conductivity of the porous material.

Table 6.2 Thermal conductivity of magnesium oxide in air

Temperature (K)	Thermal Conductivity (W/cm-k)
273	0.0636
673	0.0517
923	0.0306
1673	0.0294

The thermal conductivity of the magnesium oxide with pores filled with water is, then, estimated to be 0.0636 W/cm-K for the temperature range of interest rather than 0.0606 W/cm-K when the pores are filled with air. The effect of water in the pores, if it does not convect, is not significant for the purposes of the analyses done here.

The wall area exposed to the water pool was 3270 cm^2. There was, presumably, a temperature

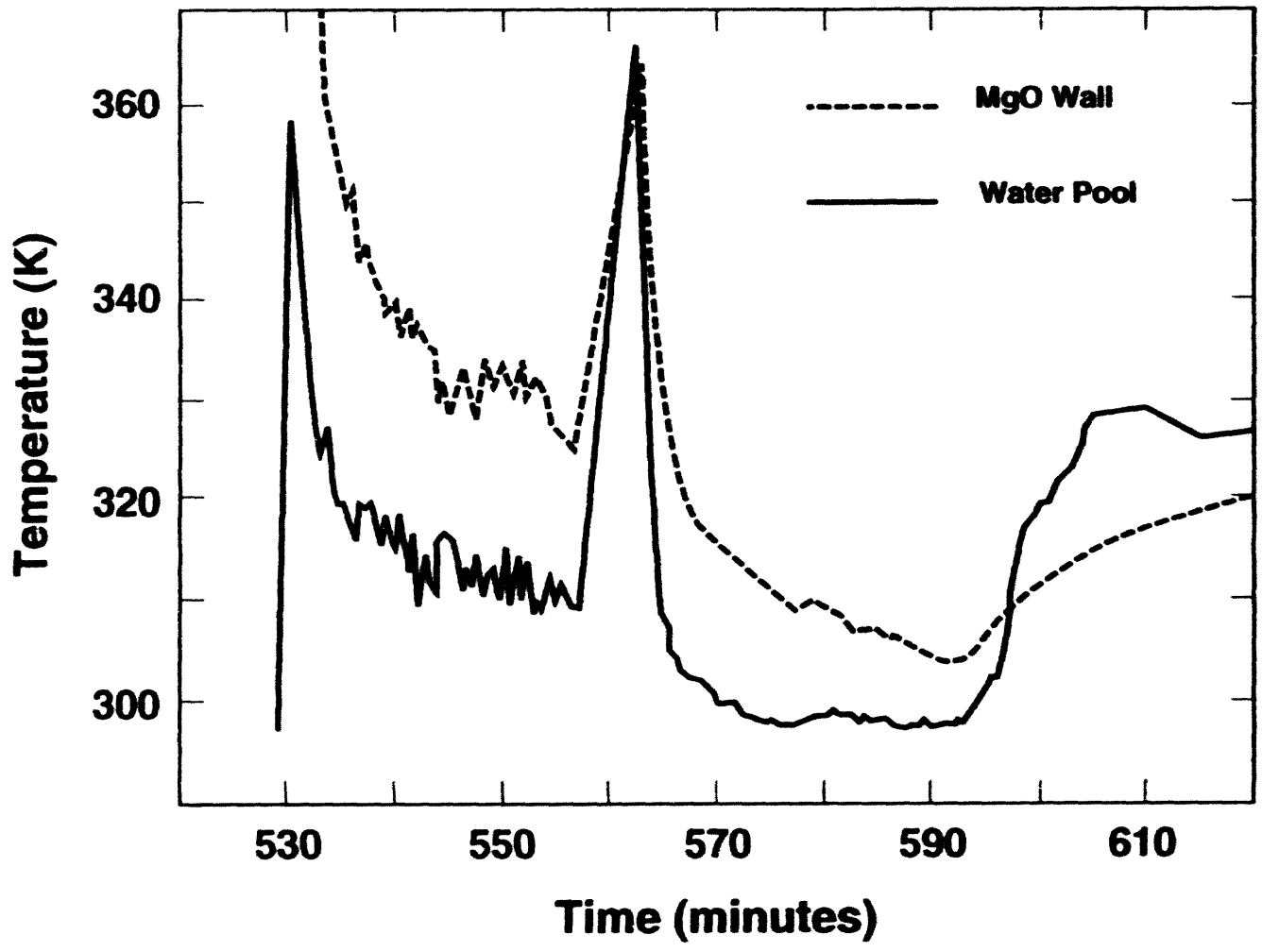

Figure 6.10 Temperature of the water pool and the magnesium oxide wall (at a depth of 0.5 cm) as functions of time.

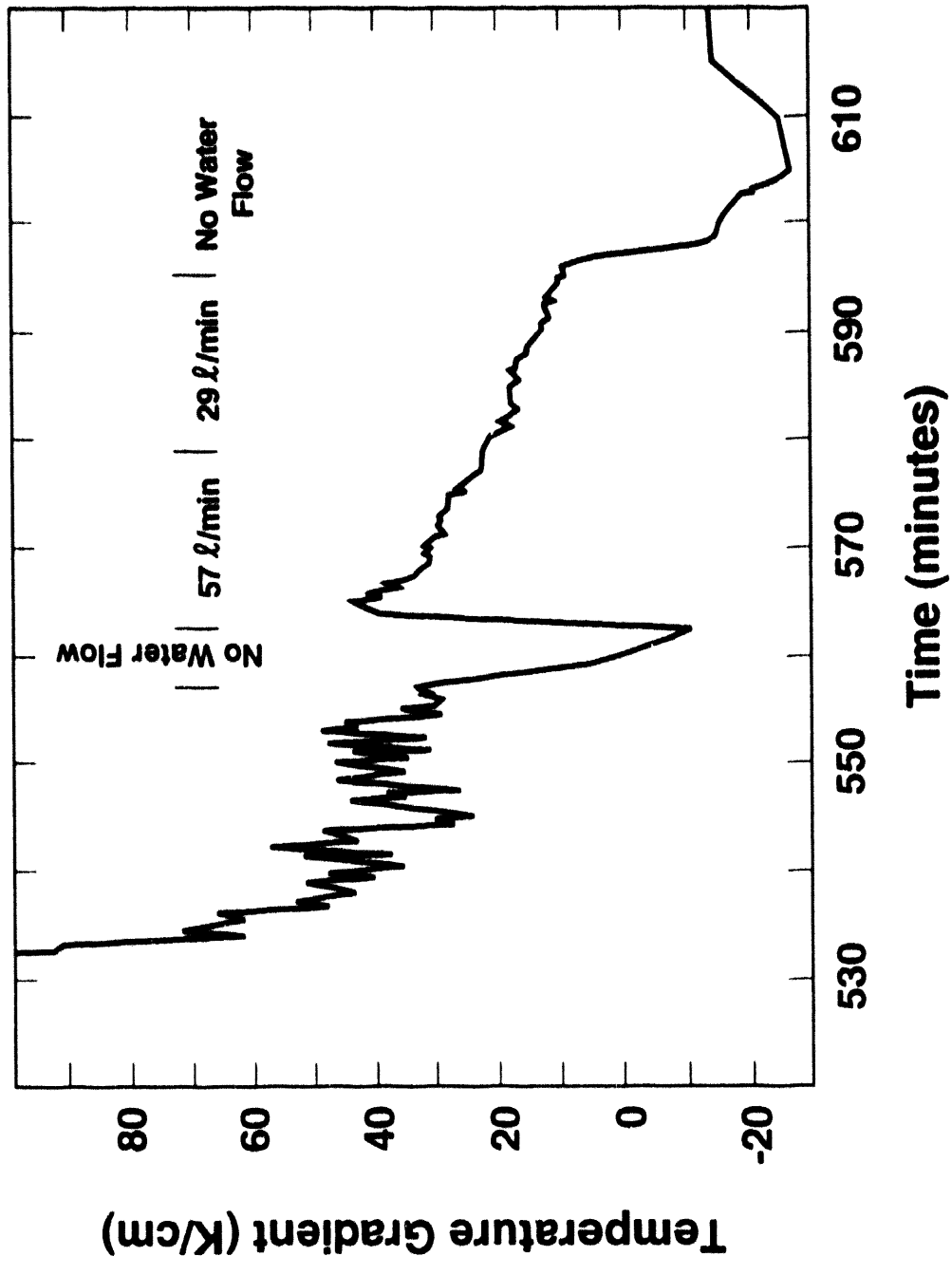

Figure 6.11 Thermal gradient in the magnesium oxide wall at the interface with water

gradient up the test fixture walls. Unfortunately, the thermocouple array at +50 cm (array 11) yielded anomolous signals as though it were damaged perhaps by the melt expulsion observed at 555 minutes. As a result, gradients indicated by this array could not be compared to those shown in Figure 6.11 obtained from the thermocouple array at +35 cm (array 10). Consequently, it was necessary to assume gradients indicated by the thermocouple array at +35 cm applied to the entire surface of the magnesium oxide annulus exposed to the water pool. Then, from the thermal gradient data and the thermal conductivity of the magnesium oxide wall material it was calculated that heat transfer from the walls to the water pool varied from 6650 W to -1660 W over the period of 557 to 563 minutes.

There appears to be no convenient way to estimate how much heat was transferred to the water pool through the susceptor collar that protruded into the water pool. Posttest sectioning of the test fixture certainly showed solidified melt material surrounding this collar. The collar was not in direct contact with the meltpool. Nevertheless, the collar must have constituted a thermal "short-circuit" that augmented heat transfer to the water pool. It will be most important that such a short circuit does not exist in tests directed toward the determination of the heat flux through the crust and into the water pool.

Because of the uncertainty in the spatial distribution of wall temperatures, an average heat flux from the walls to the water pool was assumed. This was done instead of pursuing an analysis in which the heat flux over the period of no water flow was taken to be time dependent. Such a time-dependent analysis seems inappropriately precise in comparison to other uncertainties in the data. Correcting the calculated heat transfer to the water pool for the average heat transfer from the walls yielded an estimate for the heat transfer through the crust of 22735 $\pm$ 4940 W.

Another estimate of the heat transfer to the water pool can be derived from the temperature difference between inlet and outlet water during the period that flow was at 29 lpm. This temperature difference is shown in Figure 6.12. By this time the meltpool had cooled substantially, perhaps solidified, and much lower rates of heat transfer were expected. Over the period from 582.4 minutes to 589.0 minutes the temperature difference between the inlet and the outlet water varies from 3.5 $\pm$ 1.00 K to 2.74 $\pm$ 1.00 K. During this period, the thermal gradient at the interface between the magnesium oxide test fixture walls varied from 18.5 $\pm$ 1.5 K/cm to 14.9 $\pm$ 1.5 K/cm. The heat transfer through the crust to the water pool was then calculated to vary from 10900 $\pm$ 3100 to 8600 $\pm$ 3200 W. Indeed these heat transfer rates are much less than was calculated for the period from 557 to 563 minutes.

Were the entire crust geometric surface area transferring heat to the water pool uniformly, heat fluxes derived from the heat transfer rates described above would be as shown in Table 6.3.

Table 6.3 Heat fluxes to water through the crust based on geometric surface area of crust

t (min)	Heat Transfer Rate (W)	Heat Flux (MW/M^2)
557 to 563	22735 $\pm$ 4940	0.29 $\pm$ 0.06
582.4	10900 $\pm$ 3100	0.14 $\pm$ 0.04
589.0	8600 $\pm$ 3200	0.11 $\pm$ 0.04

Inspection of the crust after the test showed the crust to have a variable thickness. Near the walls of the test article the crust was about 10 $\pm$ 1 cm thick. Near the center of the crucible the crust was only 3.8 to 4.5 cm thick. The rate of heat transfer through the crust must have been controlled largely by conduction through the crust. Since the temperatures of the two faces of the crust were the same at all locations, heat transfer probably occurred predominantly through the thinner portion of the crust.

The crust can be approximated as consisting of a 4.2 $\pm$ 0.4 cm thick disk 13.2 $\pm$ 2.1 cm in diameter within an annulus that is 10 $\pm$ 1 cm thick. If the heat flux to the water pool is apportioned according to the thicknesses and areas of the crust then the following heat fluxes are derived:

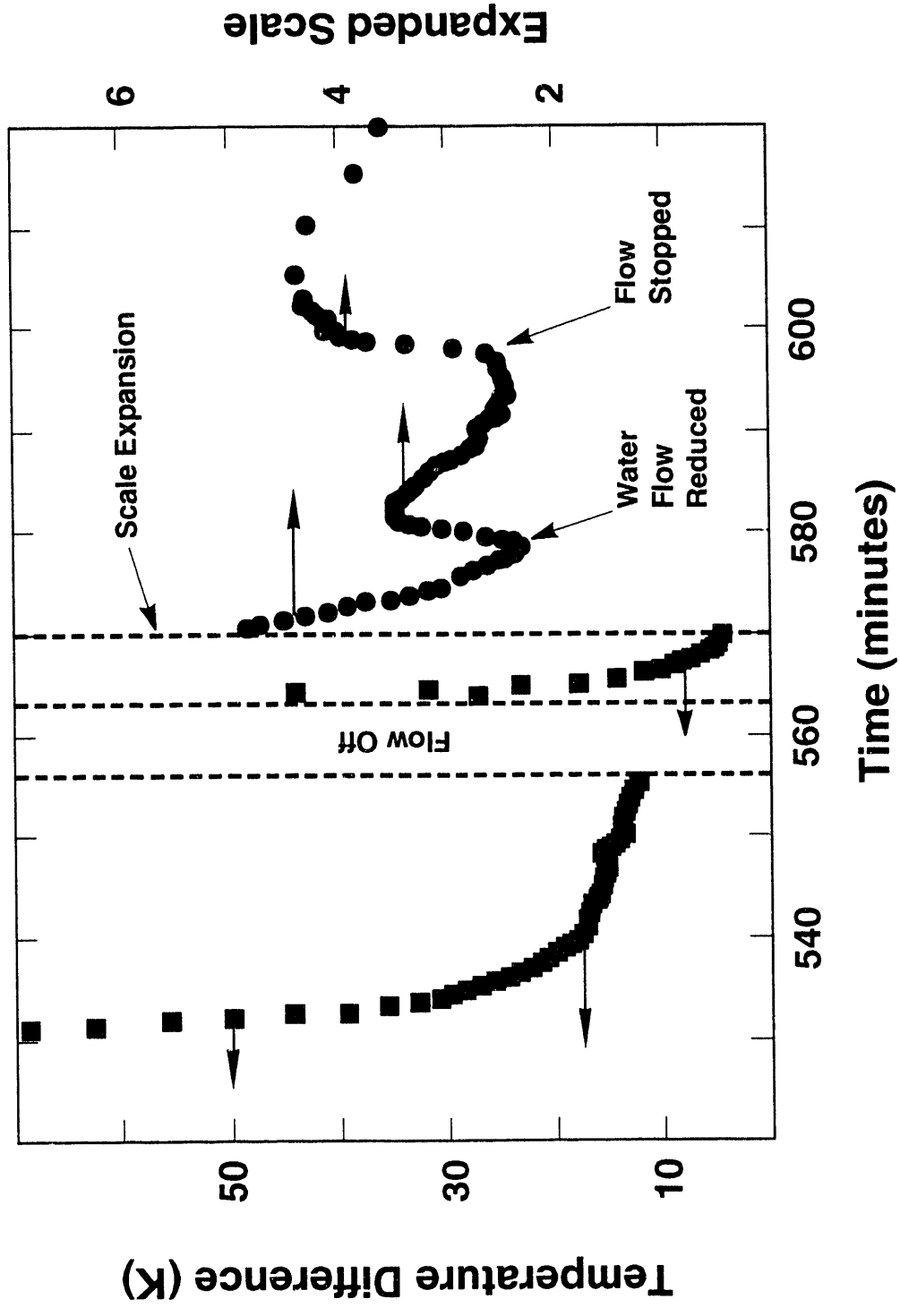

Figure 6.12 Difference between inlet and outlet water temperature during the WETCOR-1 test

Table 6.4 Heat fluxes to water through the thin portion of the crust

t (min)	Heat Transfer Rate (W)	Heat Flux Corrected for Varying Crust Thickness (MW/m^2)
557 to 563	22735 ± 4940	0.52 ± 0.13
582.4	10900 ± 3100	0.25 ± 0.08
589.0	8600 ± 3200	0.20 ± 0.08

The corrected heat flux found for the period of no water flow (557 to 563 minutes) may be of some significance for the analysis of melt cooling during reactor accidents. Within the stated uncertainty limits the heat flux during this period was consistent with that obtained in the SWISS-II test [Blose et al., 1987], especially heat fluxes observed during an interruption in the power supplied to the melt in the SWISS-II test. During the period of no water flow, the charge material below the crust was still molten. Corrected heat fluxes found for the times 582.4 and 589 minutes were more difficult to interpret since the charge used in the WETCOR-1 test had cooled and probably solidified by these times. Certainly, these results indicate the heat flux through the crust decreases rapidly once melt solidifies.

The efforts undertaken here to derive crude estimates of the heat flux through the crust do provide some insight about changes that should be made in the design of future tests that focus on the determination of this heat flux. Clearly, the susceptor rings must not protrude into the water pool or even significantly through the crust that forms between the water pool and the melt. At the very least, the uppermost susceptor ring can provide a high thermal conductivity pathway through the crust. At worst, it can impart heat directly to the water pool. In any case, the uppermost susceptor ring ought to be more heavily and robustly instrumented so that any influence it might have on heat transfer processes of interest in future tests can be estimated. The walls of the test fixture in contact with the water pool cannot be neglected in the heat transfer analysis. If intensely heated prior to water addition, the walls impart heat to the water pool. If kept cool, the walls act as heat sinks.

Consideration should be given to more heavily instrumenting the walls adjacent to the pool and to measuring the thermal conductivity of the wall material when the material is saturated with water. This can be done in place using water as the working fluid.

Heat transport to the water pool can also occur up the walls of the test fixture. It would be useful in future tests to locate thermocouple arrays above the crust line in the walls to measure this heat flux.

Thermistor bridges provide excellent data on the temperature difference between inlet and outlet water even in the presence of an induction field. A redundant thermistor bridge system ought to be incorporated in future tests.

Temperature differences between inlet and outlet water were too small in the WETCOR-1 test for accurate determinations of heat transfer. Water flow rates should be controlled so that inlet and outlet temperature are no less than 10 degrees.

The operational step of stopping water flow periodically to monitor the rate of pool heating provides a useful, complementary method to monitor heat transfer. The largest source of uncertainty in this method for monitoring heat transfer to the pool is the mass of water involved. Altering operational procedures so that the water mass is specified should be considered.

Continued exploration of crust formation and heat transfer across the crust would be advanced considerably if data could be obtained on the crust thickness as a function of time and location. Consideration should be given to incorporating ultrasonic or radar instrumentation into future tests to measure this thickness.

It goes without saying that temperature measurements within the crust would be useful. No reliable means of measuring these temperatures has been identified to date. Consideration should, however, be given to heavily instrumenting the test fixture walls in the vicinity of the points of crust attachment to the walls.

6.3 Gas, Flow, and Aerosol Data

The gas composition, gas flow, and aerosol concentration data can be used to determine the decontamination factor produced by a 30-cm-deep water pool overlying the melt. Video records indicate that gas release was continuous before, during, and after the water addition and that aerosol release was relatively light. The figures describing the gas and purge gas flow rate system pressures and temperatures and aerosol data are shown in Appendix G.

A purge rate of air through the test chamber was held at a high rate throughout the test to maximize the potential for good video coverage. The initial purge rate was 1600 lpm, and the purge rate between 500-600 minutes was 600 lpm. The sensitivity of measuring the compositions of gases produced from the melt/concrete interaction was masked by the high flow rate of air used to purge the containment chamber. Analysis of the six grab samples and mass spectrometer data showed that the composition of gases throughout the experiment was essentially that of air used to purge the experimental apparatus.

Chamber temperatures ranged from 353-373 K during the 500-600 minute interval. The gas released from the concrete was predominantly CO_2 with some CO (20-25%) present after the pool became fully molten. The gas release rate averaged 30 lpm between 500 and 600 minutes. This would yield an average gas face velocity of 3 cm/sec through the meltpool.

The aerosol data are shown in Table 6.5. Twenty-two aerosol filter samples were taken in WETCOR-1. The 5 samples taken before water addition at 529 minutes indicated an average concentration of 1.0 g/m^3. Samples taken after water was added had progressively less material, and the last samples taken when power was shut down at 554 minutes indicated an average concentration of 0.2 g/m^3.

The mass concentration calculated from impactor data generally agreed with the mass concentration after water addition. The normalized mass distribution for the impactors indicated particle sizes in the range of 0.65 to 10 μm regime. Impactor data were presented in Appendix G.

The materials used for the melt in the test were selected for their suitability in meeting the objectives for the study of coolability rather than for reproducing the rates of aerosol generation during core debris interactions with concrete. No fission product simulants were included in the charge material, and posttest analysis confirmed that the chemical composition of these aerosols were primarily concrete decomposition products. Variations in the rates of aerosol generation observed in the WETCOR-1 test do, however, provide important phenomenological information pertinent to the prediction of aerosol generation during severe reactor accidents.

There has only been one previous, detailed measurement of the effects on aerosol production of water pools overlying high temperature melts. This measurement, made in the SWISS-II test [Blose et al. 1987], showed that when a 60-cm deep, subcooled water pool was present, the aerosol emission rate was reduced by factors of 13-19. The test procedure adopted in the SWISS tests made it impossible to distinguish the effects of the water pool and the effects of solidified crust on the reduction of aerosol emissions.

Subcooled water pools are expected to attenuate aerosol release during melt interactions with concrete [Powers and Sprung, 1992]. Bubbles of aerosol-laden gases rising through the water pool should be scrubbed of aerosol. The scrubbing occurs because aerosol particles diffuse to the bubble walls, inertially impact the walls, and, if large enough, sediment within the bubble. Surface tension and van der Walls forces are sufficiently strong that once an aerosol contacts the water at the bubble walls it is trapped and removed. Predictions of these removal processes have always been integral parts of the VANESA model of aerosol generation and radionuclide release during core debris interactions with concrete [Powers et al. 1986].

Considering the effects crusts might have on the production of aerosol during melt attack on concrete, it has been suggested that crusts could suppress the mechanical production of aerosols by bubbles bursting at the melt surface. This mechanical production of aerosol is, however,

Table 6.5 WETCOR-1 filter data

Filter Sample	On Time (minutes)	Duration (minutes)	Total Mass (gm)	Mass Conc (gm/m^3)
1	520.7	1.0	0.00278	1.74
2	522.7	1.0	0.00137	0.88
3	524.7	1.0	0.00126	0.79
4	526.7	1.0	0.00536	0.50
5	528.8	1.0	0.01156	1.08
Water Quench Initiated				
6	530.6	1.0	0.00339	0.32
7	532.7	1.0	0.00356	0.33
8	534.7	1.0	0.00306	0.29
9	536.7	1.0	0.00262	0.24
10	538.7	1.0	0.00353	0.33
11	547.3	1.0	0.00156	0.15
12	549.4	2.0	0.00389	0.36
A	552.4	2.0	0.00291	0.27
B	555.7	2.0	0.00213	0.20
C	557.7	2.0	0.00131	0.12
D	560.1	2.0	0.00063	0.06
E	562.4	3.0	0.00214	0.20
F	565.6	2.0	0.00401	0.37
G	567.9	2.0	0.00119	0.11
H	570.1	2.0	0.00108	0.10
I	572.4	2.0	0.00159	0.15
J	574.6	2.0	0.01639	1.53

estimated to be a minute fraction of the total aerosol production during high temperature melt interactions with concrete. By far the largest aerosol production is driven by the vaporization of volatile constituents of the melt. The effects of crusts on the vaporization process are decidedly less clear. On the one hand, vapors might condense on the solid surfaces as they cross the thermal gradient created by an interfacial crust. Thermophoretic forces as well as simple impaction and interception might reduce the mass of particulate that can pass through a crust. On the other hand, if gases produced by melt attack on concrete are vented through gaps and so-called "blowholes" in the crusts neither vapor condensation or aerosol trapping would very effectively attenuate the aerosol mass produced during melt interactions with concrete. No model of the effects of crusts alone on aerosol generation during melt/concrete interactions exists.

The WETCOR-1 test provides some indications of the effects of both water pools and crusts on aerosol production. It must, however, be noted that the primary purpose of the test was the study of heat transfer processes. Test procedures necessary to further the pursuit of this primary purpose took precedence over operations that could have provided more definitive indications of aerosol production and attenuation processes. Nevertheless, useful data can be derived from the test. Major factors that facilitate deriving data pertinent to the issues of aerosol production are that neither the bulk melt temperature nor the bulk composition of the melt changed substantially during the test. On a molar basis, the erosion of concrete does not in the WETCOR test cause a dramatic alteration of melt chemistry.

Filter samples of aerosols produced in the WETCOR-1 test were taken:

- prior to crusting in air (filter sample 1),
- during the period a crust covered the melt without water present (filter samples 2, 3, 4),
- after the crust in air was remelted (filter sample 5), and
- after water was admitted to the test fixture so both a crust and a subcooled water pool covered the debris (filter samples 6-12, A, B, C, D, E, F, G, H, and I).

From a comparison of results obtained with filter samples 1 and 5 to the results obtained with filter samples 2, 3, and 4 an indication of the effects of a crust alone on aerosol production is obtained. Using the aerosol concentration found with filter sample 1 as the measure of unattenuated aerosol production, a crust produces decontamination factors of 1.98 (filter sample 2), 2.20 (filter sample 3) and 3.48 (filter sample 4). Results obtained with filter sample 1 might, however, include products of vaporization of unavoidable "tramp" impurities in the test fixture. A more conservative indication of the effects of a crust on aerosol production is obtained by using results obtained with filter sample 5 as an indication of the unattenuated aerosol generation rate. Then, the decontamination factors produced by a crust are 1.23 (filter sample 2), 1.37 (filter sample 3), and 2.16 (filter sample 4).

The trend observed in the analyses of the decontamination by a crust alone is that the decontamination increases with time. This seems entirely consistent with qualitative observations concerning the crust formation derived from the video record of the test. Initially, islands of crust formed. Between the islands were gaps in which melt could vaporize directly into the air. With time, episodic expulsions of melt sealed these gaps and less melt could vaporize into the air. Vapor necessarily had to pass through or over more crustal material and there were opportunities for greater attenuation of the amount of aerosol reaching the flow pathway to the samplers.

Simple comparisons of the calculated decontamination factors and the melt surface exposed directly to the air show that a crust does not act as an impermeable barrier to aerosols. Nevertheless, a crust does appear to provide enough attenuation of the aerosol production during melt interactions with concrete that the effects of crusts should be included in the analyses of radionuclide releases during core debris interactions with concrete. The results obtained from the WETCOR-1 test suggest a coherent crust alone can reduce the aerosol production by a factor of 1.3 to 3.5. This decontamination by a crust is reduced when the crust ruptures or the episodic eruptions of

melt through the crust allow vaporization directly into the atmosphere.

Comparison of aerosol concentrations obtained with filter samples 1 and 5 to concentrations with filter samples obtained once a water pool is present provides an indication of the attenuation of aerosol production by the combination of a crust and a 30-cm deep water pool subcooled by about 50°C. Decontamination factors calculated using results from samples 1 and 5 as the unattenuated rate of aerosol production are plotted against test time in Figure 6.13. Decontamination factors vary from 3-5 to 10-15. There is overall an appearance that the decontamination factor increases with time. There is, however, significant scatter in the data. It is tempting to attribute this scatter to episodic events taking place in the crust. There is, however, no substantiation of this hypothesis from other data taken in the test.

A cautionary note concerning the results shown in Figure 6.13 is raised by size distributions for aerosols sampled during the WETCOR-1 test (see Appendix G). The size distribution data indicate there to be substantial amounts of aerosol with particle sizes greater than about 2μm. Current models of aerosol scrubbing by water pools [Powers and Sprung, 1992] indicate that little aerosol mass of this particle size could penetrate a water pool even as shallow as 30 cm. Some of the mass collected on filters after water was admitted to the WETCOR-1 test fixture may have come from entrainment of liquid containing suspended solids or resuspension of material deposited in the apparatus prior to water addition. In fact, the observed time dependent decontamination factor could be rationalized in terms of a time dependent resuspension flux of deposited, dry aerosol as observed by Fromentin [1989] in the PARESS experiments. In either case, the apparent decontamination factors shown in Figure 6.13 would be lower bounds on the true decontamination that can be achieved by the combination of a crust and a water pool. Elimination of uncertainties in the decontamination factor calculations caused by possible entrainment of water, or resuspension of aerosol deposits, would require a test configuration rather different than that used in the WETCOR-1 test.

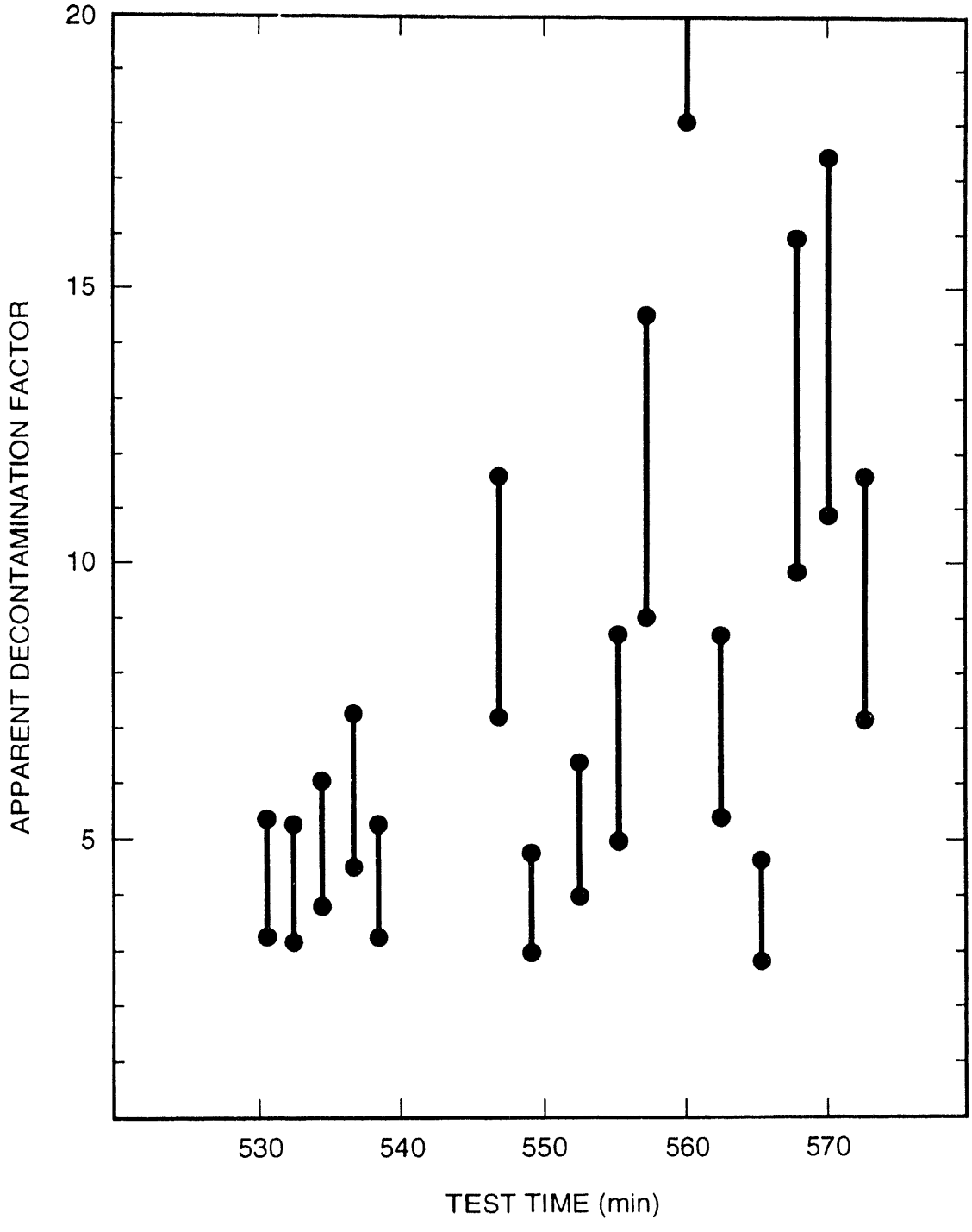

Figure 6.13. Apparent decontamination factors produced by a crust and a 30 cm deep, 50°C subcooled water pool in the WETCOR-1 test. Ranges indicated by the vertical bars were obtained using filter samples 1 and 5 as indicative of the unattenuated aerosol production.

7.0 Test Summary and Conclusions

The main purpose for performing the WETCOR-1 test was to ascertain whether or not crust formation is stable when water interacts with high temperature melts on concrete. Instabilities in the crust would allow very high rates of heat transfer which would result in relatively rapid bulk freezing and very little interaction with the concrete basemat. Extra effort was made in the design and execution of the WETCOR-1 experiment to extend the time for unstable melt/coolant interaction. This included the use of tungsten sidewalls, which were heated to temperatures well in excess of the freezing point for the molten pool, the use of slowly freezing oxide materials with a relatively high specific heat of 1.12 J/g-K as compared to 0.4 J/g-K for UO_2, and the use of a concrete basemat which produced large amounts of gas as it was ablated by melt. In addition, the power input to the melt was held at relatively low levels and the meltpool depth was relatively shallow. The main observations from the WETCOR-1 test were that there was indeed an initial period of vigorous melt/water interaction but that this period only lasted for 1 to 2 minutes and was replaced with a relatively stable crust/water geometry with substantially reduced rates of energy transfer to the overlying water. These rates of energy transfer were insufficient to either quench the melt or to discontinue the pre-established melt/concrete ablation process.

The WETCOR-1 test involved two crust formation events--one before water admission and one after water admission. This first crust formation event was reversed simply by increasing the power to the susceptor collar. But this first crust formation event proved crucial to (1) demonstrating that the test fixture design worked as expected, and (2) interpreting the observations during the second crust formation event when water was present and the actual crust could not be observed.

The crust that formed in the first event clearly did not adhere to the susceptor collar. A distinct brightness line of molten material marked the interface between the crustal material and the susceptor. Manifestly the hottest portion of the melt was adjacent to the susceptor. This observation makes it clear that design criteria necessary to meet both the contention concerning the direction of crust growth and the contention concerning suppression of the instabilities of crust growth were met in the WETCOR-1 test.

A second observation during the first crust formation event was that the crust was not monolithic. It consisted of several (≈ 5) plates separated by gaps. Independence in the small movements of these plates caused by gases produced by melt attack on the concrete was apparent in the video tape record of the test. The very small displacements of the crustal plates caused by these sparging gases may have some bearing on contentions concerning the importance of crust flexing and core debris quenching with water. Of more importance, it was observed that episodically small amounts of melt were forced up through gaps in the plates. This melt would promptly freeze, and eventually gaps between the plates were filled with frozen material.

Prior to admission of water, power to the susceptor collar was increased so that all the solidified material present at the surface as a result of crust formation in air remelted. It was evident from the video record of the test that a completely molten surface was present when water was added.

Upon addition of water, nearly all sight of the surface was lost because of steam formation and the loss of radiant illumination as the surface cooled. For about 40 seconds after a water pool had formed over the melt, glowing globules of melt were seen to rise up within the water pool, cool and sink. The globules were, it is thought, the products of the same episodic expulsion of melt through gaps in crust plates observed in the first crust formation event. With water present, some fraction of melt forced up through the gaps could be entrained at least briefly in the water pool so that still-glowing globules were visible. This interpretation, and no other that is not pure speculation has been found, implies that crusting caused by water was essentially identical to the first crusting event observed in air at lower power.

The results of the WETCOR-1 test are qualitatively the same as the results of all other tests of water admission to melts interacting with concrete. A crust of solidified material forms that isolates the remainder of the melt from the water pool. There was no evidence of any crust instability. The contentions that crust growth from the perimeter of the melt toward the center leads to different results than growth from the center to the perimeter are not supported by results of the WETCOR-1 test.

Heat fluxes through the crust to the water pool during the WETCOR-1 test when power was no longer being input to the melt were calculated to be 0.52 ± 0.13 MW/m^2. Once the bulk melt froze, heat fluxes through the crust were found (by two methods of analysis) to be only about 0.25 ± 0.08 and 0.20 ± 0.08 MW/m^2. The heat flux calculated for the period when melt was present agrees very well with heat fluxes found during an interruption in the power in the SWISS-II test [Blose et al., 1987].

More precise estimates of heat flux through the crust during the period when power was being supplied to the melt are difficult to make. The unique configuration of the experimental apparatus used to test crust stability interferes in the measurement of heat fluxes through the crust. Results obtained from the test do indicate how instrumentation employed in the WETCOR-1 test could be improved in future tests directed specifically at the determination of heat flux through the crust.

The WETCOR-1 test also confirmed results obtained in the SWISS-II test [Blose et al., 1987] that even shallow water pools can substantially attenuate aerosol production during melt interactions with concrete. The WETCOR-1 test also showed that interfacial crust alone, with no water present can reduce the rate of aerosol production. The reduction in aerosol production that could be attributed just to a crust in the WETCOR-1 test amounted to a decontamination factor of 1.3 to 3.5. Rupture of the crust or expulsion of molten material through gaps or holes in the crust increases the aerosol production.

The WETCOR-1 test showed that the combination of a crust and a water pool 30 cm deep and 50°C subcooled produced apparent decontamination factors of 3 to over 15. Analysis of aerosol size distribution data obtained once a water pool was established suggests that the apparent decontamination factors may be lower bounds on the true extent to which water pools and crusts reduce aerosol production. Entrainment of water containing suspended and dissolved solids may partially reduce the aerosol attenuation by water pools.

References

Barin, I., F. Sauert, E. Schultze-Rhonhof and W.S. Sheng, Thermochemical Data of Pure Substances, VCH Press, (1989).

Blose, R.E., J.E. Gronager, A.J. Suo-Antilla, and J.E. Brockman, SWISS: Sustained Heated Metallic Melt/Concrete Interactions with Overlying Water Pools, NUREG/CR-4727, SAND85-1546, Sandia National Laboratories, Albuquerque NM, (1987).

Copus, E.R., R.E. Blose, J.E. Simpson, R.B. Simpson, and D.A. Lucero, Core/Concrete Interactions Using Molten UO_2 with Zirconium on a Basaltic Basemat: The SURC-2 Experiment, NUREG/CR-5564, SAND90-1022, Sandia National Laboratories, Albuquerque, NM, (August 1992).

Copus, E.R., et al., Core-Concrete Interactions Using Molten Steel with Zirconium on a Basaltic Basemat: The SURC-4 Experiment, NUREG/CR-4994, SAND87-2008, Sandia National Laboratories, Albuquerque, NM, (1989).

Fauske and Associates, Technical Support for the Debris Coolability Requirements for Advanced Light Water Reactors in the Utility/EPRI Light Water Reactor Requirements Document, DOE/ID-10278, (June 1990).

Fromentin, A., Particle Resuspension from a Multilayer Deposit by Turbulent Flow, PSI-Bericht Nr. 38, September 1989.

Halstedt, B., J. Amer. Ceram. Soc. 73, (1990) 15.

Kingery, W.D., Introduction to Ceramics, Wiley, (1967).

Mackenzie, J.K., Proc. Phys. Soc., (London) B63 (1950) 2.

Metals and Ceramics Information Center, Engineering Property Data on Selected Ceramics, Volume 3, Single Oxides, MCIC-HB-07-Vol. 3, Battelle Columbus Division, Columbus, OH, (July 1981).

Morey, G.W., Phase Equilibrium Relations of the Common Rock-Forming Oxides Except Water, Geological Survey Paper 440-L, 1964.

Nurse, R.W., et al., British Ceramic Society Transactions and Journal, 64, (1965) 409.

Office of Nuclear Regulatory Research, Severe Accident Research Program Plan Update, NUREG-1365, Rev. 1, U.S. Nuclear Regulatory Commission, Washington, D.C., 1992.

Parker, E.R., Materials Data Book, McGraw-Hill Book Co. (1967).

Powers, D.A., and F.E. Arellano, Large Scale, Transient Tests of the Interaction of Molten Steel With Concrete, NUREG/CR-2282, SAND81-1753, Sandia National Laboratories, Albuquerque, NM, (January 1982).

Powers, D.A., J.E. Brockmann and A.W. Shiver, VANESA: A Mechanistic Model of Radionuclide Release and Aerosol Generation During Core Debris Interactions with Concrete, NUREG/CR-4308, SAND85-1370, Sandia National Laboratories, Albuquerque, NM (July 1986).

Powers, D.A. and J.L. Sprung, A Simplified Model of Aerosol Scrubbing by a Water Pool Overlying Core Debris Interacting with Concrete, NUREG/CR-5901, SAND92-1422, Sandia National Laboratories, Albuquerque, NM, (October 1992).

Romberger, K.A., C.F. Bates, Jr., and H.H. Stone, J. Inorg. Nucl. Chem. 29 (1966), 1619.

Skokan, A., "High Temperature Phase Relations in the U-Zr-O System", Proc. Fifth International Mtg. Thermal Reactor Safety, Kfk 388011, pp. 1035-42, December 1984.

Spencer, B.W., M. Fischer, M.T. Farmer, and D.R. Armstrong, MACE Scoping Test Data Report, MACE-TR-DO3, Argonne National Laboratory, Argonne, IL (1991).

Stull, D.R. and H. Prophet, JANAF Thermochemical Tables, 2nd Edition, NSRDS-NBS 37. National Bureau of Standards, Washington, D.C. (June 1971).

Tarbell, W.W., D.R. Bradley, R.E. Blose, et al., Sustained Concrete Attack by Low Temperature, Fragmented Core Debris, NUREG/CR-3024, SAND82-2476, Sandia National Laboratories, Albuquerque, NM (1987).

Yamano, N. and J.E. Brockmann, Aerosol Sampling and Transport Efficiency Calculation (ASTEC) and Application to Surtsey/DCH Aerosol Sampling System, NUREG/CR-5252, SAND88-1447, Sandia National Laboratories, Albuquerque, NM, 1989.

Appendix A: Power Calibration Data

Test Setup

A posttest power calibration was performed to quantify the coupling efficiency of the tungsten sleeve susceptors. During the experiment the tungsten sleeves were heated inductively. The sleeves transferred heat to the oxide charge by conduction melting the debris and sustaining the interaction. The charge was composed of approximately 76.8% Al_2O_3, + 17.9% CaO + 4.0% SiO_2 + 0.9% Fe_2O_3. For the calorimeter test, three pressed and sintered 99.9% tungsten sleeves, identical to those used in the experiment were used for the calibration. Each sleeve was nominally 36-cm OD x 33-cm ID x 5.6 cm high. The mass of each sleeve averaged 22.4 kg.

The test apparatus for conducting the calorimetric tests is shown in Figure A-1. A 208 liter Nalgene tank (56-cm ID x 91 cm high) fitted with a 7.6-cm PVC bulkhead feed-through was placed on top of three 22.9-cm x 11.4-cm x 7.6-cm MgO bricks inside the induction coil. This was done so that the water exit port would clear the top of the coil. Placed on the bottom of the tank were three 19.1-cm x 19.1-cm x 19.1-cm concrete blocks, spaced approximately 120 degrees apart. On top of each block was placed an MgO brick having the same dimensions as described above. Three tungsten susceptor sleeves instrumented with type-K thermocouples were stacked on the MgO bricks concentric with the coil. The location of the sleeves within the coil was identical to the initial location of sleeves used in the experiment.

Four type K thermocouples were placed between the susceptor sleeves to monitor the ring temperatures when the power was applied. Two of the thermocouples were positioned between the bottom and middle sleeve 180 degrees apart. The remaining two thermocouples were positioned between the middle sleeve and top sleeve 180 degrees apart directly above the ones installed between the lower sleeves. The thermocouples were first secured with five minute epoxy and later coated with GE Silicon RTV. This was done to isolate the tips of the thermocouples from exposure to the water pool and maximize contact with the susceptor sleeves. The sleeves were instrumented to ensure that the sleeves did not attain a temperature sufficient enough to cause the water adjacent to them to flash into film boiling.

Water was delivered to the tank using 1.9-cm-OD (0.75 in) stainless steel tubing terminating in a Swagelok tee located in the center of the tungsten sleeve susceptor assembly. The flow rate of the water was controlled by a remotely actuated ball valve. A Signet turbine meter was installed upstream of the ball valve to record the flow rate of water delivered to the pool formed in the tank. A type-K thermocouple was installed in the inlet and exit water flow circuit to monitor temperature. A thermistor was also installed at the inlet and exit. The two thermistors were configured into a half-bridge circuit to measure the differential temperature.

Since the thermocouple and thermistor were located some distance downstream from the tank, a type-K thermocouple was installed in the center of a cylindrical aluminum heat sink to measure water temperature at the exit of the tank. The heat sink was 1.6 cm (0.625 in) diam and 1.3 cm (0.5 in) long.

Power was delivered from the 280 kW induction power supply to the coil using flexible, high-current, water cooled leads. Parameters measured for operating the power supply included the power at the buss bars, differential temperature and flow rate of the coolant flowing through the coil and power supply.

This whole assembly was placed inside the 13 m^3 steel containment vessel to simulate the actual experimental conditions.

Test Procedures

Fourteen channels were used to record the data for analyzing power and calculating coupling efficiency. Seven of these channels recorded the temperatures measured by type-K thermocouples, and the remaining seven were voltage channels. Figure A-2 shows a listing of the channels in the configure file used for storing the information on the HP 1000 data acquisition system. Also shown are the equations used to convert voltage data into engineering units.

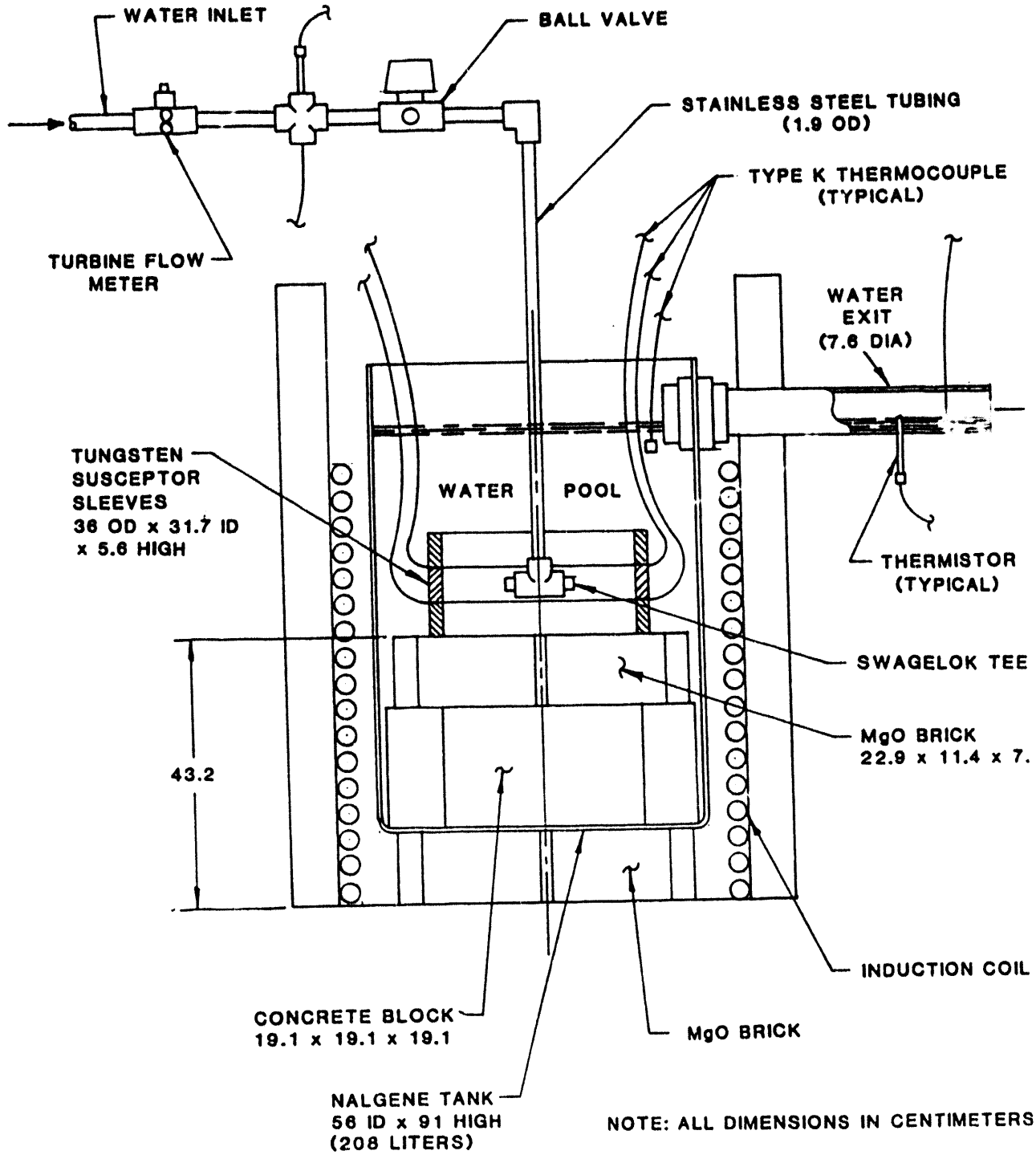

Figure A-1. Test apparatus used for conducting the posttest calorimetric tests for the WETCOR-1 experiment

```
ILE =wetcorpwrcal.cnfg:::1                          Mon Oct  7, 1991  6:09:24 pm
         CHAN.   INSTRUMENT          MAXIMUM
CHANNEL   NAME       TYPE             VOLTAGE
  1      RNG1 0        K TC              .02
  2      RNG1180       K TC              .02
  3      RNG2 0        K TC              .02
  4      RNG2180       K TC              .02
  5      POOLEXT       K TC              .02
149      H2O IN        K TC              .02
150      H2O EXT       K TC              .02
171      TBRIDGE    USER EQ11           5.00
172      H2O FLO    USER EQ12           5.00
181      POWER      USER EQ13           5.00
182      PS DT      USER EQ14          10.00
183      PS FLOW    USER EQ15           5.00
184      COIL DT    USER EQ16            .01
185      COILFLO    USER EQ17           5.00
USER EQUATION # 11 COEFFIECENTS ARE:
          .187793x^0          9.701769x^1          .749658x^2          -.351472x^3
USER EQUATION # 12 COEFFIECENTS ARE:
          .208090x^0          5.959747x^1          .041628x^2
USER EQUATION # 13 COEFFIECENTS ARE:
   .000000000E+00x^0    .100000000E+03x^1
USER EQUATION # 14 COEFFIECENTS ARE:
   .000000000E+00x^0    .759200000E+01x^1
USER EQUATION # 15 COEFFIECENTS ARE:
          .923270x^0         20.101101x^1
USER EQUATION # 16 COEFFIECENTS ARE:
   .000000000E+00x^0    .250000000E+04x^1
USER EQUATION # 17 COEFFIECENTS ARE:
          .771447x^0         18.957371x^1
```

Figure A-2. Description of the data acquisition channels used for the calorimeter tests, WETCOR-1

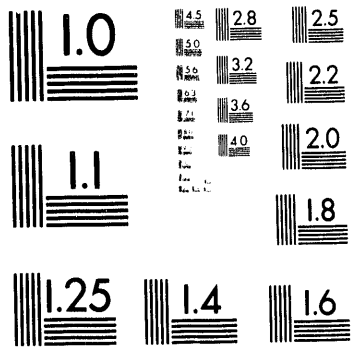
1.0
1.1
1.25
1.4
1.6
1.8
2.0
2.2
2.5
2.8
3.2
3.6
4.0
4.5
5.0
5.6

2 of 2

Appendix A

Three calibration tests were performed at input powers of 50, 100 and 150 kW based on power meter readings. The voltage and current measurements establishing power levels were made near the two water-cooled, copper buss bars used to connect the coil with the high current flexible leads.

The calorimetric test was initiated by starting the data acquisition system establishing a baseline for the instrumentation. Data was sampled every 15 sec for calculating power delivered to the susceptor sleeves for buss powers of 50, 100 and 150 kW. The ball valve was opened and the flow rate of water to the tank was set to a value that would provide a reasonable temperature difference for the water between inlet and exit. After a few minutes of baseline data the power supply was started and a constant power input was applied to the coil. The power supply was run until the differential temperature in the water pool reached a steady state condition.

The power imparted to the tungsten susceptor sleeves was assumed to be identical to the heat transferred to the water defined by the common heat transfer equation shown below.

$$P_{gain} = \dot{m}\, C_p \Delta T \qquad \text{(A-1)}$$

where

P_{gain} = Power delivered to the water pool by the susceptor sleeves (kW)

$\dot{m}$ = Mass flow rate of water (kg/sec)

C_p = Specific heat of water at the steady state exit temperature (J/kg/K)

ΔT = Differential temperature between the inlet and exit of the water pool, $T_{exit} - T_{inlet}$ (K or C)

Figure A-3 shows a plot of the power with respect to time for the three calibration runs. Figure A-4 shows the temperature of the tungsten sleeve susceptors. Figure A-5 shows the temperature of the water entering and exiting the Nalgene tank. Figure A-5 also shows the differential temperature measured by the thermistor ridge. Figure A-6 shows the flow rate of the water delivered to the Nalgene tank. Figure A-7 and A-8 show a plot of the differential temperature and flow rate of the coolant, respectively, in the coil and power supply. Figure A-9 shows a plot of the specific heat of water plotted as a function of temperature in degrees K. Table A-1 presents values of specific heat in J/kg/K for corresponding values of water temperature in degrees K.

Extracting the appropriate values of data from Figures A-5 and A-6 and substituting these into Equation A-1 above, the power delivered to the susceptor sleeves can be calculated.

In order to account for all the power applied to the water, the heat loss from the water pool must be considered. Data were collected at the end of the calibration runs to determine the heat lost from the Nalgene tank. From this the equivalent power was calculated from the cooling rate of water in the tank using the equation

$$P_{loss} = m\, C_p \Delta T/\Delta t \qquad \text{(A-2)}$$

where

P_{loss} = Power loss due to cooling rate of water pool in Nalgene tank (kW)

m = Mass of water in the tank = 155 kg

C_p = Specific heat of water at the mean temperature, $(T_{initial} + T_{final})/2$ (J/kg/K)

$\Delta T/\Delta t$ = Rate of water pool cooling (K/sec or C/sec)

The equivalent power loss calculated from the above equation for the 50 kW calorimetric test was negligible and for the 100 and 150 kW tests was found to be 0.4 kW.

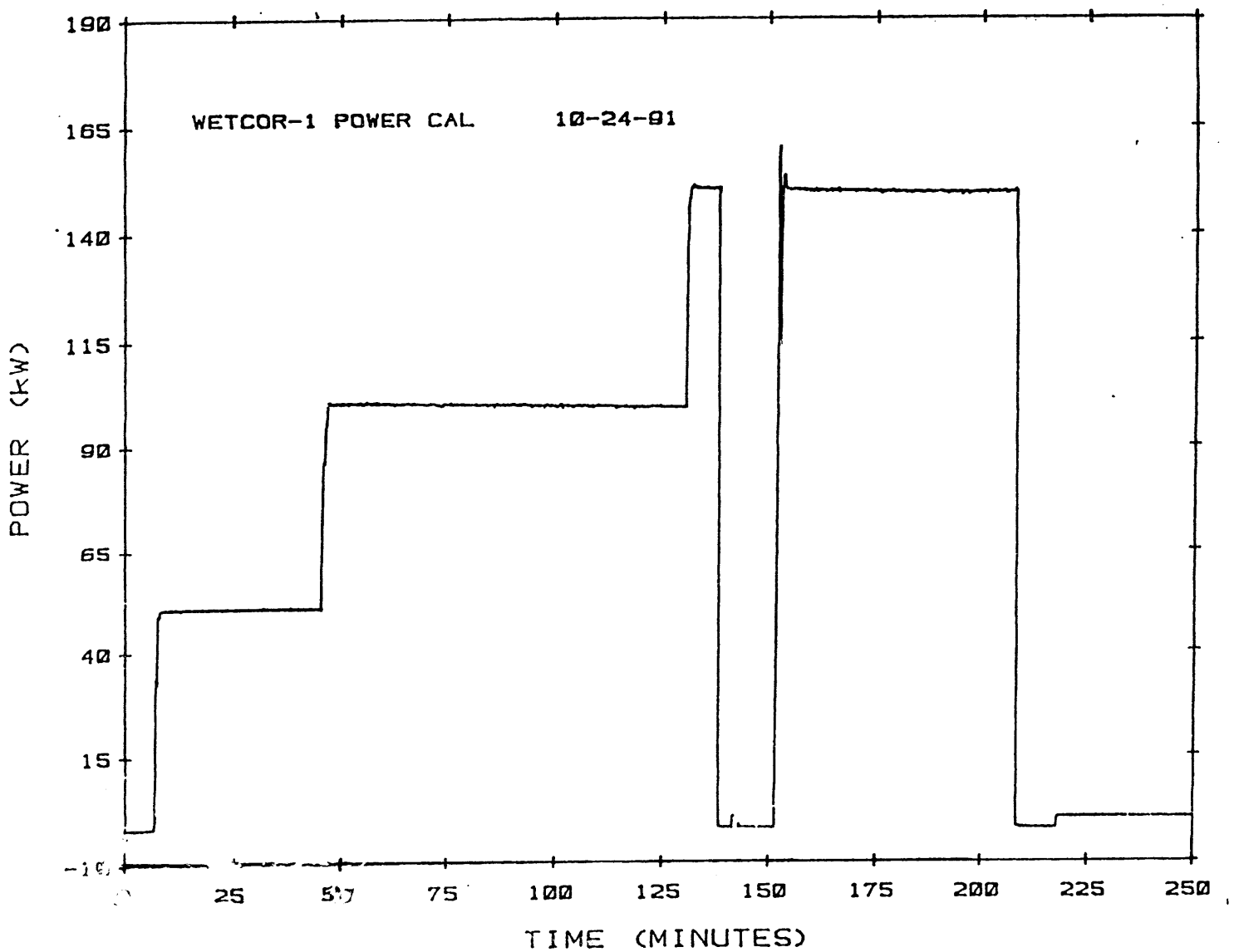

Figure A-3. Plot of buss power as a function of time for the calorimetry tests, WETCOR-1

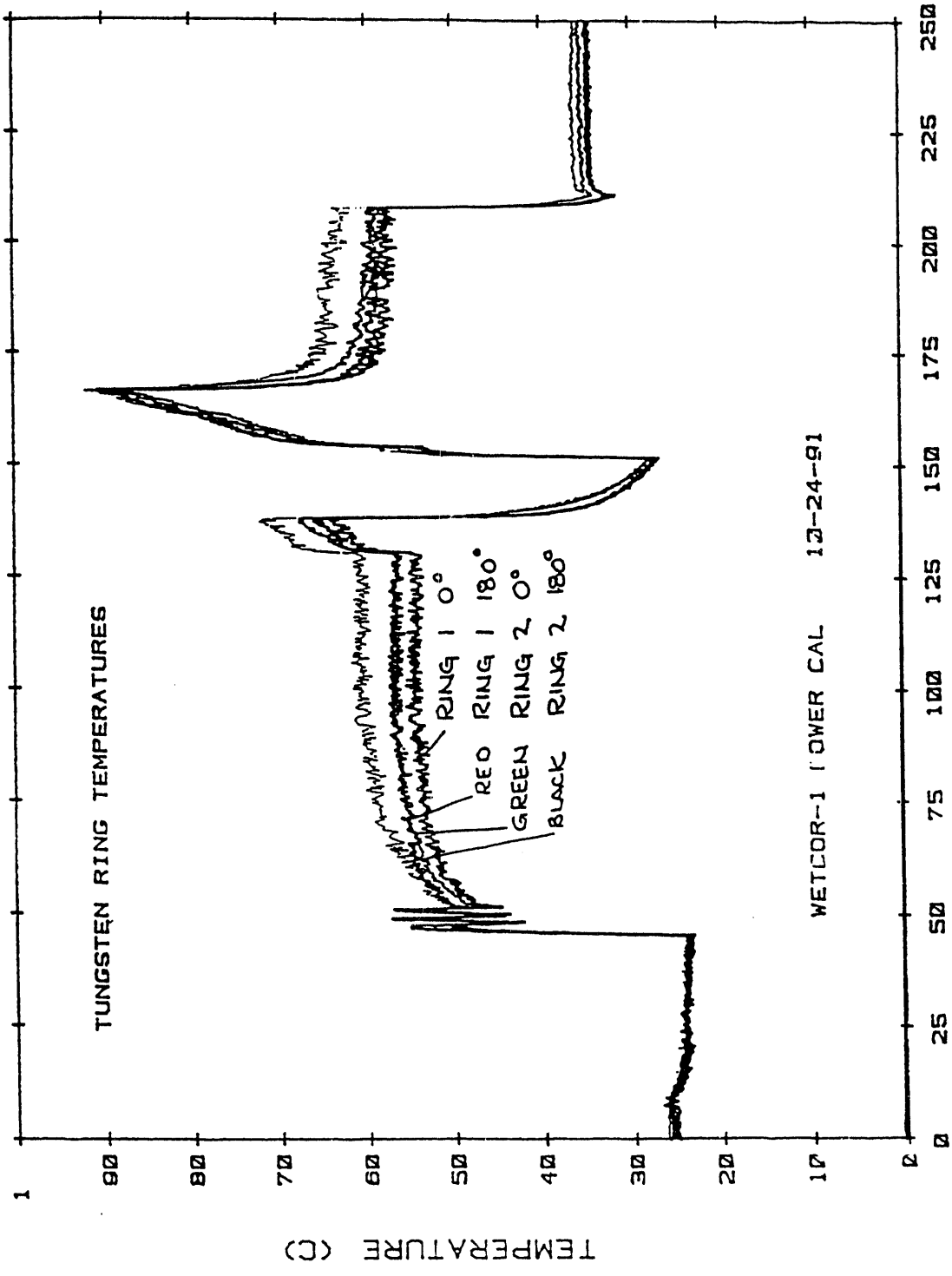

Figure A-4. Temperature of the tungsten sleeve susceptors

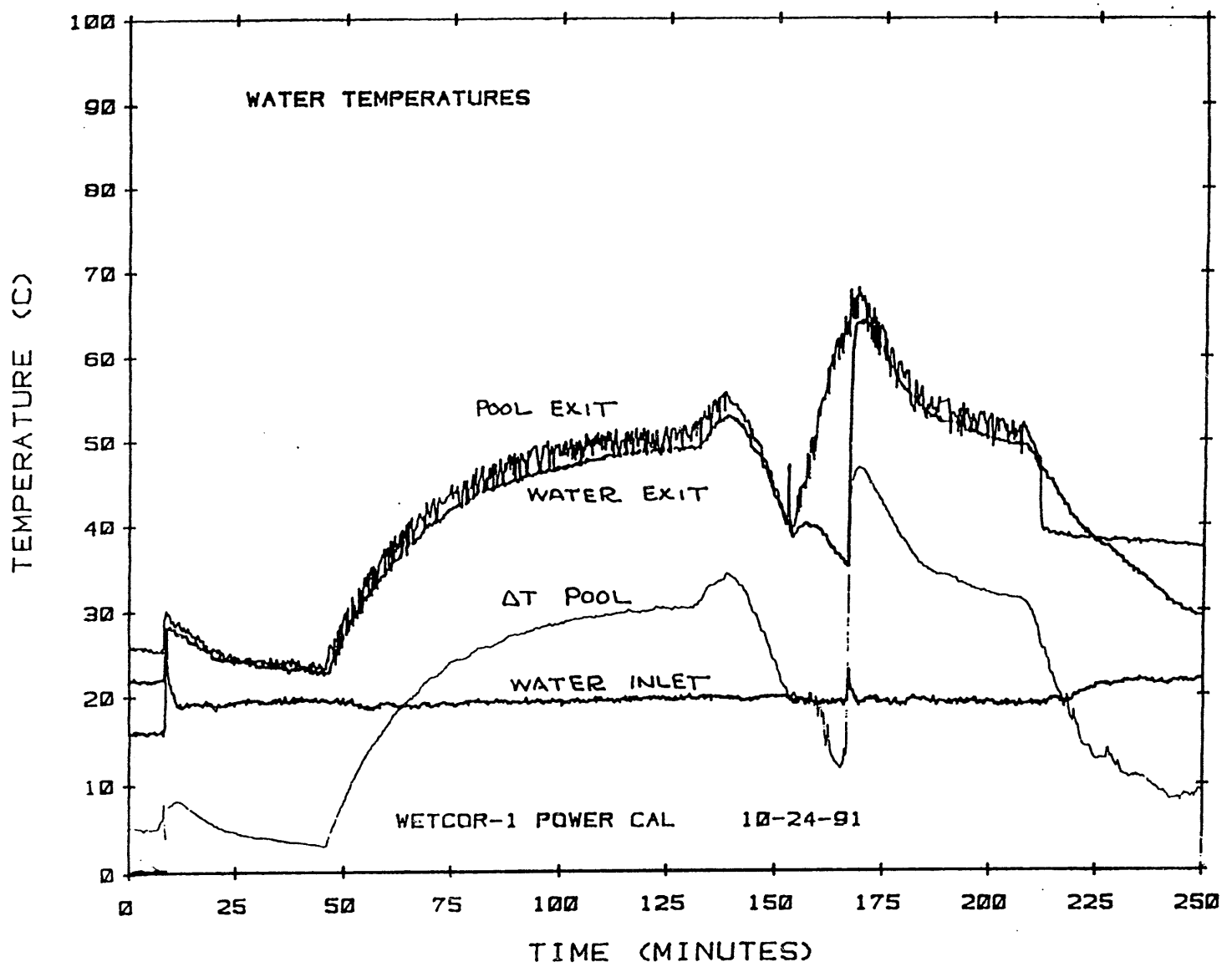

Figure A-5. Temperature of the water delivered to and exiting the nalgene tank

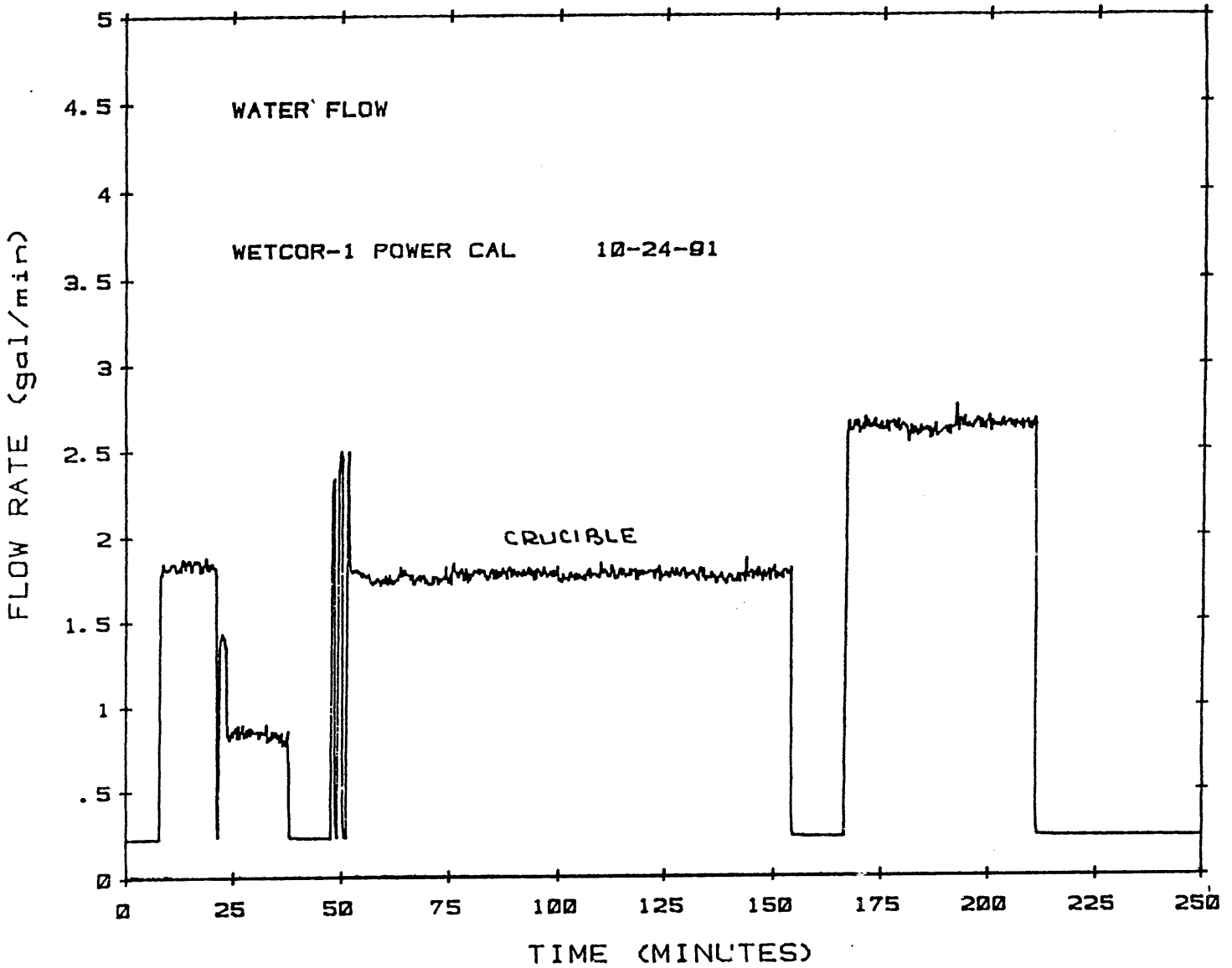

Figure A-6. Flow rate of water to the nalgene tank

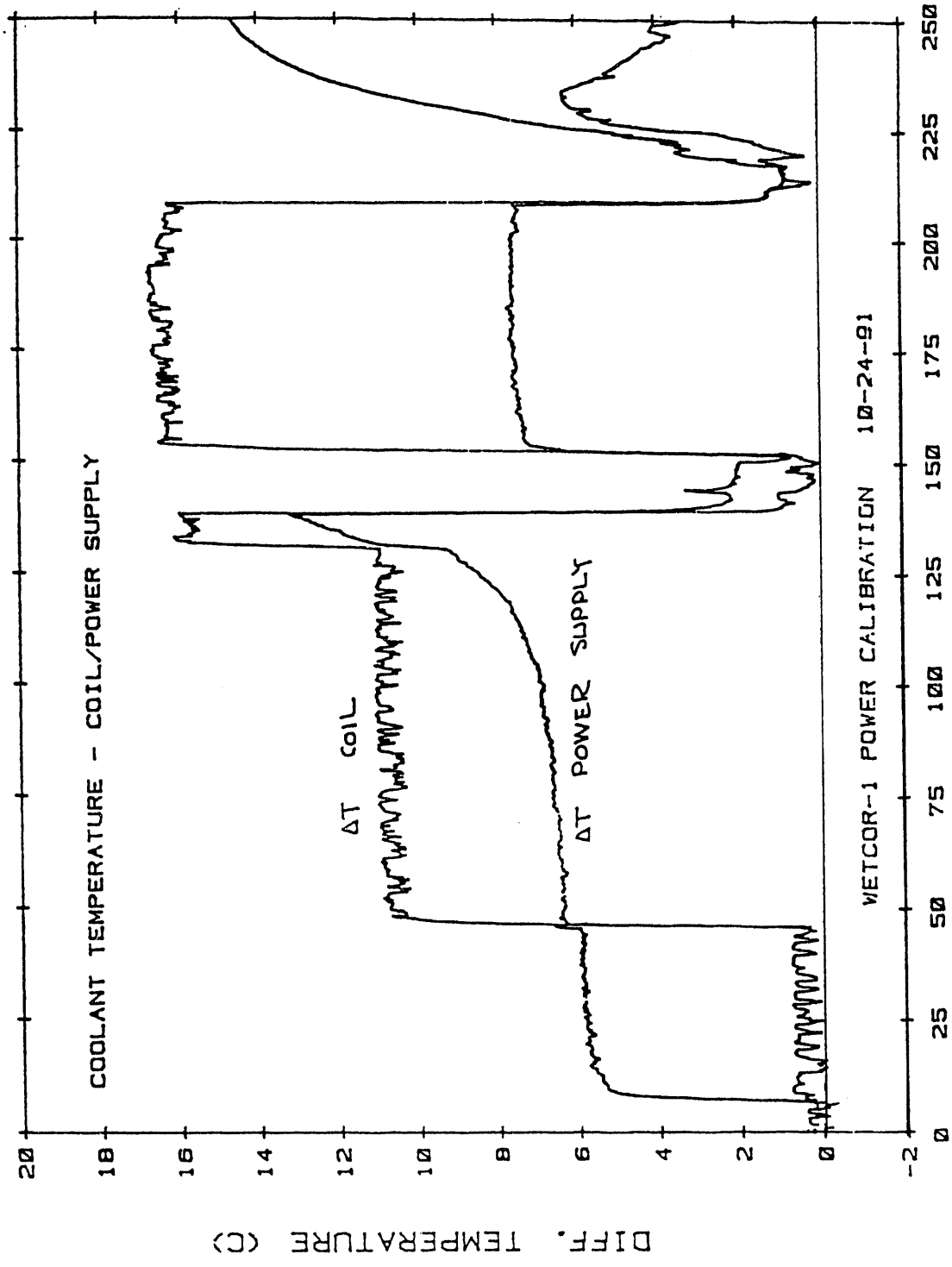

Figure A-7. Differential temperature of the coolant flowing through the coil and power supply

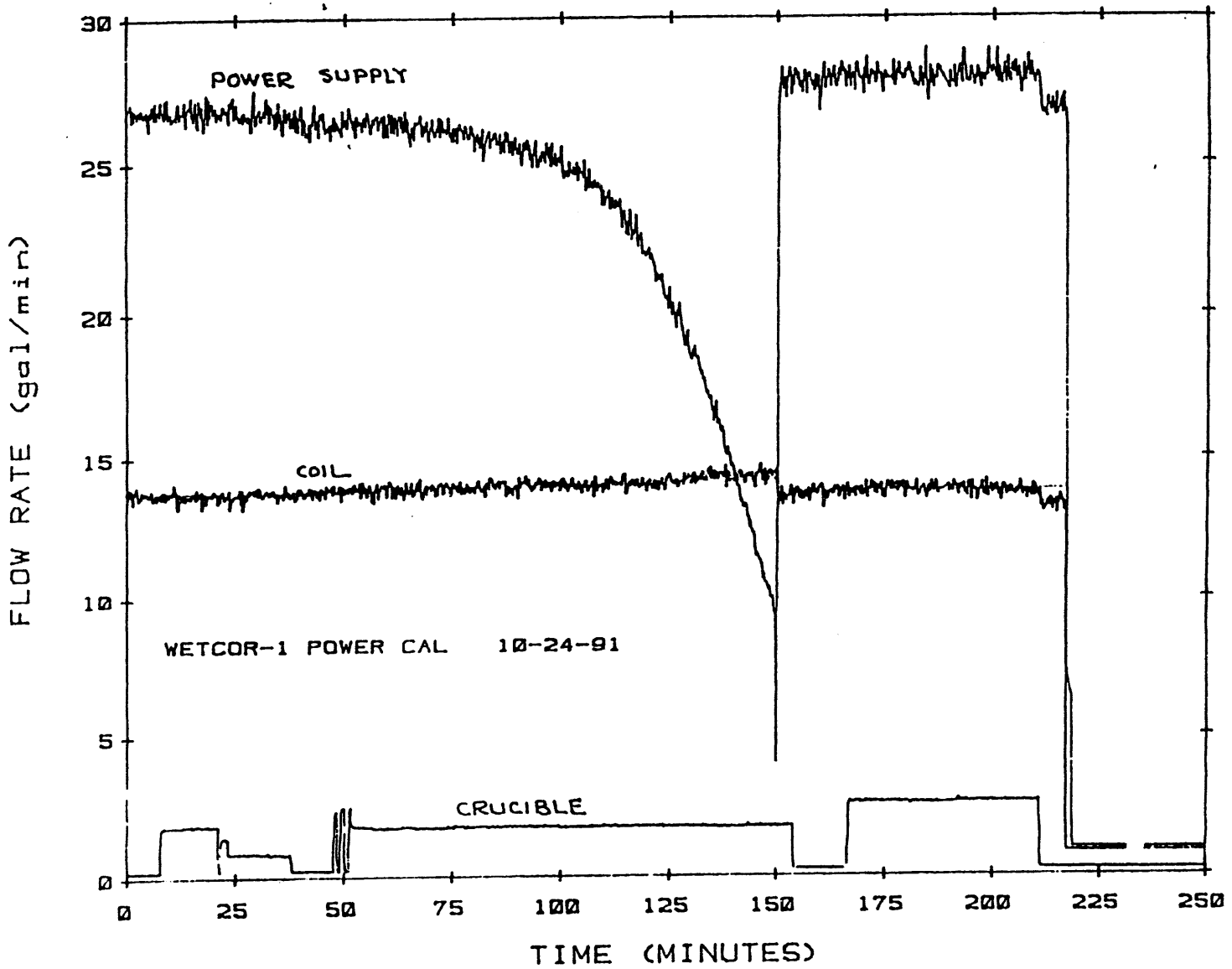

Figure A-8. Flow rate of the coolant flowing through the coil and power supply

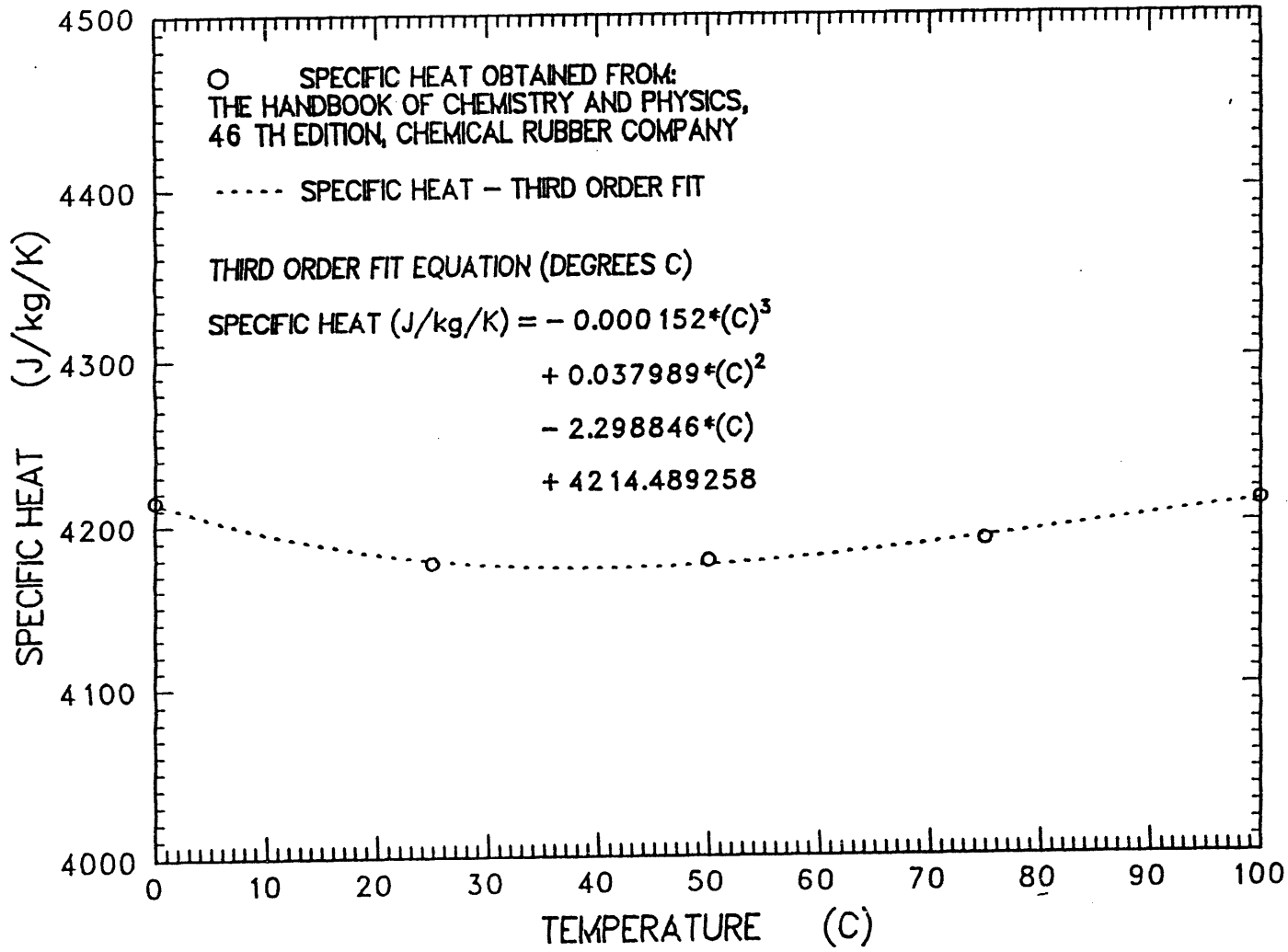

Figure A-9. Plot of the specific heat of water as a function of water temperature

Table A-1. Specific heat of water

Temperature (C)	Heat Flux (W/kg/K)
0.00	0.42145E+04
1.00	0.42122E+04
2.00	0.42100E+04
3.00	0.42079E+04
4.00	0.42059E+04
5.00	0.42039E+04
6.00	0.42020E+04
7.00	0.42002E+04
8.00	0.41985E+04
9.00	0.41968E+04
10.00	0.41952E+04
11.00	0.41936E+04
12.00	0.41921E+04
13.00	o.41907E+04
14.00	0.41894E+04
15.00	0.41881E+04
16.00	0.41869E+04
17.00	0.41857E+04
18.00	0.41846E+04
19.00	0.41835E+04
20.00	0.41825E+04
21.00	0.41816E+04
22.00	0.41807E+04
23.00	0.41799E+04
24.00	0.41791E+04
25.00	0.41784E+04
26.00	0.41778E+04
27.00	0.41771E+04
28.00	0.41766E+04
29.00	0.41761E+04
30.00	0.41756E+04
31.00	0.41752E+04
32.00	0.41749E+04
33.00	0.41745E+04
34.00	0.41743E+04
35.00	0.41741E+04
36.00	0.41739E+04
37.00	0.41737E+04
38.00	0.41736E+04
39.00	0.41736E+04
40.00	0.41736E+04
41.00	0.41736E+04
42.00	0.41737E+04
43.00	0.41738E+04
44.00	0.41739E+04

Table A-1. Specific heat of water (Continued)

Temperature (C)	Heat Flux (W/kg/K)
45.00	0.41741E+04
46.00	0.41743E+04
47.00	0.41745E+04
48.00	0.41748E+04
49.00	0.41751E+04
50.00	0.41755E+04
51.00	0.41758E+04
52.00	0.41762E+04
53.00	0.41767E+04
54.00	0.41771E+04
55.00	0.41776E+04
56.00	0.41781E+04
57.00	0.41787E+04
58.00	o.41792E+04
59.00	0.41798E+04
60.00	0.41804E+04
61.00	0.41810E+04
62.00	0.41817E+04
63.00	0.41824E+04
64.00	0.41831E+04
65.00	0.41838E+04
66.00	0.41845E+04
67.00	0.41852E+04
68.00	0.41860E+04
69.00	0.41867E+04
70.00	0.41875E+04
71.00	0.41883E+04
72.00	0.41891E+04
73.00	0.41899E+04
74.00	0.41908E+04
75.00	0.41916E+04
76.00	0.41924E+04
77.00	0.42933E+04
78.00	0.41941E+04
79.00	0.41950E+04
80.00	0.41959E+04
81.00	0.41967E+04
82.00	0.41976E+04
83.00	0.41985E+04
84.00	0.41994E+04
85.00	0.42002E+04
86.00	0.42011E+04
87.00	0.42020E+04
88.00	0.42029E+04
89.00	0.42037E+04

Table A-1. Specific heat of water (Concluded)

Temperature (C)	Heat Flux (W/kg/K)
90.00	0.42046E+04
91.00	0.42054E+04
92.00	0.42063E+04
93.00	0.42071E+04
94.00	0.42080E+04
95.00	0.42088E+04
96.00	0.42096E+04
97.00	0.42104E+04
98.00	0.42112E+04
99.00	0.42120E+04
100.00	0.42128E+04

The coupling efficiency was calculated by the equation below

$$\% \ Efficiency = P_{sleeves} / P_{buss} \qquad (A\text{-}3)$$

where

P_{sleeve} = Power calculated from calorimetry combining gains Eq. 1 and losses Eq. 2. (kW)

P_{buss} = Power measured by the power transducer (kW)

The coupling efficiencies calculated for the 50, 100, and 150 kW test was presented in Table A-2. A calorimetry test at 200 kW was not possible because the operational voltage limit of the induction power supply (600 Vac) was reached just above the 150 kW calibration.

The efficiency calculated for the 50 kW calorimetry test was not consistent with that calculated for the 100 and 150 kW tests. For the 50 kW test, the differential temperature of the coolant flowing through the coil was essentially negligible. Typically, the power deposited into the coil cooling fluid during calorimetry tests was approximately 35% to 50% of the buss power depending on charge material and configuration. This was equivalent to a differential temperature of between 5.0 and 7.1°C.

The measured differential temperature for the 50 kW test was 0.5°C as shown in Figure A-7.

The efficiency calculated for the 100 and 150 kW calorimetry tests agree quite well. The 100 kW yielded an efficiency of 15.1% and the 150 kW calibration 13.9%. Based on these independent calculations, the efficiency was determined to be 14.5% $\pm$ 0.8% based on the average of the two calorimetry tests.

There was a question raised as to the effect of the capacitor setting on the maximum power delivered to the coil. To study the effect, five capacitor settings were selected over the range of 0 through 7. At each setting the controls on the power supply were adjusted to obtain the maximum power output. At each setting the indicated power (console meter), actual power (power transducer), frequency (console meter) and AC voltage (console meter) were recorded. These results were presented in Table A-3.

Based on the data in Table A-3, the actual power increased 15 kW over the range of selectable capacitor settings from 170.5 to 185.5 kW. This represents only a 9% increase in the power that could be available. The power supply for the WETCOR-1 test was operated with a capacitor setting of 2. Operating the power supply at this setting provided sufficient heating of the tungsten sleeve susceptors to melt and sustain the interaction for the WETCOR-1 experiment.

Table A-2. System coupling efficiencies for WETCOR-1

Total Power Buss Power (kW)	Net Power Sleeve Power (kW)	Power Losses (KW)	Coupling Efficiency (%)
50	0.7	0.0	1.4
100	14.7	0.4	15.1
150	20.5	0.4	13.9

Table A-3. Operational power limits for different capacitor settings, WETCOR-1 susceptor sleeve configuration

Capacitor Setting (#)	Indicated Power (kW)	Actual Power (kW)	Operational Frequency (Hz)	Operational Voltage (volts)
0	198	170.5	920	600
2	200	175.7	900	600
4	202	180.5	875	600
6	203	184.0	850	600
7	203	185.5	850	600

Appendix B: Power Supply Operational Data

In this appendix data are presented that relate to the operation of the induction power supply. The data includes buss power, flow rate and temperature data of the cooling fluid flowing through the power supply and induction coil. The cooling fluid was an 8 w/o ethylene glycol in water.

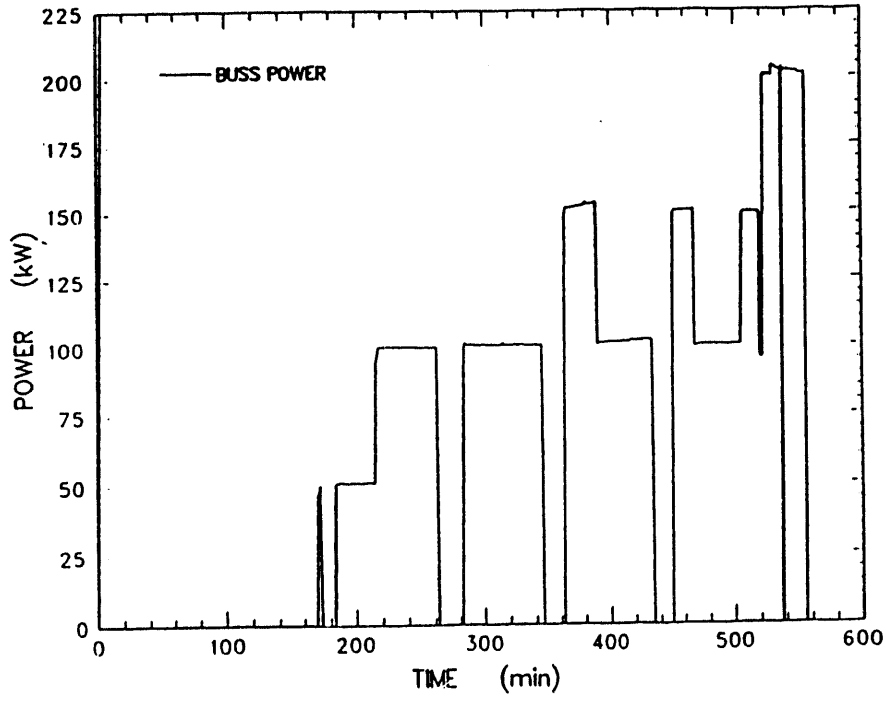

Figure B-1. Power Applied at the Buss Bars During the WETCOR-1 Experiment

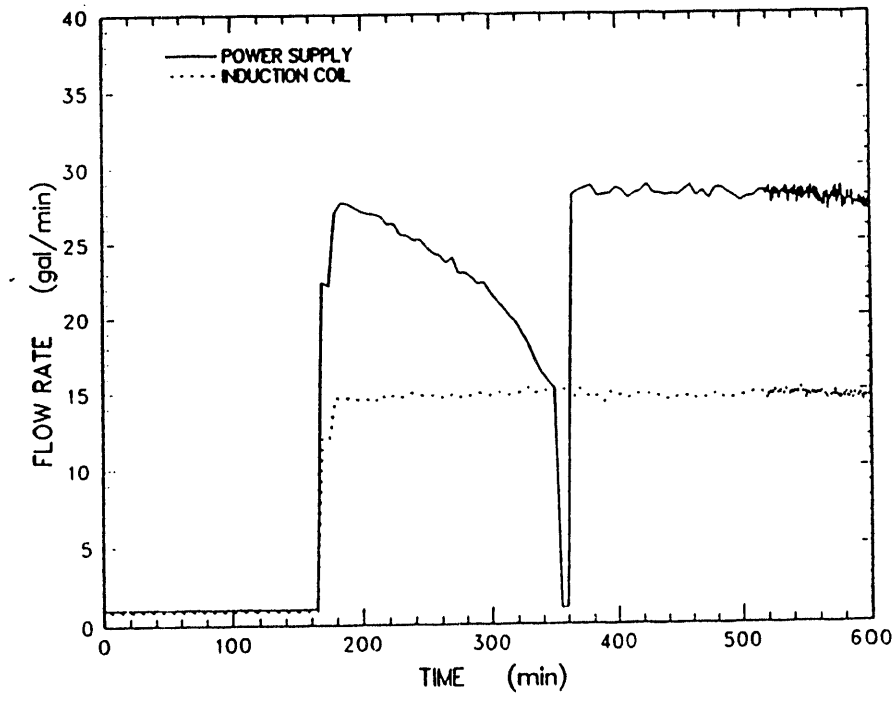

Figure B-2. Flow Rate of Cooling Fluid Flowing Through the Power Supply and Induction Coil

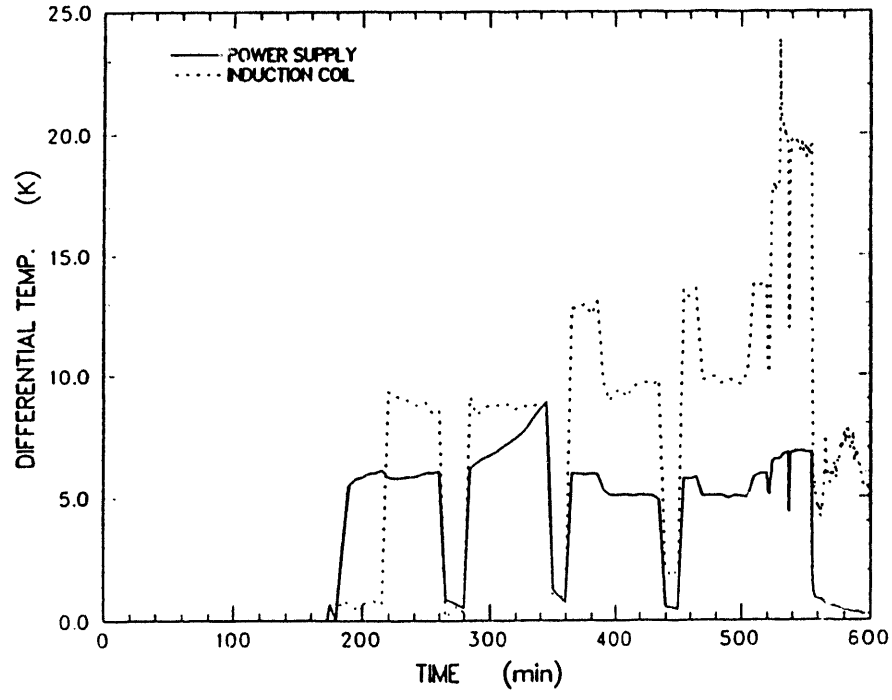

Figure B-3. Differential temperature of the cooling fluid flowing through the power supply and induction coil

Appendix C: Crucible Thermocouple Profiles

Presented in this appendix are the temperature profiles produced from type-K and -C thermocouples imbedded in the concrete basemat, and MgO castable sidewalls.

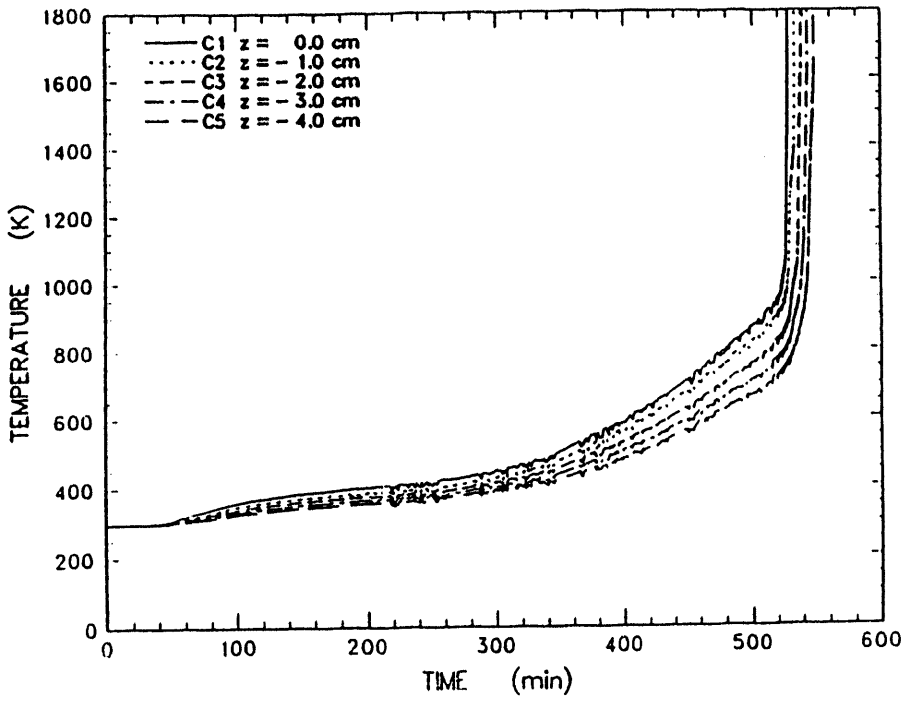

Figure C-1. Concrete temperature data measured by thermocouples located in the midradius array between z = 0.0 and -4.0 cm

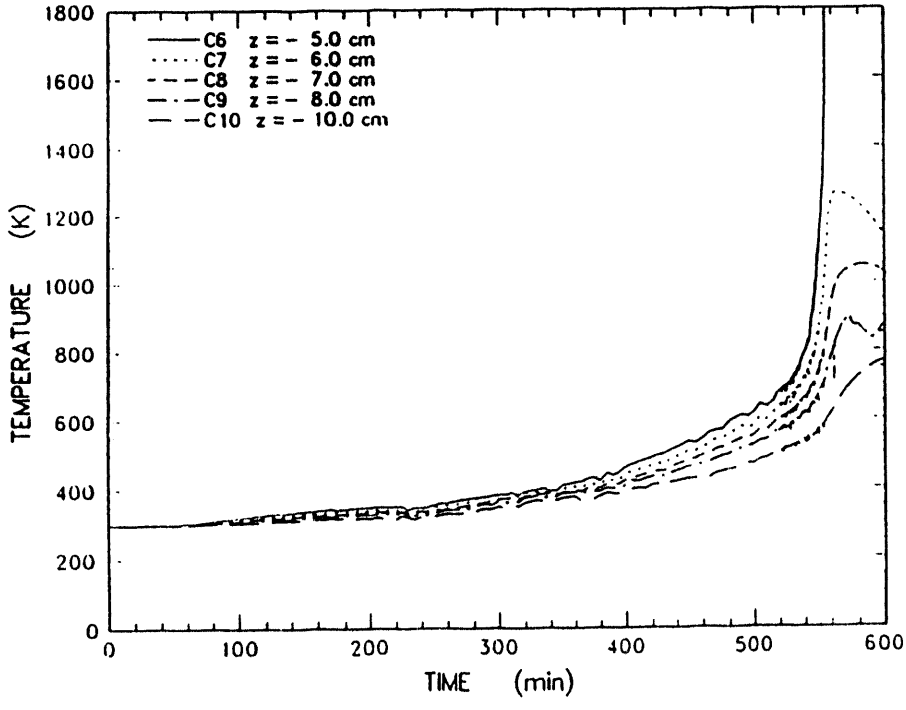

Figure C-2. Concrete temperature data measured by thermocouples located in the midradius array between z = -5.0 and -10.0 cm

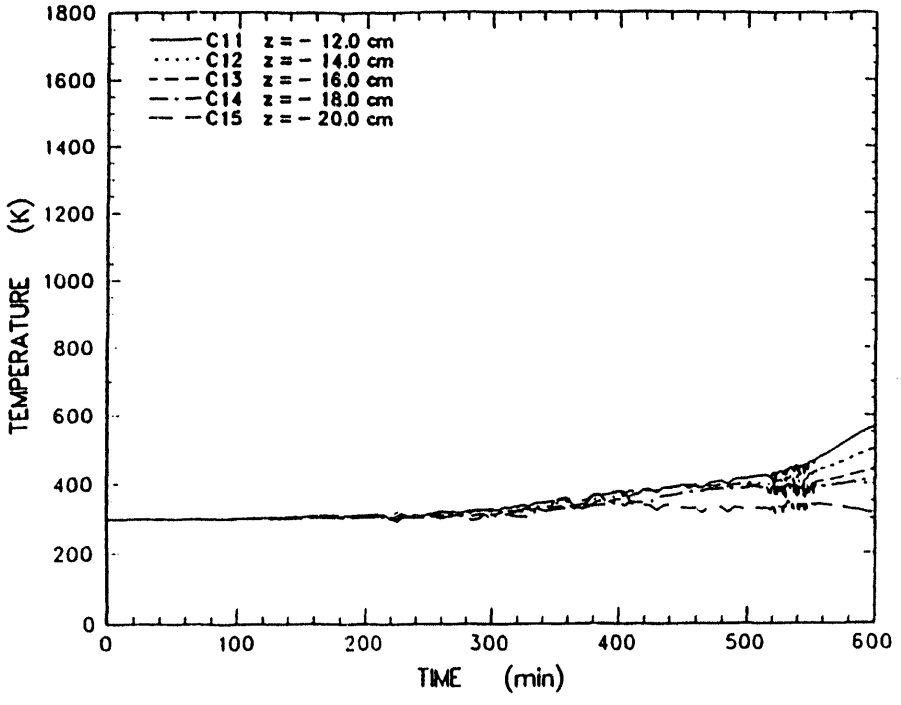

Figure C-3. Concrete temperature data measured by thermocouples located in the midradius array between z = -12.0 and -20.0 cm

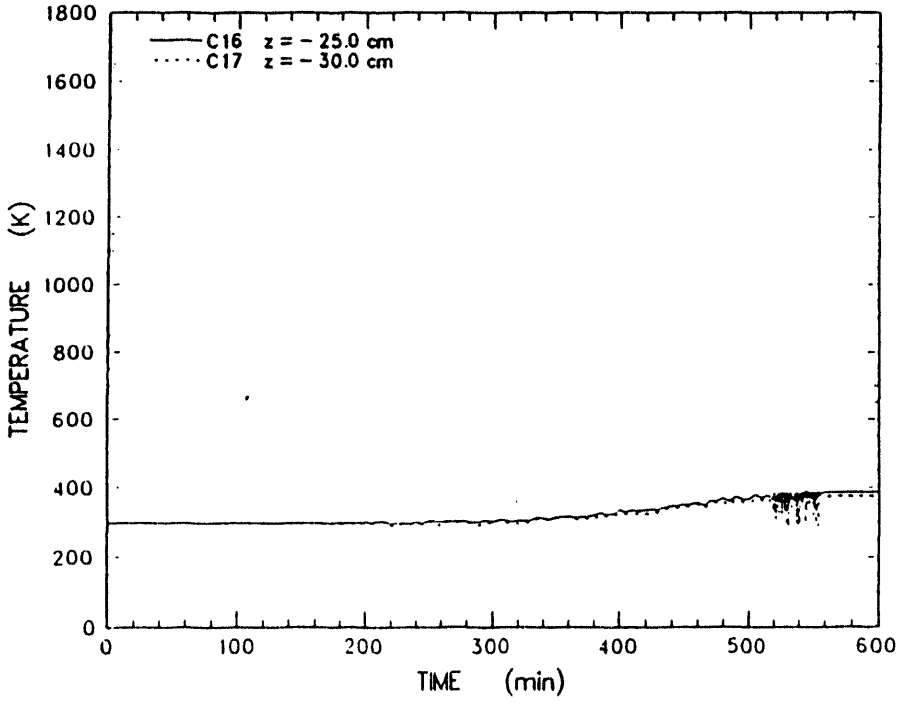

Figure C-4. Concrete temperature data measured by thermocouples located in the midradius array between z = -25.0 and -30.0 cm

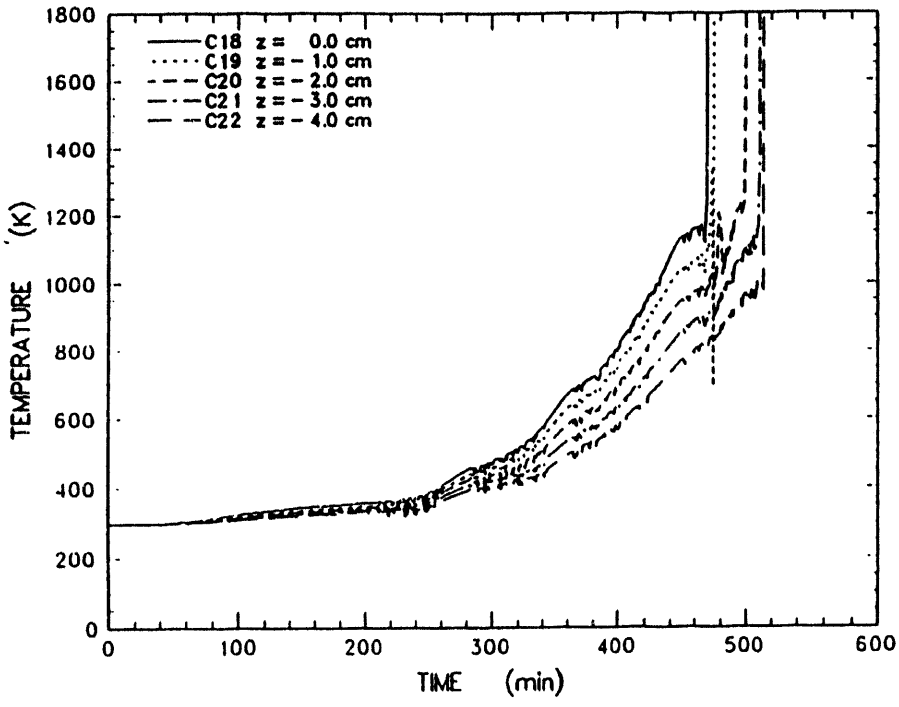

Figure C-5. Concrete temperature data measured by thermocouples located in the axial array between z = 0.0 and -4.0 cm

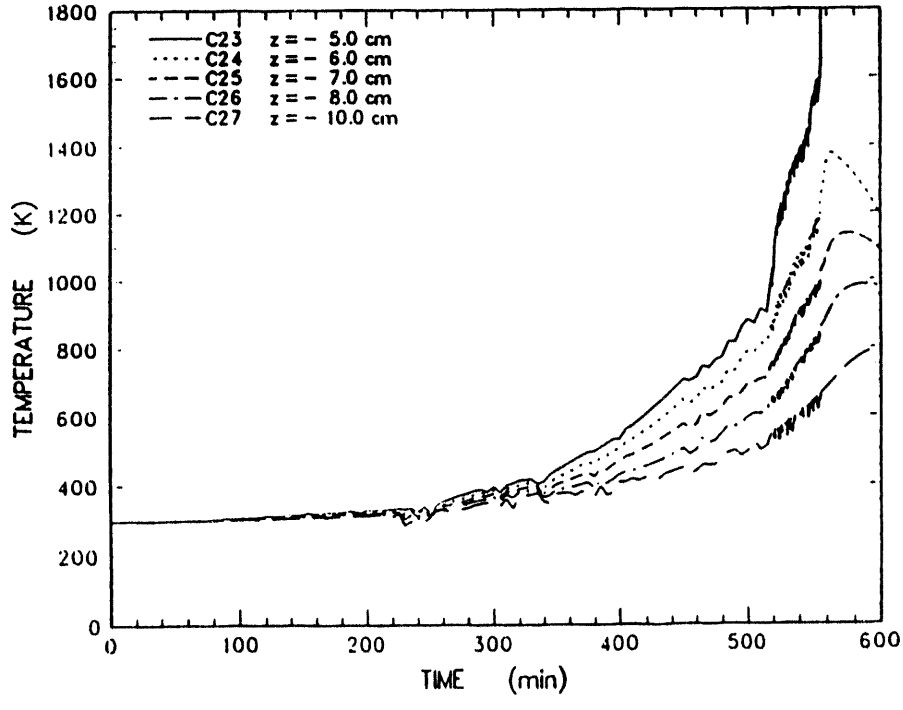

Figure C-6. Concrete temperature data measured by thermocouples located in the axial array between z = -5.0 and -10.0 cm

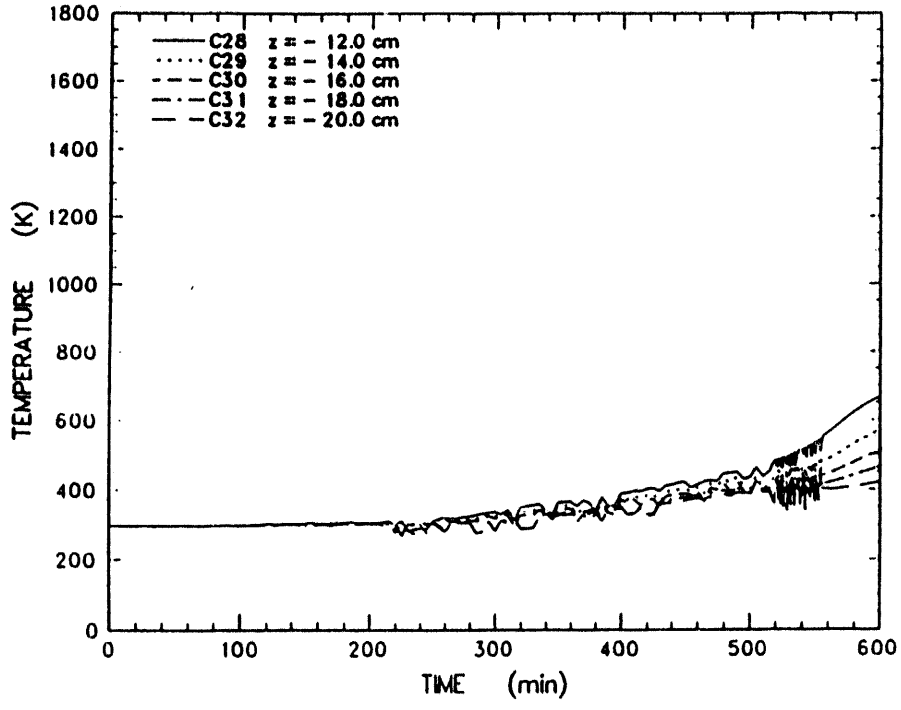

Figure C-7. Concrete temperature data measured by thermocouples located in the axial array between z = -12.0 and - 20.0 cm

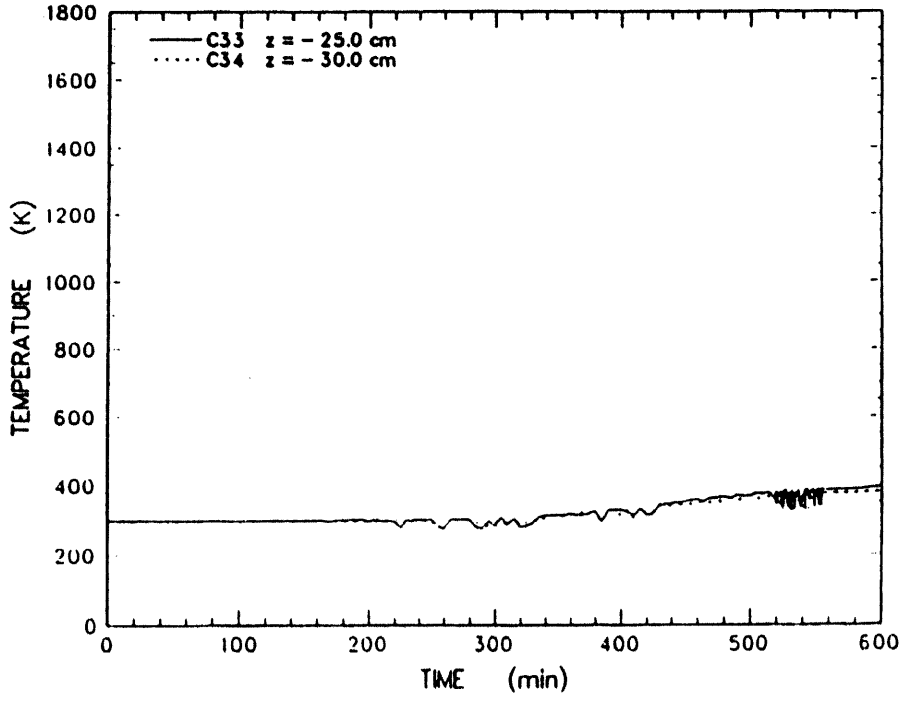

Figure C-8. Concrete temperature data measured by thermocouples located in the axial array between z = - 25.0 and - 30.0 cm

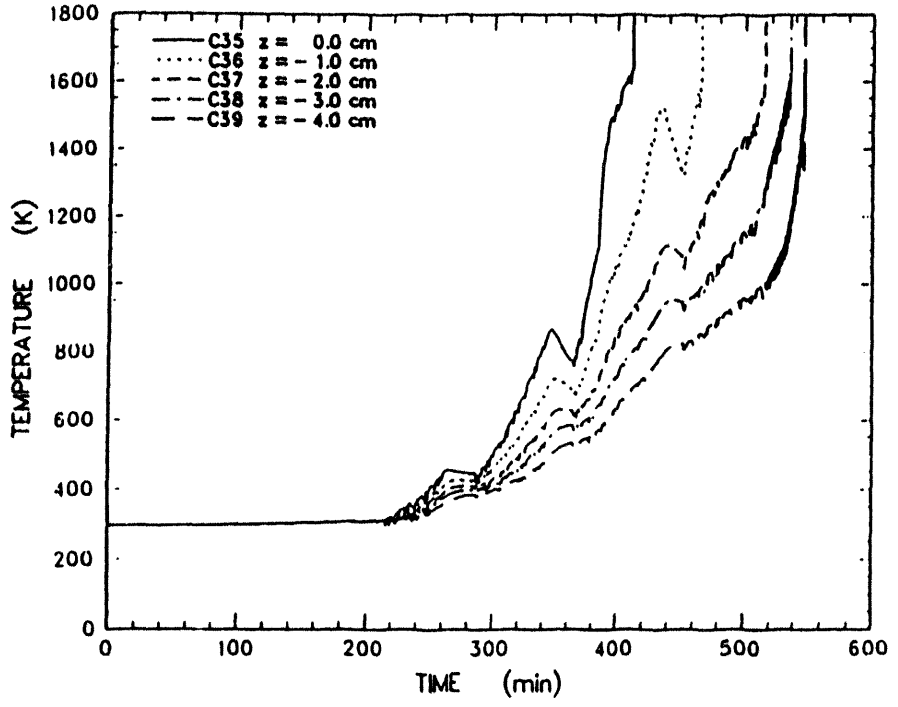

Figure C-9. Concrete temperature data measured by thermocouples located in the perimeter array between z = 0.0 and -4.0 cm

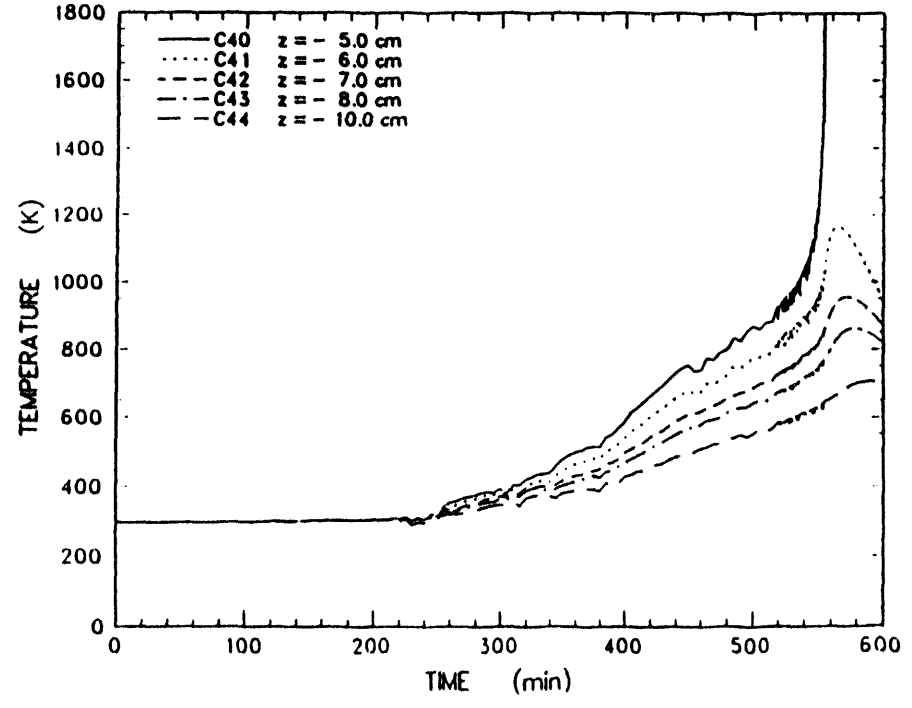

Figure C-10. Concrete temperature data measured by thermocouples located in the perimeter array between z = -5.0 and -10.0 cm

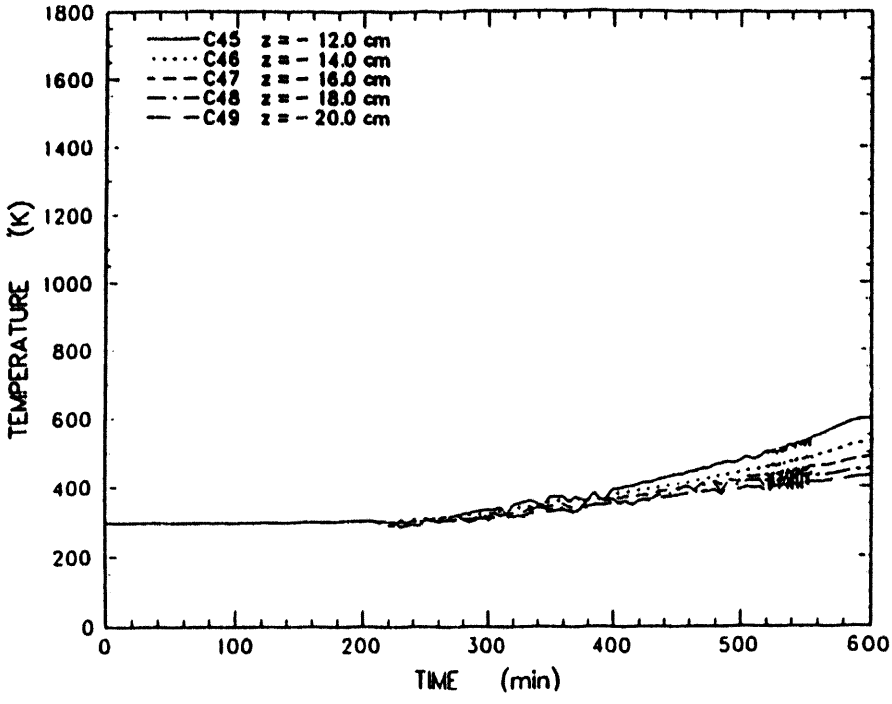

Figure C-11. Concrete temperature data measured by thermocouples located in the perimeter array between z = -12.0 and -20.0 cm

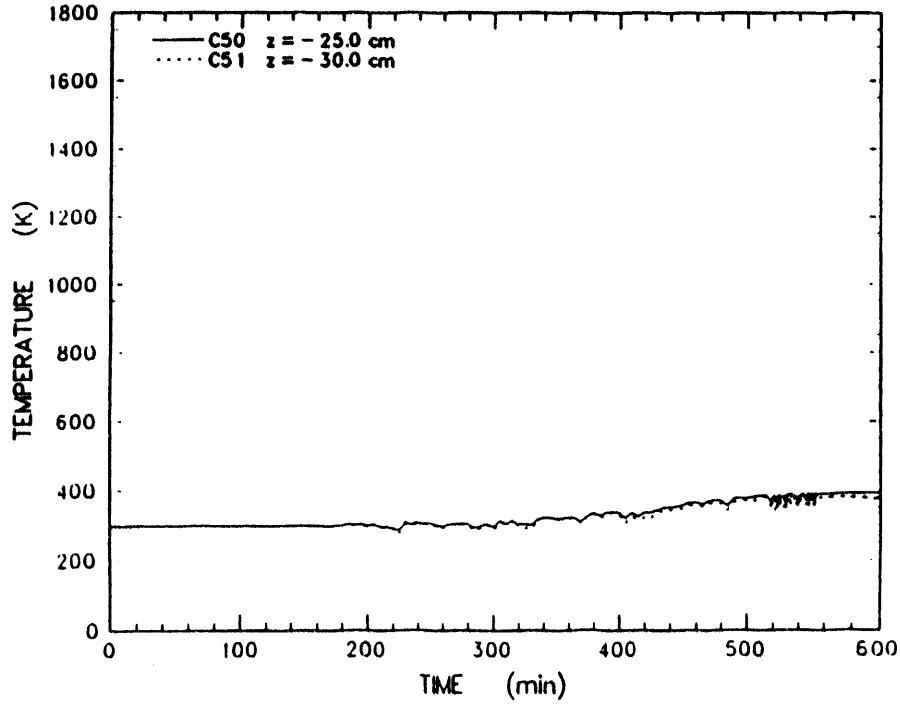

Figure C-12. Concrete temperature data measured by thermocouples located in the perimeter array between z = -25.0 and -30.0 cm

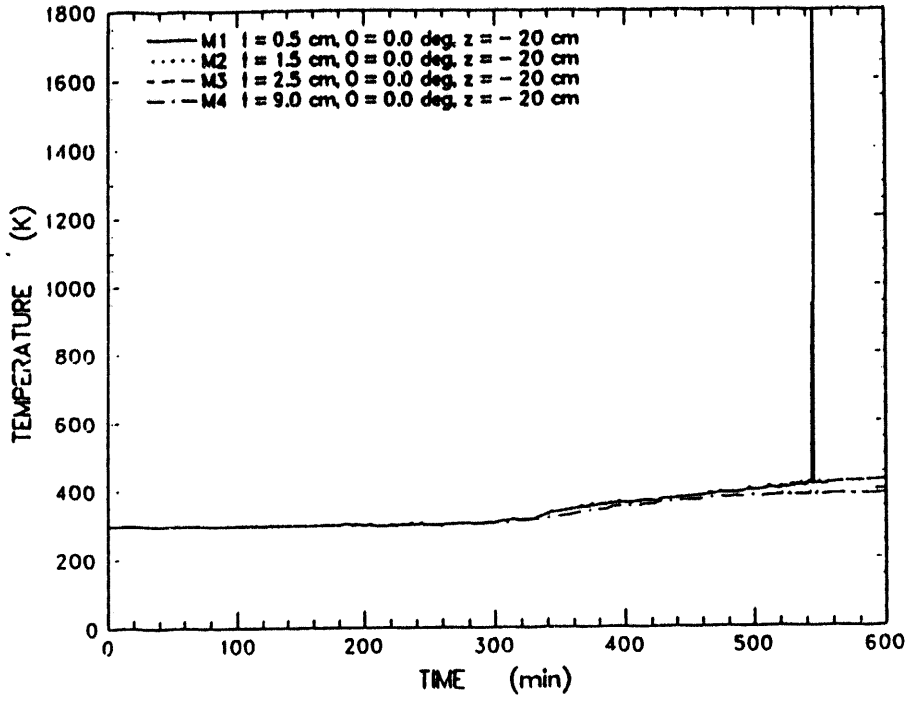

Figure C-13. MgO sidewall temperature data measured by thermocouples in the array located at z = - 20.0 cm

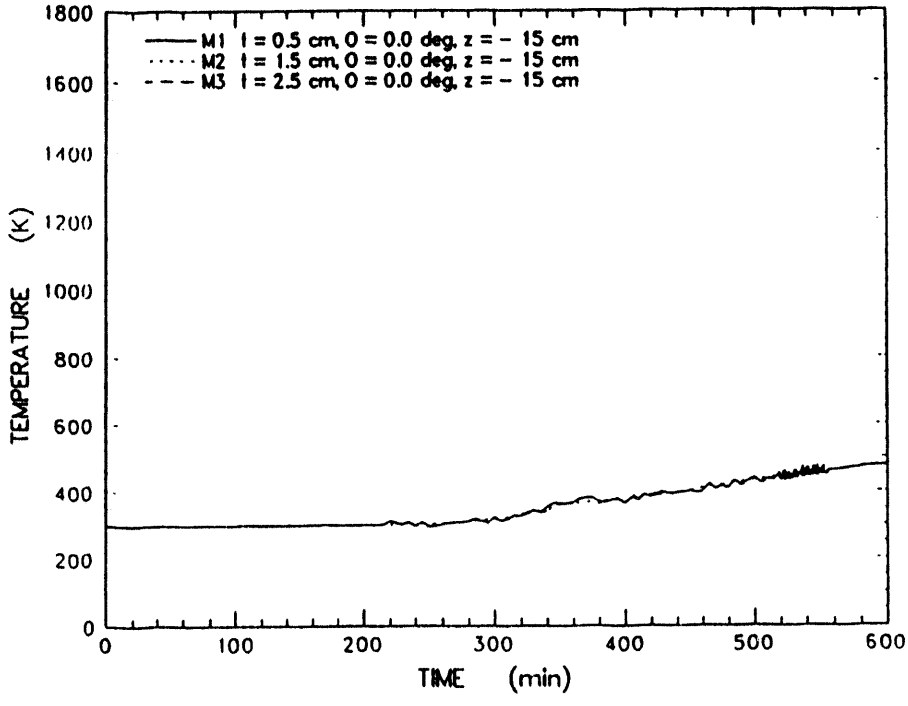

Figure C-14. MgO sidewall temperature data measured by thermocouples in the array located at z = - 15.0 cm

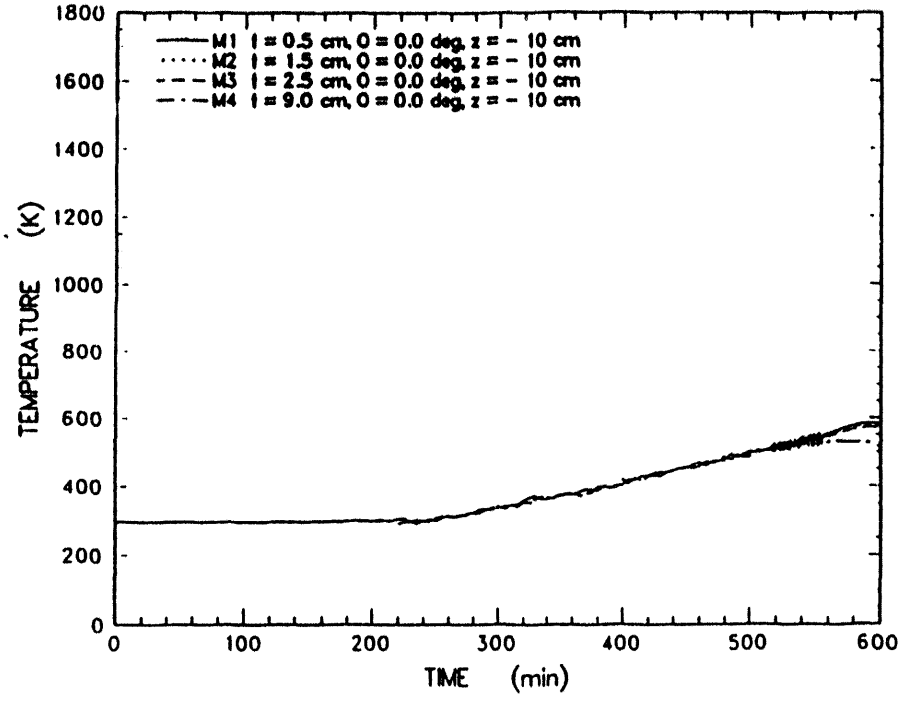

Figure C-15. MgO sidewall temperature data measured by thermocouples in the array located at z = - 10.0 cm

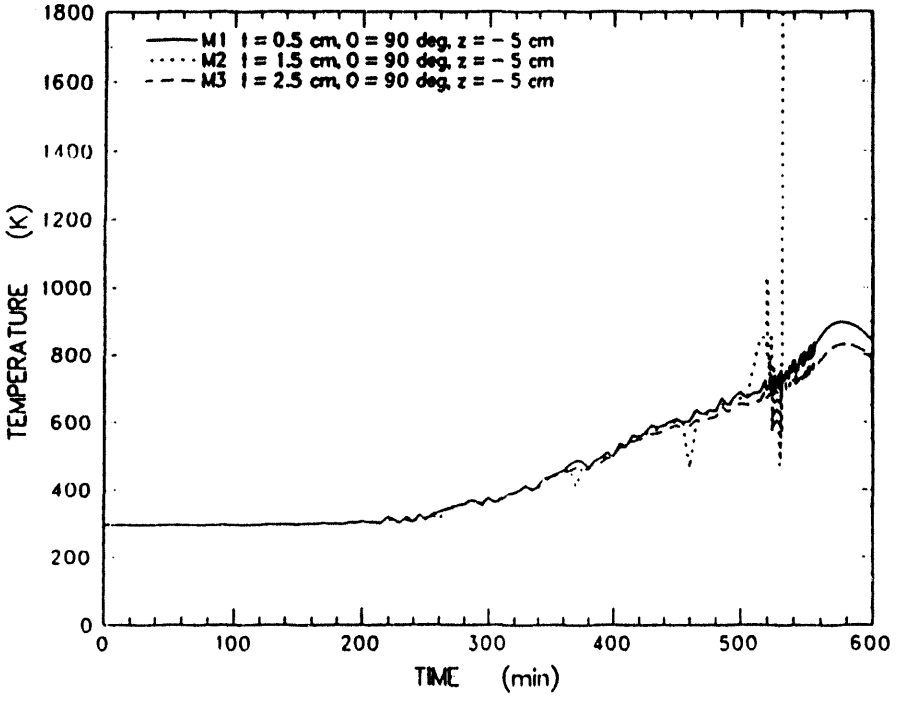

Figure C-16. MgO sidewall temperature data measured by thermocouples in the array located at z = - 5.0 cm

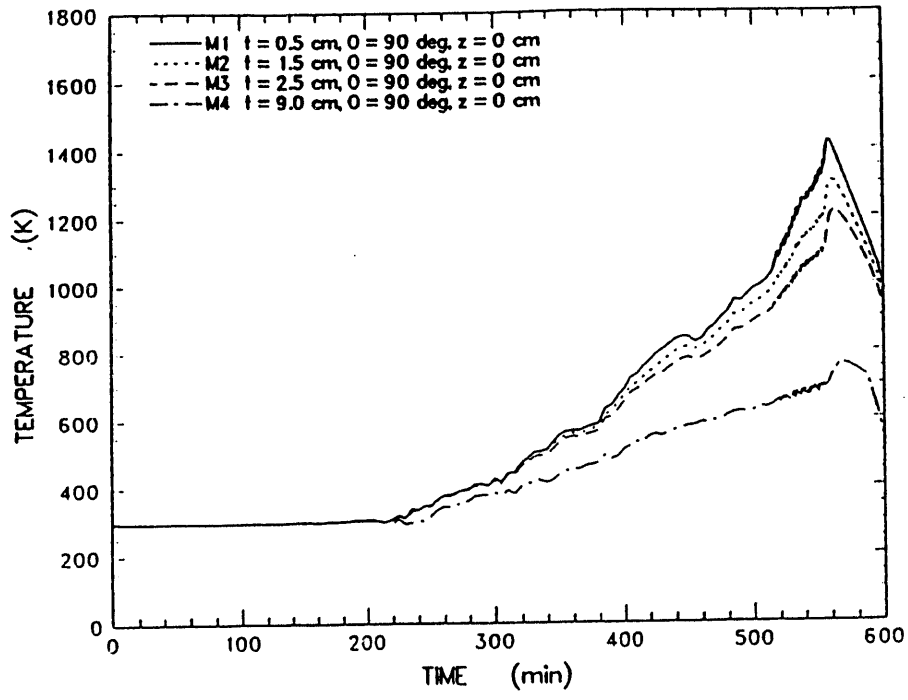

Figure C-17. MgO sidewall temperature data measured by thermocouples in the array located at z = + 0.0 cm

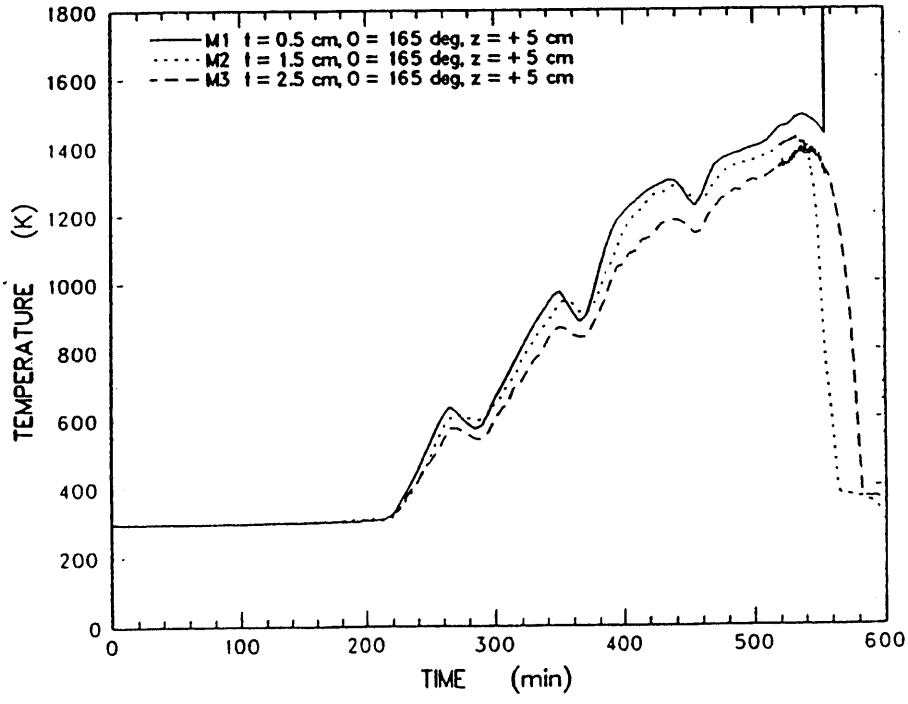

Figure C-18. MgO sidewall temperature data measured by thermocouples in the array located at z = + 5.0 cm

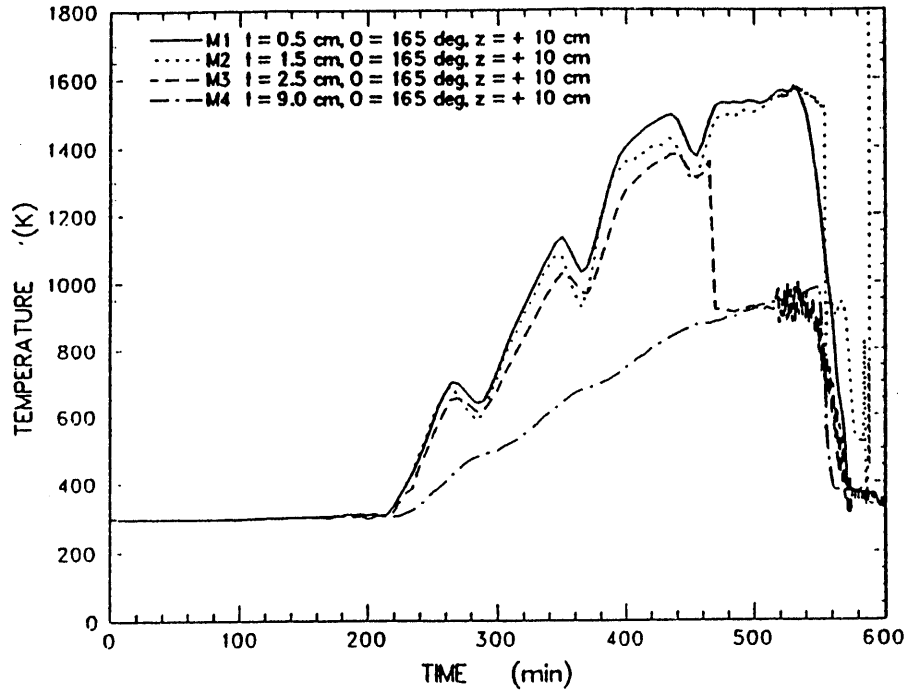

Figure C-19. MgO sidewall temperature data measured by thermocouples in the array located at z = + 10.0 cm

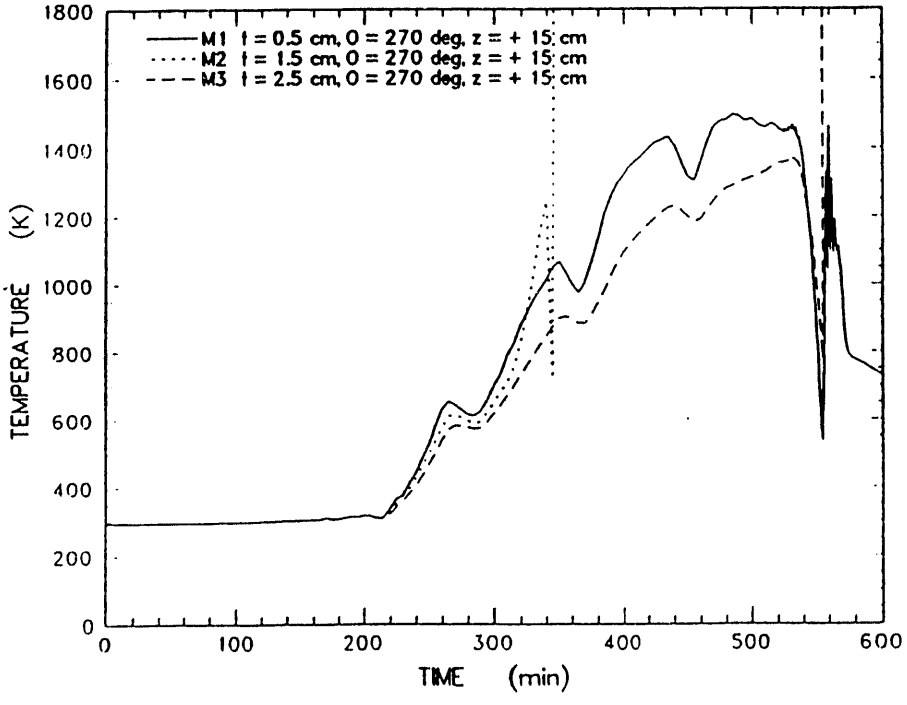

Figure C-20. MgO sidewall temperature data measured by thermocouples in the array located at z = + 15.0 cm

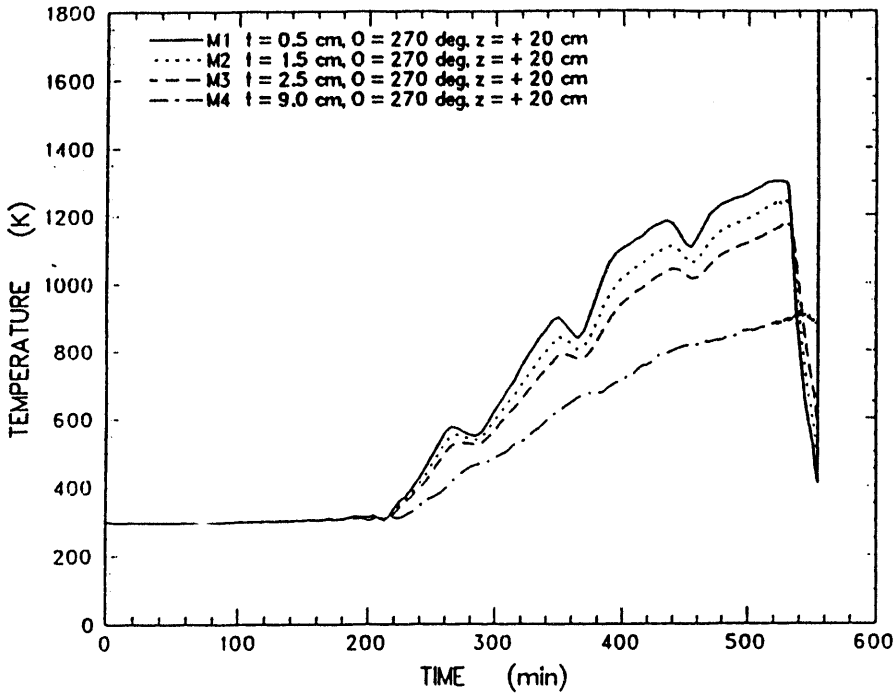

Figure C-21. MgO sidewall temperature data measured by thermocouples in the array located at z = + 20.0 cm

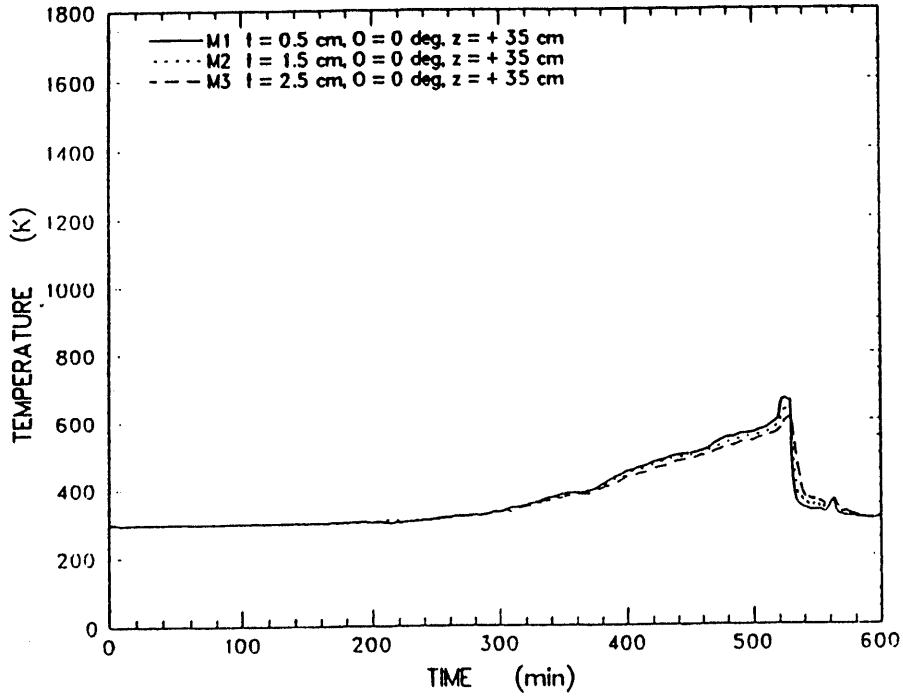

Figure C-22. MgO sidewall temperature data measured by thermocouples in the array located at z = + 35.0 cm

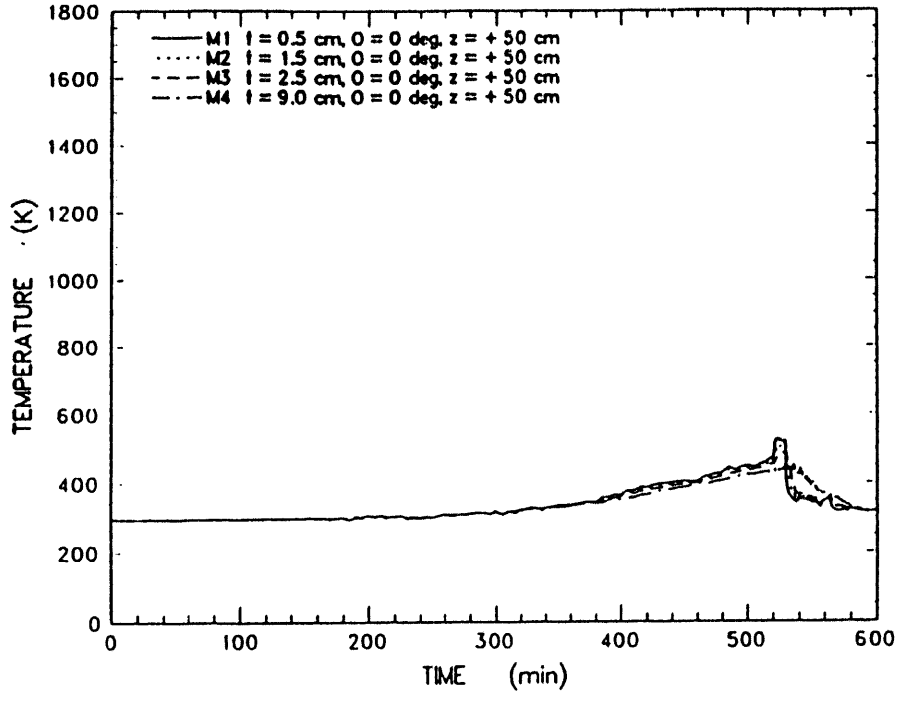

Figure C-23. MgO sidewall temperature data measured by thermocouples in the array located at z = +50.0 cm

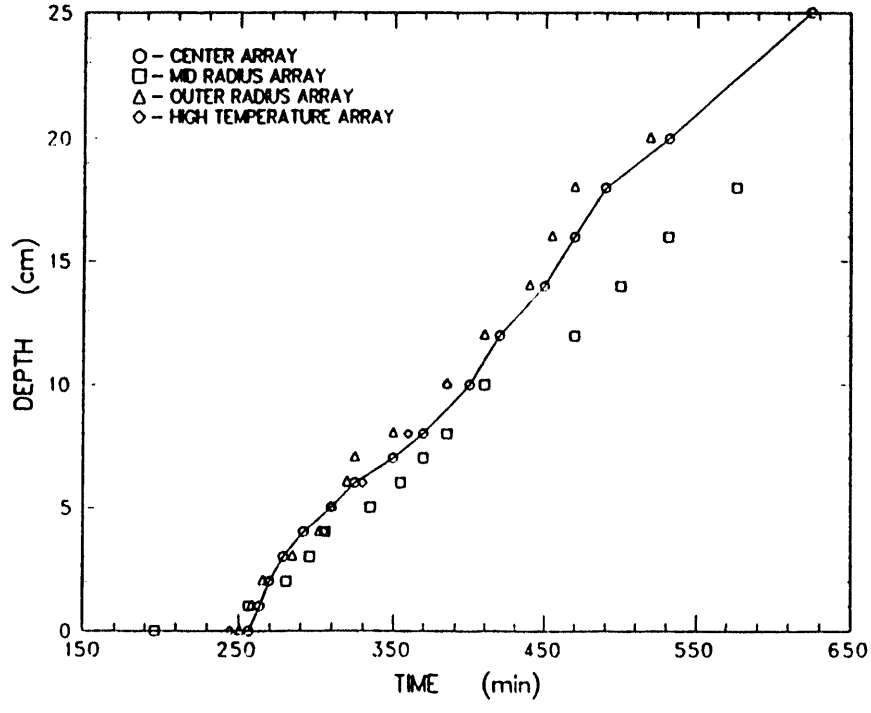

Figure C-24. Position of the 400 K isotherm plotted as a function of time

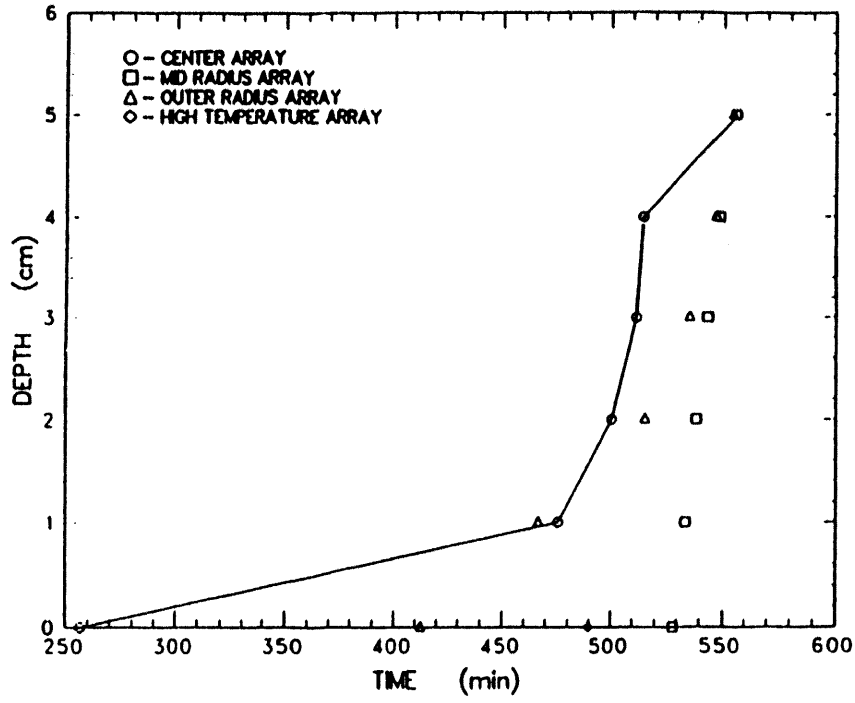

Figure C-25. Position of the concrete erosion front plotted as a function of time

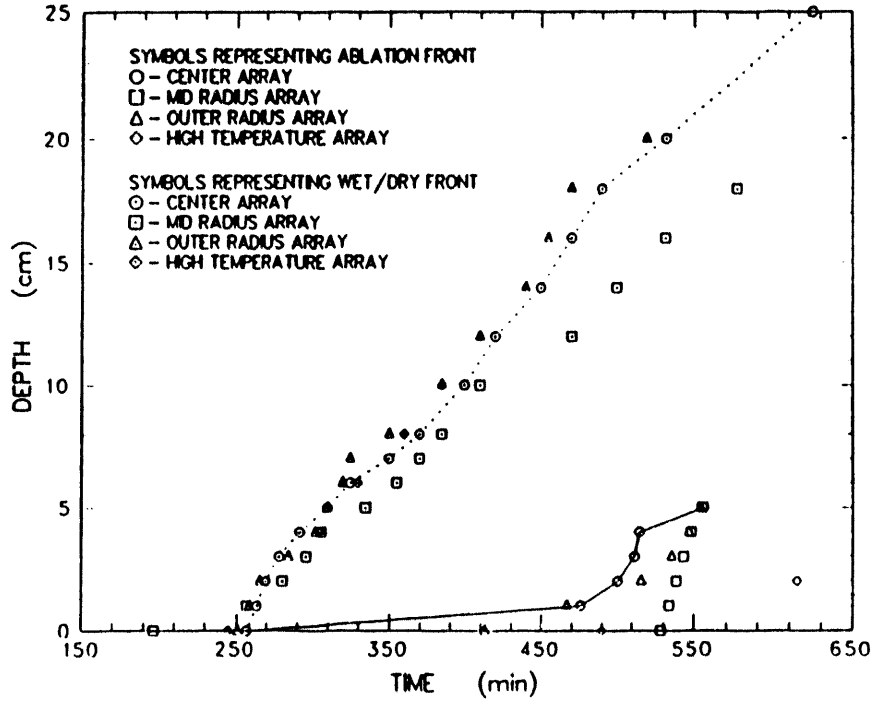

Figure C-26. Comparison of the position of the 400 K isotherm and the concrete erosion front

Appendix D: Charge, Concrete and Tungsten Sleeve Susceptor Temperature Data

Temperature data are presented in this appendix for the oxide charge, concrete melt front, tungsten sleeve susceptors and MgO castable temperatures adjacent to the tungsten susceptors.

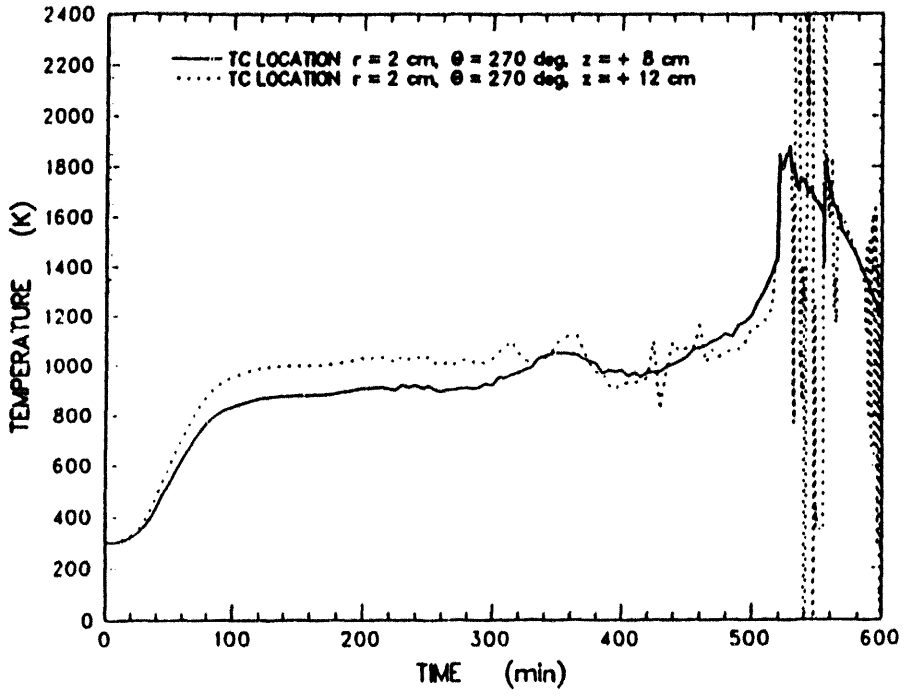

Figure D-1. Charge temperature measured by C type thermocouples installed in a tungsten thermowell at r = 2 cm

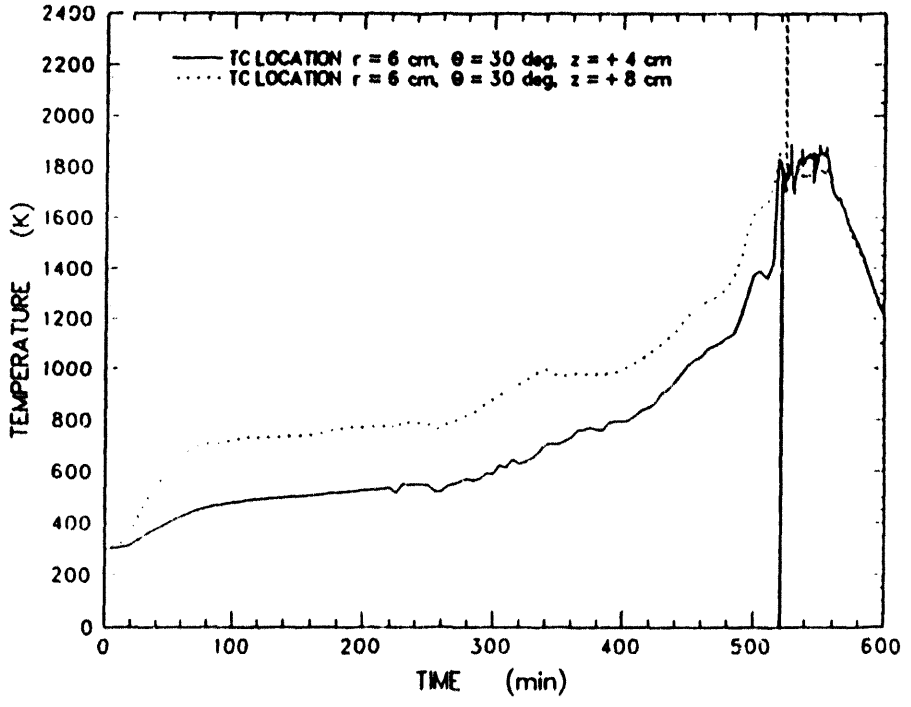

Figure D-2. Charge temperature measured by C type thermocouples installed in a tungsten thermowell at r = 6 cm

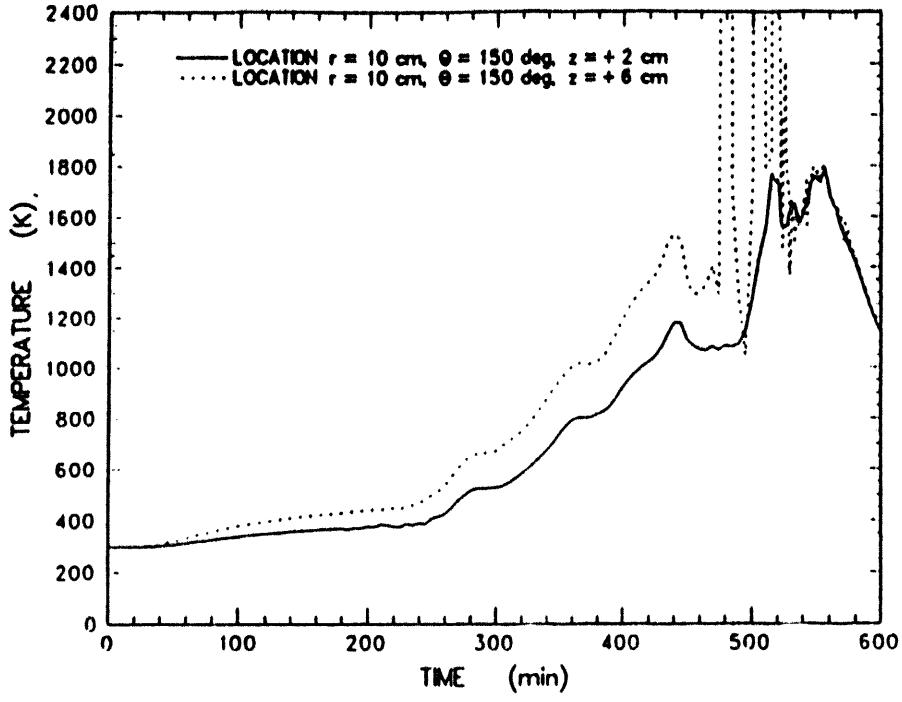

Figure D-3. Charge temperature measured by C type thermocouples installed in a tungsten thermowell at r = 10 cm

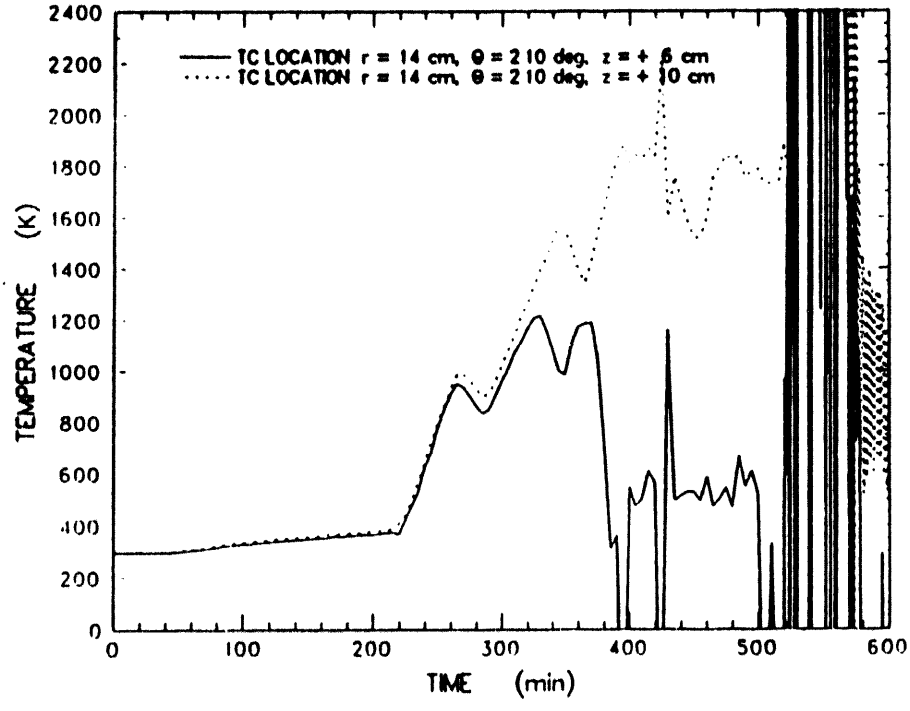

Figure D-4. Charge temperature measured by C type thermocouples installed in a tungsten thermowell at r = 14 cm

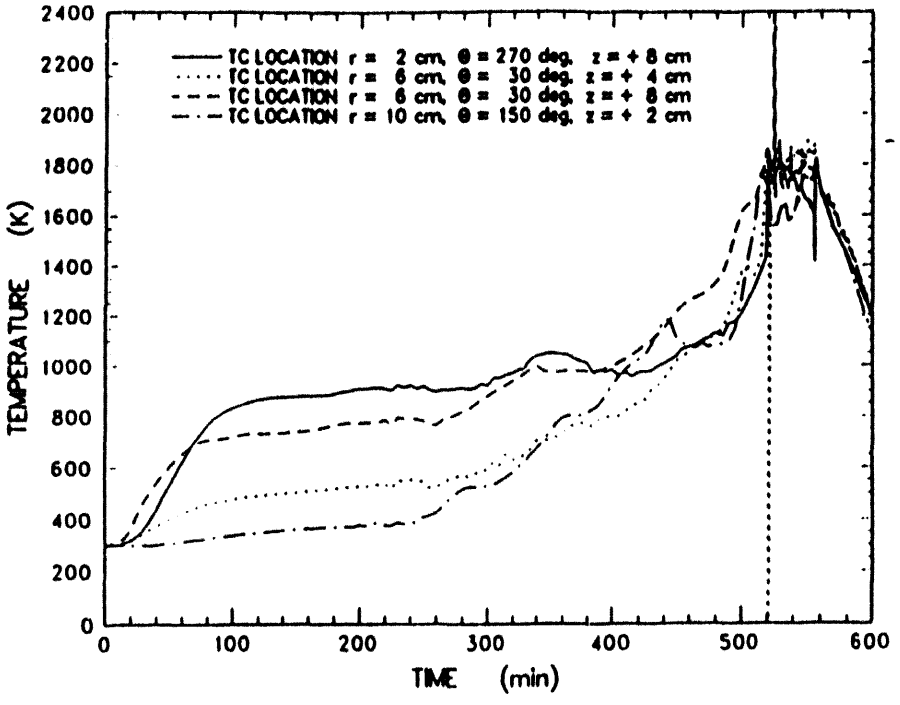

Figure D-5. Composite of charge temperatures measured by C type thermocouples installed in selected tungsten thermowells at r = 2, 6, and 10 cm

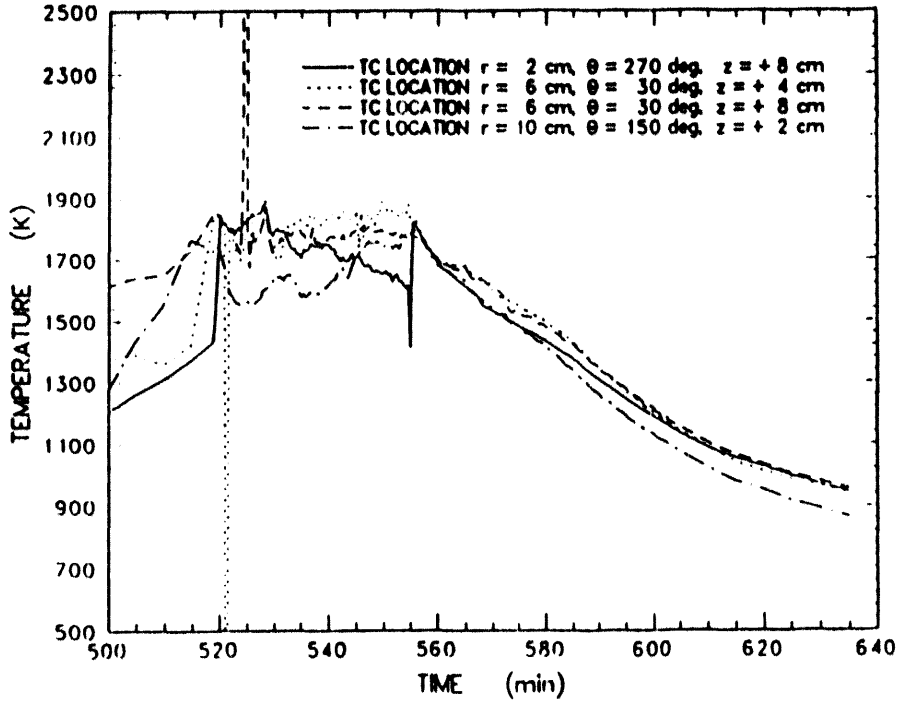

Figure D-6. Composite expansion of charge temperatures measured by C type thermocouples installed in selected tungsten thermowells at r = 2, 6, and 10 cm

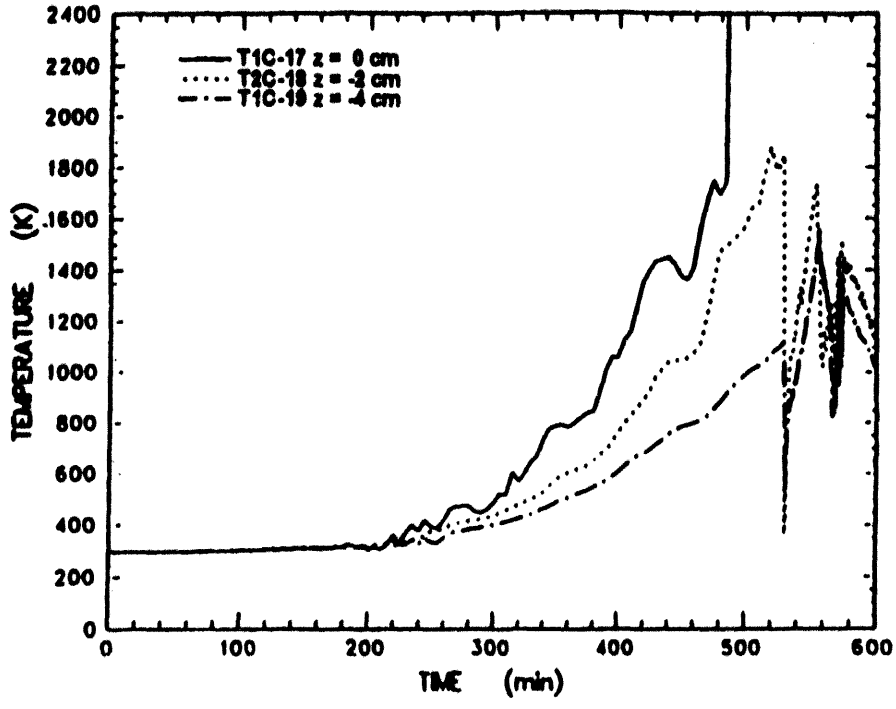

Figure D-7. Melt temperature measured by type C thermocouples installed into alumina protection tube at z = 0, -2, and -4 cm

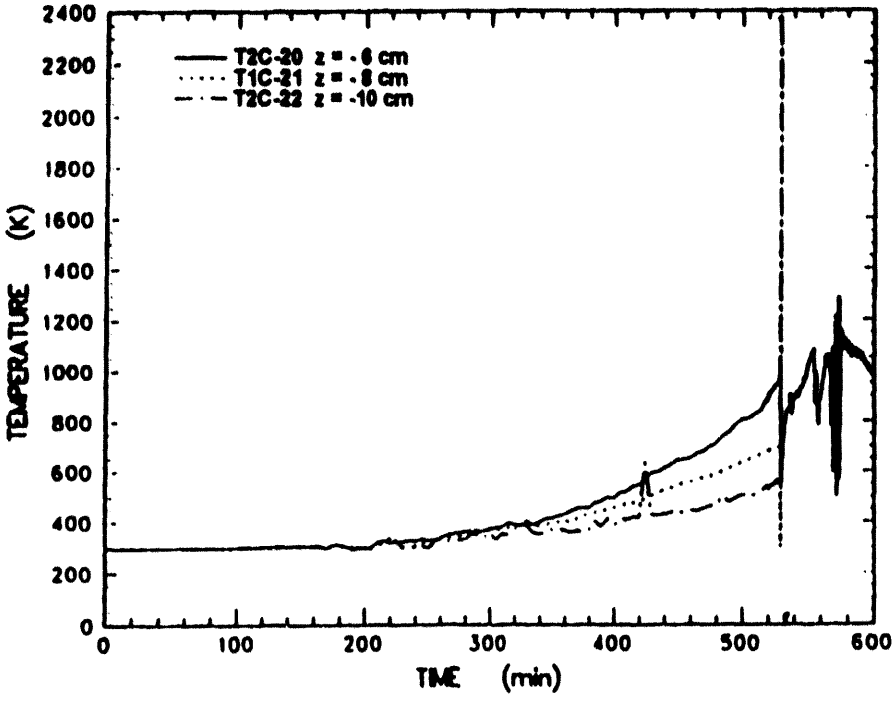

Figure D-8. Melt temperature measured by type C thermocouples installed into alumina protection tube at z = -6, -8, and -10 cm

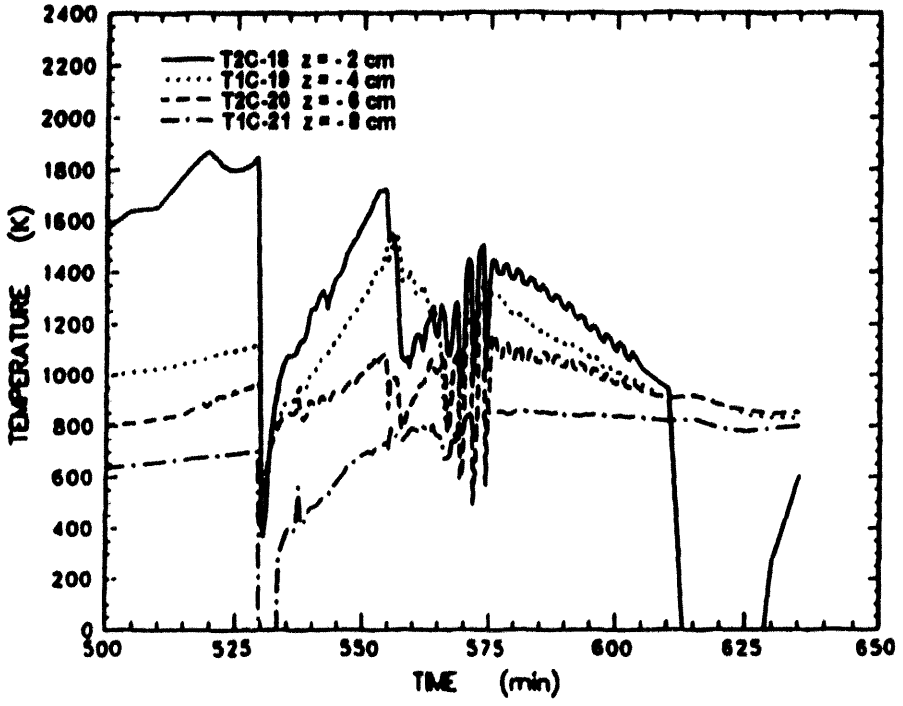

Figure D-9. Expansion of melt temperature measured by type C thermocouples installed into alumina protection tube at z = -2, -4, -6 and -8 cm

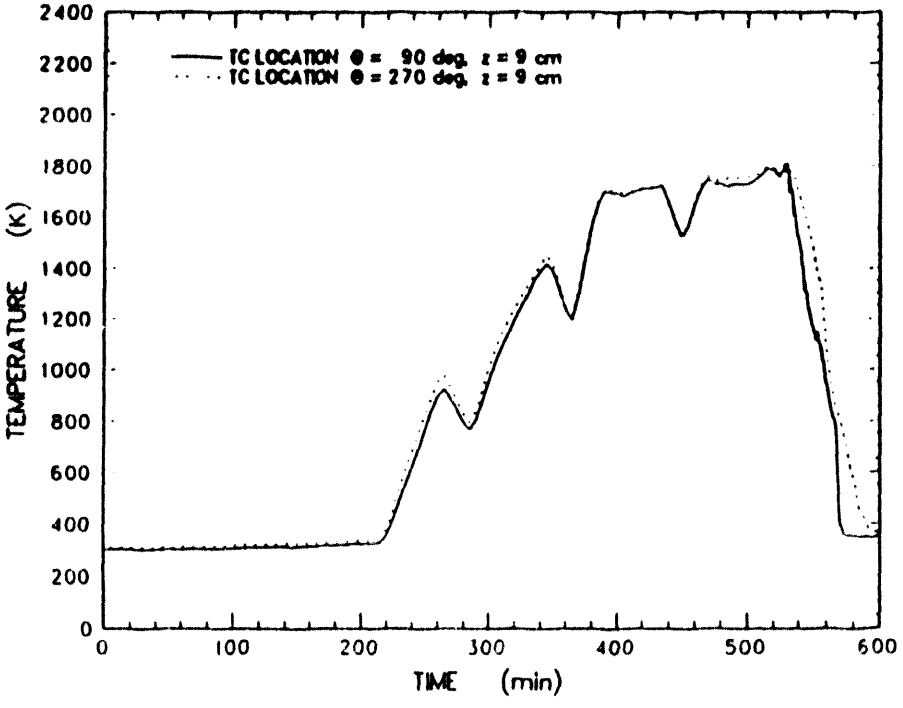

Figure D-10. Temperature of the tungsten sleeve susceptors measured by type K thermocouples installed between the sleeves

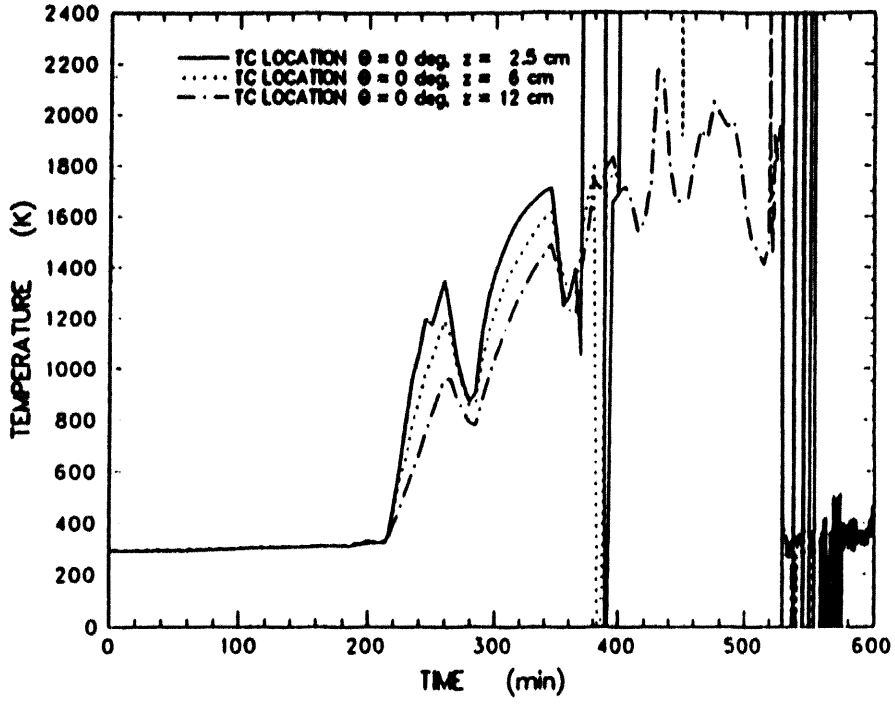

Figure D-11. Temperature of the MgO castable placed between the susceptor sleeves and cavity sidewall at J = 0

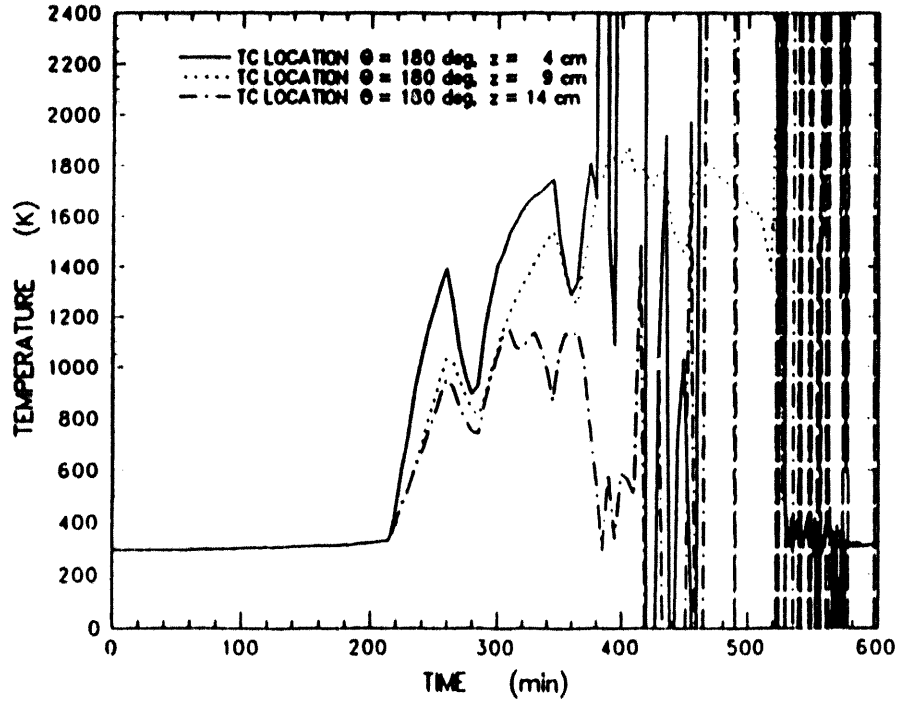

Figure D-12. Temperature of the MgO castable placed between the susceptor sleeves and cavity sidewall at J = 180

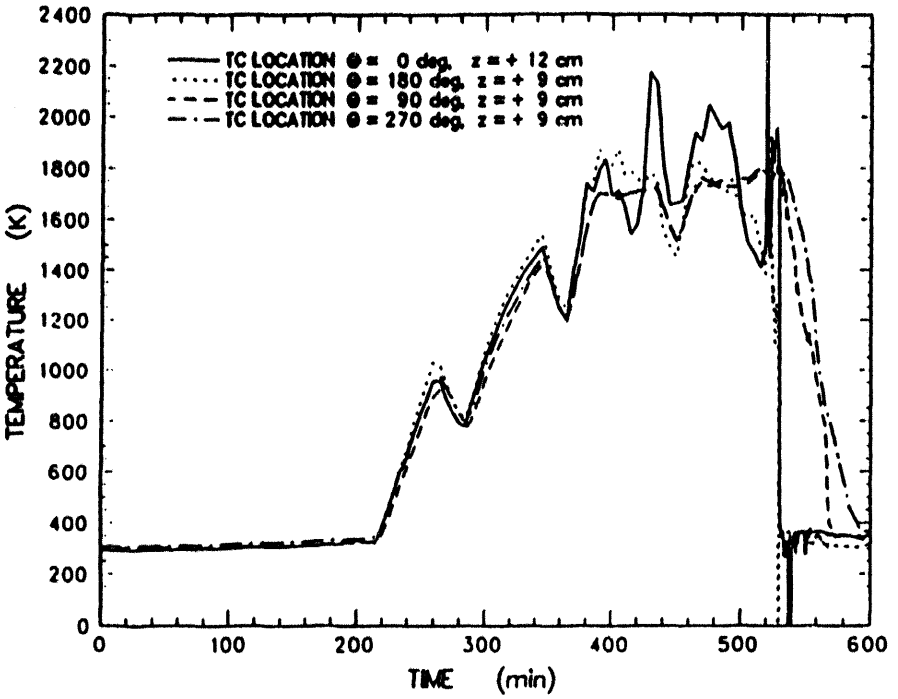

Figure D-13. Temperature of the MgO castable placed between the susceptor sleeves and cavity sidewall at J = 0, 90, 180, and 270

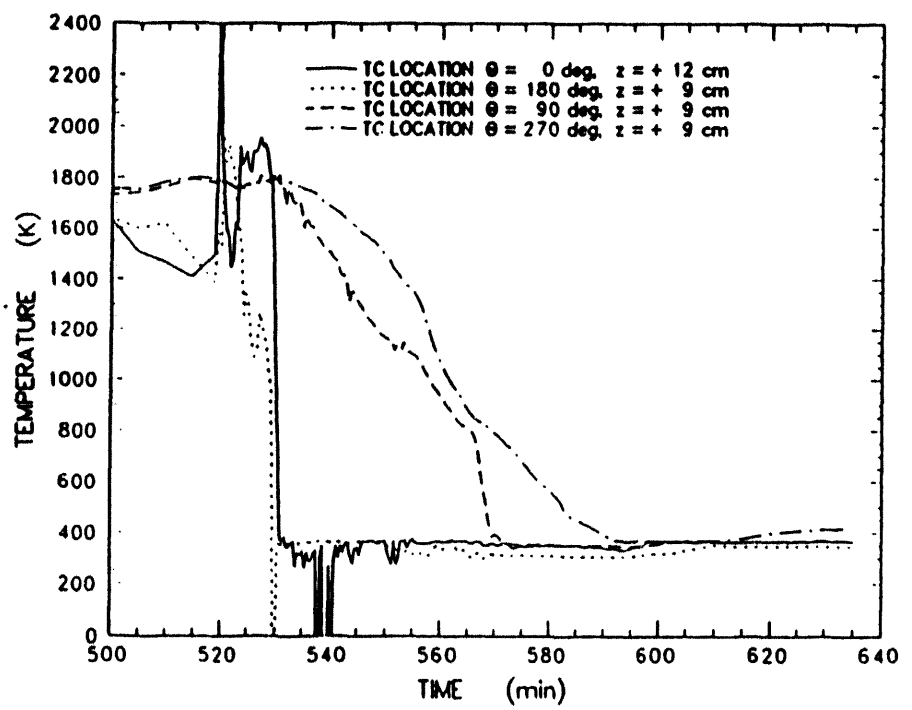

Figure D-14. Expansion of the temperature measured in the MgO castable placed between the susceptor sleeves and cavity sidewall at J = 0, 90, 180, and 270

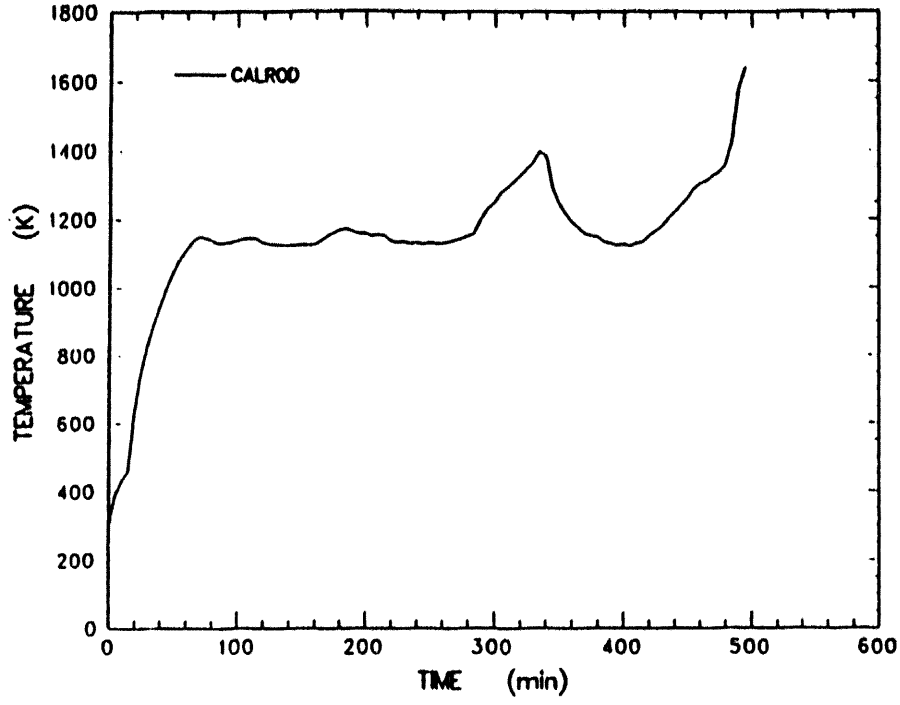

Figure D-15. Voltage history for calrod used to heat the center of the charge

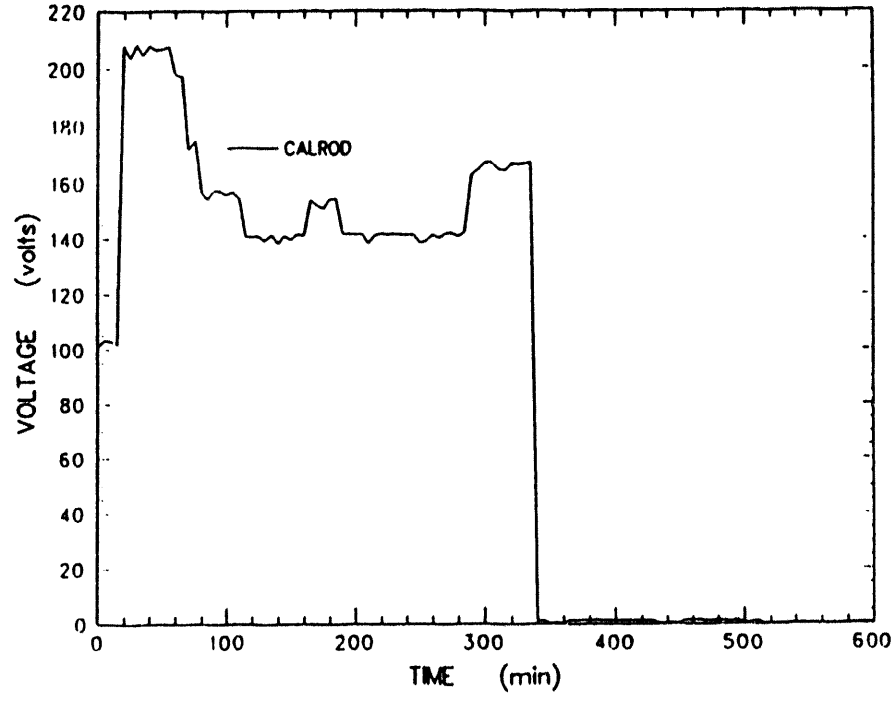

Figure D-16. Temperature history of the calrod heater

Appendix E: Calculated Sidewall Heat Flux Data

Presented in this appendix are sidewall heat fluxes calculated using an inverse heat conduction code. Calculations were made based on temperature data produced from type-K thermocouple arrays imbedded in the MgO annulus at various elevations.

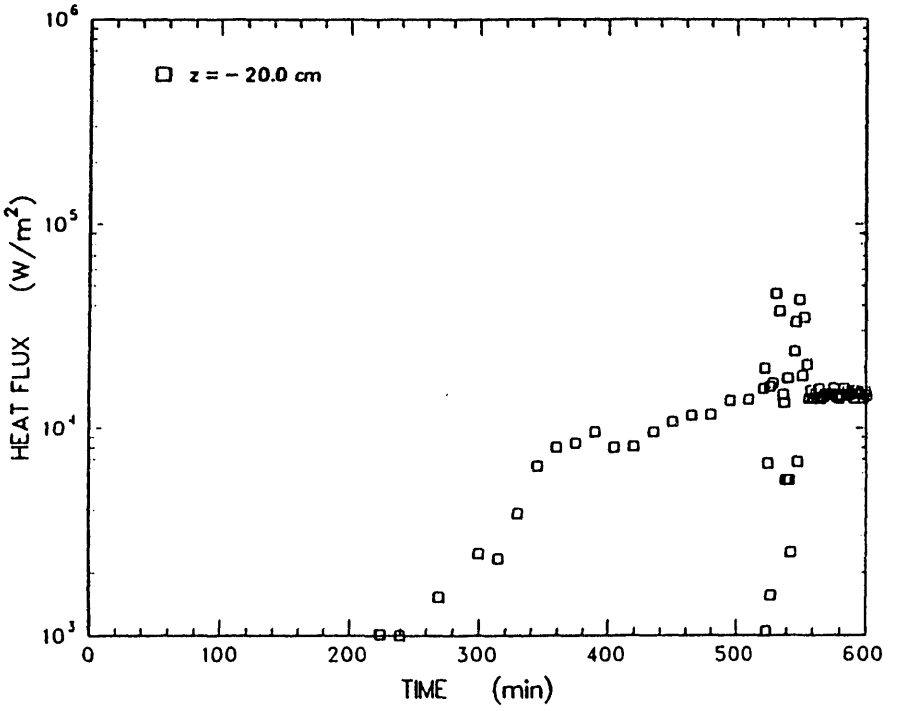

Figure E-1. MgO sidewall heat flux calculated from thermocouple data for the array located at z = - 20 cm

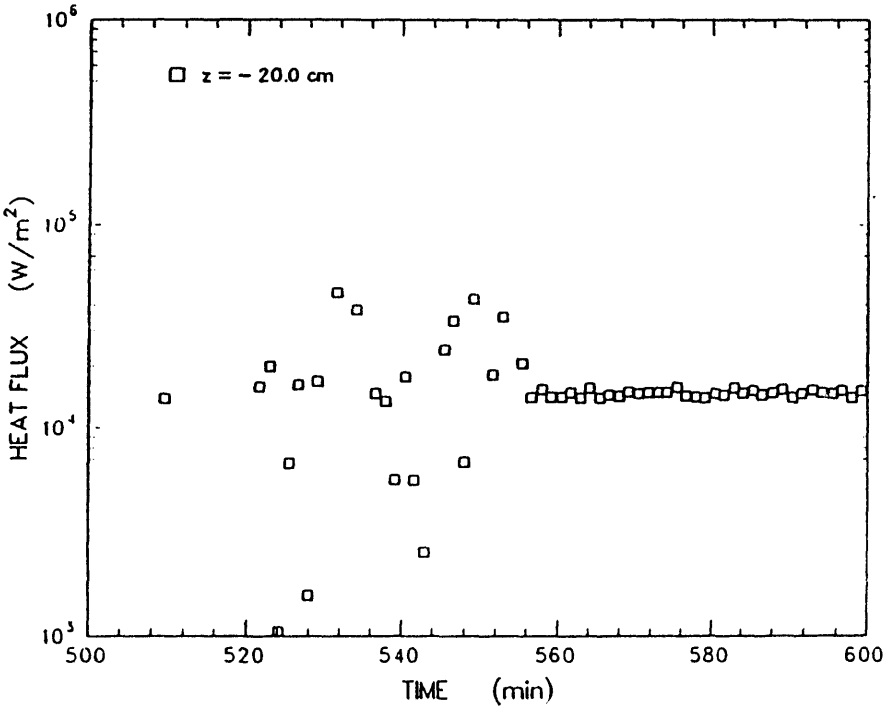

Figure E-2. Expansion of MgO sidewall heat flux data calculated for the array located at z = - 20 cm

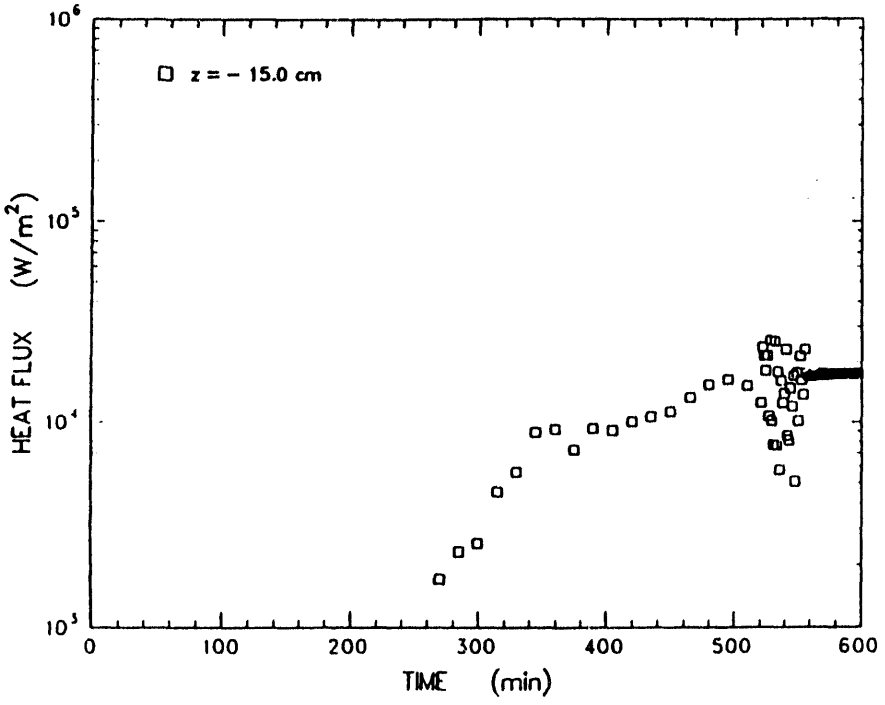

Figure E-3. MgO sidewall heat flux calculated from thermocouple data for the array located at z = -15 cm

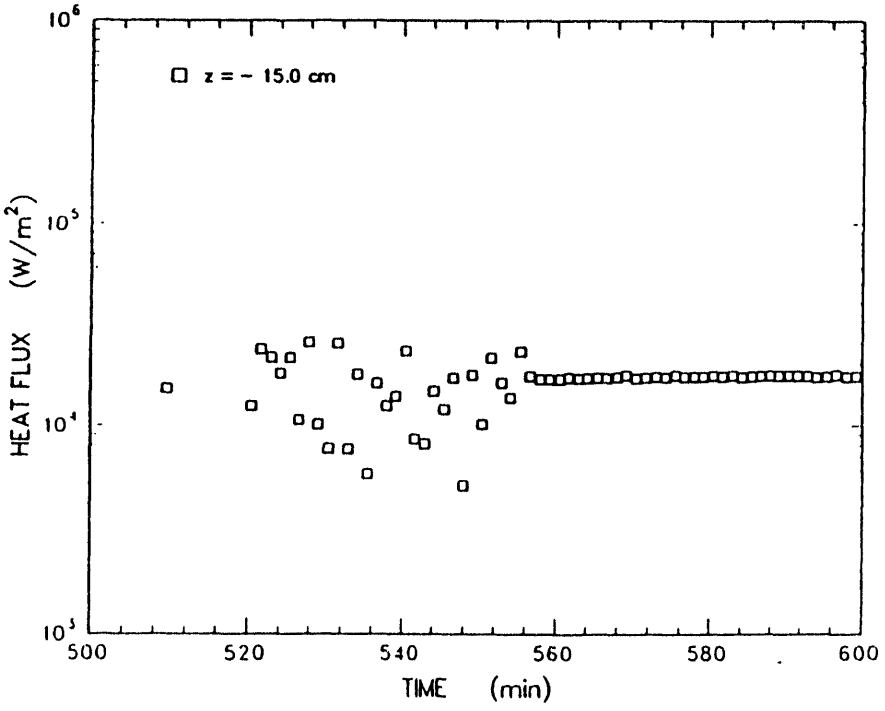

Figure E-4. Expansion of MgO sidewall heat flux calculated for the array located at z = -15 cm

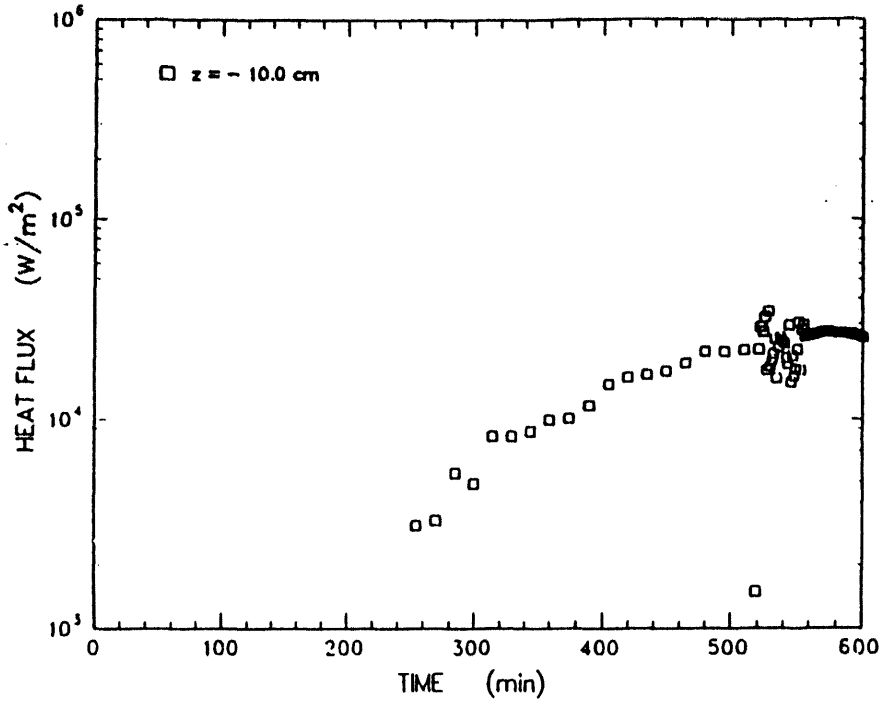

Figure E-5. MgO sidewall heat flux calculated from thermocouple data for the array located at z = - 10 cm

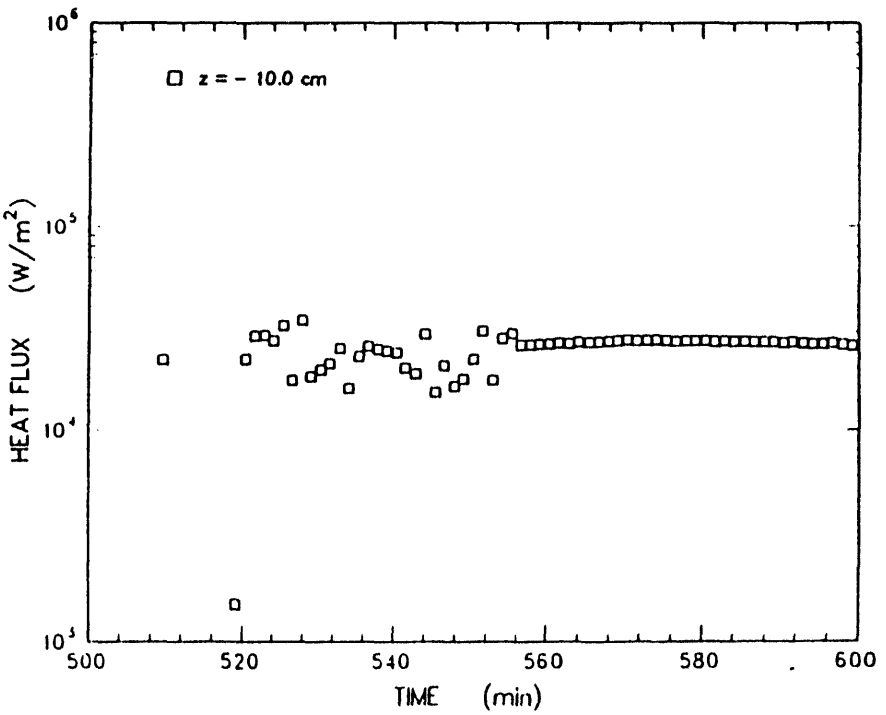

Figure E-6. Expansion of MgO sidewall heat flux data calculated for the array located at z - 10 cm

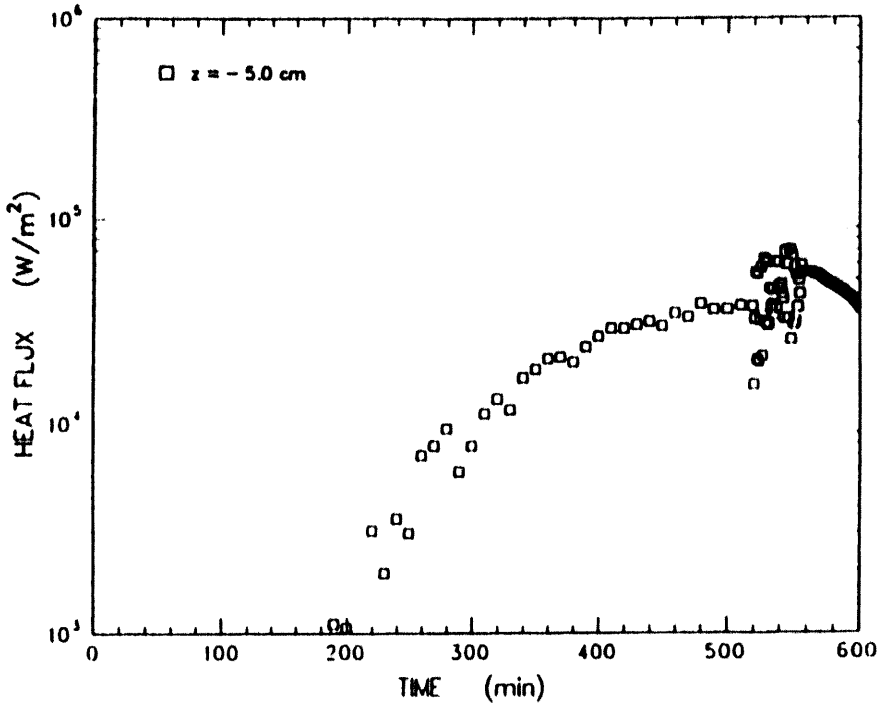

Figure E-7. MgO sidewall heat flux calculated from thermocouple data for the array located at z = -5 cm

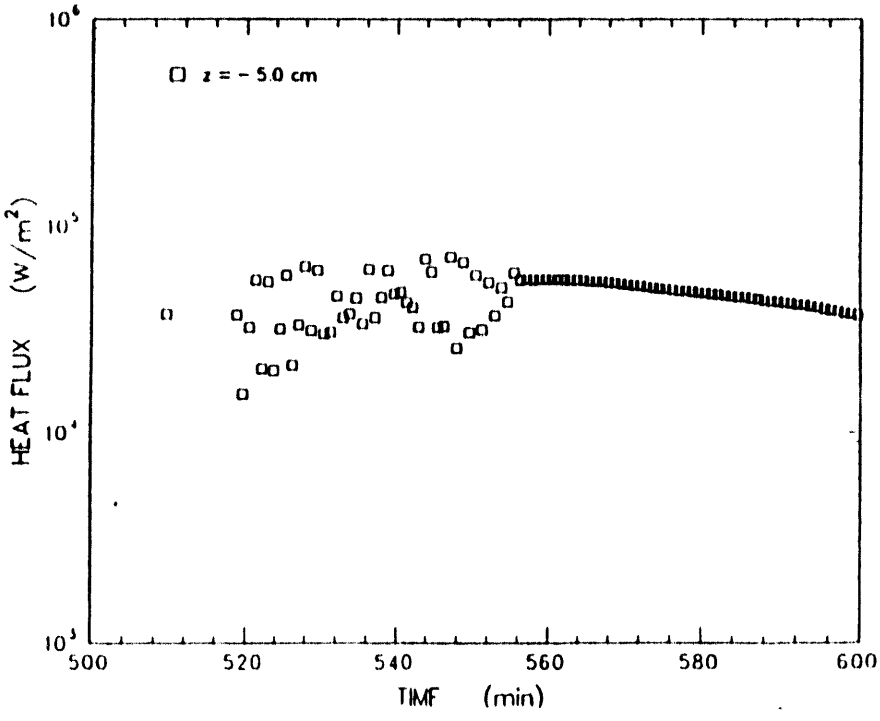

Figure E-8. Expansion of MgO sidewall heat flux data calculated for the array located at z = - 5 cm

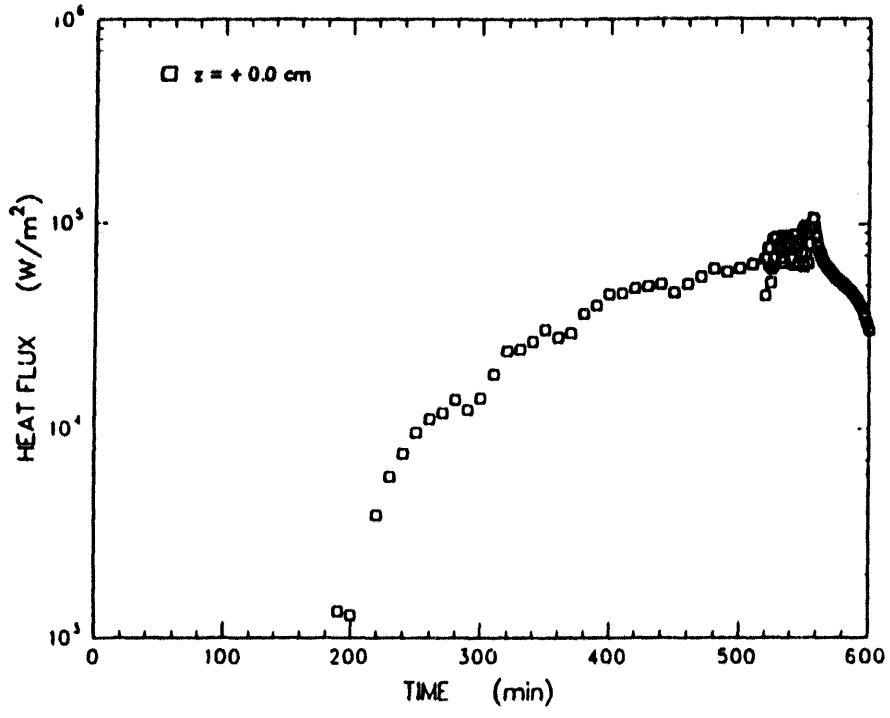

Figure E-9. MgO sidewall heat flux calculated from thermocouple data for the array located at z = 0 cm

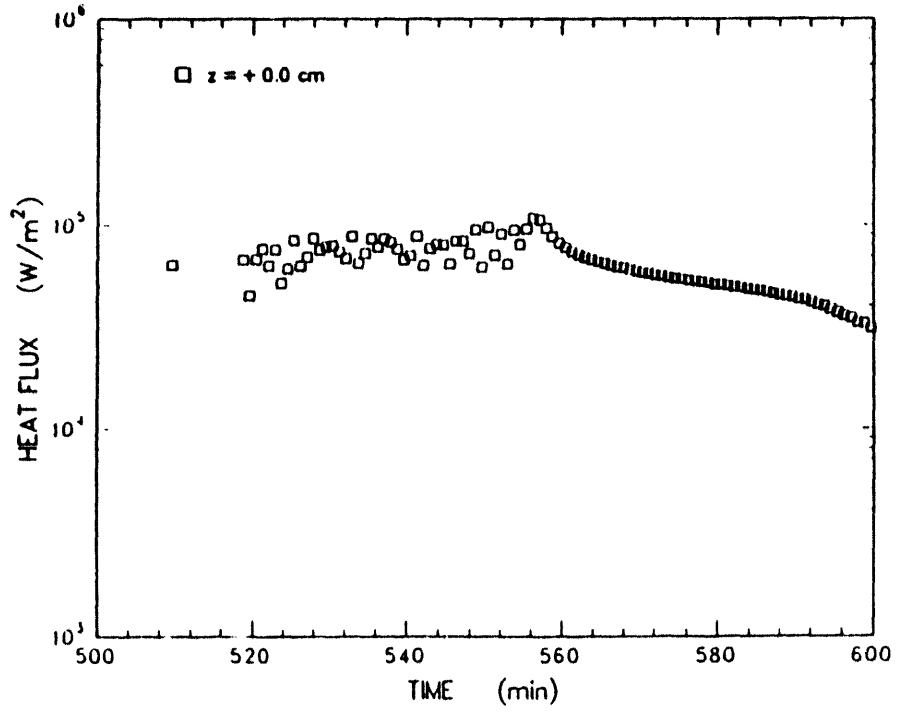

Figure E-10. Expansion of MgO sidewall heat flux data calculated for the array located at z = 0 cm

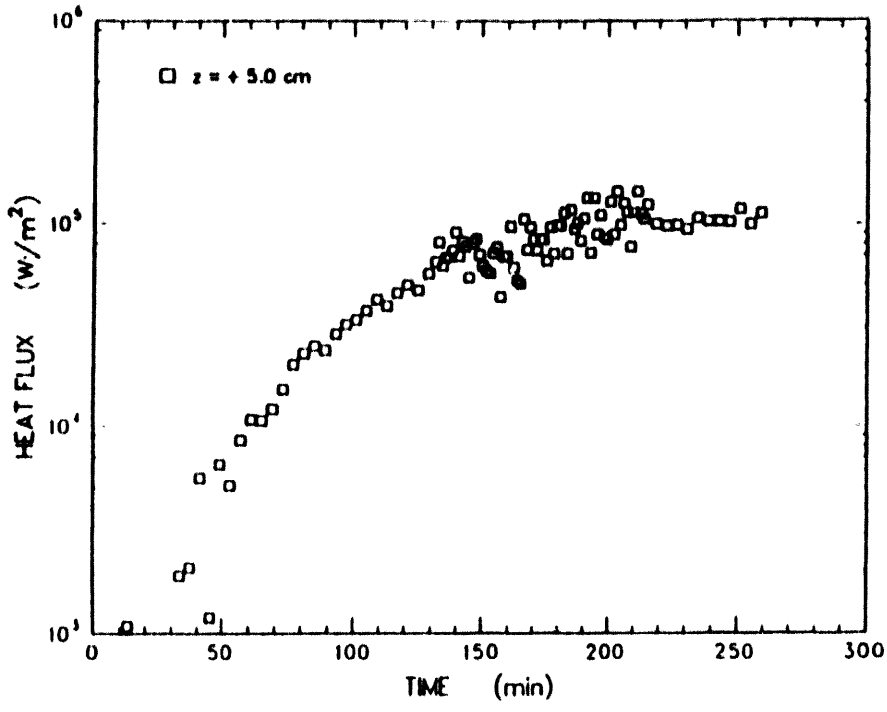

Figure E-11. MgO sidewall heat flux calculated from thermocouple data for the array located at z = + 5 cm

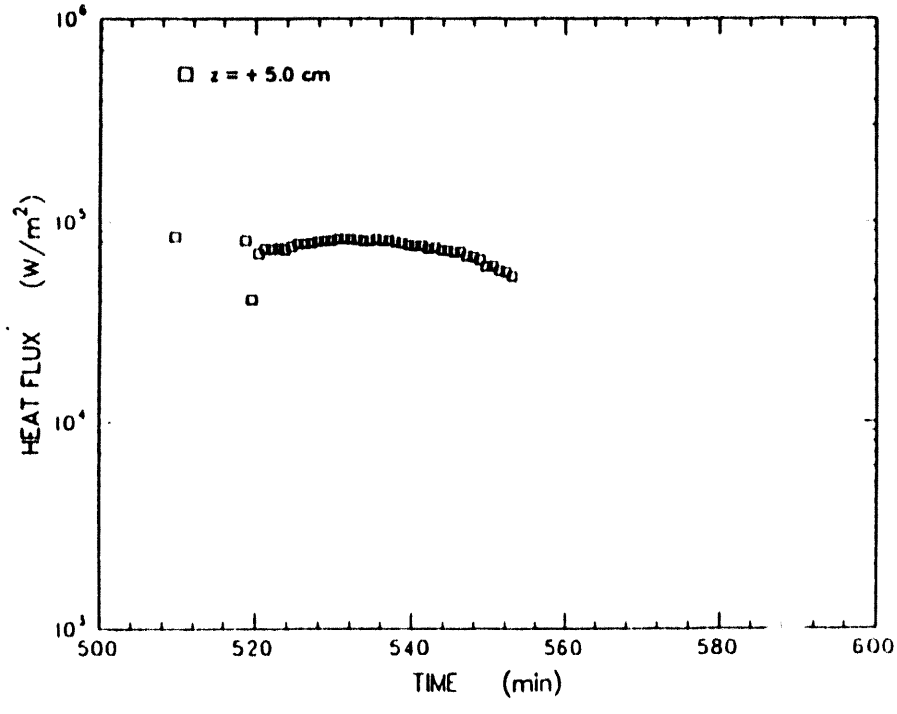

Figure E-12. Expansion of MgO sidewall heat flux data calculated for the array located at z = + 5 cm

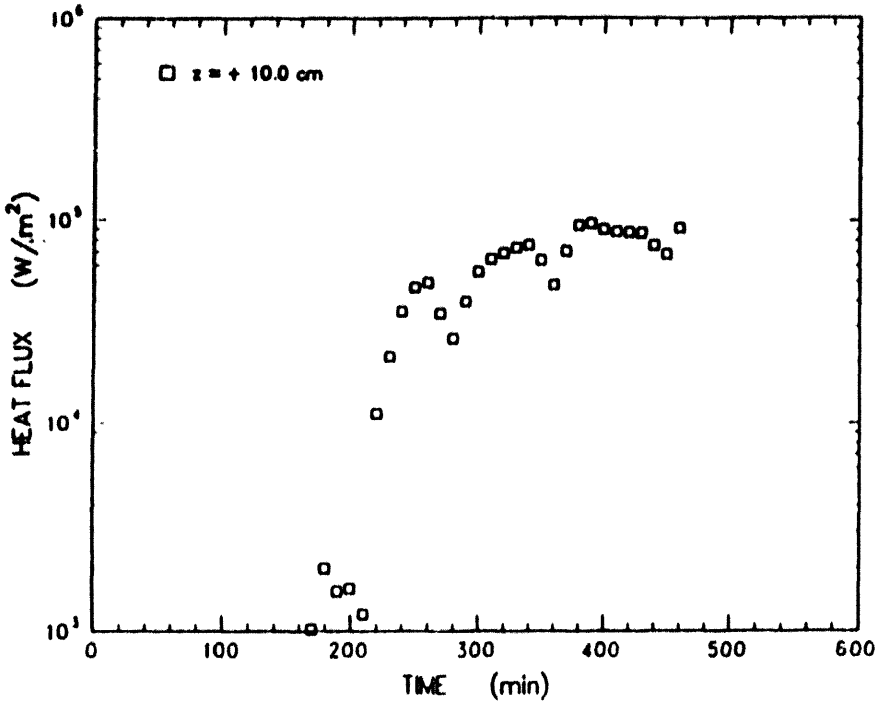

Figure E-13. MgO sidewall heat flux calculated from thermocouple data for the array located a z = + 10 cm

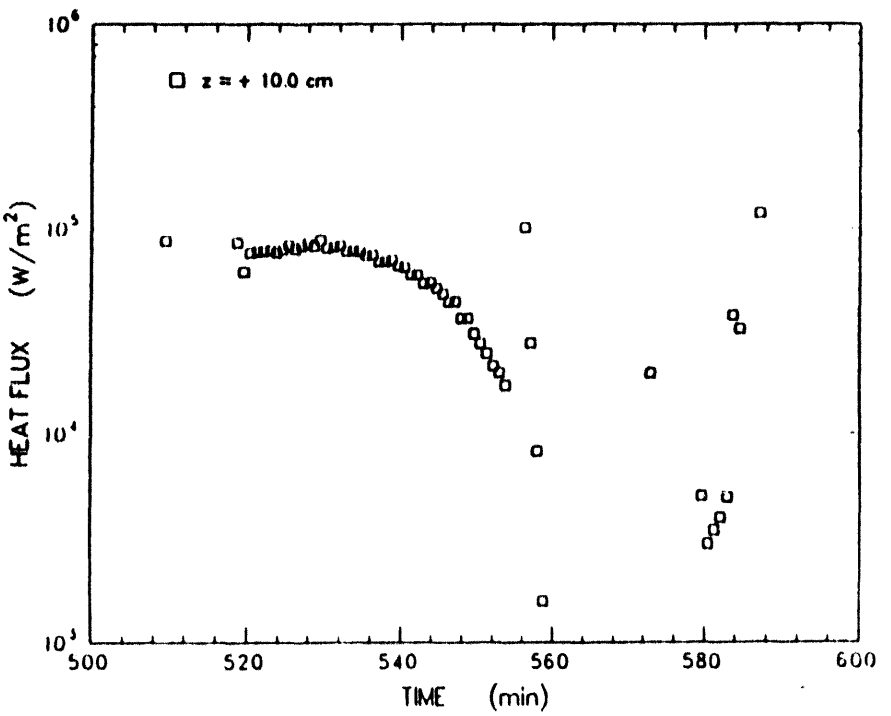

Figure E-14. Expansion of MgO sidewall heat flux data calculated for the array located at z = + 10 cm

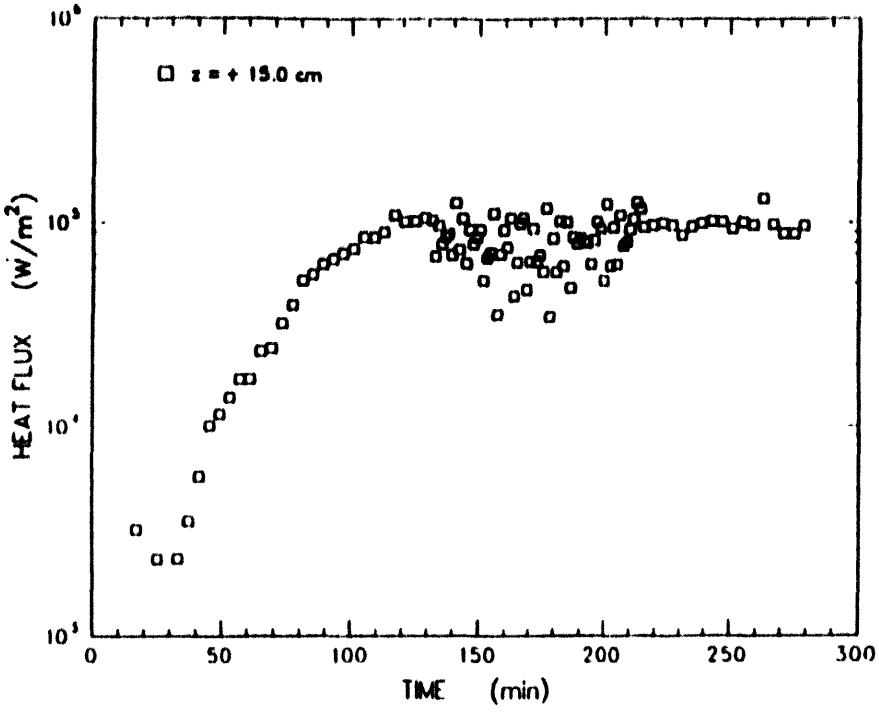

Figure E-15. MgO sidewall heat flux calculated from thermocouple data for the array located at z = + 15 cm

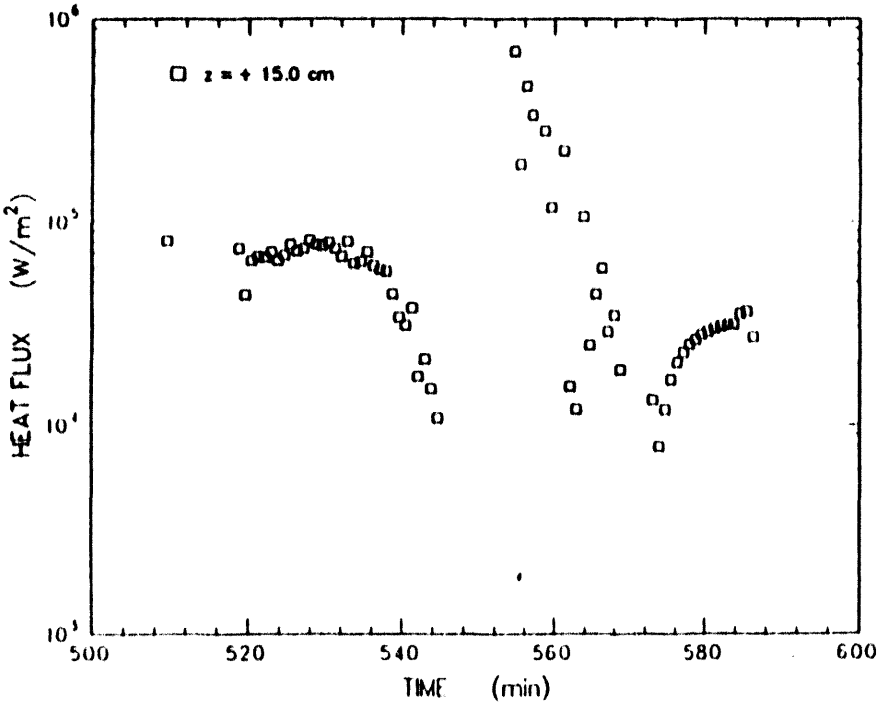

Figure E-16. Expansion of MgO sidewall heat flux data calculated for the array located a z = + 15 cm

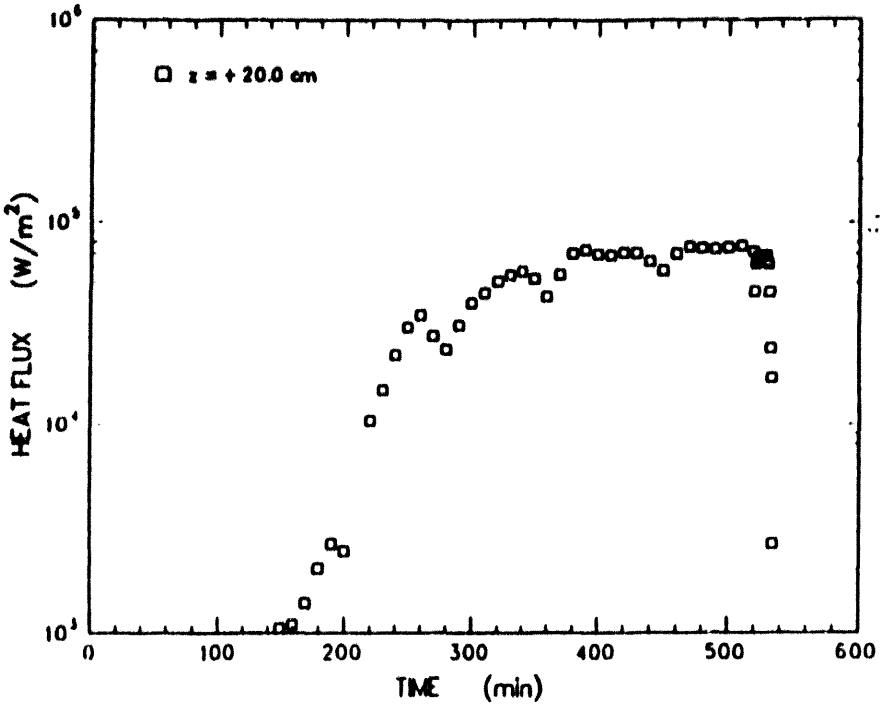

Figure E-17. MgO sidewall heat flux calculated from thermocouple data for the array located at z = + 20 cm

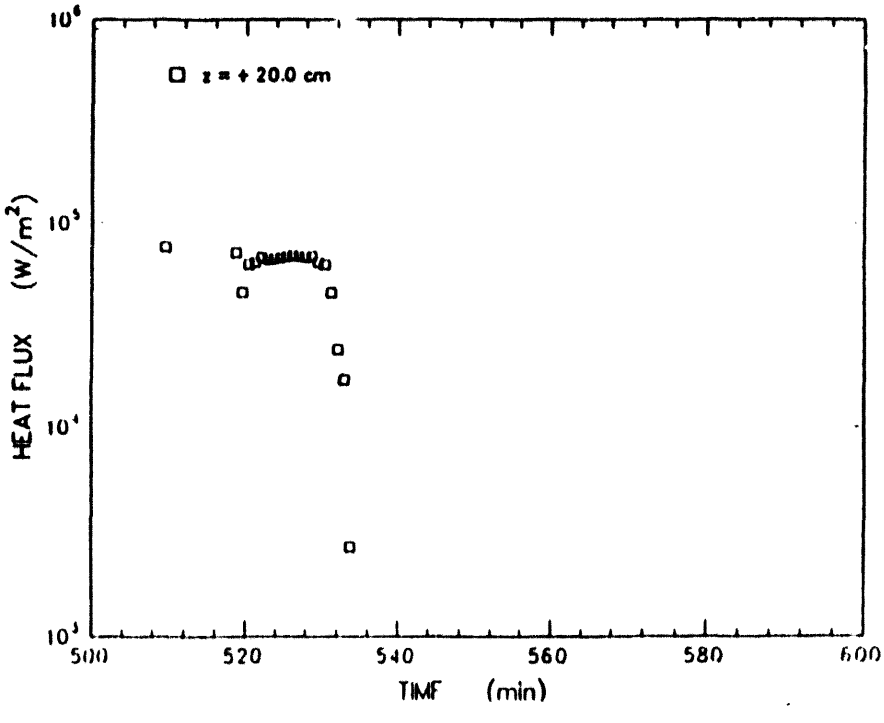

Figure E-18. Expansion of MgO sidewall heat flux data calculated for the array located at z = + 20 cm

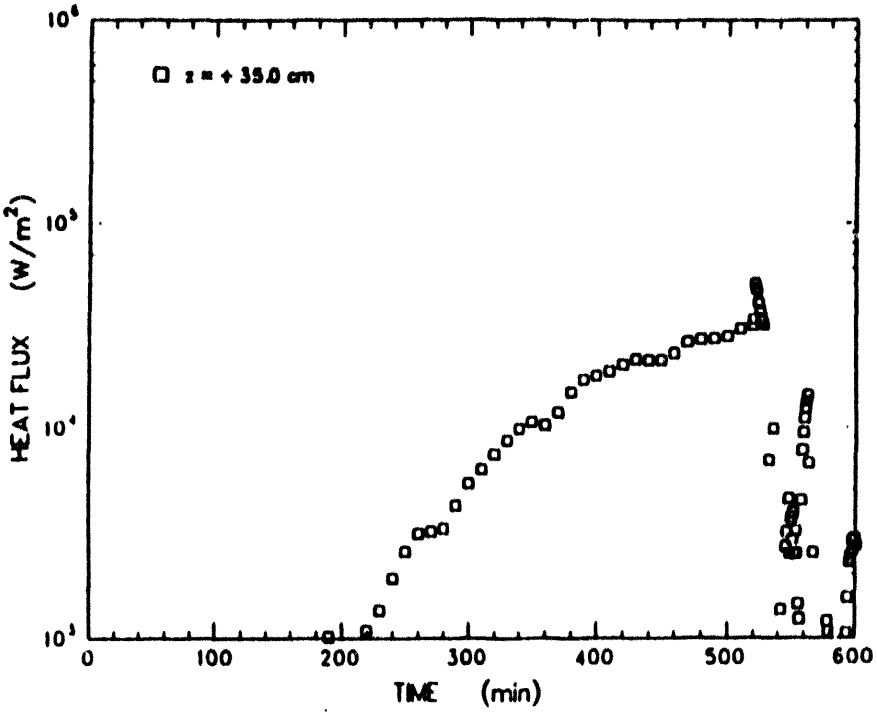

Figure E-19. MgO sidewall heat flux calculated from thermocouple data for the array located at z = + 35 cm

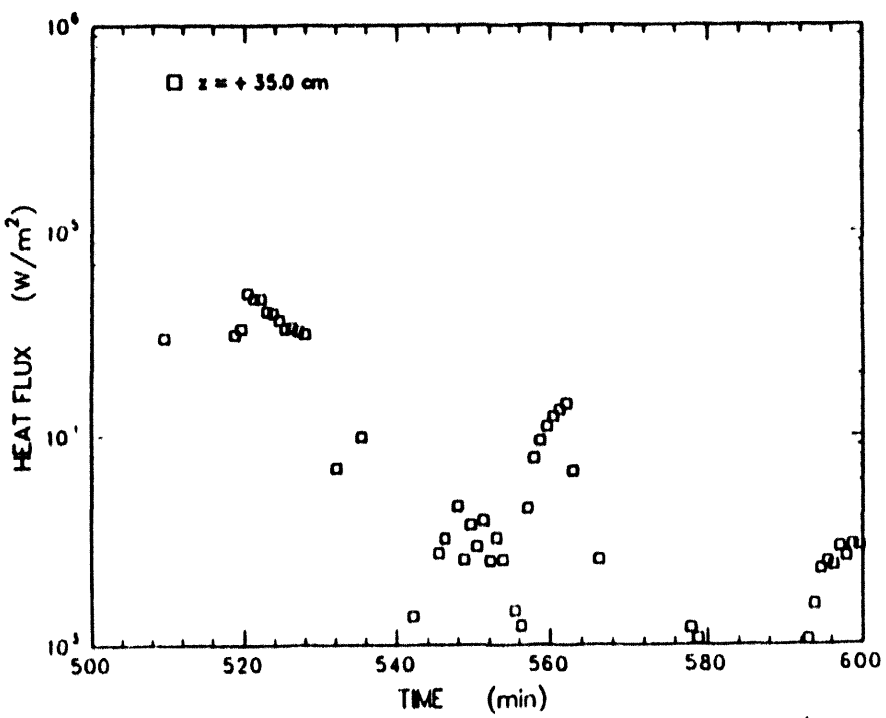

Figure E-20. Expansion of MgO sidewall heat flux data calculated for the array located at z = + 35 cm

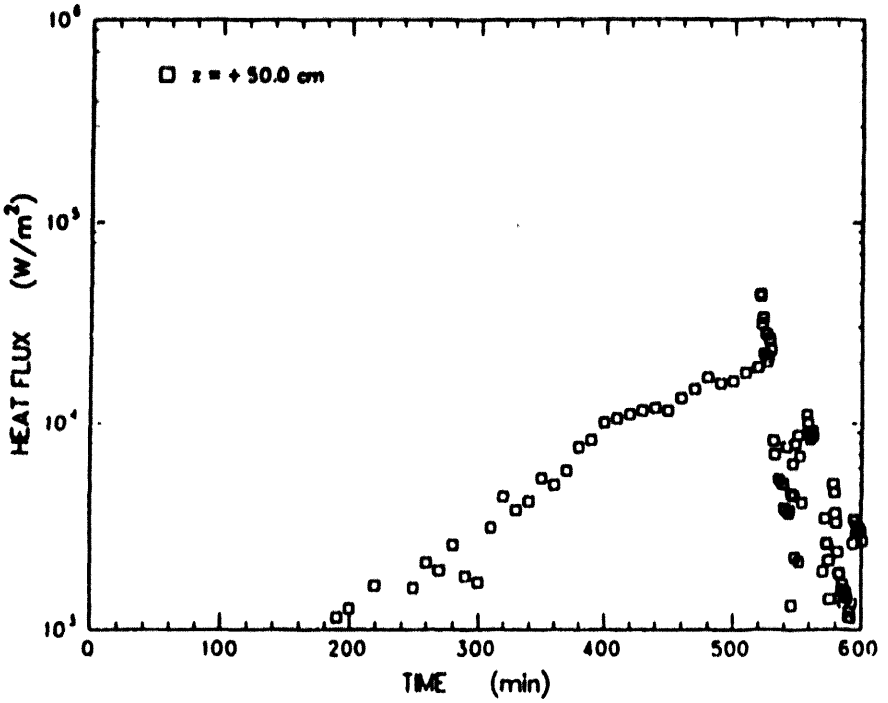

Figure E-21. MgO sidewall heat flux calculated from thermocouple data for the array located at z = + 50 cm

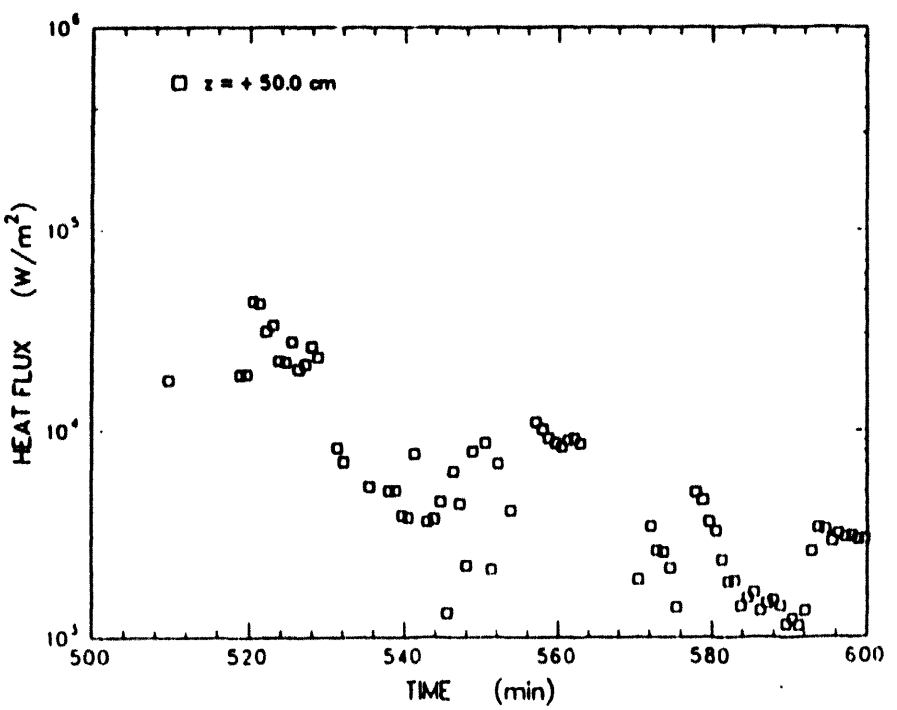

Figure E-22. Expansion of MgO sidewall heat flux data calculated for the array located at z = + 50 cm

Appendix F: Water Quench, Heat Flux and Pool Temperature Data

Presented in this appendix are the temperature, flow rate, volume and heat flux data acquired during the quenching of the molten oxidic debris.

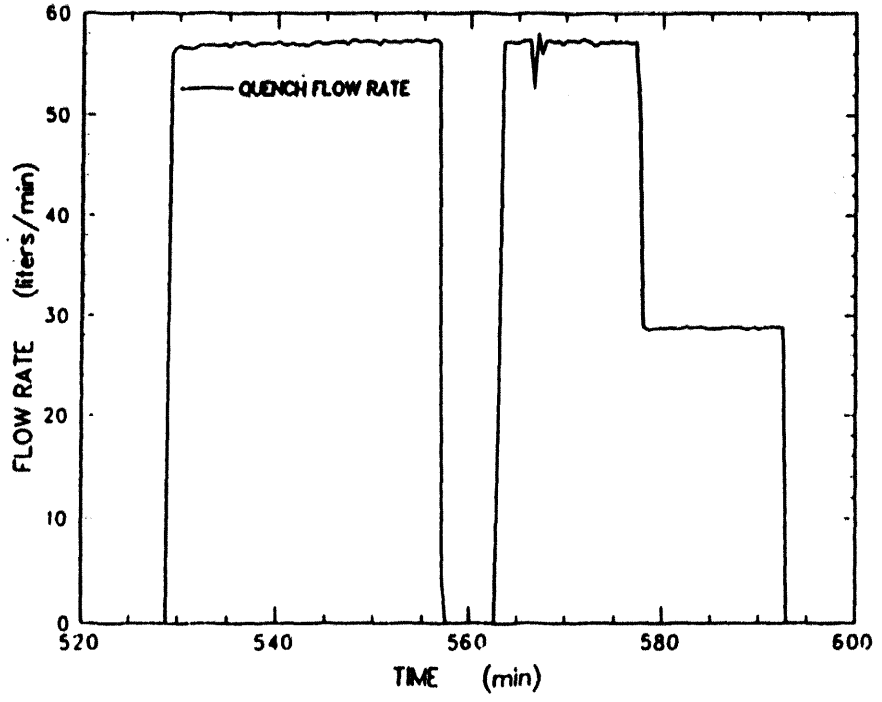

Figure F-1. Flow rate of water used to quench the core debris

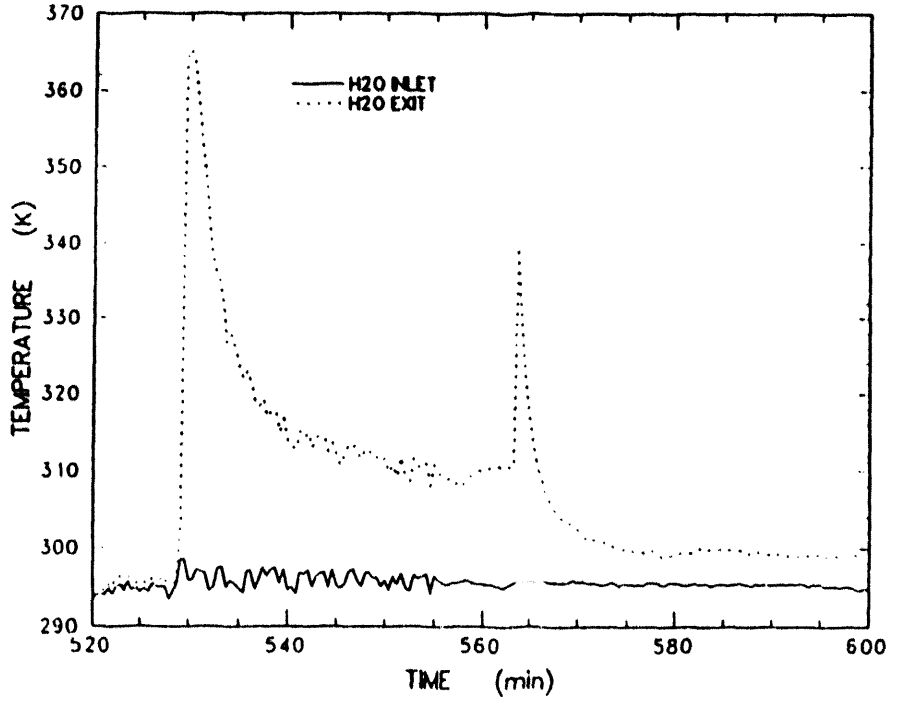

Figure F-2. Temperature of the quench water entering and exiting the interaction crucible measured by type K thermocouples

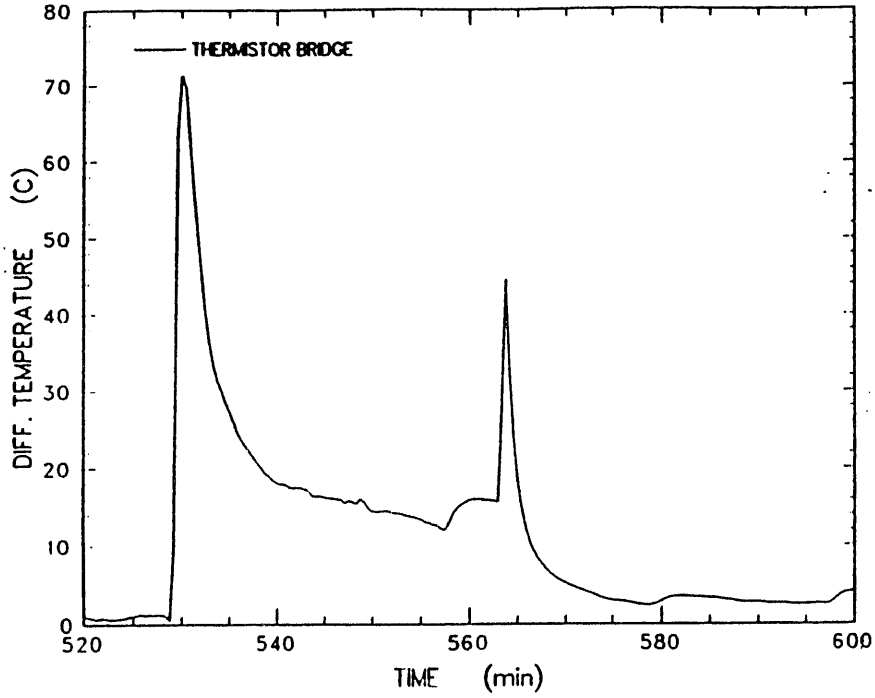

Figure F-3. Differential temperature of the overlying water pool measured by the thermistor bridge

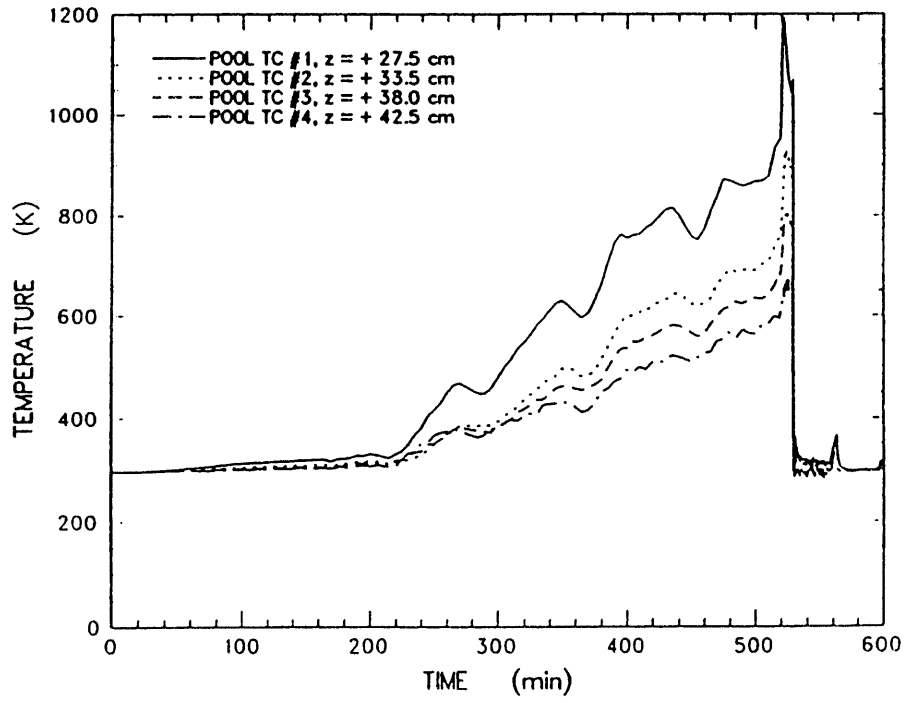

Figure F-4. Temperatures indicated by the type K thermocouples installed just above the charge in the area covered by the formation of the water pool

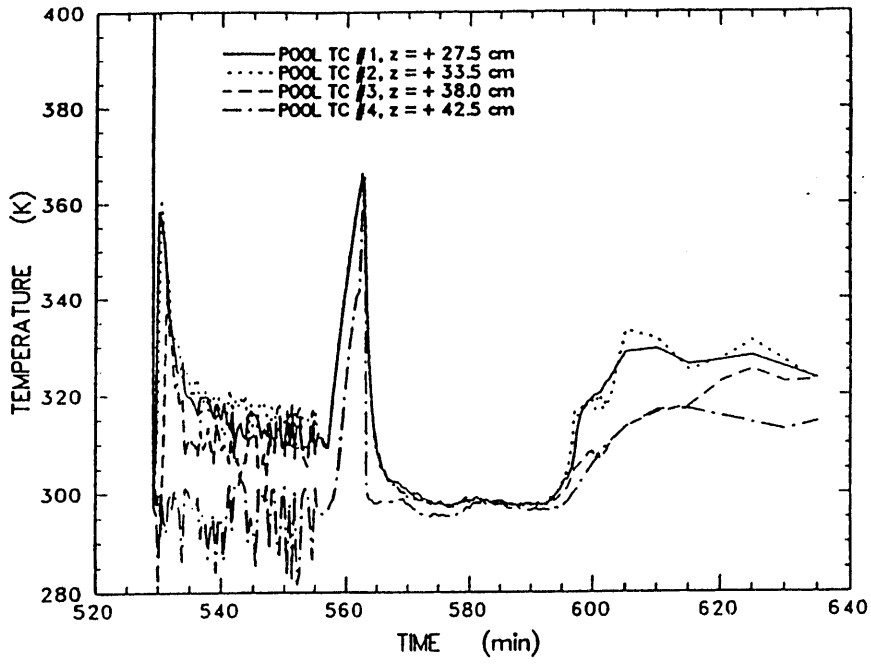

Figure F-5. Temperature history of type K thermocouples submerged in the water pool

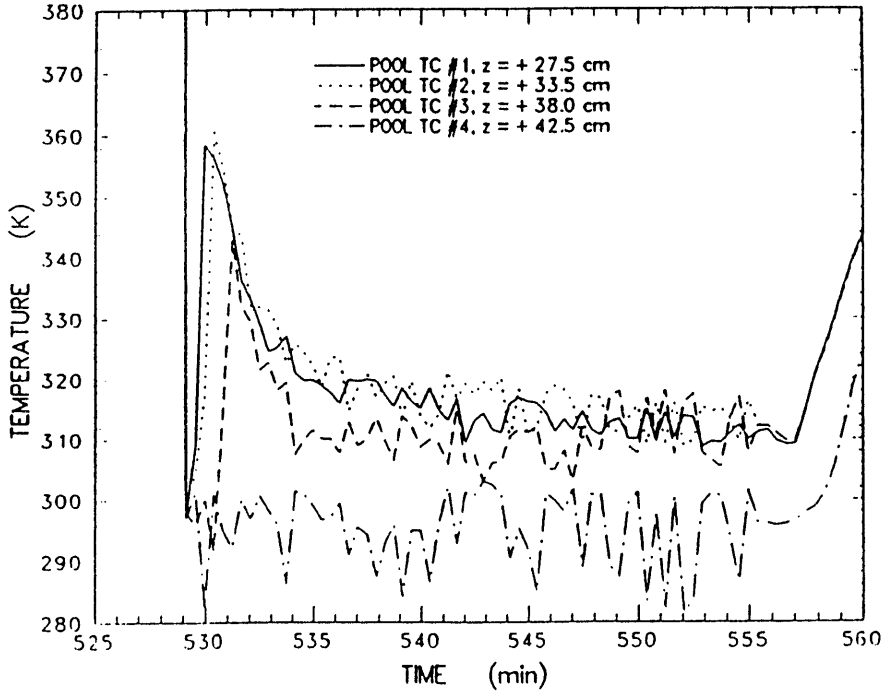

Figure F-6. Expansion of temperature history indicated by type K thermocouples submerged in the water pool

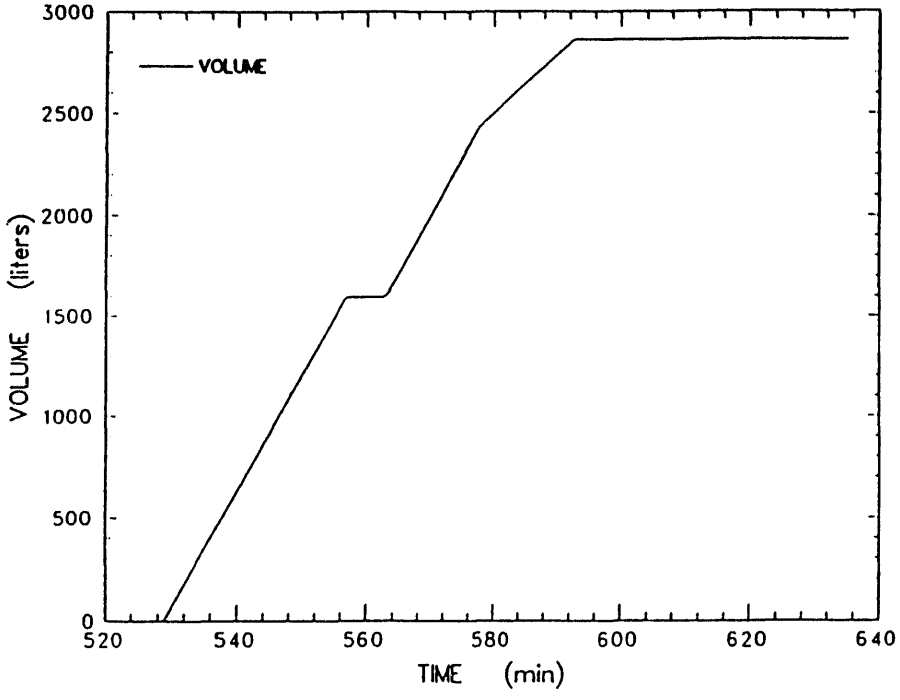

Figure F-7. Volume of quench water delivered to the interaction crucible

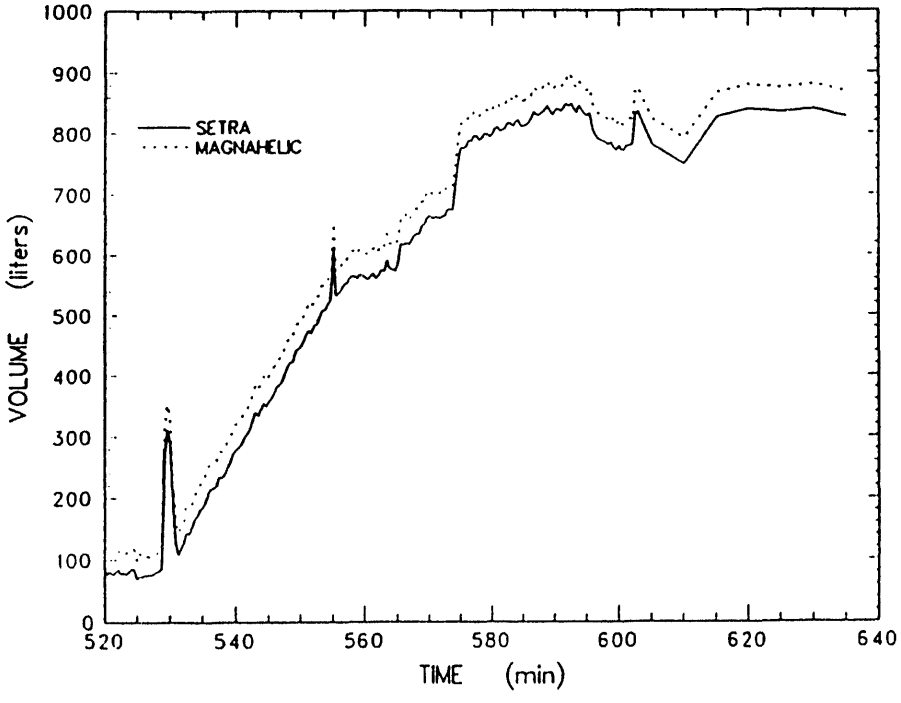

Figure F-8. Volume of quench water collected in the overflow reservoir

Appendix G: Flow Circuit Pressures and Temperatures, Gas Composition, Flow Rate and Aerosol Data

In this appendix data are presented for pressure, temperature, flow, gas composition and aerosol recorded using instrumentation installed on the containment chamber, gas and aerosol sampling systems.

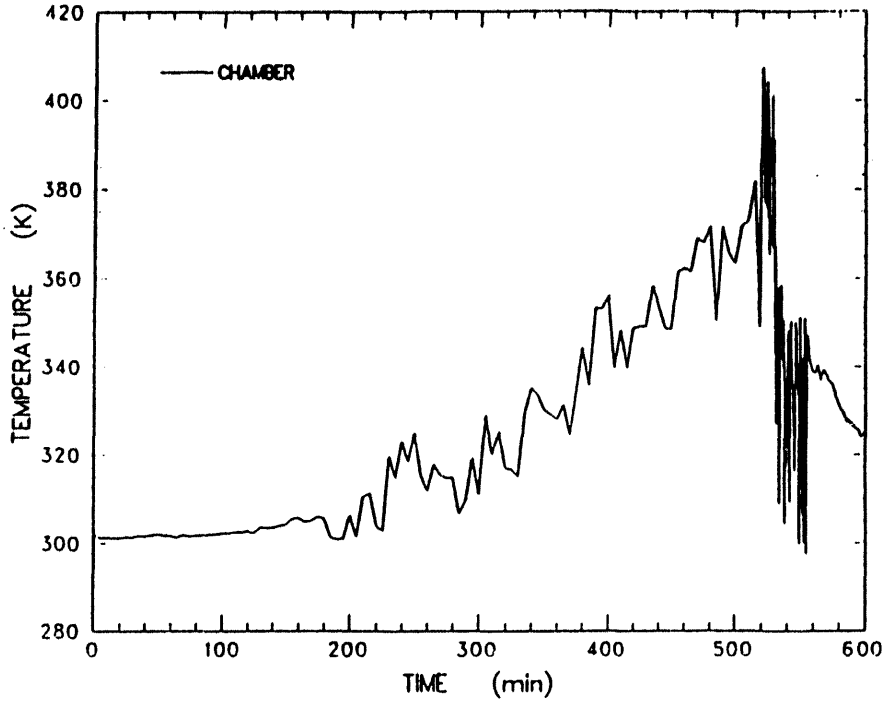

Figure G-1. Temperature measured inside the containment vessel

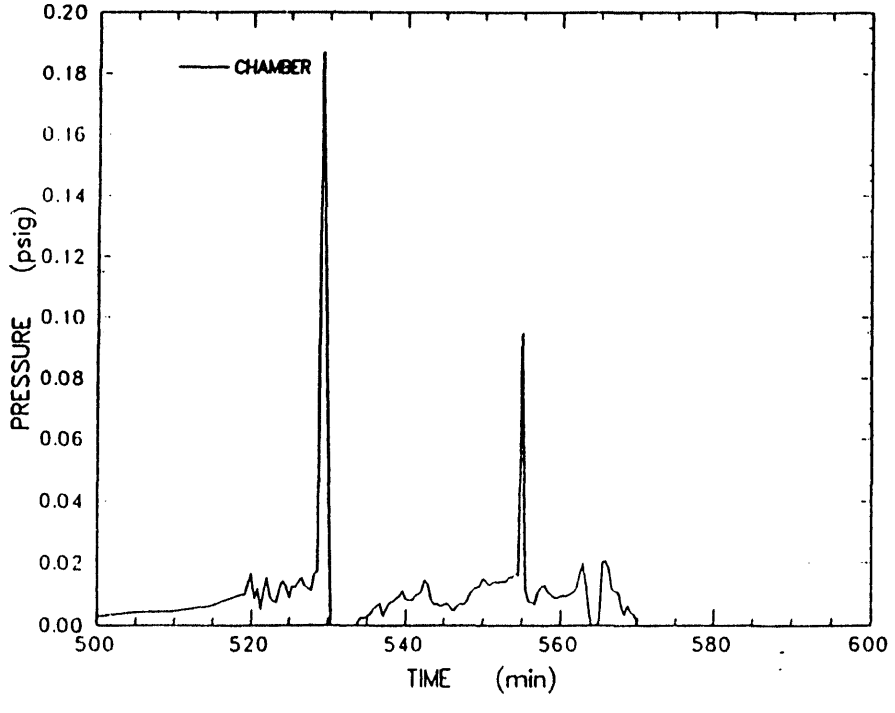

Figure G-2. Gauge pressure measured inside the containment vessel

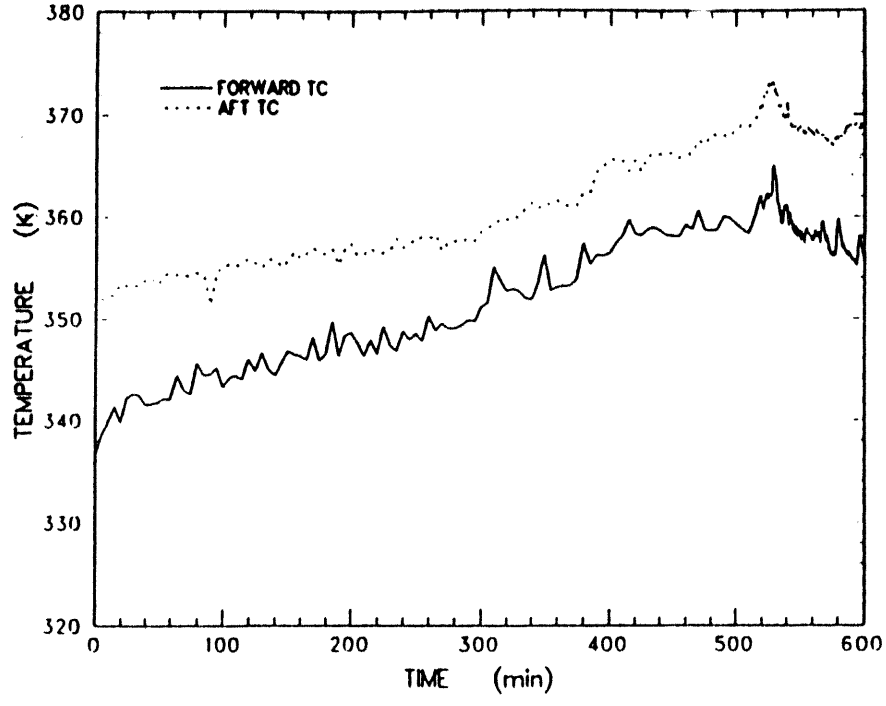

Figure G-3. Temperature of the flow tube exiting the containment vessel

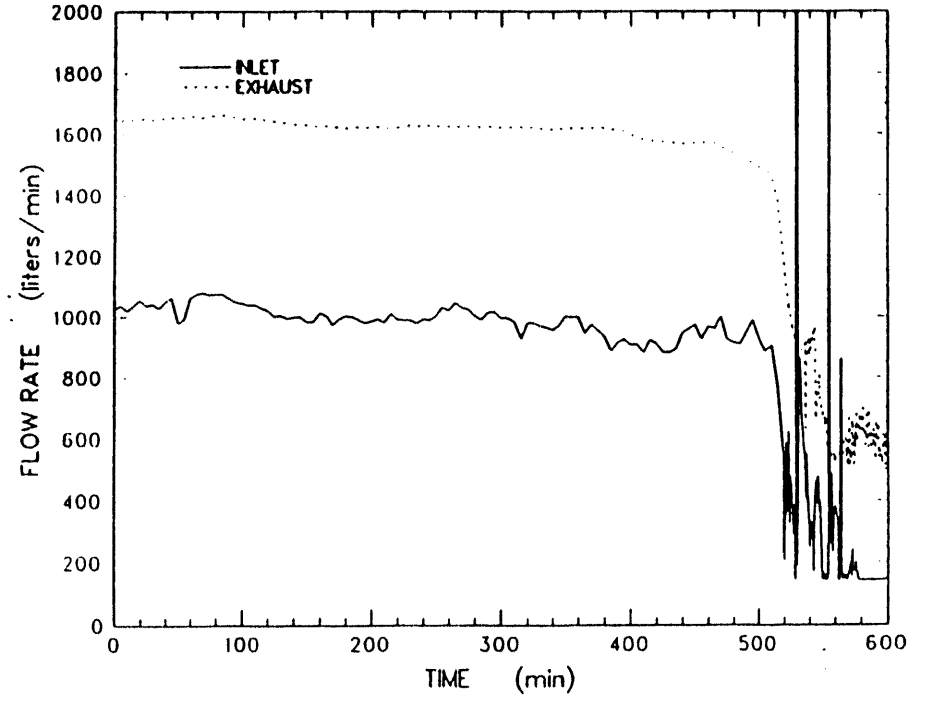

Figure G-4. Containment vessel inlet and exit flow rate data indicated by turbine flow meters

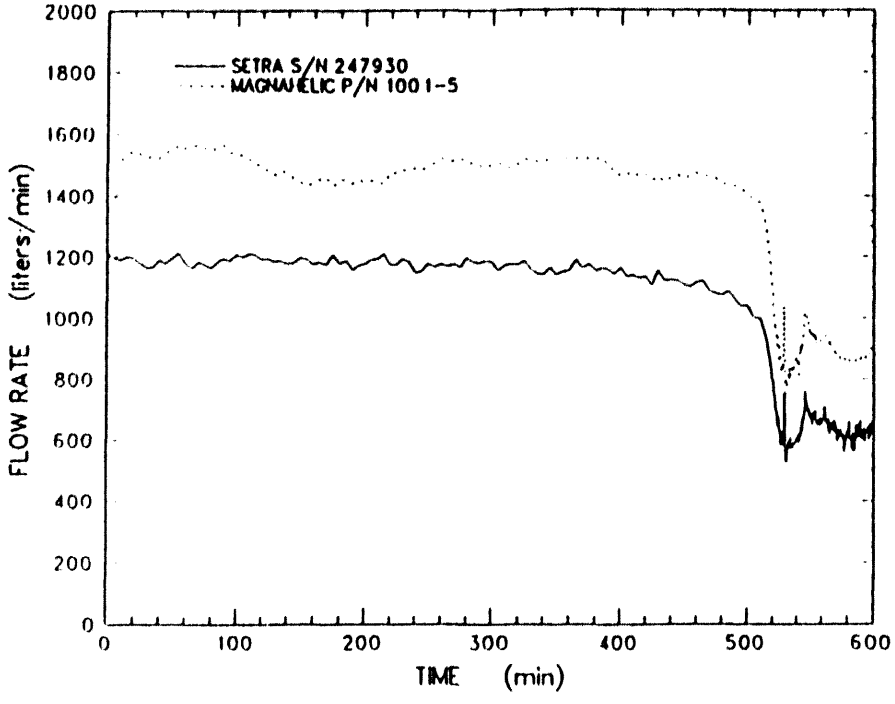

Figure G-5. Flow rate indicated by the mariam laminar flow element

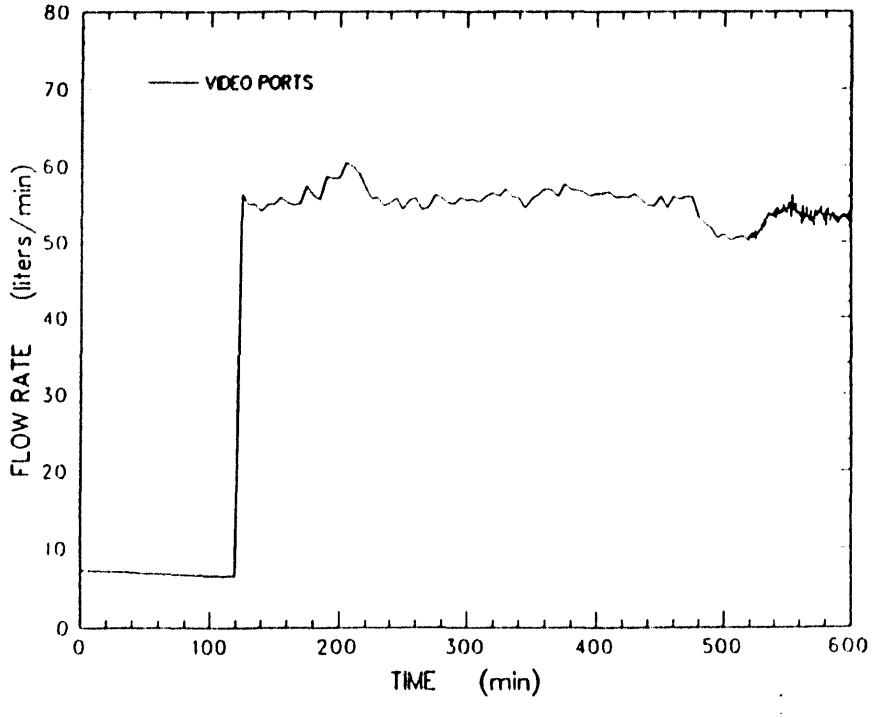

Figure G-6. Flow rate of purge air to the two video camera ports located on the containment vessel

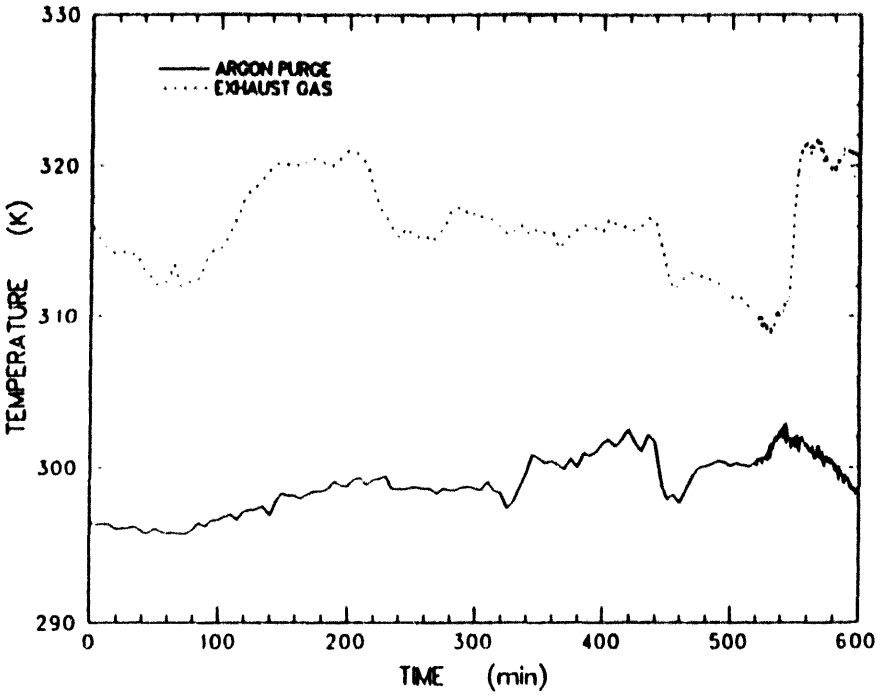

Figure G-7. Temperature of the argon gas used to purge the tungsten thermowells in the charge and exhaust gas exiting the flow system

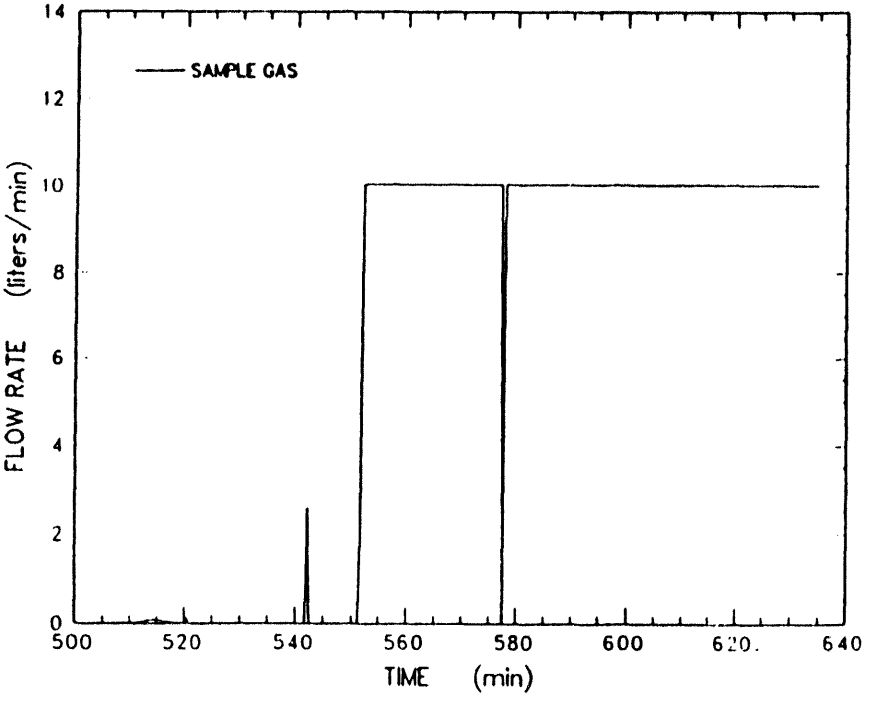

Figure G-8. Flow rate of sample gas from the containment vessel

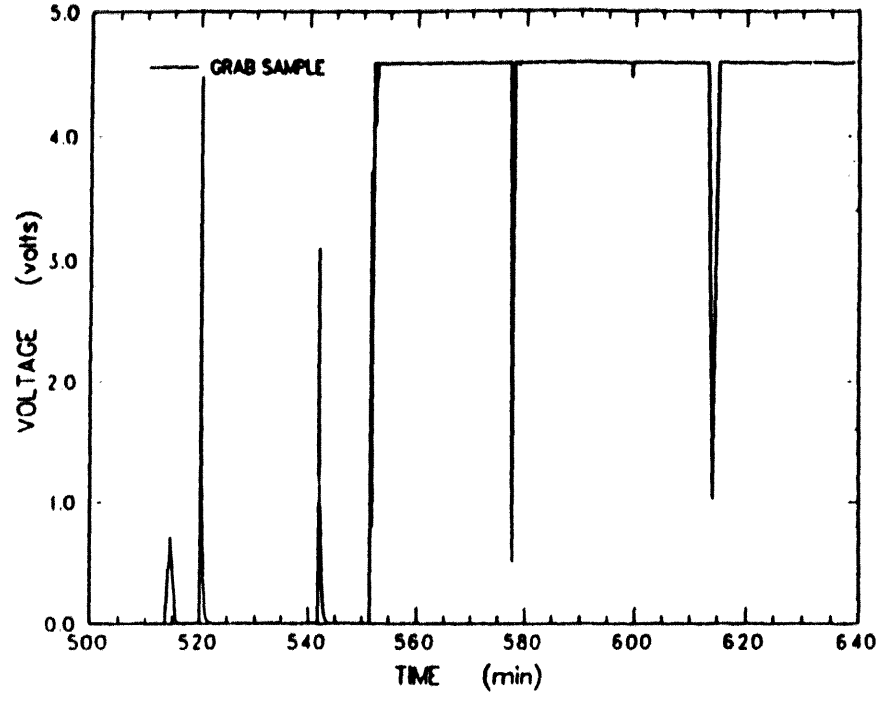

Figure G-9. Voltage fiducial indicating the timing of the gas grab sample

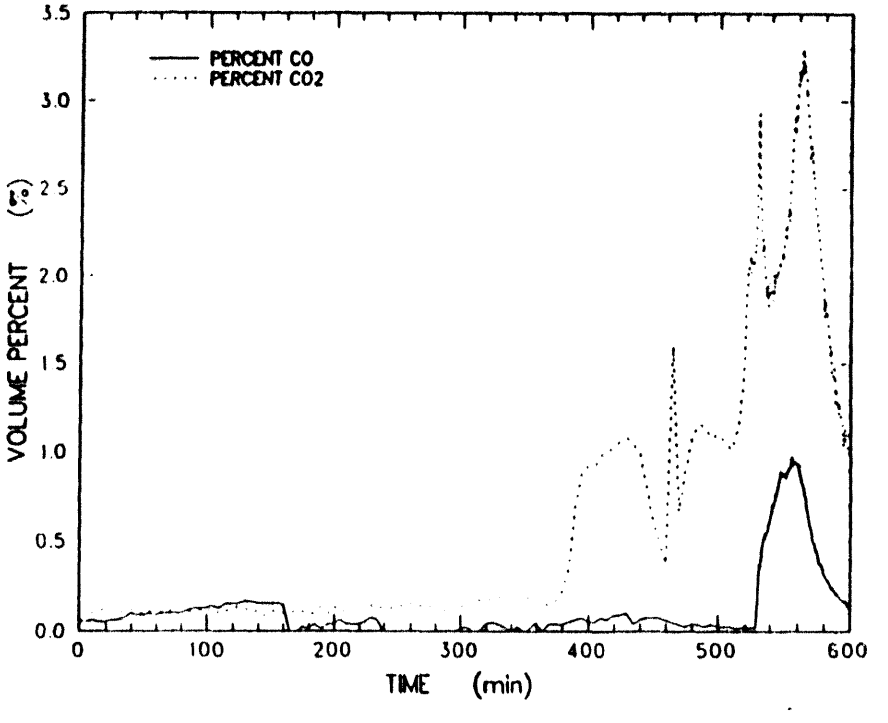

Figure G-10. Volume percent of carbon monoxide and carbon dioxide in the containment vessel

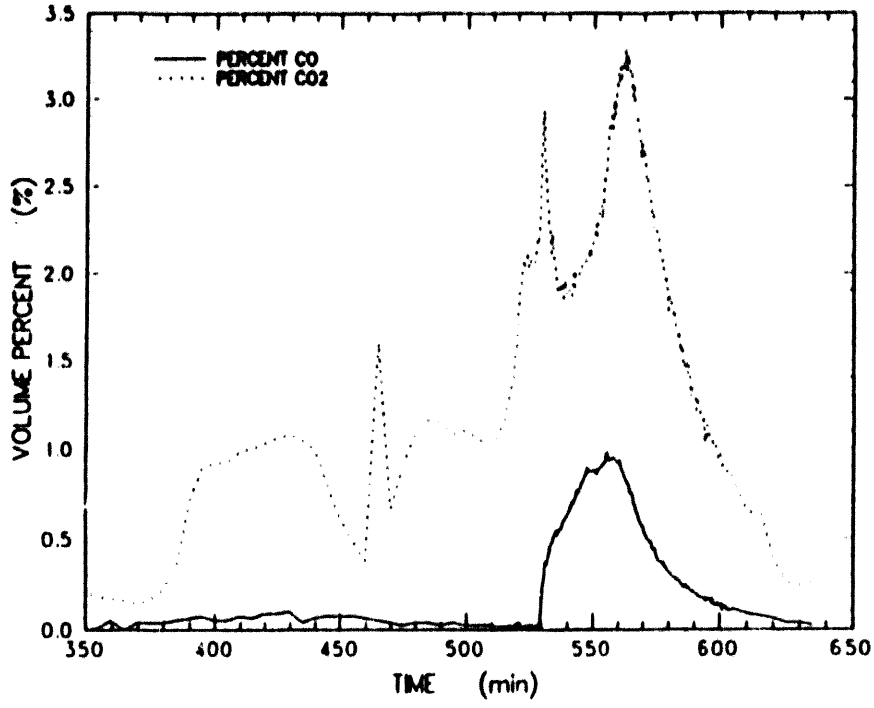

Figure G-11. Expansion of the volume percent of carbon monoxide and carbon dioxide data in the containment vessel

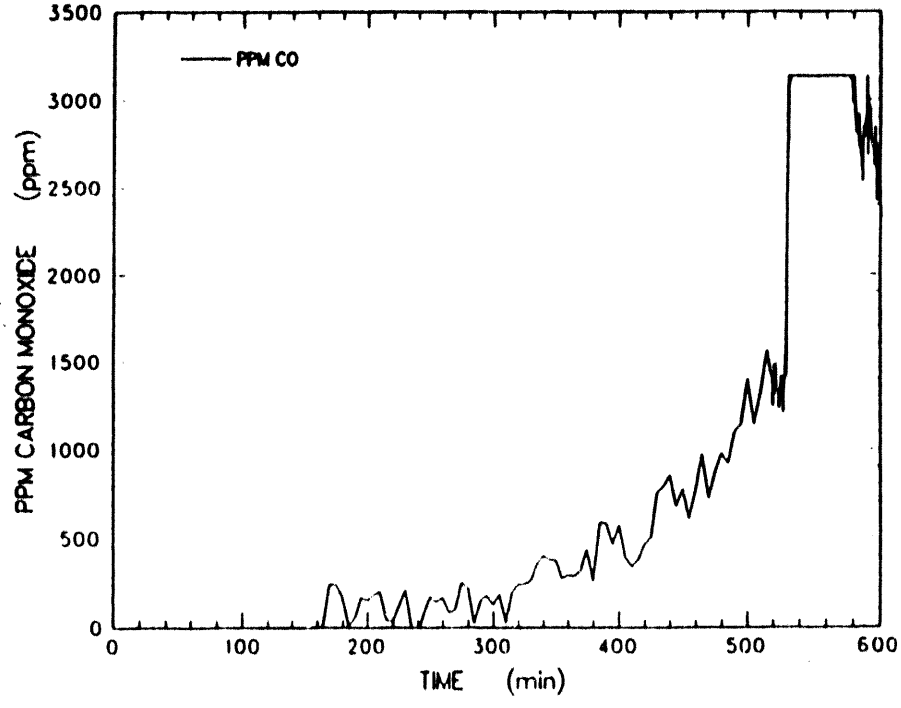

Figure G-12. Parts per million carbon monoxide inside the containment vessel

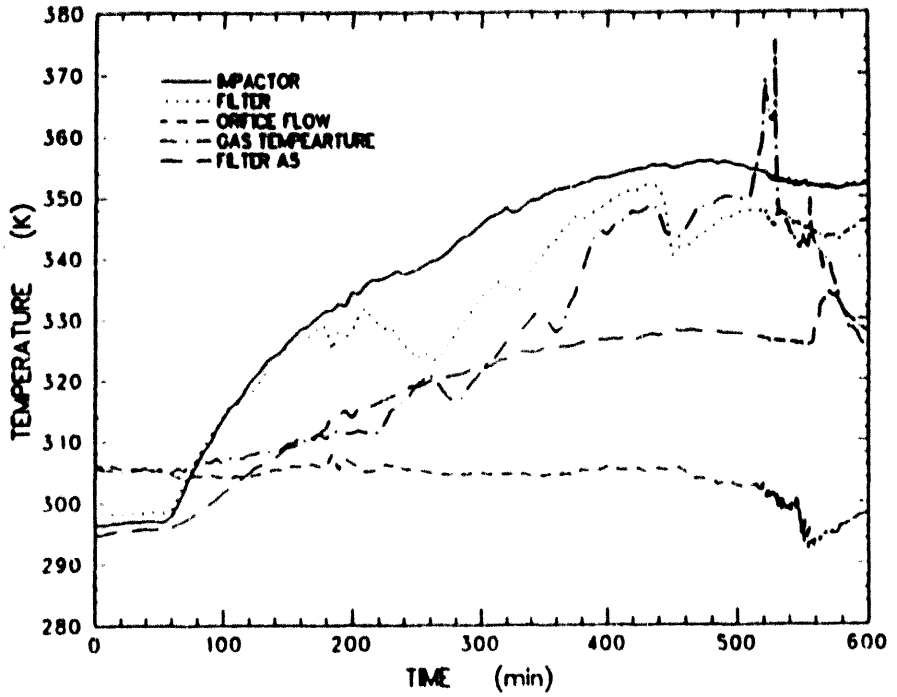

Figure G-13. Temperatures measured at different locations in the aerosol sampling system

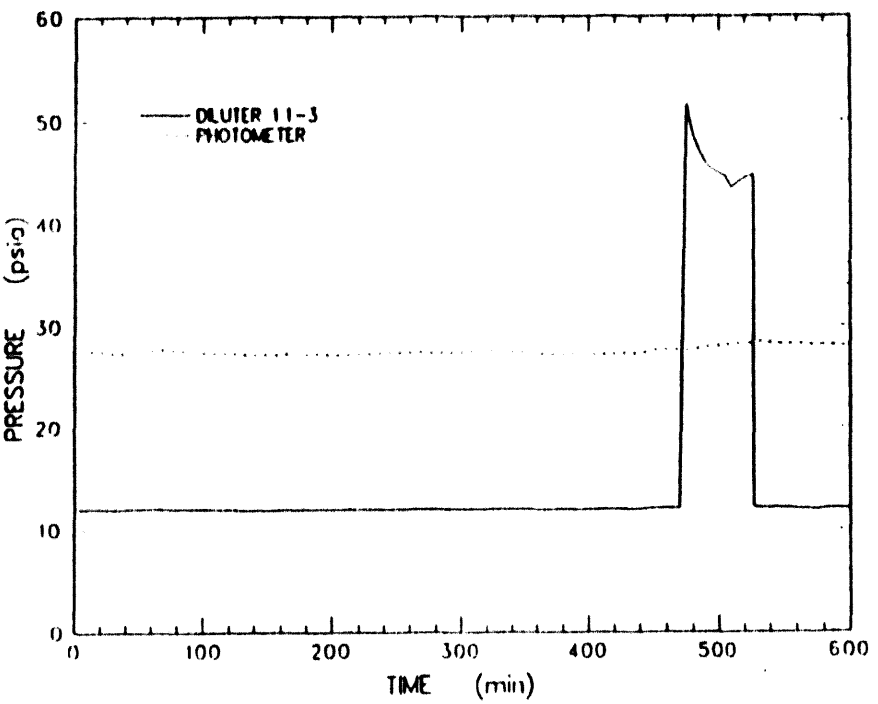

Figure G-14. Absolute pressure measured upstream of the critical orifices installed in the aerosol sample line for the diluter and photometers

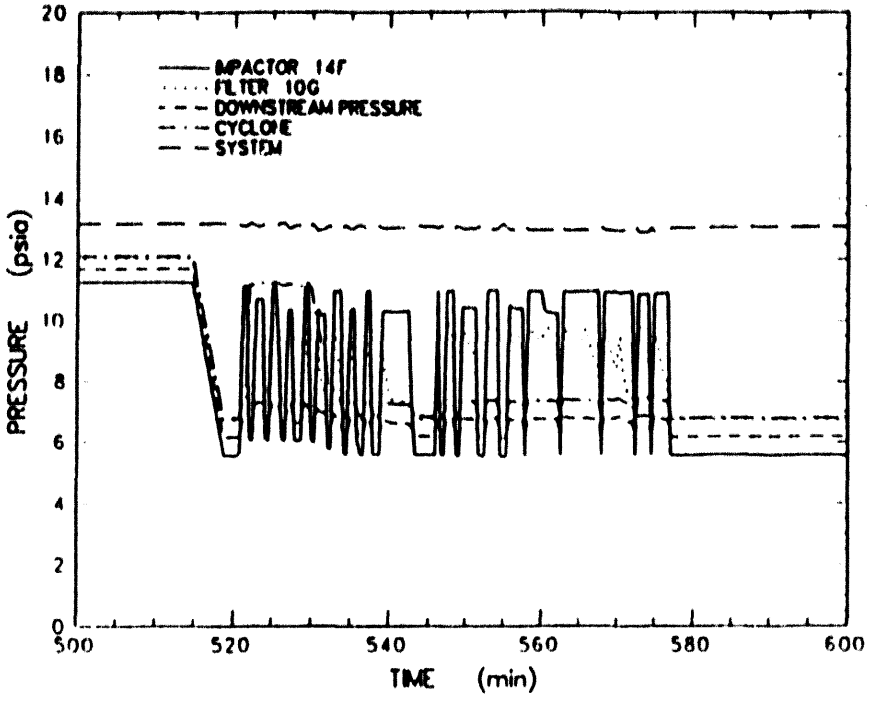

Figure G-15. Absolute pressure measured upstream of critical orifices installed in the aerosol sample line for the impactors, filters, cyclone and system

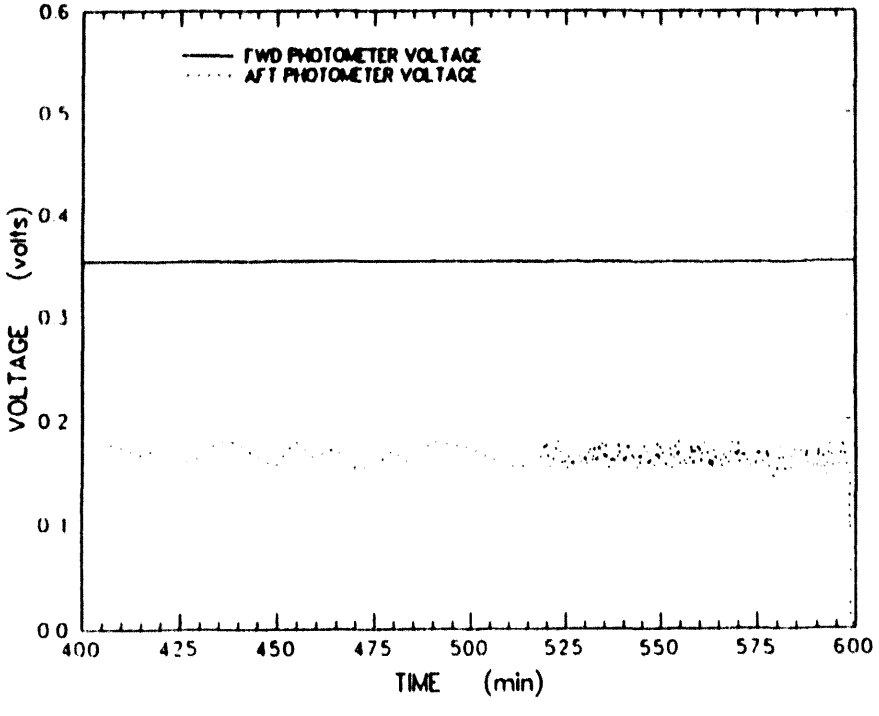

Figure G-16. Opacity meter output. Voltage level above the baseline was proportional to aerosol concentration

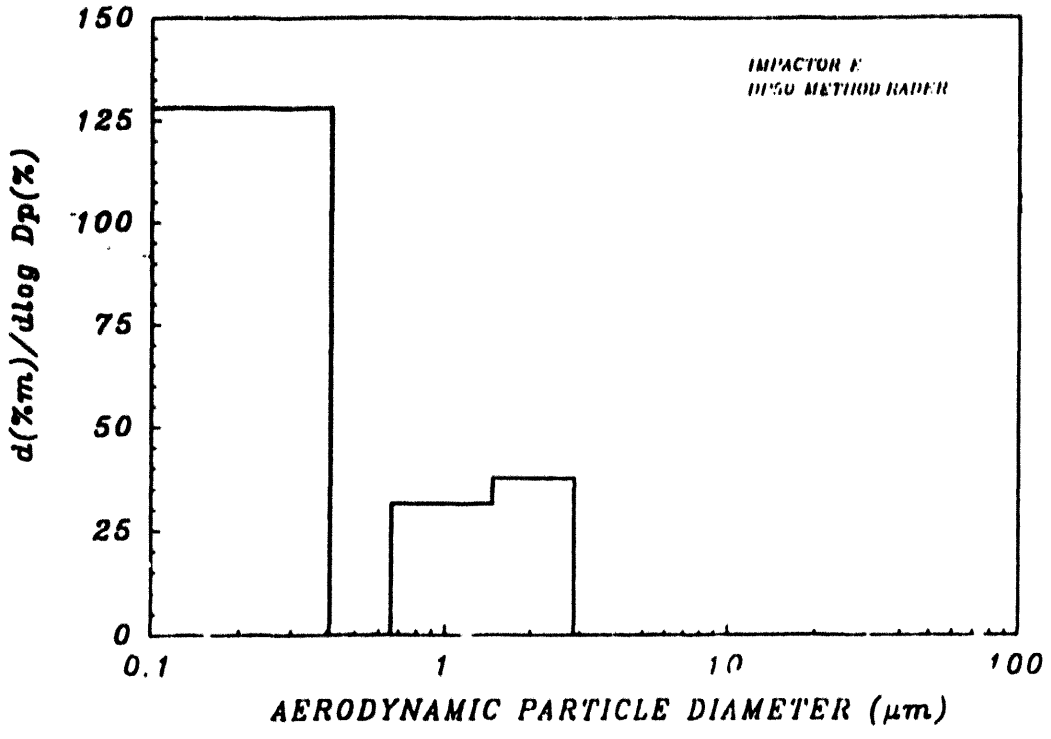

Figure G-17. Normalized aerosol mass distribution from Impactor E taken at 522.7 minutes

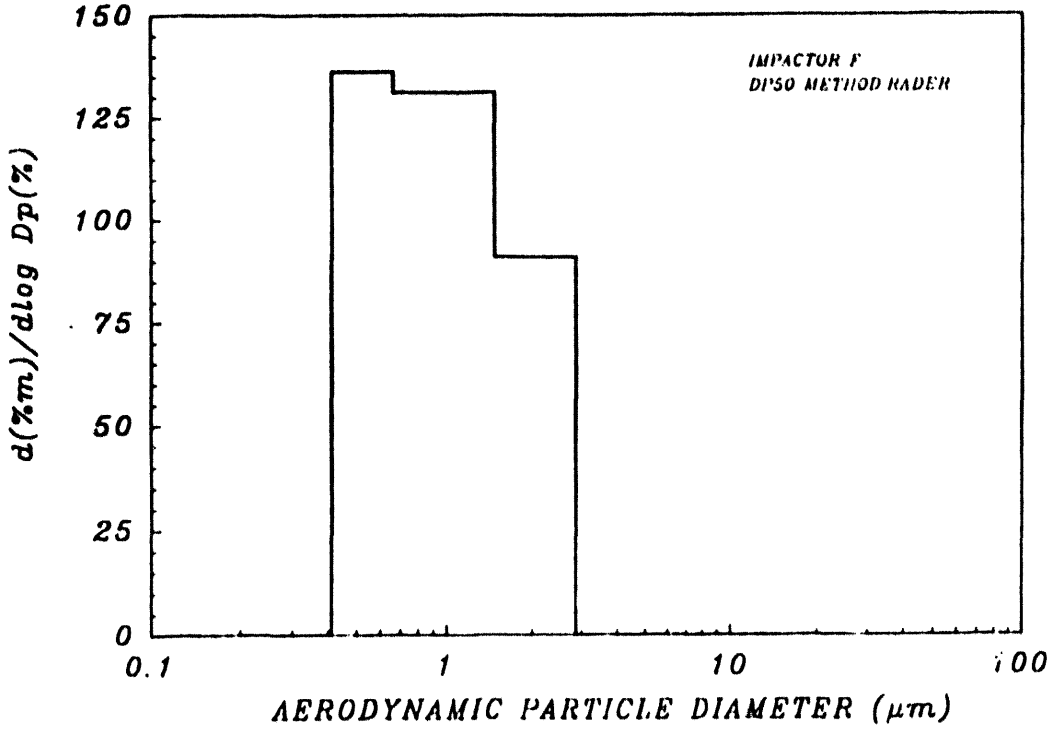

Figure G-18. Normalized aerosol mass distribution from Impactor F taken at 526.7 minutes

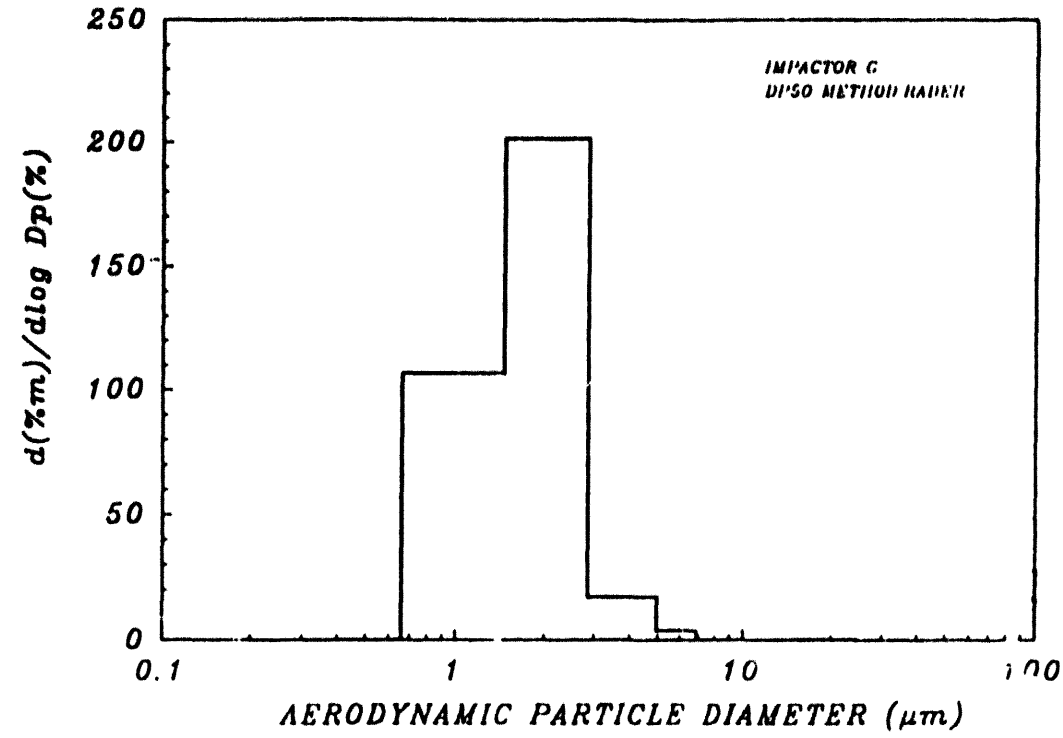

Figure G-19. Normalized aerosol mass distribution from Impactor G taken at 530.6 minutes

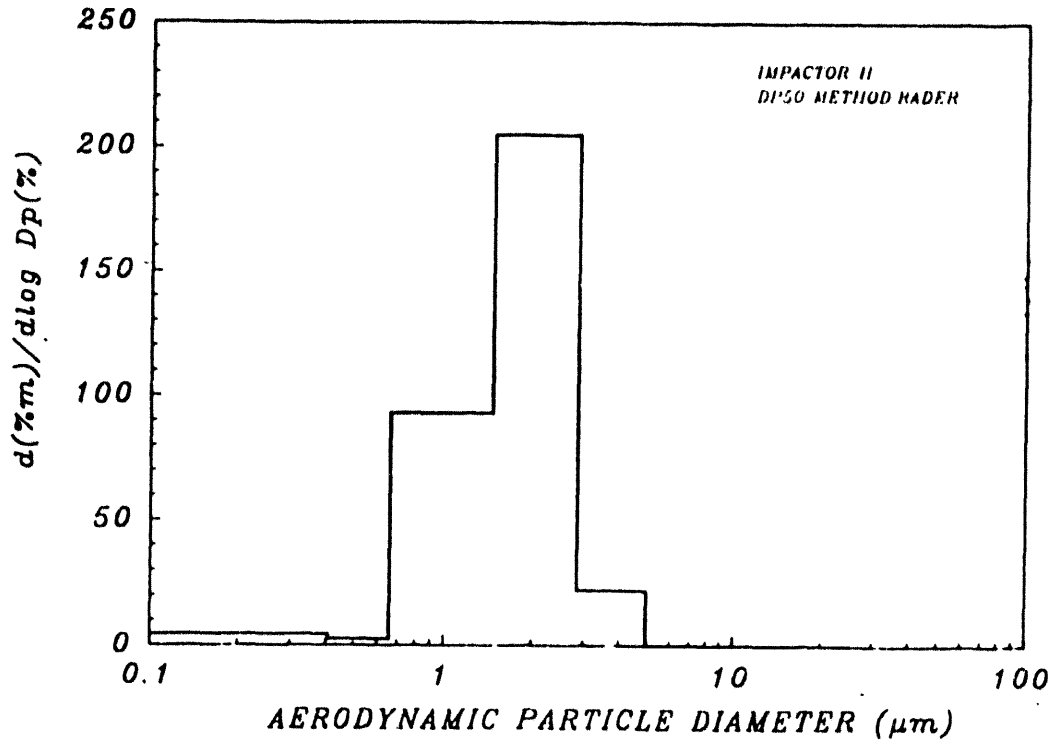

Figure G-20. Normalized aerosol mass distribution from Impactor H taken at 534.7 minutes

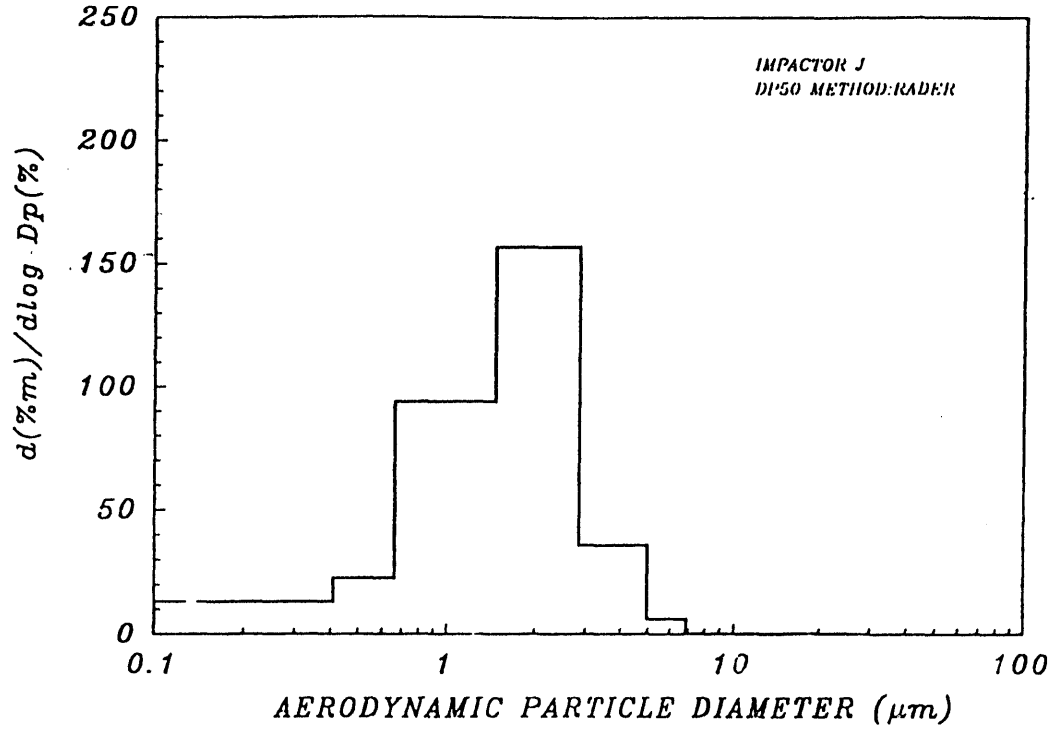

Figure G-21. Normalized aerosol mass distribution from Impactor J taken at 538.7 minutes

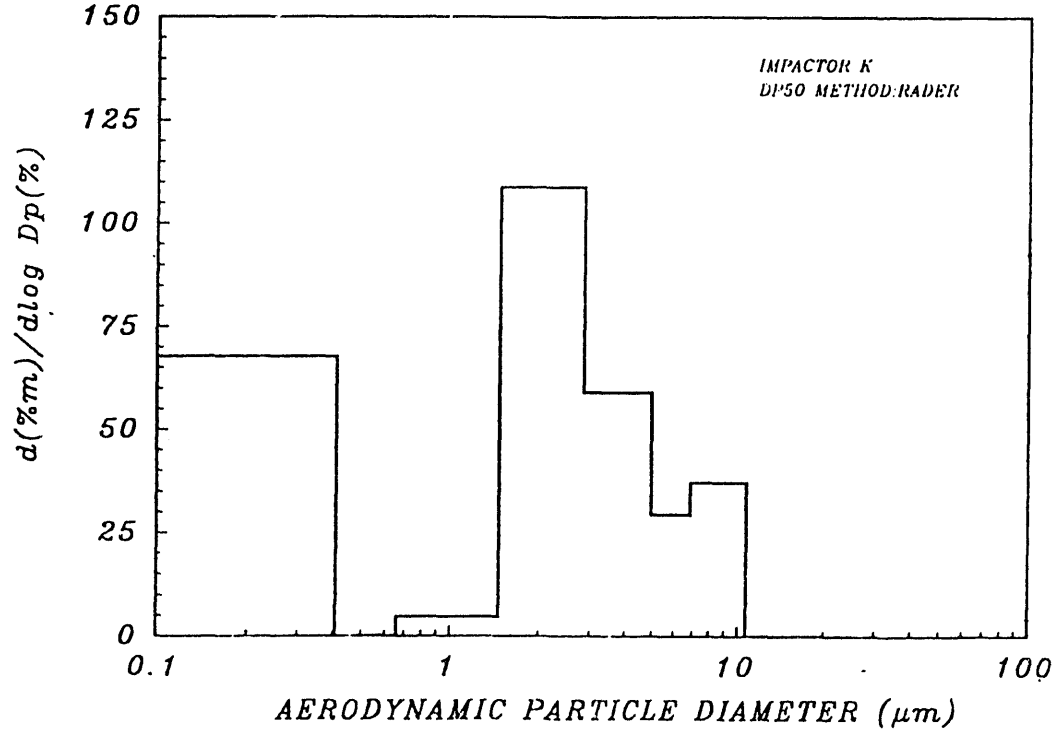

Figure G-22. Normalized aerosol mass distribution from Impactor K taken at 549.4 minutes

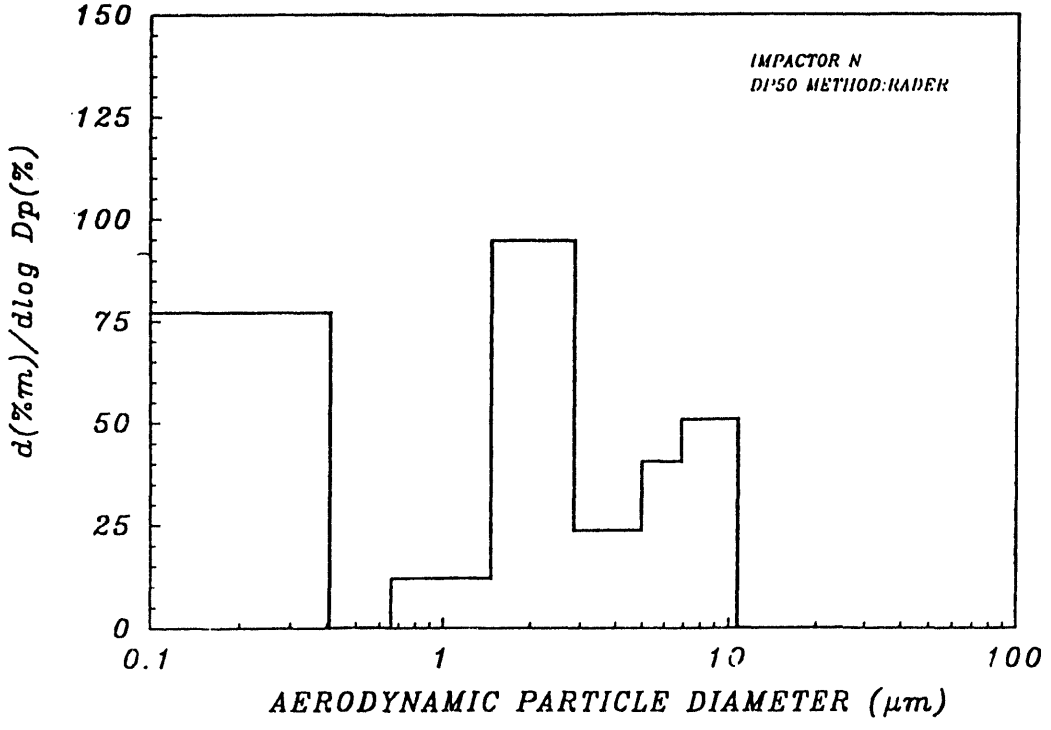

Figure G-23. Normalized aerosol mass distribution from Impactor N taken at 549.4 minutes

Distribution List

No. of Copies

25 U.S. Nuclear Regulatory Commission
Office of Nuclear Regulatory Research
Washington, DC 20555
Attn: B.W. Sheron, NLS007
C.G. Tinkler, Jr., NLN344
G.R. Marino, NLS007
A.M. Rubin, NLN344
R.B. Foulds, NLN344
J.A. Murphy, NLS007
S. Basu, NLN344 (15)
E.S. Beckjord, NLS007
F. Eltawila, NLN344
Z. Rosztoczy, NLS169
T.P. Speis, NLS007

5 U.S. Nuclear Regulatory Commission
Office of Nuclear Reactor Regulation
Washington, DC 20555
Attn: T.C. Murley, 12G18
F.P. Gillespie, 12G18
A.C. Thadani, 8E2 (3)

2 U.S. Department of Energy
Albuquerque Operations Office
P.O. Box 5400
Albuquerque, NM 87185
Attn: C.E. Garcia, Director

2 Electric Power Research Institute
3412 Hillview Avenue
Palo Alto, CA 94303
Attn: A. Machiels

3 Brookhaven National Laboratory
130 BNL
Upton, NY 11973
Attn: T. Pratt

3 Oak Ridge National Laboratory
P.O. Box Y
Oak Ridge, TN 37830
Attn: T. Kress

3 Argonne National Laboratory
9700 S. Cass Avenue
Argonne, IL 60439
Attn: B. Spencer

No. of Copies

1 Nuclear Safety Oversight Commission
1133 15th Street, NW
Room 307
Washington, DC 20005
Attn: Cathy Anderson

1 Battelle Columbus Laboratory
505 King Avenue
Columbus, OH 43201
Attn: P. Cybulskis

1 Los Alamos National Laboratories
P.O. Box 1663
Los Alamos, NM 87545
Attn: M. Stevenson

1 UCLA
Nuclear Energy Laboratory
405 Hilgaard Avenue
Los Angeles, CA 90024
Attn: I. Catton

1 University of Wisconsin
Nuclear Engineering Department
1500 Johnson Drive
Madison, WI 53706
Attn: M.L. Corradini

1 EG&G Idaho
Willo Creek Building, W-3
P.O. Box 1625
Idaho Falls, ID 83415
Attn: R. Hobbins

1 Battelle Pacific Northwest Laboratory
P.O. Box 999
Richland, WA 99352
Attn: M. Freshley

1 Department of Energy
Scientific and Tech. Info. Center
P.O. Box 62
Oak Ridge, TN 37831

No. of Copies

1 Fauske and Associates, Inc.
16W070 West 83rd Street
Burr Ridge, IL 60952
Attn: R. Henry

1 U.S. Nuclear Regulatory Commission
Advisory Comm. on Reactor Safeguards
Washington, DC 20555
Attn: M.D. Houston, P-315

1 IAEA
Division of Nuclear Reactor Safety
Wagranesrstrasse 5
P.O. Box 100
A/1400 Vienna
AUSTRIA
Attn: M. Jankowski

1 Department LWR Fuel
Belgonucleaire
Rue de Champde Mars, 25
B-1050 Brussels
BELGIUM
Attn: Mr. H. Bairiot, Chief

2 Atomic Energy Canada, Ltd.
Chalk River, Ontario KOJ IJO
CANADA
Attn: R.D. MacDonald

1 institute of Nuclear Energy Research
P.O. Box 3
Lungtan
Taiwan 325
REPUBLIC OF CHINA
Attn: Sen-I Chang

1 Department of Nuclear Safety
Finnish Center for Radiation and
Nuclear Safety
P.O. Box 268
SF-00181 Helsinki
FINLAND
Attn: Jorma V. Sandberg

No. of Copies

1 CEN Cadarache
18108 Saint Paul Lez Durance
FRANCE
Attn: A. Meyer-Heine

1 Centre d'Estudes Nuclearies (IPSN-DAS)
Commisariat a l'Energie Atomique
Boite Postale No. 6
F-92265 Fontenay-aux-Roses Cedex
FRANCE
Attn: Jacques Duco

1 Gesellschaft fur Reaktorsicherheit (GRS)
Postfach 101650
Glockengrasse 2
5000 Koeln 1
GERMANY

1 Kraftwerk Union
Hammerbacher Strasse 1214
Postfach 3220
D-8520 Erlangen 2
GERMANY
Attn: Dr. M. Peeks

2 Kernforschungszentrum Karlsruhe
Postfach 3640
75 Karlsruhe
GERMANY
Attn: S. Hagen

1 Nucleare e della Protezione
Sanitaria (DISP)
Ente Nazionnle Energie
Alternative 7 (ENEA)
Viale Regina Margherita, 125
Casella Postale M. 2358
1-00100 Roma A.D.
ITALY
Attn: Alan V. Jones

2 Japan Atomic Energy Research Institute
Tokai-Mura, Naka-Gun
Ibaraki-Ken 319-11
JAPAN
Attn: K. Soda

No. of Copies

1 Reactor Centrum Nederland
1755 ZG Petten
THE NETHERLANDS
Attn: Dr. K.J. Brinkman

1 I.V. Kurchatov Institute of Atomic Energy
Nuclear Safety Department
Moscow, 123182
RUSSIA
Attn: V. Asmalov

1 Sub. Emplazamientos y Programas
Consejo de Seguridad Nuclear
Justo Dorado II
28040 Madrid
SPAIN
Attn: Jose Angel Martinez

1 Consejo de Seguridad Nuclear
SOR Angela de la Cruz No. 3
Madrid
SPAIN
Attn: Professor Agustin Alonso

1 Department of Nuclear Power Safety
Royal Institute of Technology
S-100 44 Stockholm
SWEDEN
Attn: B. Raj Sehgal

2 Statens Karnkraftinspektion
P.O. Box 27106
S-10252 Stockholm
SWEDEN
Attn: W. Frid

1 Light Water Reactor Safety Program
Paul Scherrer Institute
CH-5232 Villigen PSI
SWITZERLAND
Attn: J. Peter Hosemann

1 Swiss Federal Nuclear Safety Directorate
CH-5303 Wurenlingen
SWITZERLAND
Attn: S. Chakraborty

No. of Copies

1 Korea Atomic Energy Research Inst.
Korea Adv. Energy Research Inst.
P.O. Box 7
Daeduk-Danji 305-353
Taejan
KOREA
Attn: C.K. Park

2 UKAEA
Winfrith, Dorchester
Dorset DT2 8DH
UNITED KINGDOM
Attn: A. Nichols 102/A50
S. Kinnersly 204/A32

1 UKAEA Culham Laboratory
Abingdon
Oxfordshire OX14 3DB
UNITED KINGDOM
Attn: B.D. Turland E5.157

30 1810 D.W. Schaeffer
7141 Technical Library (5)
7151 Technical Publications (1)
6400 N.R. Ortiz
6403 W. von Riesemann
6404 D.A. Powers (5)
6422 M.D.Allen
6422 N. Bixler
6422 T.K. Blanchat
6422 R.E. Blose
6422 J.E. Brockmann
6422 R.M. Elrick
6422 T. Heames
6422 M. Pilch
6423 K.O. Reil
6429 K.E. Washington
7042 F.E. Arellano
7725 E.R. Copus
8523-2 Central Technical Files

DATE
FILMED
1/12/94
END